INTERNATIONAL DOCTORAL
SCHOOL OF THE USC

Marcelina
Abal Sanisidro

PhD Thesis

Bioconjugation of proteins to nanoparticles for the development of advanced therapies

Santiago de Compostela, 2023

Doctoral Programme in Molecular Medicine

USC UNIVERSIDADE DE SANTIAGO DE COMPOSTELA

ESCOLA DE DOUTORAMENTO INTERNACIONAL DA USC

DOCTORAL THESIS

BIOCONJUGATION OF PROTEINS TO NANOPARTICLES FOR THE DEVELOPMENT OF ADVANCED THERAPIES

Author

Marcelina Abal Sanisidro

Director: María de la Fuente Freire

Tutor: Rafael López López

DOCTORAL PROGRAMME IN MOLECULAR MEDICINE

SANTIAGO DE COMPOSTELA

ESCOLA DE DOUTORAMENTO
INTERNACIONAL DA USC

I, **Marcelina Abal Sanisidro**, author of this thesis, have no conflict of interest to declare.

This doctoral thesis was supported by the Health Research Institute of Santiago de Compostela under the grant program "Axudas predoutorais, en réxime de concorrencia competitiva, para a realización de teses de doutoramento no marco dos grupos de investigación do Instituto de Investigación Sanitaria de Santiago (IDIS)" (2020).

A Kira, mi todo.

"I... a universe of atoms, an atom in the universe"

RICHARD P. FEYNMAN

"Dans la vie, rien n'est à craindre, tout est à comprendre"

MARIA SKŁODOWSKA-CURIE

"There is no gate, no lock, no bolt that you can set upon the freedom of my mind"

VIRGINIA WOOLF

Table of contents

TABLE OF CONTENTS

Abstract 7

Resumen 10

Resumo 13

Resumo *in extenso* 16

Introduction 27

Hypotheses 61

Objectives 63

Chapter I 65

Self-illuminating nanoconjugates (SI-NCs) trigger an effective anti-tumor Photodynamic Therapy (PDT) response in pancreatic ductal adenocarcinoma 66

Chapter II 110

Biocompatible and Versatile Self-Illuminating Sphingomyelin Nanosystems as a Potent Tool to Improve Cancer Therapies 111

Chapter III 175

Versatile and efficient protein association through chemically modified Sphingomyelin Nanosystems (SNs) for enhanced delivery 176

Chapter IV 217

Anakinra-loaded Sphingomyelin Nanosystems (ANK-SNs) to Immunomodulate the Tumor Microenvironment (TME) in Pancreatic Ductal Adenocarcinoma (PDAC) 218

Chapter V 249

Sphingomyelin Nanoparticles (SNPs) for the efficient intracellular delivery of CRISPR/Cas9 genome editing systems 250

Overall discussion 251

Conclusions 275

Abbreviations 278

Agradecimientos 289

Ethical issues and annexes 294

Abstract

ABSTRACT

Proteins are biomacromolecules that exist in a wide range of biological processes, such as the activation/inhibition of signaling pathways, molecular recognition and biocatalysis, characteristics that make them promising therapeutic agents. In fact, its greater affinity and specificity compared to drugs based on small molecules, presents itself as a perfect alternative treatment option. Also, for replacement therapies when endogenous proteins are not functional, aiming to restore or supplement the deficient biological substances, ensuring that essential physiological processes are supported and regulated appropriately within the body. In addition, the nature of proteins guarantees their biocompatibility and biodegradability, since their degradation products (amino acids) are well known and excreted by the body, reducing their potential toxicity. The use of genetic engineering allows to modify its properties, improving its functional activity and biological stability. However, problems related to their unfolding, enzymatic degradation in biological systems, short half-life, little or no permeability through cell membranes, and low bioavailability in parenteral and non-parenteral routes, make their administration difficult and inefficient for their use in the clinic. Since the approval of human insulin in recombinant protein form by the US Food and Drug Administration (FDA) in 1982, many more therapeutic proteins have been approved in recent years. However, most of them are based on recombinant proteins or monoclonal antibodies (mAb) that depend on continuous administration and are mainly used in immunotherapies or metabolic disorders. In this sense, nanotechnology has become an innovative and powerful tool for protein delivery, overcoming the aforementioned limitations.

In this frame, the main aim of this thesis is the development of novel protein nanotherapeutics by exploring several bioconjugation strategies to different types of nanoparticles, quantum dots and sphingomyelin nanoemulsions (SNs), providing evidence of the potential of this approach in cancer therapy and gene editing.

In the first and second chapters of this thesis, two types of "self-illuminating" nanosystems (metallic quantum dots and biocompatible sphingomyelin nanosystems, SNs) were developed to

associate a bioluminescent enzyme RLuc8 that in combination with a photosensitizer will trigger a BioLight photodynamic therapy (BL-PDT) to induce cell death in pancreatic cancer patient-derived xenografts PDX models *in vitro* and *in vivo*. Concretely in the second chapter, SNs were adaptaed to incorporate the photosensitizer in the oil core and surface-associated the RLuc8. Moreover, SNs only containing RLuc8 enzyme was studied as an imaging and reporter tool to decipher *in vivo* fate. In the third chapter, we explored the incorporation of PEG-lipids modified with active chemical functional groups enabling the covalently linkage of proteins onto the surface of SNs (P-SNs) independently of their molecular weight (MW) and net charge at physiological pH (isoelectrical point; pI). The established P-SNs were characterized for their physicochemical properties. *In vitro* experiments allowed confirming and highly efficient cell internalization and the absence of cytotoxic effects. In the fourth chapter, SNs were loaded with the therapeutic protein Anakinra (Kineret®; IL-1 antagonist) to target the extracellular receptor IL-1R. *In vitro* testing of ANK-SNs confirmed an immunomodulatory effect in PDAC tumor microenvironment (TME), and a strong inhibition of pro-inflammatory cytokines secretion by CAFs and Th17 differentiated cells was observed. *[Confidential section]*

Overall, this thesis proves the real potential and development of a novel nanotherapeutic based on the association of a versatile group of proteins to quantum dots and SNs by exploring several bioconjugation strategies. In addition, SNs were combined with the encapsulation of small drugs and/or *[Confidential section]* to effectively induce a potent therapeutic response in different biomedical diseases such as cancer and gene editing. Moreover, the developed nanotherapeutics were evaluated in several preclinical models (*[Confidential section]* and mice) providing valuable information for the future research and translation.

Resumen

RESUMEN

Las proteínas son biomacromoléculas que participan en una amplia gama de procesos biológicos, como la activación/inhibición de vías de señalización, el reconocimiento molecular y la biocatálisis, características que las convierten en prometedores agentes terapéuticos. De hecho, su mayor afinidad y especificidad en comparación con los medicamentos basados en moléculas pequeñas, se presenta como una opción de tratamiento alternativa perfecta. Además, se utilizan en terapias de reemplazo cuando las proteínas endógenas no son funcionales, con el objetivo de restablecer o complementar las sustancias biológicas deficientes, asegurando que los procesos fisiológicos esenciales sean respaldados y regulados adecuadamente en el cuerpo. La naturaleza de las proteínas garantiza su biocompatibilidad y biodegradabilidad, ya que sus productos de degradación (aminoácidos) son conocidos y excretados por el cuerpo, reduciendo su toxicidad potencial. El uso de la ingeniería genética permite modificar las propiedades de las proteínas, mejorando su actividad funcional y estabilidad biológica. Sin embargo, problemas relacionados con su desdoblamiento, degradación enzimática en sistemas biológicos, corta vida media, escasa permeabilidad a través de membranas celulares y baja biodisponibilidad en rutas parenterales y no parenterales hacen que su administración sea difícil e ineficiente para su uso clínico. Desde la aprobación de la insulina humana en forma de proteína recombinante por la Administración de Alimentos y Medicamentos de los Estados Unidos (FDA) en 1982, se han aprobado muchas más proteínas terapéuticas en años recientes. Sin embargo, la mayoría de ellas se basan en proteínas recombinantes o anticuerpos monoclonales (mAb) que dependen de una administración continua y se utilizan principalmente en inmunoterapias o trastornos metabólicos.

En este sentido, la nanotecnología se ha convertido en una herramienta innovadora y poderosa para la entrega de proteínas, superando las limitaciones mencionadas anteriormente. En esta tesis, el objetivo principal es el desarrollo de nuevos nanoterapéuticos de proteínas mediante la exploración de diversas estrategias de bioconjugación con diferentes tipos de nanopartículas, puntos cuánticos (QDots) y nanoemulsiones de esfingomielina (SNs), proporcionando evidencia del potencial de este enfoque en la terapia del cáncer y la edición génica.

En los primeros dos capítulos de esta tesis, se desarrollaron dos tipos de nanosistemas "autoiluminadores" (puntos cuánticos metálicos, QDots, y nanosistemas de esfingomielina biocompatibles, SNs) para asociar una enzima bioluminiscente RLuc8 que, en combinación con un fotosensibilizador, desencadenará una terapia fotodinámica BioLight (BL-PDT) para inducir la muerte celular en modelos de xenoinjertos derivados de pacientes con cáncer de páncreas *in vitro* e *in vivo*. Concretamente, en el segundo capítulo, se adaptaron los SNs para incorporar el fotosensibilizador en el núcleo oleoso y asociar la RLuc8 en la superficie. Además, se estudiaron SNs que solo contenían la enzima RLuc8 como una herramienta de imagen y reportero para descifrar el destino *in vivo*. En el tercer capítulo, se exploró la incorporación de lípidos PEG modificados con grupos químicos activos que permiten la unión covalente de proteínas a la superficie de los SNs (P-SNs), independientemente de su peso molecular (MW) y carga neta a pH fisiológico (punto isoeléctrico; pI). Los P-SNs establecidos se caracterizaron por sus propiedades fisicoquímicas. Experimentos *in vitro* confirmaron una internalización celular altamente eficiente y la ausencia de efectos citotóxicos. En el cuarto capítulo, se cargaron los SNs con la proteína terapéutica Anakinra (Kineret®; antagonista de IL-1) para dirigirse al receptor extracelular IL-1R. Las pruebas *in vitro* de ANK-SNs confirmaron un efecto inmunomodulador en el microambiente tumoral (TME) del adenocarcinoma ductal de páncreas (PDAC), y se observó una fuerte inhibición de la secreción de citoquinas proinflamatorias por los fibroblastos asociados al cáncer (CAF) y células diferenciadas Th17. *[Sección confidencial]*

En general, esta tesis demuestra el potencial real y el desarrollo de un nuevo nanoterapéutico basado en la asociación de un grupo versátil de proteínas con QDots y SNs mediante la exploración de diversas estrategias de bioconjugación. Además, los SNs se combinaron con la encapsulación de pequeños medicamentos y/*[sección confidencial]* para inducir de manera efectiva una respuesta terapéutica potente en diferentes enfermedades biomédicas como el cáncer y la edición génica. Además, los nanoterapéuticos desarrollados se evaluaron en varios modelos preclínicos (*[sección confidencial]* y ratones), proporcionando información valiosa para la investigación y aplicación futuras.

Resumo

RESUMO

As proteínas son biomacromoléculas que participan nunha ampla gama de procesos biolóxicos, como a activación/inhibición de vías de sinalización, o recoñecemento molecular e a biocatálise, características que as converten en axentes terapéuticos prometedores. De feito, a súa maior afinidade e especificidade en comparación cos fármacos baseados en moléculas pequenas preséntase como unha opción de tratamento alternativa perfecta. Ademais, empréganse en terapias de reemplazo cando as proteínas endóxenas non son funcionais, co obxectivo de restaurar ou complementar substancias biolóxicas deficientes, garantindo que os procesos fisiolóxicos esenciais estean apoiados e regulados adecuadamente no organismo. A natureza das proteínas garante a súa biocompatibilidade e biodegradabilidade, xa que os seus produtos de degradación (aminoácidos) son coñecidos e excretados polo organismo, reducindo a súa potencial toxicidade. O uso da enxeñaría xenética permite modificar as propiedades das proteínas, mellorando a súa actividade funcional e a estabilidade biolóxica. Non obstante, problemas relacionados coa seu desdobramento, degradación enzimática nos sistemas biolóxicos, curta vida media, escasa permeabilidade a través das membranas celulares e baixa biodisponibilidade nas vías parenterais e non parenterais fan que a súa administración sexa difícil e ineficiente para o seu uso clínico. Desde a aprobación da insulina humana en forma de proteína recombinante pola Administración de Fármacos e Alimentos dos Estados Unidos (FDA) en 1982, aprobáronse moitas máis proteínas terapéuticas nos últimos anos. Non obstante, a maioría deles baséanse en proteínas recombinantes ou anticorpos monoclonais (mAb) que dependen da administración continuada e que se utilizan principalmente en inmunoterapias ou trastornos metabólicos.

Neste sentido, a nanotecnoloxía converteuse nunha ferramenta innovadora e poderosa para a entrega de proteínas, superando as limitacións mencionadas anteriormente. Nesta tese, o obxectivo principal é o desenvolvemento de novas nanoterapéuticas proteicas mediante a exploración de diversas estratexias de bioconxugación con diferentes tipos de nanopartículas, puntos cuánticos

(QDots) e nanoemulsións de esfingomielina (SN), proporcionando evidencias do potencial deste enfoque na terapia do cancro e na terapia de edición do xenoma.

Nos dous primeiros capítulos desta tese desenvolvéronse dous tipos de nanosistemas "autoiluminantes" (puntos cuánticos metálicos, QDots, e nanosistemas de esfingomielina biocompatibles, SNs) para asociar un enzima bioluminiscente RLuc8 que, en combinación cun fotosensibilizador, desencadeará unha terapia de fotodinámica BioLight (BL-PDT) para inducir a morte celular en modelos de xenoinjertos derivados de pacientes con cancro de páncreas *in vitro* e *in vivo*. En concreto, no segundo capítulo, adaptáronse os SNs para incorporar o fotosensibilizador ao núcleo oleoso e asociar RLuc8 na superficie. Ademais, os SNs que conteñen só o enzima RLuc8 foron estudados como ferramenta de imaxe e reportero para descifrar o destino *in vivo*. No terceiro capítulo explorouse a incorporación de lípidos PEG modificados con grupos químicos activos que permiten a unión covalente de proteínas á superficie dos SNs (P-SNs), independentemente do seu peso molecular (PM) e carga neta a pH fisiolóxico. (punto isoeléctrico; pI). Os P-SN establecidos caracterizáronse polas súas propiedades fisicoquímicas. Experimentos *in vitro* confirmaron unha internalización celular altamente eficiente e a ausencia de efectos citotóxicos. No cuarto capítulo, os SNs cargáronse coa proteína terapéutica Anakinra (Kineret®; antagonista de IL-1) para dirixirse ao receptor extracelular IL-1R. As probas *in vitro* de ANK-SN confirmaron un efecto inmunomodulador sobre o microambiente tumoral (TME) do adenocarcinoma ductal pancreático (PDAC) e unha forte inhibición da secreción de citocinas proinflamatorias por fibroblastos asociados ao cancro (CAF) e células diferenciadas Th17. *[Sección confidencial]*.

En xeral, esta tese demostra o potencial real e o desenvolvemento dunha nova nanoterapéutica baseada na asociación dun grupo versátil de proteínas con QDots e SNs mediante a exploración de diversas estratexias de bioconxugación. Ademais, os SNs combináronse coa encapsulación de pequenos fármacos e/*[sección confidencial]* para inducir eficazmente unha potente resposta terapéutica en diferentes enfermidades biomédicas como o cancro e a edición de xenes. Ademais, os nanoterapéuticos desenvolvidos foron avaliados en varios modelos preclínicos (*[sección confidencial]* e ratos), proporcionando información valiosa para futuras investigacións e aplicacións.

Resumo *in extenso*

RESUMO *IN EXTENSO*

As proteínas son macromoléculas biolóxicas que desempeñan un papel fundamental nunha ampla variedade de procesos e funcións biolóxicas tales como catalizar reaccións bioquímicas, recoñecemento molecular de alta afinidade, transporte de moléculas, forman parte das estruturas celulares e, participan activamente na activación/inhibición de vías celulares, entre outros. Por estes motivos, destácanse como candidatas ideais para actuar como fármacos debido á súa natureza endóxena e propiedades específicas. A pesar da súa importancia, o desenvolvemento de fármacos terapéuticos baseados en proteínas presenta desafíos, como a fraxilidade da súa estrutura e a súa susceptibilidade á degradación enzimática, o que dificulta a súa modificación e formulación.

A orixe dos fármacos terapéuticos baseados en proteínas remóntase á purificación da insulina en 1922 para o tratamento da diabete tipo I. Con todo, o seu crecemento explosivo comezou coa aprobación da insulina humana en forma de proteína recombinante pola US Food and Drug Administration (FDA) en 1982 para o tratamento da diabete mellitus tipo I e tipo II. Dende entón, máis de 130 proteínas e péptidos foron aprobados para uso clínico, mostrando eficacia en tratamentos contra o cancro, enfermidades infecciosas, metabólicas e autoinmunes. A pesar dos seus beneficios, as proteínas terapéuticas enfrontan importantes limitacións debidas ás súas características inherentes, como a súa curta vida media, inmunoxenicidade e dificultades na súa entrega. Para superar estas desvantaxes, desenvolvéronse sistemas de entrega de proteínas versátiles, como a súa encapsulación en micropartículas, a súa modificación química con polímeros hidrofílicos ou cadeas carbonadas hidrofóbicas para aumentar a circulación sanguínea e a enxeñaría de proteínas recombinantes. Con todo, a nanotecnoloxía emerxe como unha solución poderosa.

Ata a data, máis de 80 nanomedicinas recibiron a aprobación da FDA e da Axencia Europea de Medicamentos (EMA). Dende a primeira aprobación en 1989 de Diprivan®, un anestésico encapsulado en componentes PEGilados, comercializáronse moitos máis para tratar unha ampla gama de enfermidades. Exemplos notables inclúen Doxil® (1995), aprobado para a terapia do cancro e aínda en uso, así como as recentes vacinas de ARNm desenvolvidas por BioNTech/Pfizer

e Moderna, amplamente utilizadas en todo o mundo para combater a enfermidade COVID-19. Con todo, a pesar do considerable número de nanomedicinas aprobadas nas últimas tres décadas, moitas aínda están en ensaios clínicos e a investigación continúa crecendo cada ano para abordar diversas aplicacións. Non obstante, é crucial destacar que o 90% dos candidatos a nanomedicinas non logran obter a aprobación, enfrontándose a desafíos como a baixa traslación que presentan moitas formulacións de nanopartículas, o mantemento das súas propiedades durante o escalado industrial, a rendibilidade e a heteroxeneidade entre os pacientes. Con todo, a comprensión da biodistribución e destino *in vivo* das nanopartículas é a característica máis esencial. A pesar destes desafíos, varias candidatas superaron as dificultades e introducíronse con éxito na clínica. Neste contexto, as nanomedicinas dispoñibles comercialmente centránse principalmente en terapias contra o cancro. Con todo, destaca o aumento significativo no desenvolvemento de nanomedicinas de ARNm, impulsado polo impacto da situación da COVID-19 e a tendencia a aplicar esta tecnoloxía en outros campos biomédicos. Ademais, investigacións recentes deron lugar ao deseño de nanopartículas máis sofisticadas que poden conter múltiples compoñentes para funcionar como sistemas duais, permitindo o direccionamento activo, a liberación controlada de fármacos, terapias combinadas e enfoques teranósticos. Avances considerables en xenética e proteómica revelan que as respostas a tratamentos poden variar entre pacientes coa mesma enfermidade. Aquí, as nanomedicinas abriron o camiño cara á aplicación dunha "medicina personalizada", deseñando nanomedicinas precisas para casos particulares.

Polo tanto, o uso de nanomedicinas para a entrega e liberación de proteínas ten varios beneficios e vantaxes, tales como: 1) protexer a carga da degradación; 2) mellorar a solubilidade e estabilidade e, por tanto, a súa biodispoñibilidade; 3) liberación controlada, reducindo a dose total e a toxicidade potencial, mellorando o perfil farmacocinético; 4) administración a sitios específicos mediante a adición de ligandos dirixidos; 5) mellor eficacia e seguridade; e 6) redución dos custos das nano-farmacéuticas e da atención médica en xeral, beneficiando aos pacientes. Ademais, as nanomedicinas poden deseñarse e modularse facilmente cambiando a composición para a súa aplicación desexada. En canto á composición, as baseadas en lípidos e polímeros son as máis representativas no mercado. En canto á súa aplicación, as nanomedicinas dispoñibles comercialmente utilízanse para unha gran variedade de enfermidades, sendo o cancro o máis representativo. Con todo, outras enfermidades como as hematolóxicas, infecciosas, neurodexenerativas, endocrinas e máis, obtiveron beneficios das nanomedicinas e moitas máis están en desenvolvemento e ensaios clínicos.

Nesta tese de investigación, propoñemos o desenvolvemento dun enfoque innovador e adecuado para a creación dunha variedade de nanosistemas destinados á entrega eficiente de proteínas de diferente natureza mediante o desenvolvemento de diferentes tipos de nanoplataformas, como puntos cuánticos metálicos (quantum dots) para a súa aplicación en terapia fotodinámica (PDT), nanoemulsións de esfingomielina biodegradables e biocompatibles (SNs) e nanopartículas lipídicas baseadas en esfingomielina (SNPs). Cabe destacar que as SNs para a entrega eficiente de pequenos fármacos, axentes de imaxe e outras biomoléculas xa foron exploradas en publicacións anteriores do noso grupo.

En primeiro lugar, asociouse a proteína bioluminiscente luciferasa (RLuc8) aos nanomateriais metálicos chamados puntos cuánticos (quantum dots; QDots), formando así os nanosistemas denominados nanoconxugados auto-iluminados ("self-illuminating" nanoconjugates; SI-NCs), para unha vez activados mediante o substrato específico coelenterazina (CTZ) excitar ao fármaco fotosensible (photosensitizer; PS) verteporfina e producir unha terapia fotodinámica (PDT) desencadeada por bioluz (BL) (**Figura 1**). Para iso, en primeiro lugar, sintetizáronse os SI-NCs mediante unha reacción química denominada condensación de amidas vía activación do grupo carboxílica mediante o reactivo EDC (1-Ethyl-3-(3-dimetilaminopropil) carbodiimide). Posteriormente, caracterizáronse fisicoquimicamente o seu tamaño, carga superficial, morfoloxía, porcentaxe de proteína asociada e a súa capacidade para emitir bioluz.

Unha vez caracterizados, avaliáronse *in vitro*. Primeiramente, testouse a súa internalización en diversas liñas celulares de adenocarcinoma ductal de páncreas (Mia PaCa-2, PANC-1, L3.6pl, PaTu8889T, PaTu8889S) sendo altamente eficaz a tan só 30 minutos de incubación, chegándose a testar até 3 horas. A distribución citosólica do PS verteporfina foi tamén levada a cabo. Consecuentemente, avaliouse o % de viabilidade dos SI-NCs e da verteporfina nas liñas celulares Mia PaCa-2, PANC-1 e L3.6pl tras 4 horas de incubación e determináronse as doses de traballo para os seguintes experimentos. Posteriormente, realizáronse os ensaios de eficacia da BL-PDT avaliando a viabilidade celular, a formación de especies reactivas de osíxeno (ROS) e a indución de apoptose tras o tratamento nas liñas de PDAC establecidas Mia PaCa-2 e L3.6pl e na liña de células primarias derivadas de paciente (PDX) Panc354, que serán usadas para a avaliación *in vivo* da BL-PDT.

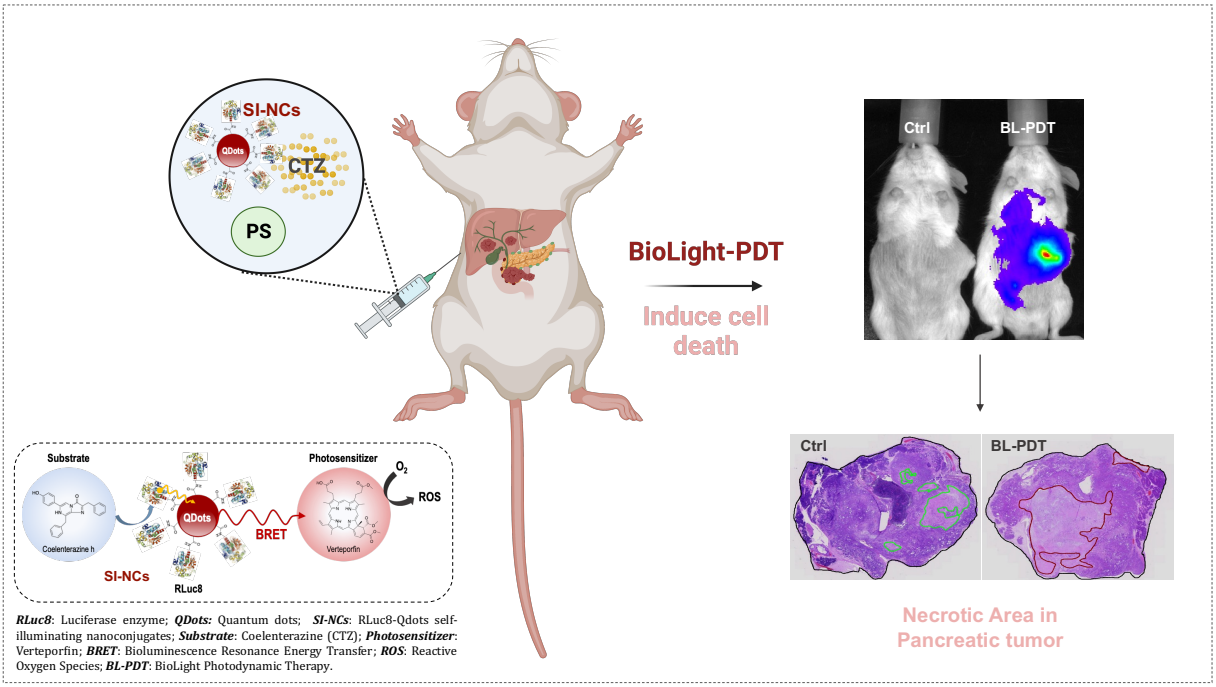

Figura 1. Representación gráfica do traballo realizado no Capítulo I no que se prepararon e caracterizaron nanoconxugados autoiluminados (SI-NCs) para a aplicación da terapia fotodinámica activada por bioluz (BL-PDT) en modelos de cancro de páncreas que inducen morte celular.

Finalmente, demostrouse a eficacia da BL-PDT *in vivo*. Para iso, realizáronse dous implantes ortotópicos de PDX de tumores pancreáticos, Panc354 e PancA6L, en ratos machos NOD/SCID. Mediante IVIS seguiuse a acumulación no tumor dos SI-NCs tras a súa inxección intraperitoneal, logrando chegar ao tumor 30 minutos despois da administración. Tras a realización de toda a terapia BL-PDT, sacrificáronse os ratos e leváronse a cabo estudos dos tumores e dos seus cortes histolóxicos. En xeral, nos ratos tratados de ambos grupos (c354 e A6L) observouse unha proporción maior de área necrótica en comparación cos controis. Ademais, os ensaios TUNEL mostraron niveis aumentados de apoptose nas mostras tratadas. Con todo, aínda que observamos unha forte tendencia na redución da proliferación celular no grupo de tratamento, non se reduciu de maneira significativa en comparación cos controis. Isto levounos á hipótese de que probablemente unha dose máis alta de SI-NCs sería beneficiosa para o tratamento de BL-PDT *in vivo*. Con todo, foi necesario axustar coidadosamente a dose debido á toxicidade intrínseca do núcleo de metais pesados dos QDots. Ademais, cabe destacar que logramos unha dose máis alta que a reportada na literatura.

En segundo lugar, propúxose aplicar o coñecemento adquirido na proba de concepto da BL-PDT a un nanosistema máis biocompatible e composto por materiais biodegradables, para así evitar a toxicidade e desconfianza na traslabilidade dos QDots na clínica. Así, baseándonos nos nanosistemas patentados polo noso grupo con Vitamina E e SM (SNs), modificamos a composición e proporción dos lípidos para enlazar quimicamente o RLuc8. Por tanto, engadimos DSPE-PEG(2k)-DBCO á composición lipídica e modificamos o RLuc8 cun enlazador de azida (N3-) para levar a cabo a reacción SPAAC "click" chemistry. Ademais, o fotosensibilizador Rose Bengal (RB) engadiuse ao núcleo de aceite e encapsulouse no nanosistema resultante. Deste modo, desenvolvéronse dous nanosistemas "autoiluminantes", SI-NS e SI-RB-NS que resultaron ser moi robustos e estables, e que foron caracterizados en profundidade mediante múltiples técnicas analíticas. Así, SI-NS utilizouse principalmente como sistema reporteiro para seguimento celular ("cell tracking") e SI-RB-NS coa incorporación do fotosensibilizador RB para a súa aplicación en BL-PDT en PDAC (**Figura 2**).

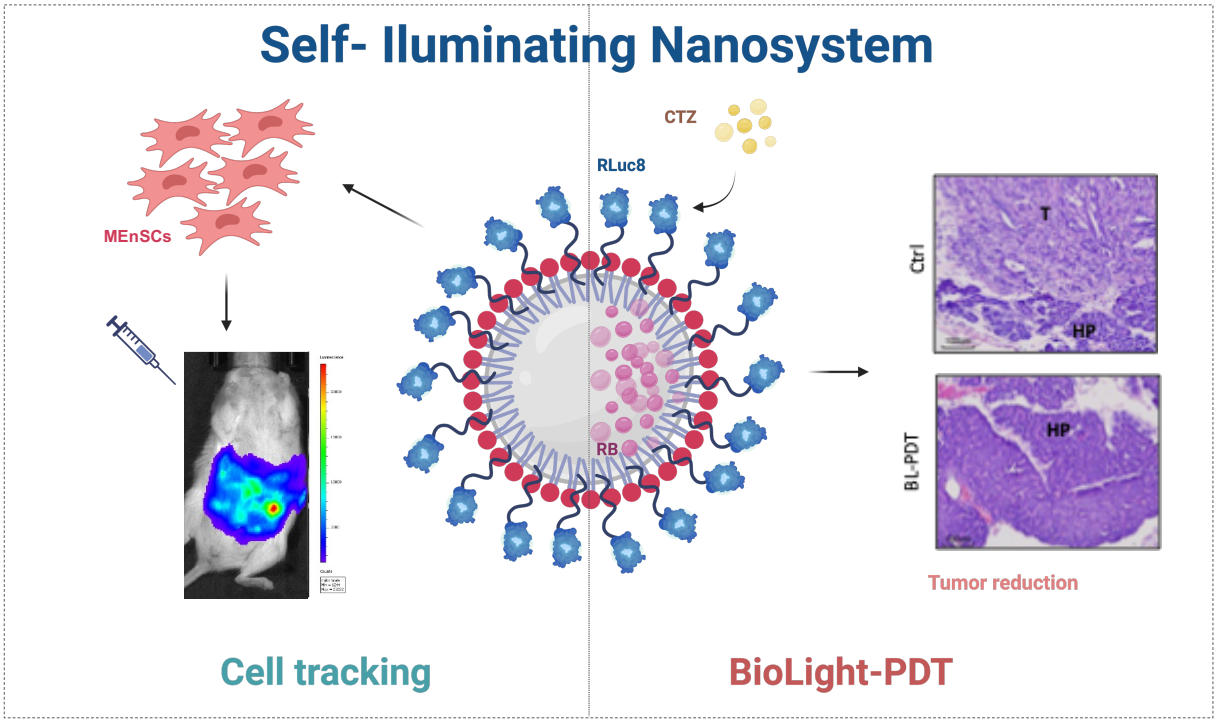

Figura 2. Representación gráfica do traballo realizado no Capítulo II no que se prepararon e caracterizaron nanosistemas autoiluminados (SI-NS e SI-RB-NS) para a súa aplicación como reporteiros para o seguimento celular ("cell tracking") e para a terapia fotodinámica activada por Biolight (BL-PDT) en modelos de cancro de páncreas para reducir a masa tumoral.

Para avaliar a capacidade bioluminiscente de SI-NS, administráronse retro-orbitalmente en ratos sanos e observouse a súa biodistribución mediante *in vivo* imaging systems (IVIS) tras a activación con coelenterazina. Posteriormente, sacrificáronse os ratos, extraéronse os órganos e analizáronse por citometría de fluxo onde se obtivo unha maior acumulación de SI-NS en pulmóns e fígado. A continuación, realizáronse ensaios de seguimento celular, marcáronse células mesenquimais de orixe menstrual (MenSCs) con SI-NS e á súa vez coinfectáronse cun adenovirus para o tratamento de tumores. Así, MenSCs foron administradas intraperitonealmente en ratos con tumor e a súa acumulación no tumor foi seguida mediante IVIS e a duración da bioluminiscencia no mesmo foi analizada durante días. Os ratos foron sacrificados en diferentes tempos para extraer os tumores e analizouse a emisión de bioluminiscencia das SI-NS acumuladas.

Tras a incorporación de RB no núcleo das SI-NS para formar SI-RB-NS, realizáronse varios ensaios *in vitro* para testar a súa capacidade de desencadear BL-PDT en varias liñas celulares de cancro de páncreas e en cultivos primarios de PDX, dando lugar a prometedores resultados. Unha vez aplicado o tratamento BL-PDT con SI-RB-NS, observouse unha forte diminución na viabilidade, un aumento nos niveis de ROS e a produción de apoptose en diferentes ensaios. SI-RB-NS logrou resultados sobresaíntes en comparación con intentos anteriores de aplicar RLuc8 vinculado ao RB para unha PDT efectiva. En canto aos experimentos *in vivo* con SI-RB-NS, implantáronse ortotópicamente ratos con células PDX Panc185 (cancro de páncreas). Nunha primeira instancia, marcaron SI-RB-NS con Cy5 para avaliar mediante citometría de fluxo que os nanosistemas chegaban e acumulaban no tumor, mediante administración retro-orbital (IV) e intraperitoneal (IP), acadouse unha maior acumulación tras a vía IP. Posteriormente, levouse a cabo a terapia BL-PDT *in vivo*. Dous ratos do grupo de tratamento mostraron unha marcada reducción do tumor en comparación co grupo non tratado. Ademais, as tincións H&E e os experimentos de cuantificación mostraron que a totalidade do tecido era un páncreas saudable. Con todo, esta tendencia non se observou en todos os ratos tratados por igual, deixando aberta a posibilidade de aumentar a dose ou o número de inxeccións de substrato, xa que os ratos non presentaron ningún signo de toxicidade. Aínda así, os resultados foron positivos e prometedores para a aplicación BL-PDT desencadeada por SI-RB-NS.

Ao longo deste traballo presentáronse os nanosistemas como unha ferramenta vantaxosa para a entrega de proteínas bioluminiscentes sen alterar a súa conformación nin actividade dunha maneira eficiente. Así deste modo, os nanosistemas desenvolvidos poden mellorar as limitacións descritas anteriormente para mellorar as terapias baseadas en proteínas terapéuticas ao aumentar a

súa solubilidade; ofrecer liberación controlada e sostida, evitando efectos secundarios; mellorar a biodistribución e, por tanto, a biodisponibilidade; e dirixirse a tecidos específicos. Para iso, os nanosistemas deben cumprir certos requisitos como manter a conformación e bioactividade das proteínas e ser formulados con materiais biocompatibles e biodegradables que proporcionen propiedades vantaxosas para evitar e minimizar respostas tóxicas ou inmunitarias adversas nos pacientes. A pesar dos bos resultados que moitos nanotransportadores para a entrega de proteínas lograron, a maioría deles non son versátiles para asociar diferentes tipos de proteínas, xa que a súa formulación e composición se axusta a cada biomolécula, dificultando así a formulación dunha nanoplataforma única ou con lixeiras modificacións.

Por iso, o desenvolvemento dunha nanopartícula única que cumpra cos requisitos para a súa traslación á clínica, que conteña materiais biocompatibles e biodegradables non inmunoxénicos, unha metodoloxía de preparación sinxela, aplicación versátil nunha ampla gama de proteínas e preservación da conformación e actividade das proteínas, foi o noso próximo obxectivo nesta tese. Con isto en mente, e con toda a investigación previa no desenvolvemento de nanopartículas para a entrega de proteínas nos capítulos anteriores, desenvolvemos unha nanoplataforma para a entrega dunha ampla gama de proteínas que abranguen diferentes pesos moleculares e pI. Baseándonos nas SNs (vitamina E e SM) engadíronse lípidos PEGilados modificados con grupos químicos activos para unir covalentemente proteínas. Tamén se estudaron lípidos con carga positiva ou negativa para explorar a asociación por interaccións electrostáticas. O obxectivo do Capítulo III foi validar un sistema nanométrico (SNs) baseado nunha composición de lípidos simple e reproducible que podería actuar como un transportador efectivo para proteínas (**Figura 3**).

Entre as estratexias químicas avaliadas, a SPAAC "click" chemistry (cicloadición azida-alquino) mostrou o mellor rendemento con todas as proteínas. Así, os nanosistemas que contiñan o grupo DBCO resultaron ser moi robustos, versátiles e estables ao longo do tempo en condicións de almacenamento sen comprometer as actividades das proteínas, sendo funcionais durante un ano, como se mostra na bioluminiscencia do nanosistema RLuc8-SNs(DBCO). Ademais, tamén foi o mellor nanosistema en termos de internalización celular en comparación con outros prototipos de SNs (Maleimida, NHS, TFP e DOTAP).

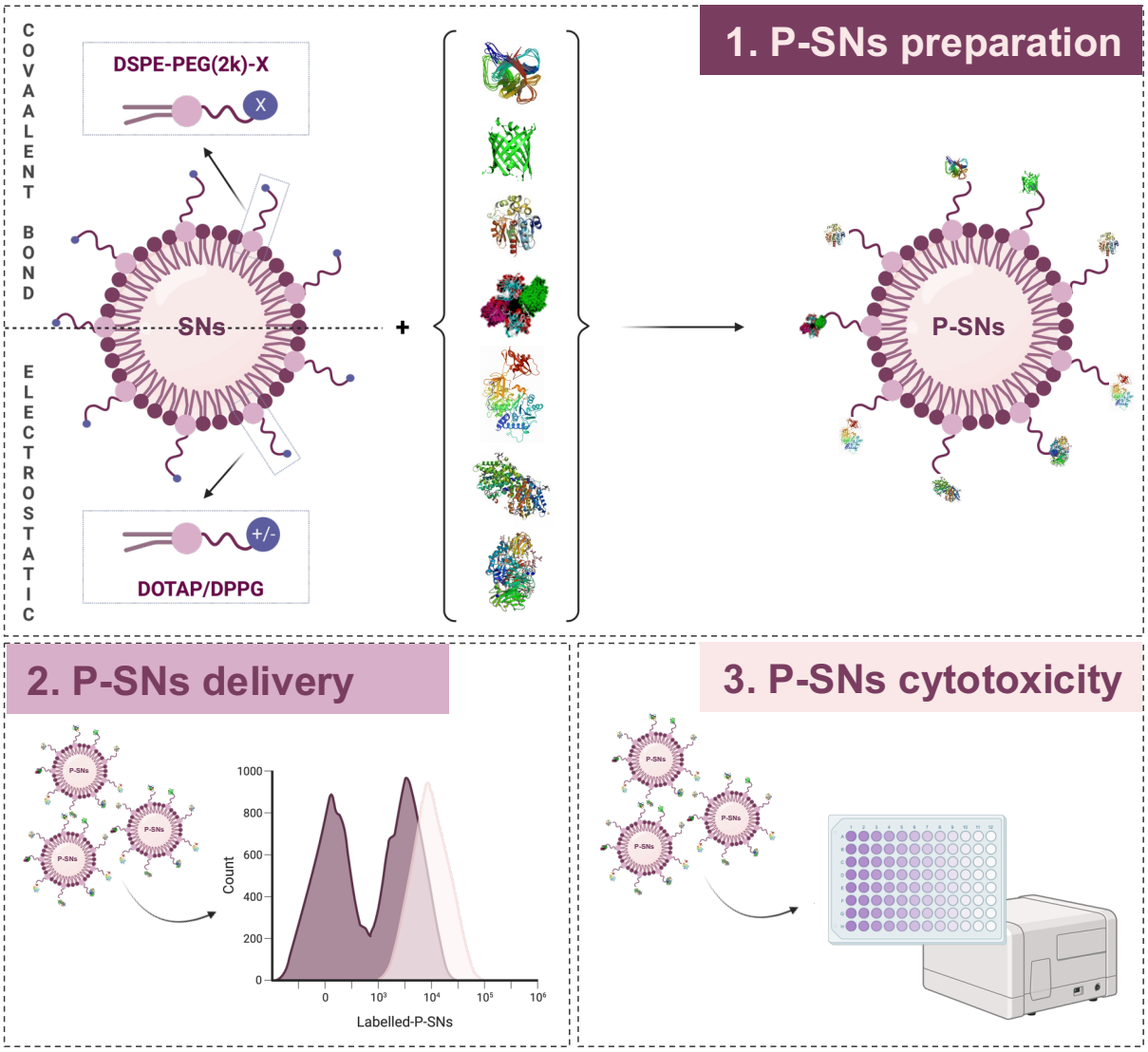

Figura 3. Representación gráfica do traballo realizado no Capítulo III cuxo obxectivo principal foi o desenvolvemento dunha nanoplataforma para a entrega eficiente de proteínas (Protein sphingomyelin nanosystems; P-SNs) independentemente do seu tamaño molecular (MW) e carga neta ou punto isoeléctrico (pI). Ademais, avaliouse a súa internalización eficiente en diferentes liñas e células e o seu perfil citotóxico para o seu posterior uso en cancro, terapia xénica e terapias de reemplazo de proteínas, entre outros usos biomédicos. (DSPE-PEG2k-X; X= DBCO, maleimida, NHS, TFP, COOH).

Ademais, aínda que as proteínas se amosan dispostas na superficie dos nanosistemas, a unión covalente e a composición dos nanosistemas ofrecen protección, permitindo ao mesmo tempo que o núcleo de aceite dos nanosistemas quede libre para cargarse con outras moléculas, como fármacos (Capítulo II) ou *[sección confidencial]* (Capítulo V). É importante destacar que a nosa nanoplataforma desenvolvida pode ser aplicable tanto para obxectivos extracelulares como intracelulares. En canto

aos obxectivos intracelulares, logramos a entrega intracelular de varias proteínas reporteras como GFP e R-ficoeritrina. Pero o máis destacado foi a entrega eficaz da enzima β-galactosidasa debido ao seu alto peso molecular (~465 kDa) e o mantemento dos seus catro dominios estruturais e a súa actividade.

Por outro lado, en canto aos obxectivos extracelulares confirmamos a interacción exitosa co receptor IL-1R, que xoga un papel clave nas respostas inflamatorias en PDAC, ao administrar a súa molécula antagonista anakinra asociada aos SNs, cuxo efecto antitumoral se estudou previamente en investigacións preclínicas (**Figura 4**). Neste contexto, tendo en conta o papel clave que xoga IL-1 na inflamación que promove o crecemento tumoral, desenvolvemos os nanosistemas ANK-SNs para mellorar a activación da resposta inmune no microambiente tumoral (TME) en PDAC.

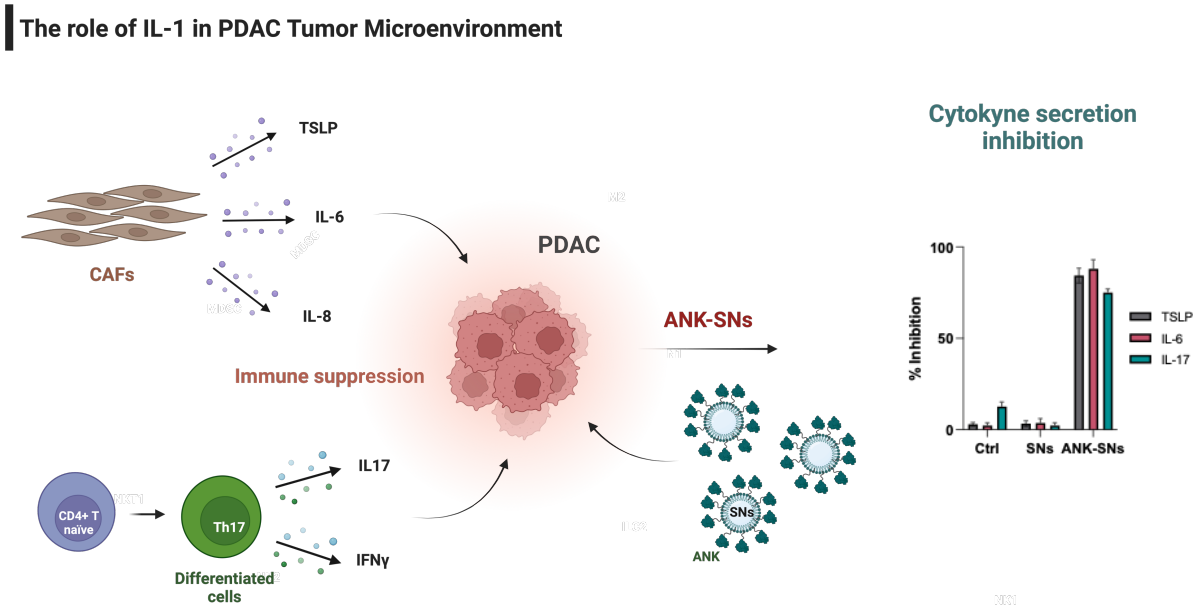

Figura 4. Representación gráfica do traballo realizado no Capítulo IV no que se deseñaron varias estratexias para unir a enzima terapéutica anakinra (ANK), antagonista do receptor IL-1R, a nanosistemas (SN) de esfingomielina para a súa avaliación como inmunomoduladores do microambiente tumoral (TME) en PDAC ao inducir a inhibición das citocinas secretadas polas células do TME e activando a resposta inmune neste tipo de tumores.

Preparáronse varios conxuntos de ANK-SNs unidos por diferentes estratexias químicas, a saber, a SPAAC "click chemistry" (DBCO), a reacción tiol-maleimida (MAL), a reacción con éster activo NHS (NHS) e mediante interaccións electrostáticas (DOTAP). En xeral, todas as formulacións presentaron tamaños de partícula pequenos (<200 nm) e unha poboación homoxénea. Posteriormente, avaliouse a súa capacidade para inhibir a secreción de citoquinas en células que compoñen o TME como CAFs e células Th17 diferenciadas extraídas de mostras de pacientes. Así, medíronse mediante un ensaio ELISA os niveis de TSLP, IL-6 e IL-8 segregados nas CAFs onde a maior inhibición produciuse nas mostras tratadas con ANK-SNs(NHS). Ademais, ANK-SNs(NHS) superaron ao fármaco libre ANK ao inhibir a secreción de IL-17 en células Th17 diferenciadas. Deste modo, probouse a eficaz actuación de ANK-SNs para inmunomodular o TME en PDAC.

[Sección confidencial]

En resumo, nesta tese establecemos o entendemento para a bioconxugación de proteínas a nanopartículas mediante diversas estratexias químicas para a súa aplicación en múltiples enfermidades e áreas biomédicas. Destacamos que demostramos a eficacia de dous nanosistemas diferentes "autoiluminantes" para o seu uso na terapia fotodinámica (PDT) no cancro de páncreas, xa sexa *in vitro* ou *in vivo*. Ademais, a versatilidade dos SNs permitiunos coencapsular medicamentos (fotosensibilizadores) e *[Sección confidencial]* xunto coa decoración superficial con proteínas. Os SNs poden adaptarse de maneira precisa para a incorporación dunha ampla variedade de proteínas, o que os converte nunha plataforma nanotecnolóxica prometedora para a entrega de proteínas tanto extracelulares como intracelulares. Por último, como perspectiva futura, esta tese abre a posibilidade de realizar estudos adicionais sobre o destino *in vivo* cargando axentes de imaxe, estudos toxicolóxicos, capacidade para desencadear respostas inmunitarias e a elucidación do perfil farmacocinético das P-SNs e dar un paso máis no desenvolvemento da medicina personalizada de precisión.

Introduction

INTRODUCTION

1. Proteins as therapeutics.

Proteins are biological macromolecules that play a key role in a broad range of biological processes and functions such as catalyzing biochemistry reactions, high affinity molecular recognition, controlling cell fates, transporting molecules, cellular structures, and activation/inhibition of cell pathways, among others [1,2]. Indeed, their endogenous nature and properties make them perfect candidates as therapeutics [3] **(Figure 1)**. Furthermore, compare to small drugs, proteins present a unique therapeutic window related to their biocompatibility and biodegradability alongside a higher specificity and activity [2,4,5]. It must be remarked that their degradation metabolites are recognized and eliminated by the body, reducing any potential toxicity of the treatment [6].

PROTEINS							
ENZYMES	**HORMONES**	**STRUCTURE**	**TRANSPORT**	**DEFENSE**	**CONTRACTILE**	**STORAGE**	**RECEPTORS**
	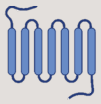	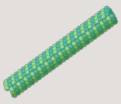					
FUNTION:	**FUNTION:**	**FUNTION:**	**FUNTION:**	**FUNTION:**	**FUNTION:**	**FUNTION:**	**FUNTION:**
Enzymes are the catalysts of all metabolic reactions, enable an organism to build up the chemical substances necessary for life.	Hormonal proteins are messenger proteins that help coordinate certain bodily functions.	Structural proteins maintains and protects the structure of the animal body.	Transport proteins are carrier proteins that move molecules from one place to another in the body.	Antibodies or immunoglobulins, are a core part of our immune system, attacking harmful microorganisms, rendering them inactive.	Contractile proteins are responsible for muscle contraction and movement	Storage proteins reserve amino acids for the body until ready for use.	Located on the outer part of the cells, they control the substances that enter and leave the cells. They activate enzymes or endocrine cells.
EXAMPLES:	**EXAMPLES:**	**EXAMPLES:**	**EXAMPLES:**	**EXAMPLES:**	**EXAMPLES:**	**EXAMPLES:**	**EXAMPLES:**
Proteases, trypsin…	Growth factors, cortisol, testosterone…	Collagen, keratin…	Hemoglobin, cytochromes…	IgG, IgE, IgA…	Actin, myosin…	Ferritin, ovalbumin…	GPCRs, ion-channel receptors…

Figure 1. Schematic representation of the different types of existing proteins.

The development of proteins therapeutics can be traced back to the first-time purified insulin from bovine pancreas for its use in type 1 diabetes in 1922 [7]. However, protein therapeutics did not attract the attention until the first Food and Drug Administration (FDA) approved recombinant protein human insulin in 1982 for the treatment of diabetes mellitus type I and type II [2,8]. Since then, over the last 4 decades, the development and exploitation of proteins therapeutics have experienced an enormous surge. Proteins drugs are now a key player for the treatment of a wide range of diseases, including cancer, metabolic disorders and autoimmune diseases [9,10]. Ever since, the market has been dramatically growing with more than 130 proteins or peptides for clinical use by the FDA [2,4]. These drugs are based in human antibodies, chimeric proteins, and protein scaffolds that have the ability to bind to undruggable targets resulting very effective in cancer, infections and inflammatory diseases [4,11–15]. Monoclonal antibodies (mAbs) have represented promising protein therapeutics since Muromonab-CD3 approval in 1986 [16]. For instance, the clinical validation of immune checkpoint mAbs that target the programmed death-1 (PD-1) receptor as Nivolumab and Pembrolizumab were considered a great advanced in cancer immunotherapy [11,17]. On the other side, many other proteins therapeutics have been marketed (**Tables 1-4**) such as PEGINTRON (for hepatitis C), Fabrazyme (for Fabry disease), Cotazym (for cystic fibrosis or pancreatic insufficiency), and many others [2].

Therapeutic	**Marketed name**	**Function**	**Clinical use**
Endocrine disorders (hormone deficiencies)			
Insulin human inhalation	Exubera®	Insulin formulated for inhalation with faster onset of action	Diabetes mellitus
Pramlintide acetate	Symlin®	Recombinant synthetic peptide analogue of human amylin	Diabetes mellitus, in combination with insulin
Growth Hormone (GH) somatotropin	Genotropin®, Humatrope®, Saizen®…	Anabolic and anticatabolic effector	GH deficiency, Turner syndrome, AIDS …

Therapeutic	Marketed name	Function	Clinical use
Haemostasis and thrombosis			
Factor VIII	Helixate®, Kogenate®, recombinate™, reFacto®	Coagulation factor	Haemophilia A
Factor IX	BeneFIX®	Coagulation factor	Haemophilia B
Protein C concentrate	Ceprotin®	Protein C inhibits coagulation factors Va and VIIIa	Treatment of venous thrombosis in patients with hereditary protein C deficiency
Metabolic enzyme deficiencies			
β-Glucocerebrosidase	Cerezyme®	Hydrolyzes glucocerebroside to glucose and ceramide	Gaucher's disease
Galsulphase	Naglazyme®	Cleaves the terminal sulphate from the GAG dermatan sulphate.	Mucopolysaccharidosis VI
Agalsidase-β	Fabrazyme®	Enzyme that hydrolyzes globotriao-sylceramide (GL3)	Fabry disease
Immunodeficiencies			
Adenosine deaminase	Adagen®	Metabolizes adenosine	Severe combined immunodeficiency disease due to adenosine deaminase deficiency
Pooled immunoglobulins	Octagam®	Intravenous immunoglobulin preparation	Primary immunodeficiencies

Table 1. Representative protein therapeutics replacing a protein that is deficient or abnormal [2,18].

Therapeutic	Marketed name	Function	Clinical use
Haematopoiesis			
Erythropoietin, epoetin-α	Epogen®, Procrit®	Stimulates erythropoiesis	Anaemia of chronic disease, myleodysplasia, anaemia or chemotherapy, preoperation
Oprelvekin	Neumega®	Stimulates megakaryocytopoiesis and thrombopoiesis	Prevention of severe thrombocytopaenia, especially after myelosuppressive chemotherapy
Filgrastim	Neupogen®	Stimulates neutrophil proliferation, differentiation and migration	Neutropaenia in AIDS or post-chemotherapy or bone-marrow transplantation, severe chronic neutropaenia
Fertility			
Human follicle-stimulating hormone (FSH)	Gonal-F®, Follistim®	Augments ovulation	Assisted reproduction
Human chorionic gonadotropin (HCG)	Ovidrel®	Stimulates ovarian follicle rupture and ovulation	Assisted reproduction
Immunoregulation			
Interferon-α2a (IFNα2a)	Roferon-A®	Mechanism unknown; immunoregulator	Hairy cell leukaemia, chronic myelogenous leukaemia, Kaposi's sarcoma, chronic hepatitis c infection
Interferon-β1b (rIFN-β)	Betaseron®	Mechanism unknown; antiviral and immunoregulator	Multiple sclerosis

Table 2. Representative protein therapeutics augmenting an existing pathway [2,18].

Therapeutic	Marketed name	Function	Clinical use
Enzymatic degradation of macromoleculess			
Botulinum toxin type A	Botox®	Cleaves sNAP25 at neuromuscular junctions to disrupt sNAre complex and prevent acetylcholine release, causing flaccid paralysis	Many types of dystonia, particularly cervical; cosmetic uses
Collagenase	Collagenase™, santyl®	Collagenase obtained from fermentation by Clostridium histolyticum; digests collagen in necrotic base of wounds	Debridement of chronic dermal ulcers and severely burned areas
Enzymatic degradation of small-molecule metabolites			
L-Asparaginase	ELSPAR®	Provides exogenous asparaginase activity, removing available asparagine from serum; purified from *E. coli*	Acute lymphocytic leukaemia, which requires exogenous asparagine for proliferation
Peg-asparaginase	Oncaspar®	Provides exogenous asparaginase activity, removing available asparagine from serum; purified from *E. coli*	Acute lymphocytic leukaemia, which requires exogenous asparagine for proliferation
Haemostasis and thrombosis			
Lepirudin	Refludan®	Recombinant hirudin, a thrombin inhibitor from the salivary gland of the medicinal leech *Hirudo medicinalis*	Heparin-induced thrombocytopaenia
Streptokinase	Streptase®	Converts plasminogen to plasmin; produced by group c β-haemolytic streptococci	Acute evolving transmural myocardial infarction, pulmonary embolism, …

Table 3. Representative protein therapeutics providing a novel function or activity [2,18].

Therapeutic	Marketed name	Function	Clinical use
Cancer			
Bevacizumab	Avastin®	Humanized mAb that binds all isoforms of VEGFA	Colorectal cancer, non-small-cell lung cancer
Cetuximab	Erbitux®	Humanized mAb that binds EGFR	Colorectal cancer, head and neck cancer
Panitumumab	Vectibix®	Human mAb that binds EGFR	Metastatic colorectal cancer
Alemtuzumab	Campath®	Humanized mAb directed against CD52 antigen on T and B cells	B-cell chronic lymphocytic leukaemia
Trastuzumab	Herceptin®	Humanized mAb that binds HER2/Neu cell surface receptor and controls cancer cell growth	Breast cancer
Immunoregulation			
Anakinra	Kineret®	Recombinant interleukin 1 (IL1) receptor antagonist	Moderate to severe active rheumatoid arthritis in adults
Etanercept	Enbrel®	Dimeric fusion protein between recombinant soluble TNF receptor and Fc portion of human immunoglobulin G1	Rheumatoid arthritis, psoriatic arthritis, ankylosing spondylitis, plaque psoriasis
Efalizumab	Raptiva®	Humanized mAb directed against cD11a	Adults with chronic moderate to severe plaque psoriasis who are candidates for systemic therapy or phototherapy

Table 4. Representative protein therapeutics that interfere with a molecule or organism [2,18].

Despite all the advantages and properties described for protein therapeutics, their fragile conformational macromolecular structure and functional activity must be preserved making them difficult to modify and/or formulate. In addition, direct delivery of protein therapeutics *in vitro* and *in vivo* is susceptible to unfolding and enzymatic degradation mainly. Protein therapeutics present short half-life within body and immunogenicity [5,19]. Their efficacy is limited to extracellular targets, considering their poor membrane permeability limiting their cellular internalization, due to their size and also to the fact that most of the proteins hold charge at neutral pH [20–22]. For this, protein therapeutics treatments require frequent administrations resulting non beneficial for their clinical use [1,4]. To overcome these unfavorable intrinsic proteins features, several approaches have been developed such as encapsulation, chemical modification with hydrophilic polymers or hydrophobic carbon chains to increase blood circulation, and recombinant protein engineering.

Versatile protein delivery systems have also been extensively studied over the last years. Delivery systems are design to protect, carry, enhance stability, and improve the release of therapeutic proteins in a controlled manner, at a sufficient dose, and at specific sites without altering the bioactivity, overall improving efficacy [3,23,24]. Despite these efforts and the launch of successful biological products into the market, such as Oncaspar® (polymer-based), there is still room for improvement. Thereby, optimal protein drugs with enhanced maintained activity, stability, pharmacokinetic and lack of immunogenicity are still in need. Nanotechnology arises as a powerful tool for the delivery of proteins. The feasibility of incorporate proteins in nano-vehicles that protect and carry them at the adequate site has increased attention during the last decades as we will further describe[25].

2. Nano-pharmaceuticals as novel medicines for the delivery of biomolecules.

The term nanotechnology can be defined as any technology operating on the nanoscale to have a functional application in the world [26,27]. This involves different fields in science such as chemistry, physics, and biology working together [26]. On the other side, nanomedicine arises in this field as the development of nano-pharmaceutical products for their use as either therapy or diagnostic tools in biomedicine [28]. Originally and by definition, nanoscale covers 1-100 nm **(Figure 2)** [29]. However, the FDA related to the fast-growing approved nanomedicines and the high number of ongoing clinical trials have set that nanomedicines are materials over 100-1000 nm [30].

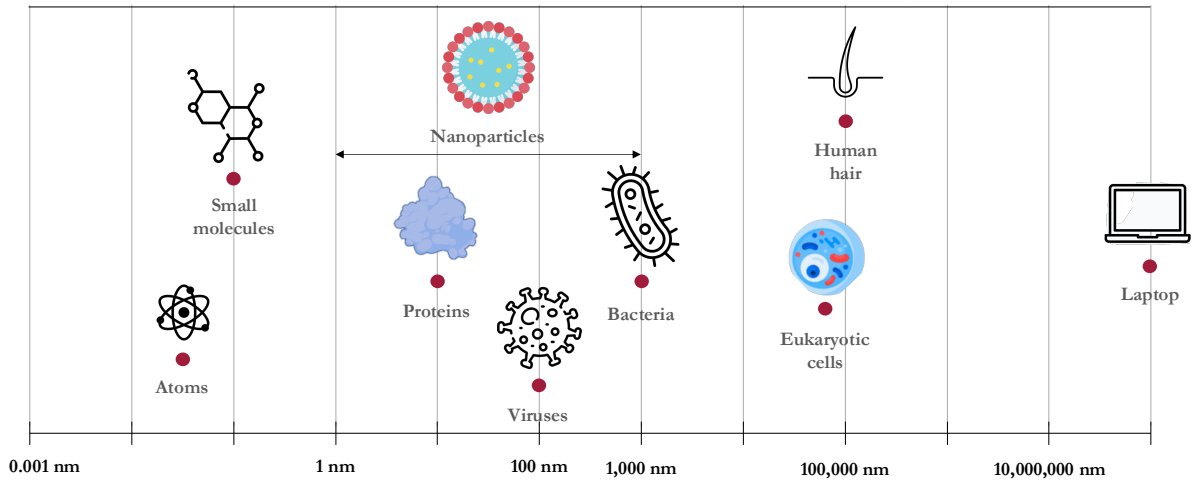

Figure 2. Size scale of relative dimensions of nanoparticles compared with other items. 'Created with BioRender.com' under a paid subscription.

Nano-pharmaceuticals play a key role in the current needs in clinic and in drug delivery, mainly related to overcoming the major limitations that affect conventional small drugs and biomolecules [31,32]. The most notably issues related to conventional drugs are that they present an immediate and high drug release after administration and poor delivery to the target site, making necessary frequent administration that may lead to associated toxicity. Low drug solubility directly affects efficacy as body tends to fast clearance drugs. In addition, they are unprotected against degradation processes when in circulation [33,34].

The use of nano-pharmaceuticals has several benefits and advantages such as: 1) protecting cargos from degradation; 2) improving drug solubility and stability, thus their bioavailability; 3) controlled drug released, reducing total dose and potential toxicity enhancing the pharmacokinetic profile; 4) delivering therapeutics to specifically sites by adding targeted ligands or allowing passive targeting and the accumulation of drugs by the enhanced permeability and retention (EPR) effect; 5) better efficacy and safety; and 6) reduction costs of nano-pharmaceuticals and overall healthcare benefiting patients [35–38]. In addition, nanomedicines can be easily designed and modulated by changing the composition for its desired application **(Figure 3)**. Attending composition, lipid-based and polymer-based nanocarriers are the most representative in the market. Regarding their application, commercially available nano-pharmaceuticals are used for a great deal of diseases being cancer the most representative. However, other diseases such as hematologic, infections,

neurodegenerative, endocrine ones, and more, have been benefitted from nanomedicines and many more that are in development and clinical trials [33,39,40].

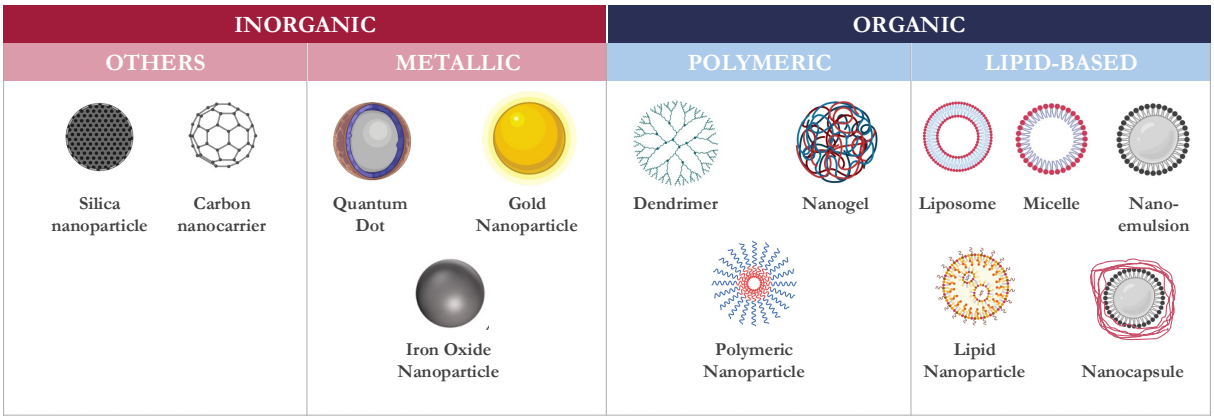

Figure 3. Schematic representation of the two main groups (inorganic and organic) of nanocarriers.

To date, more than 80 nano-pharmaceuticals have been approved by the FDA and the European Medicines Agency (EMA) [33,41]. Thus, since FDA first approval of Diprivan® in 1989 an anesthetic encapsulated in PEGylated components, many more have been marketed for a broad range of diseases. In **Figure 4**, we have resumed some of them to mention Doxil® (1995) approved for cancer therapy and still in use or the recent approved mRNA vaccines developed by BioNTech/Pfizer and Moderna worldwide used for the COVID-19 disease [42–44].

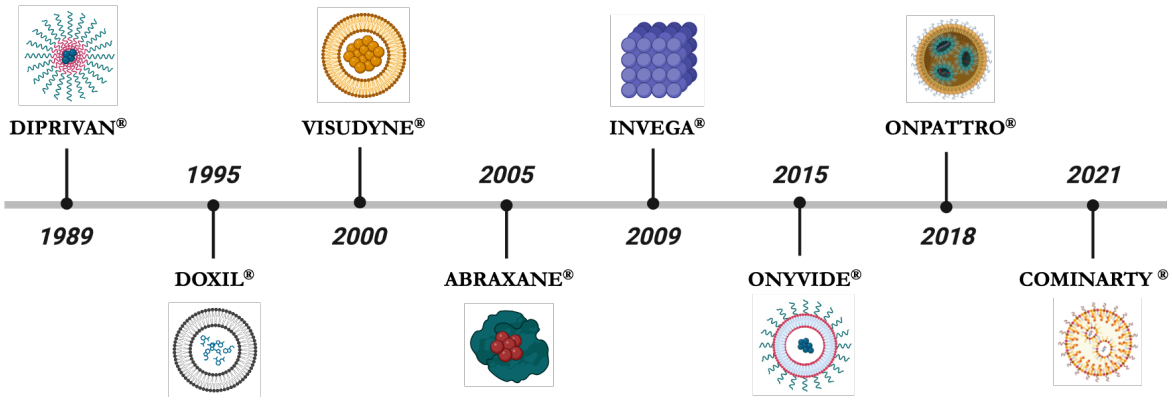

Figure 4. Representative nanomedicines approved by the FDA over time [45]. 'Created with BioRender.com' under a paid subscription.

Despite the high number of nanomedicines approved in the las 30 years, many of them are still in clinical trials, and its research keeps growing every year for multiple applications [41]. Even so, we should remark that 90% percent of the nanomedicines candidates fail the attempt to be approved [34]. This is due to many factors such as low translation of nanoparticles, maintenance of their properties through scale-up processes, cost-effectiveness, and the heterogenicity between patients [46–48]. However, the most important feature is understanding the *in vivo* fate of nanoparticles [48]. Nevertheless, many candidates have come through these challenges and are being marketed and successfully applied in clinic. In this sense, commercially available nanomedicines are mainly focused on cancer therapies [49]. However, we must remark the high increased in the development of mRNA nano-pharmaceuticals related to the impact of COVID-19 situation and the trend to apply this technology in other biomedical fields [50–52]. Recent research studies have emerged with the design of more sophisticated nanoparticles that can contain multiple components to work as dual systems for active targeting, drug-controlled release, combined therapies or theranostics approaches [53]. In this context, great advances in the research in genetics and proteomics have revealed that patients suffering from the same diseases, differ in their responses to treatments. Here, nano-pharmaceuticals have set the path to the application of a "personalized medicine" by designing a precise nanomedicine for each particular case [34,54]. For now on, we will focus on this precise nanomedicine for the delivery of protein therapeutics.

2.1. Intra- and extracellular targets in the application of novel protein therapeutics.

Target cells are those in which we have identified a receptor that regulates the specific functioning of a cell. Receptors and ligands come in many forms, but they all have something in common: a receptor only recognizes one or a few specific ligands and the other way round for ligands to receptors. Binding of the ligand to the receptor changes its shape or activity, allowing it to transmit a signal or directly produce a change within the cell[55–57]. There are many types of receptors, but they can be divided in two main groups: intracellular and extracellular receptors **(Figure 5)**. Intracellular receptors are proteins found in the cytoplasm or nucleus inside cells. Most of the ligands for intracellular receptors are small, hydrophobic molecules (e.g., steroid hormones) since they must trespass membranes to reach their receptors. Once inside cells the complex ligand-receptor changes its shape to enter the nucleus and regulate gene activity. Many signaling pathways,

involving both intracellular and extracellular receptors, produce changes in gene transcription. However, intracellular receptors are unique causing such changes directly, by binding to DNA and altering transcription themselves [58,59]. Extracellular receptors are membrane-anchored-proteins that bind ligands outside cells. In this sense, ligands do not need to trespass the cellular membranes, thus, many types of molecules including hydrophilic ones can act as ligands. Cell surface receptors contain three protein domains: extracellular domain that binds the ligand; a hydrophobic domain that trespass the membrane; and an intracellular domain that transmits the signal. The most remarkable receptors are ligand-gated ion channels, G protein-coupled receptors, and receptor tyrosine kinases [60–62].

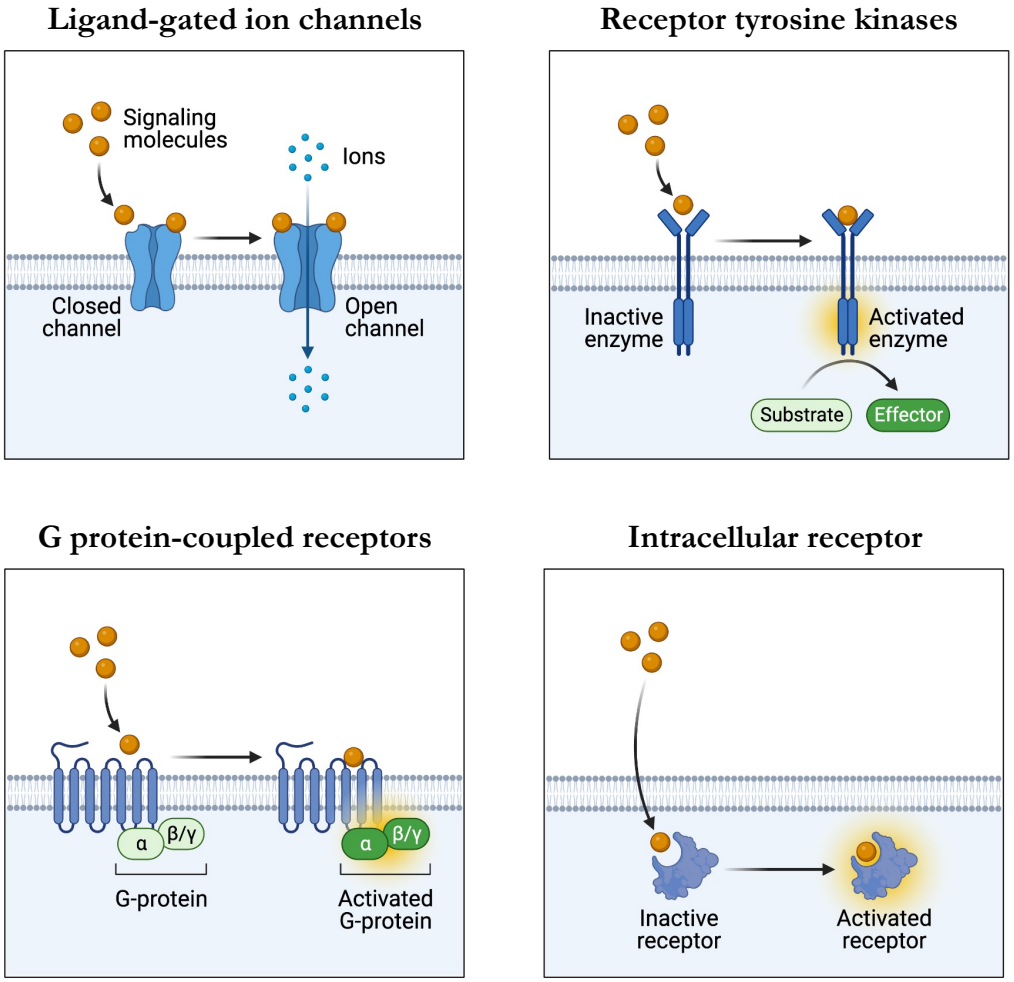

Figure 5. Schematic representation of intra- and extracellular receptors in cells. (*Reprinted from "Types of Cellular Receptors" by BioRender (2021). Retrieved from https://app.biorender.com/biorender-templates/figures/all/t-60ba45fff7aa2e00a8b7081c-types-of-cellular-receptors*).

Nowadays, there are commercially available drugs that simulate these growth factors and block these receptors at different levels, preventing cell growth[63]. They are known as directed therapies because they block the receptor, and lead cells to death. For instance, these therapeutics are frequently developed for cancer treatments due to the fact that healthy cells are not affected by this blockade and can continue to fulfill their function, therefore toxic effects are also reduced. However, only over 5% of the protein-kinases have been reached [64]. So, this has given rise to the term "undruggable" targets, referring to protein-receptors that cannot be targeted [65]. Giving the complexity of targeting intra- and extracellular targets, nanomedicines can be tailored to deliver protein therapeutics in multiple forms. Decorating the surface with antibodies, peptides or proteins allow them to reach specific site targets and perform the delivery of cargos. For instance, nano-pharmaceuticals can be designed for dual applications, by surface-coating with ligands and encapsulating drugs and/or other active pharmaceutical ingredient (APIs). On the other hand, if the API of interest is a protein therapeutic, it can be encapsulated within nanoparticles and be efficiently delivered to intracellular targets. Furthermore, nanomedicines have demonstrated their ability to reduce toxicity, to increase circulation times, and to achieve higher concentrations at the target size, leading to increased therapeutic efficiencies [66–68].

2.2. Approved nanomedicines for protein delivery and current clinical trials.

Direct delivery of proteins into cells encounter many obstacles as described above. To solve such challenges, nanotechnology has been designated as a powerful tool in the protein therapeutics field. Thus, proteins can benefit from nanoencapsulation strategies as they can be protected from premature degradation or denaturation, and circulation half-lives and stability can be enhanced, among other advantages already described [69]. Regarding this, a wide array of nanocarrier systems has been studied [20,70–72]. Protein therapeutics based on nanoparticles have been tailored to be loaded by two main methods namely, physical adsorption (entrapment) or chemical conjugation [73]. In addition to the fact that nanocarriers can be surface engineered to increase targeting to the specific subcellular compartments like cytosol, nucleus, and mitochondria [5]. In the last years, there has been an increased interest in the development of proteins nanocarriers, including polymeric nanoparticles, lipid-based nanoparticles, protein-based complex, cell-penetrating peptide-based carriers and inorganic nanoparticles [25,47,74]. Taking into consideration this, representative protein

therapeutics based on nanocarriers approved by FDA and/or EMA are described next (**Tables 5-6**) [34,38,39]. **Table 5** represents marketed protein-drugs conjugates. Proteins can be bound to drugs for their delivery (e.g. Abraxane® or Pazenir®) or act as a therapeutic as well, enhancing their effect (e.g. Ontak®). T**able 6** compiles representative nano-pharmaceuticals for protein delivery based on polymeric nanoconjugates and complexes.

Therapeutic	Carrier	Marketed name	Targeting/Function	Clinical use
Protein-drug conjugates				
Methotrexate	PEGylated certolizumab	Cimzia®	PEGylated blocker of tumor necrosis factor alpha (TNF-α)	Rheumatoid arthritis, Crohn's disease, psoriatic arthritis …
Denileukin (IL-2) Diftitox (diphteria toxin)	IL-2	Ontak®	Activated T-cells	Cutaneous T-cell lymphoma
Paclitaxel	Albumin	Abraxane®	Cancer and stroma cells	Breast. Non-small lung, Pancreatic cancer…
DM1 (or Emtansine)	Trastuzumab	Kadcyla®	Cancer cells	HER2+ breast cancer
Paclitaxel	Albumin	Pazenir®	Cancer cells	Breast. Non-small lung, Pancreatic cancer…

Table 5. Representative nano-pharmaceuticals based on proteins as delivery carriers [25,47].

Therapeutic	Carrier	Marketed name	Targeting/Function	Clinical use
Polymer-based nano-pharmaceuticals				
PEG-asparaginase	Polymers PMA/PGMA	Oncaspar®	Cancer cells	Acute lymphoblastic leukaemia
PEGylated form of filgrastim	PEGylated carrier (PEG)	Neulasta®	Leukocyte growth factor	Neutropenia
alfa-2a interferon conjugated to branched PEG	PEG derivatives	Pegasys®	Protein replacement	Hepatitis C and HBeAg positive chronic hepatitis B
PEGylated analog of human growth hormone (GH)	PEG derivatives	Somavert®	Antagonist of GH receptors,	Acromegaly
Recombinant pegylated anti-hemophilic factor	PEG derivatives	Adynovate®	Increasing levels of blood-clotting factor VIII	Hemophilia A

*PMA: Poly(methyl acrylate); PGMA: Poly(glycidyl methacrylate); PEG: Poly(ethylene glycol);

Table 6. Representative nano-pharmaceuticals for the delivery of proteins therapeutics [45,47].

The clinical development of nanoparticles with chemo-, nucleic acids peptides and proteins therapeutics have demonstrated the potential of nanotechnology in the treatment of diseases. Despite, the amount of research in this field and the successfully marketed therapies, a great deal of formulations remain in clinical trials [50,75]. Recently, researchers are focused on the rational design to overcome these limitations by improving stability, drug leakage, nanoparticle structures and composition to efficiently entrap therapeutics [76,77]. We cite some protein-nanomedicines currently undergoing clinical trials (**Table 7**), for their future approval by FDA and EMA.

Therapeutic	Carrier	Drug & Sponsor	Clinical trial	Clinical use
CKD-602	Liposome	S-CKD602, University of Pittsburgh, ALZA	Phase 1, NCT00177281, Completed	Advanced Malignancies
Oxaliplatin/Transferrin	Liposome	MBP-426®, Mebiopharm Co., Ltd.	Phase 1/2, NCT00964080	Solid Tumors
Doxorubicin/Antibody fragment	Liposome	MM-302 , Merrimack	Phase 1/2, Terminated	Breast cancer
Methotrexate/Transferrin	Liposome	MBP-Y003, Mebiopharm Co., Ltd.	Unknown	Lymphoma
Nuvaxovid/ Protein subunit	Nanoparticle vaccine composed of trimeric full-length S proteins	Novavax	Phase 4; EUCTR2020-004123-16, NCT04583995; CTRI/2021/02/031554; NCT05236491; NCT04611802	COVID-19
Nanocovax/ protein subunit	Nanoparticle vaccine of prefusion-stabilized S protein	Nanogen Pharma	Phase III; NCT04922788	COVID-19

Table 7. Representative nano-pharmaceuticals for the delivery of proteins in current clinical trials [50,75].

3. Application of protein therapeutics.

3.1. Cancer.

Despite of the great advances in cancer research, in 2020 it still remains as the second leading cause of death worldwide [78]. Even though, the enormous therapeutic advances on this area have contributed to the increment of the overall survival of many types of cancers [79]. Nevertheless, mortality rate keeps increasing since 1990's related to the high incidence of this disease. Furthermore, it is expected that death trends will increase a 47% by 2040 [78,79]. This supposes a great

issue on society health, being very necessary to put great efforts on cancer research, highlighting the need of the development of new effective treatments and therapies. In this sense, protein therapeutics play a key factor due to the versatile properties that they offer above mentioned [80–82]. Innovative applications based on proteins to provide new venues to treat cancer are described next.

3.1.1. Light in cancer treatment.

Light-based treatments are not a current trend. We have to go back over 3000 years were Ancient Indian and Chinese civilizations already used a combination of reactive chemicals and light to treat several diseases such as vitiligo, psoriasis and skin cancer [83]. More recently, at the beginning of the XX century the first clinical application was described using eosin topically prior to illumination in basal cell carcinomas (BCCs), but it took 70 years for light treatments in cancer to become recognized [84]. Nowadays, light-based therapies such as Photodynamic therapy (PDT) or Photothermal Therapy (PTT) are clinically approved and commonly used. Phototherapy is a noninvasive approach that relies on the phototherapeutic agents in conjunction with light irradiation to selectively kill cancer cells with minimal toxicity to normal tissues in the dark. PTT employs photoabsorbing agents to generate heat under near-infrared (NIR) laser irradiation, resulting in cancer cells thermal ablation. PDT involves the generation of cytotoxic reactive oxygen species (ROS), such as singlet oxygen ($^1O_2$), from photosensitizers (PSs) under the light of a specific wavelength to oxidize adjacent biomolecules and consequently kill cancer cells [85–87]. So far, PDT has been widely described for its use, alone or in combination with existing treatments, in skin diseases as actinic keratoses, Bowen's disease (early type of skin cancer), basal cell carcinoma, macular degeneration (eye condition), and a few types of external located cancers and in early stages such as esophageal cancer, mouth cancer and breast cancer [88]. As it can be noticed, all mentioned applications have something in common and it is that they involve superficial areas of the body where lasers and LEDs light can reach, having an important gap in the use of these therapies for very-deep tissues and organs. Frequently used light sources, as mentioned above, have poor capacity of penetration. UV light has the least tissue penetration between 50-150 μm, blue light only penetrates around 1mm, green light over 2 mm, having the best performance red light and IR over 10 mm [89]. Even so, it is insufficient to reach deeper organs. In this context, bioluminescent proteins attached to nanoparticles have arisen as a promising tool to overcome inefficient treatments in deep organs. So, many studies have been published for the delivery of bioluminescent protein-nanovehicles for their application in PDT [90–94].

Other light applications are cell differentiation using light as mesenchymal-epithelial transition (MET) initiator benefiting from the ROS formed after PS irradiation that promotes MET [95–97]. On the other hand, photoactivatable prodrugs may be encapsulated into nanosystems to perform their upconversion to therapeutic active drugs via photocatalysis within the target tumoral cells [97]. Other attractive approach, is the endosomal escape, a critical step to ensure activity of cell internalized drugs an gene therapies, which can be improved by photosensitizer-induced ROS oxidizing lipids in the membrane, and thereby destabilizing the lipid bilayer causing increased leakage through the membrane [98–100]. Singlet oxygen has an extremely short half-life (~0.01–0.04 μs) and therefore the effect is very local. Traditionally, this can be achieved with photosensitizers and dyes, but recently the use of bioluminescent or fluorescent proteins anchored to the nanosystems has been explored [101] **(Figure 6)**.

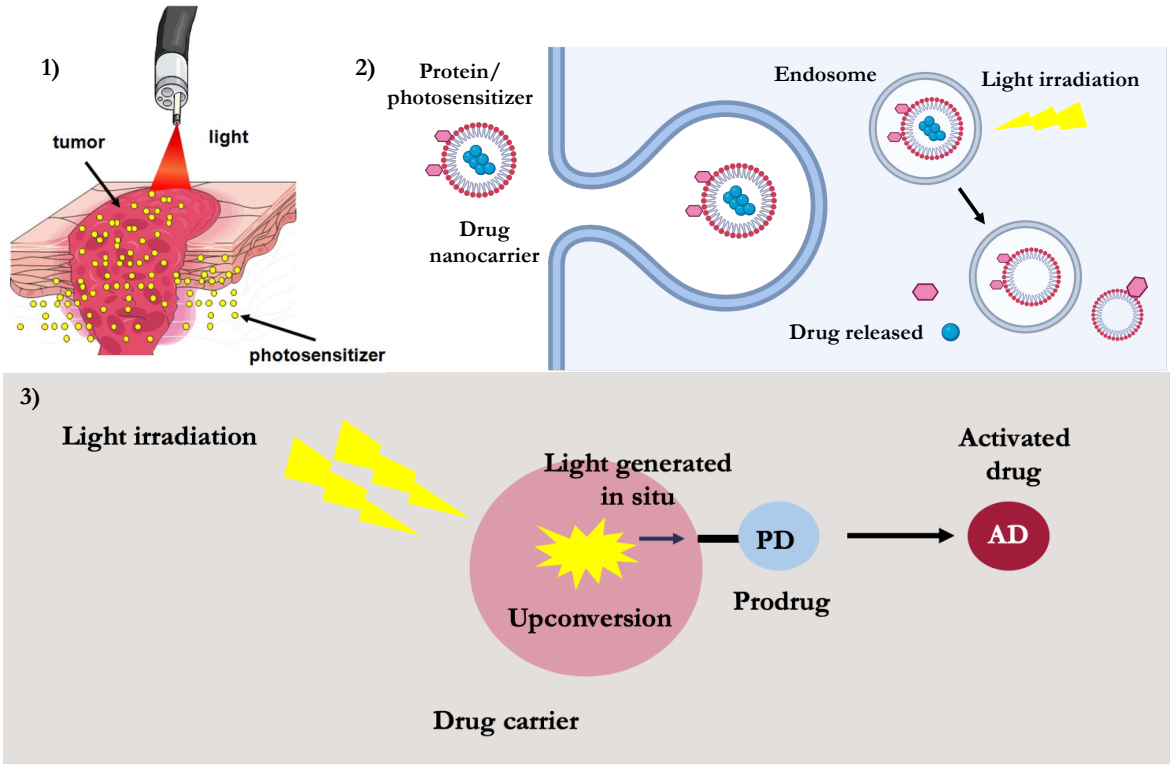

Figure 6. Representation light applications using enzymes: 1) PDT, photosensitizer is accumulated in the tumor and subsequently activated by laser irradiation; 2) Endosomal escape, nanocarriers coloaded with therapeutics molecules and proteins/dyes/photosensitizers that upon light activation will induce endosome membrane disruption with the subsequent cargo released; 3) Photocatalysis of prodrugs, after nanocarriers accumulation into targeted tissues prodrugs will be converted to active drugs upon light activation. 'Created with BioRender.com' under a paid subscription.

3.2. Protein replacement therapy.

Protein replacement therapy or Enzyme Replacement Therapy (ERT) is used when a particular protein stops functioning in the body. It involves replacing the actual protein [102] **(Figure 7)**. To illustrate this in practice, an example of protein therapy is the use of insulin in the treatment of diabetes. In many cases, enzymes therapy has focused on lysosomal storage diseases and disorders (LSDs) that are a group of inherited catabolic disorders in which typically large amounts of complex lipids accumulate in cells and tissues [103,104]. Protein replacement therapy as an area of research, has boomed in recent years as technology has allowed researchers to determine protein function (or lack thereof). Furthermore, plasma-derived products, which traditionally were the foundation of protein replacement therapy, are being replaced by recombinant engineered proteins. These recombinant engineered proteins offer advantages such as great degree of purity and resulted to be more potent therapeutics. There are over 130 FDA approved recombinant proteins for clinical use but only 10 of them for LSDs. However, the biggest issues of ERT current therapies are the high cost and ensuring purity and integrity of proteins. In addition, these therapies are administered as injections or infusions that need to be re-administered periodically to increase bioavailability being translated in high dose with the subsequent toxicity and side effects[105]. Thus, protein therapeutics delivered by nanocarriers are being extensively studied to solve these challenges and thus improving patients' lives[106].

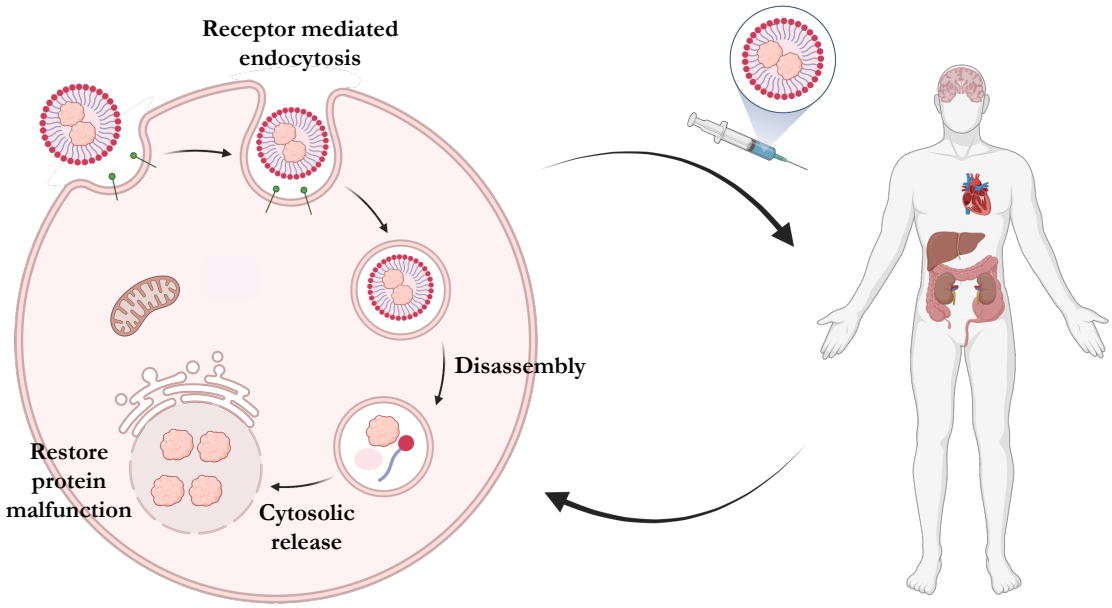

Figure 7. Schematic representation of enzyme replacement therapies based on protein nano-pharmaceuticals delivery. Nanocarriers loaded with enzymes are phagocyted by cells, once within endosomes nanocarriers will be disassembled and released to the cytosol and target desired cellular compartment with the later restoration of protein malfunction. 'Created with BioRender.com' under a paid subscription.

3.3. Gene therapy.

Nowadays, gene therapy is the major trend in the research of a wide range of diseases covering cancer, metabolic diseases, or immunotherapies, among others. Gene therapy is based on altering the genetic code to restore or recover the functions of critical proteins in the body [107]. To deliver genetic materials or gene-editing tools directly to the cells, a carrier/vector must be genetically engineered [108,109]. For instance, certain modified viruses such as Adeno-associated viruses (AAVs), can deliver the integrated DNA to the cell nucleus and insert it into our genome sequence. These viral vectors have demonstrated to be very efficient, but they carry some risks as they trigger dangerous immune responses and genotoxicity [110]. Nanotechnology have become an important and promising alternative for the delivery of gene-editing systems [109,111]. Thereby, the delivery of nucleic acids loaded on nanomedicines may improve the toxicity profile and the immune system responses and a reduction in off-targets effects. Besides they can be tailored to be delivered at specific targets and for many different purposes. However, it should be remarked that by using nanomedicines the integration in the genome is transient resulting in repeated administrations. This makes their design so important [111]. Therapeutic proteins for gene delivery may offer some advantages: (i) they can

provide efficient replacement treatment when gene is deleted or mutated; (ii) the effect of proteins is extremely specific; (iii) proteins are well tolerated by our body as they are naturally produced in it [2,19,112]. As gene therapy helps to replace deleted or mutated genes, it can provide a novel solution for many disorders [112–114]. In the therapeutic window of gene delivery, the clustered regularly interspaced short-palindromic repeat (CRISPR)-associated protein 9 (CRISPR-Cas9) nuclease system has emerged as a powerful genome editing tool. This system consists in a single-guide RNA (sgRNA) that specifically recognizes a target genomic locus and guides the Cas9 nuclease to cleave the recognize DNA sequence [115]. Cas9 introduces double-strand breaks (DSBs) at a specific site thanks to sgRNA. Subsequently, DSBs are repaired by two methods, nonhomologous end joining or homology directed repair [116]. Between various strategies, delivery of Cas9/sgRNA ribonucleoprotein (RNP) complex has been studied in many reports as it has shown reduced off-target effects and lower immunogenicity [117,118]. However, the new trends are based on the delivery of CRISPR components in nanomedicines **(Figure 8)**. Nanoparticles can be loaded with either RNP complex, cas9 protein and sgRNA or all components in form of mRNA and/or sgRNA and be surface decorated with antibodies, proteins, or peptides for active targeting.

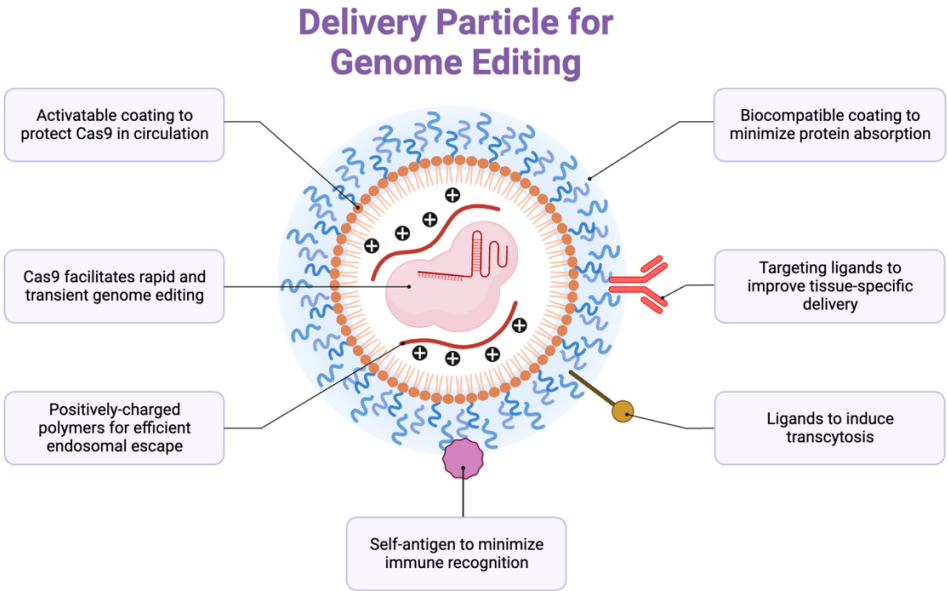

Figure 8. Illustration of the advantages of genome editing tool based on nanotechnology and proteins therapeutics. 'Created with BioRender.com' under a paid subscription.

In this research thesis, we propose the development of innovative and suitable approach for the development of a variety of nanosystems for the efficient delivery of proteins of different nature by developing different types of nanoplatforms such as metallic quantum dots for PDT and biodegradable and biocompatible sphingomyelin nanoemulsions (SNs) and sphingomyelin-based lipid nanoparticles (SNPs). It must be remarked that SNs for the efficient delivery of small drugs, imaging agents and other biomolecules have already been explored in previous reports [119–124].

REFERENCES

1. Vermonden, T., Censi, R. & Hennink, W. E. Hydrogels for protein delivery. *Chemical Reviews* vol. 112 2853–2888 Preprint at https://doi.org/10.1021/cr200157d (2012).

2. Golan, D., Beca, Q. & Leader, B. Protein therapeutics: a summary and pharmacological classification. *Nat Rev Drug Discov* **7**, 21–39 (2008).

3. Zaman, R. *et al.* Current strategies in extending half-lives of therapeutic proteins. *Journal of Controlled Release* vol. 301 176–189 Preprint at https://doi.org/10.1016/j.jconrel.2019.02.016 (2019).

4. Yu, M., Wu, J., Shi, J. & Farokhzad, O. C. Nanotechnology for protein delivery: Overview and perspectives. *Journal of Controlled Release* **240**, 24–37 (2016).

5. Lu, Y., Sun, W. & Gu, Z. Stimuli-responsive nanomaterials for therapeutic protein delivery. *Journal of Controlled Release* vol. 194 1–19 Preprint at https://doi.org/10.1016/j.jconrel.2014.08.015 (2014).

6. Bizeau, J. & Mertz, D. Design and applications of protein delivery systems in nanomedicine and tissue engineering. *Advances in Colloid and Interface Science* vol. 287 Preprint at https://doi.org/10.1016/j.cis.2020.102334 (2021).

7. Banting, F. G., Best, C. H., Collip, J. B., Campbell, W. R. & Fletcher, A. A. *THE CANADIAN MEDICAL ASSOCIATION JOURNAL PANCREATIC EXTRACTS IN THE TREATMENT OF DIABETES MELLITUS PRELIMINARY REPORT.*

8. Ziegler, T. R. *et al.* Author manuscript; available in PMC. *Am J Physiol Regul Integr Comp Physiol* **294**, 402–410 (2011).

9. Matsumura, Y. & Maeda2, H. *A New Concept for Macromolecular Therapeutics in Cancer Chemotherapy: Mechanism of Tumoritropic Accumulation of Proteins and the Antitumor Agent Smancs1*. http://aacrjournals.org/cancerres/article-pdf/46/12_Part_1/6387/2424185/cr04612p16387.pdf.

10. Cao, L. *et al.* Design of protein-binding proteins from the target structure alone. *Nature* **605**, 551–560 (2022).

11. Chiu, M. L., Goulet, D. R., Teplyakov, A. & Gilliland, G. L. Antibody structure and function: The basis for engineering therapeutics. *Antibodies* vol. 8 Preprint at https://doi.org/10.3390/antib8040055 (2019).

12. Boes, D. M., Godoy-Hernandez, A. & McMillan, D. G. G. Peripheral membrane proteins: Promising therapeutic targets across domains of life. *Membranes (Basel)* **11**, (2021).

13. Carter, P. J. & Rajpal, A. Designing antibodies as therapeutics. *Cell* vol. 185 2789–2805 Preprint at https://doi.org/10.1016/j.cell.2022.05.029 (2022).

14. Chamberlain, P. P. & Hamann, L. G. Development of targeted protein degradation therapeutics. *Nature Chemical Biology* vol. 15 937–944 Preprint at https://doi.org/10.1038/s41589-019-0362-y (2019).

15. Schmidt, C. Q. & Smith, R. J. H. Protein therapeutics and their lessons: Expect the unexpected when inhibiting the multi-protein cascade of the complement system. *Immunological Reviews* vol. 313 376–401 Preprint at https://doi.org/10.1111/imr.13164 (2023).

16. Leavy, O. Therapeutic antibodies: Past, present and future. *Nature Reviews Immunology* vol. 10 297 Preprint at https://doi.org/10.1038/nri2763 (2010).

17. Dömling, A. & Holak, T. A. Programmed death-1: Therapeutic success after more than 100 years of cancer immunotherapy. *Angewandte Chemie - International Edition* **53**, 2286–2288 (2014).

18. Usmani, S. S. *et al.* THPdb: Database of FDA-approved peptide and protein therapeutics. *PLoS One* **12**, (2017).

19. Pisal, D. S., Kosloski, M. P. & Balu-Iyer, S. V. Delivery of therapeutic proteins. *Journal of Pharmaceutical Sciences* vol. 99 2557–2575 Preprint at https://doi.org/10.1002/jps.22054 (2010).

20. Gu, Z., Biswas, A., Zhao, M. & Tang, Y. Tailoring nanocarriers for intracellular protein delivery. *Chem Soc Rev* **40**, 3638–3655 (2011).

21. Tang, R. *et al.* Direct delivery of functional proteins and enzymes to the cytosol using nanoparticle-stabilized nanocapsules. *ACS Nano* **7**, 6667–6673 (2013).

22. Kaehler T. Nanotechnology: basic concepts and definitions. *Clin Chem.* **9**, (1994).

23. Mura, S., Nicolas, J. & Couvreur, P. Stimuli-responsive nanocarriers for drug delivery. *Nature Materials* vol. 12 991–1003 Preprint at https://doi.org/10.1038/nmat3776 (2013).

24. Varanko, A., Saha, S. & Chilkoti, A. Recent trends in protein and peptide-based biomaterials for advanced drug delivery. *Advanced Drug Delivery Reviews* vol. 156 133–187 Preprint at https://doi.org/10.1016/j.addr.2020.08.008 (2020).

25. Santalices, I., Gonella, A., Torres, D. & Alonso, M. J. Advances on the formulation of proteins using nanotechnologies. *Journal of Drug Delivery Science and Technology* vol. 42 155–180 Preprint at https://doi.org/10.1016/j.jddst.2017.06.018 (2017).

26. Nasrollahzadeh, M., Sajadi, S. M., Sajjadi, M. & Issaabadi, Z. An Introduction to Nanotechnology. in *Interface Science and Technology* vol. 28 1–27 (Elsevier B.V., 2019).

27. Kaehler, T. *Nanotechnology: Basic Concepts and Definitions. CLINICAL CHEMISTRY* vol. 40 https://academic.oup.com/clinchem/article-abstract/40/9/1797/5647883 (1994).

28. Gadekar, V. *et al.* Nanomedicines accessible in the market for clinical interventions. *Journal of Controlled Release* vol. 330 372–397 Preprint at https://doi.org/10.1016/j.jconrel.2020.12.034 (2021).

29. Stiepel, R. T., Duggan, E., Batty, C. J. & Ainslie, K. M. Micro and nanotechnologies: The little formulations that could. *Bioengineering and Translational Medicine* vol. 8 Preprint at https://doi.org/10.1002/btm2.10421 (2023).

30. Administration, D. *Guidance for Industry Considering Whether an FDA-Regulated Product Involves the Application of Nanotechnology Contains Nonbinding Recommendations*. http://www.fda.gov/RegulatoryInformation/Guidances/ucm257698.htm (2014).

31. Cone, R. A. Barrier properties of mucus. *Advanced Drug Delivery Reviews* vol. 61 75–85 Preprint at https://doi.org/10.1016/j.addr.2008.09.008 (2009).

32. Yusuf, A., Almotairy, A. R. Z., Henidi, H., Alshehri, O. Y. & Aldughaim, M. S. Nanoparticles as Drug Delivery Systems: A Review of the Implication of Nanoparticles'

Physicochemical Properties on Responses in Biological Systems. *Polymers* vol. 15 Preprint at https://doi.org/10.3390/polym15071596 (2023).

33. Halwani, A. A. Development of Pharmaceutical Nanomedicines: From the Bench to the Market. *Pharmaceutics* vol. 14 Preprint at https://doi.org/10.3390/pharmaceutics14010106 (2022).

34. Farjadian, F. *et al.* Nanopharmaceuticals and nanomedicines currently on the market: Challenges and opportunities. *Nanomedicine* vol. 14 93–126 Preprint at https://doi.org/10.2217/nnm-2018-0120 (2019).

35. MG, K., V, K. & F, H. History and Possible Uses of Nanomedicine Based on Nanoparticles and Nanotechnological Progress. *J Nanomed Nanotechnol* **06**, (2015).

36. Martins, J. P. *et al.* The solid progress of nanomedicine. *Drug Deliv Transl Res* **10**, 726–729 (2020).

37. Dessale, M., Mengistu, G. & Mengist, H. M. Nanotechnology: A Promising Approach for Cancer Diagnosis, Therapeutics and Theragnosis. *International Journal of Nanomedicine* vol. 17 3735–3749 Preprint at https://doi.org/10.2147/IJN.S378074 (2022).

38. Weissig, V., Pettinger, T. K. & Murdock, N. Nanopharmaceuticals (part 1): products on the market. *International journal of nanomedicine* vol. 9 4357–4373 Preprint at https://doi.org/10.2147/IJN.S46900 (2014).

39. Hafner, A., Lovrić, J., Lakǒ, G. P. & Pepić, I. Nanotherapeutics in the EU: An overview on current state and future directions. *International Journal of Nanomedicine* vol. 9 1005–1023 Preprint at https://doi.org/10.2147/IJN.S55359 (2014).

40. Liu, R. *et al.* Advances of nanoparticles as drug delivery systems for disease diagnosis and treatment. *Chinese Chemical Letters* **34**, (2023).

41. Shan, X. *et al.* Current approaches of nanomedicines in the market and various stage of clinical translation. *Acta Pharmaceutica Sinica B* vol. 12 3028–3048 Preprint at https://doi.org/10.1016/j.apsb.2022.02.025 (2022).

42. Anselmo, A. C. & Mitragotri, S. Nanoparticles in the clinic. *Bioeng Transl Med* **1**, 10–29 (2016).

43. Anselmo, A. C. & Mitragotri, S. Nanoparticles in the clinic: An update. *Bioeng Transl Med* **4**, (2019).

44. Anselmo, A. C. & Mitragotri, S. Nanoparticles in the clinic: An update post COVID-19 vaccines. *Bioengineering and Translational Medicine* vol. 6 Preprint at https://doi.org/10.1002/btm2.10246 (2021).

45. Jia, Y. *et al.* Approved Nanomedicine against Diseases. *Pharmaceutics* vol. 15 Preprint at https://doi.org/10.3390/pharmaceutics15030774 (2023).

46. Waheed, S. *et al.* Engineering nano-drug biointerface to overcome biological barriers toward precision drug delivery. *Journal of Nanobiotechnology* vol. 20 Preprint at https://doi.org/10.1186/s12951-022-01605-4 (2022).

47. Mitchell, M. J. *et al.* Engineering precision nanoparticles for drug delivery. *Nature Reviews Drug Discovery* vol. 20 101–124 Preprint at https://doi.org/10.1038/s41573-020-0090-8 (2021).

48. Pérez-Medina, C., Teunissen, A. J. P., Kluza, E., Mulder, W. J. M. & van der Meel, R. Nuclear imaging approaches facilitating nanomedicine translation. *Advanced Drug Delivery Reviews* vols 154–155 123–141 Preprint at https://doi.org/10.1016/j.addr.2020.07.017 (2020).

49. Rodríguez, F. *et al.* Nano-Based Approved Pharmaceuticals for Cancer Treatment: Present and Future Challenges. *Biomolecules* vol. 12 Preprint at https://doi.org/10.3390/biom12060784 (2022).

50. Thi, T. T. H. *et al.* Lipid-based nanoparticles in the clinic and clinical trials: From cancer nanomedicine to COVID-19 vaccines. *Vaccines* vol. 9 Preprint at https://doi.org/10.3390/vaccines9040359 (2021).

51. Rohner, E., Yang, R., Foo, K. S., Goedel, A. & Chien, K. R. Unlocking the promise of mRNA therapeutics. *Nature Biotechnology* vol. 40 1586–1600 Preprint at https://doi.org/10.1038/s41587-022-01491-z (2022).

52. Taina-González, L. & de la Fuente, M. The Potential of Nanomedicine to Unlock the Limitless Applications of mRNA. *Pharmaceutics* vol. 14 Preprint at https://doi.org/10.3390/pharmaceutics14020460 (2022).

53. Zhang, Y., Li, J. & Pu, K. Recent advances in dual- and multi-responsive nanomedicines for precision cancer therapy. *Biomaterials* vol. 291 Preprint at https://doi.org/10.1016/j.biomaterials.2022.121906 (2022).

54. Manzari, M. T. *et al.* Targeted drug delivery strategies for precision medicines. *Nature Reviews Materials* vol. 6 351–370 Preprint at https://doi.org/10.1038/s41578-020-00269-6 (2021).

55. Burbelo, P. D., Iadarola, M. J., Keller, J. M. & Warner, B. M. Autoantibodies Targeting Intracellular and Extracellular Proteins in Autoimmunity. *Frontiers in Immunology* vol. 12 Preprint at https://doi.org/10.3389/fimmu.2021.548469 (2021).

56. Schmitt, E., Gehrmann, M., Brunet, M., Multhoff, G. & Garrido, C. Intracellular and extracellular functions of heat shock proteins: repercussions in cancer therapy. *J Leukoc Biol* **81**, 15–27 (2007).

57. Song, D., Yang, D., Powell, C. A. & Wang, X. Cell–cell communication: old mystery and new opportunity. *Cell Biology and Toxicology* vol. 35 89–93 Preprint at https://doi.org/10.1007/s10565-019-09470-y (2019).

58. Bassiouni, W., Ali, M. A. M. & Schulz, R. Multifunctional intracellular matrix metalloproteinases: implications in disease. *FEBS Journal* vol. 288 7162–7182 Preprint at https://doi.org/10.1111/febs.15701 (2021).

59. Andraos, C. & Gulumian, M. Intracellular and extracellular targets as mechanisms of cancer therapy by nanomaterials in relation to their physicochemical properties. *Wiley Interdisciplinary Reviews: Nanomedicine and Nanobiotechnology* vol. 13 Preprint at https://doi.org/10.1002/wnan.1680 (2021).

60. Fasciani, I. *et al.* GPCRs in Intracellular Compartments: New Targets for Drug Discovery. *Biomolecules* vol. 12 Preprint at https://doi.org/10.3390/biom12101343 (2022).

61. Qin, K., Dong, C., Wu, G. & Lambert, N. A. Inactive-state preassembly of Gq-coupled receptors and G q heterotrimers. *Nat Chem Biol* **7**, 740–747 (2011).

62. Pance, K. *et al.* Modular cytokine receptor-targeting chimeras for targeted degradation of cell surface and extracellular proteins. *Nat Biotechnol* **41**, 273–281 (2023).

63. Schlesinger, J. & Ullricht, A. *Growth Factor Signaling by Receptor Tyrosine Kinases Review*. *Neuron* vol. 9 (1992).

64. Bedard, P. L., Hyman, D. M., Davids, M. S. & Siu, L. L. Small molecules, big impact: 20 years of targeted therapy in oncology. *The Lancet* vol. 395 1078–1088 Preprint at https://doi.org/10.1016/S0140-6736(20)30164-1 (2020).

65. Dang, C. V., Reddy, E. P., Shokat, K. M. & Soucek, L. Drugging the 'undruggable' cancer targets. *Nature Reviews Cancer* vol. 17 502–508 Preprint at https://doi.org/10.1038/nrc.2017.36 (2017).

66. Singh, N. *et al. In vivo*protein corona on nanoparticles: does the control of all material parameters orient the biological behavior? *Nanoscale Adv* **3**, 1209–1229 (2021).

67. Xiao, Q. *et al.* The effects of protein corona on *in vivo* fate of nanocarriers. *Advanced Drug Delivery Reviews* vol. 186 Preprint at https://doi.org/10.1016/j.addr.2022.114356 (2022).

68. Cao, H. *et al.* Albumin Biomimetic Nanocorona Improves Tumor Targeting and Penetration for Synergistic Therapy of Metastatic Breast Cancer. *Adv Funct Mater* **27**, (2017).

69. Spicer, C. D., Jumeaux, C., Gupta, B. & Stevens, M. M. Peptide and protein nanoparticle conjugates: Versatile platforms for biomedical applications. *Chemical Society Reviews* vol. 47 3574–3620 Preprint at https://doi.org/10.1039/c7cs00877e (2018).

70. Rother, M., Nussbaumer, M. G., Renggli, K. & Bruns, N. Protein cages and synthetic polymers: A fruitful symbiosis for drug delivery applications, bionanotechnology and materials science. *Chemical Society Reviews* vol. 45 6213–6249 Preprint at https://doi.org/10.1039/c6cs00177g (2016).

71. Scaletti, F. *et al.* Protein delivery into cells using inorganic nanoparticle-protein supramolecular assemblies. *Chemical Society Reviews* vol. 47 3421–3432 Preprint at https://doi.org/10.1039/c8cs00008e (2018).

72. Pachioni-Vasconcelos, J. D. A. *et al.* Nanostructures for protein drug delivery. *Biomaterials Science* vol. 4 205–218 Preprint at https://doi.org/10.1039/c5bm00360a (2016).

73. Harel, O. & Jbara, M. Chemical Synthesis of Bioactive Proteins. *Angewandte Chemie - International Edition* vol. 62 Preprint at https://doi.org/10.1002/anie.202217716 (2023).

74. Qin, X. *et al.* Rational Design of Nanocarriers for Intracellular Protein Delivery. *Advanced Materials* vol. 31 Preprint at https://doi.org/10.1002/adma.201902791 (2019).

75. Kovalenko, A., Ryabchevskaya, E., Evtushenko, E., Nikitin, N. & Karpova, O. Recombinant Protein Vaccines against Human Betacoronaviruses: Strategies, Approaches and Progress. *International Journal of Molecular Sciences* vol. 24 Preprint at https://doi.org/10.3390/ijms24021701 (2023).

76. Rauf, A. *et al.* Nanoparticles in clinical trials of COVID-19: An update. *International Journal of Surgery* vol. 104 Preprint at https://doi.org/10.1016/j.ijsu.2022.106818 (2022).

77. Kaltbeitzel, J. & Wich, P. R. Protein-based Nanoparticles: From Drug Delivery to Imaging, Nanocatalysis and Protein Therapy. *Angewandte Chemie International Edition* (2023) doi:10.1002/anie.202216097.

78. Sung, H. *et al.* Global Cancer Statistics 2020: GLOBOCAN Estimates of Incidence and Mortality Worldwide for 36 Cancers in 185 Countries. *CA Cancer J Clin* **71**, 209–249 (2021).

79. Siegel, R. L., Miller, K. D., Fuchs, H. E. & Jemal, A. Cancer Statistics, 2021. *CA Cancer J Clin* **71**, 7–33 (2021).

80. Cheng, L., Yang, L., Meng, F. & Zhong, Z. Protein Nanotherapeutics as an Emerging Modality for Cancer Therapy. *Adv Healthc Mater* **7**, (2018).

81. SLIWKOWSKI, M. X. & MELLMAN, I. Antibody Therapeutics in Cancer. *Science (1979)* **341**, 1192–1198 (2013).

82. Kintzing, J. R., Filsinger Interrante, M. V. & Cochran, J. R. Emerging Strategies for Developing Next-Generation Protein Therapeutics for Cancer Treatment. *Trends Pharmacol Sci* **37**, 993–1008 (2016).

83. Dos Santos, A. F., De Almeida, D. R. Q., Terra, L. F., Baptista, M. S. & Labriola, L. Photodynamic therapy in cancer treatment - an update review. *J Cancer Metastasis Treat* **2019**, (2019).

84. Calin, M. A. & Parasca, S. V. Photodynamic therapy in oncology. *Journal of Optoelectronics and Advanced Materials* **8**, 1173–1179 (2006).

85. Maharjan, P. S. & Bhattarai, H. K. Singlet Oxygen, Photodynamic Therapy, and Mechanisms of Cancer Cell Death. *J Oncol* **2022**, 1–20 (2022).

86. Zhen, X., Cheng, P. & Pu, K. Recent Advances in Cell Membrane–Camouflaged Nanoparticles for Cancer Phototherapy. *Small* vol. 15 Preprint at https://doi.org/10.1002/smll.201804105 (2019).

87. Lee, C. N., Hsu, R., Chen, H. & Wong, T. W. Daylight Photodynamic Therapy: An Update. *Molecules (Basel, Switzerland)* vol. 25 Preprint at https://doi.org/10.3390/molecules25215195 (2020).

88. Agostinis, P. *et al.* Photodynamic therapy of cancer: An update. *CA Cancer J Clin* **61**, 250–281 (2011).

89. Cios, A. *et al.* Effect of different wavelengths of laser irradiation on the skin cells. *International Journal of Molecular Sciences* vol. 22 1–19 Preprint at https://doi.org/10.3390/ijms22052437 (2021).

90. So, M. K., Loening, A. M., Gambhir, S. S. & Rao, J. Creating self-illuminating quantum dot conjugates. *Nat Protoc* **1**, 1160–1164 (2006).

91. So, M. K., Xu, C., Loening, A. M., Gambhir, S. S. & Rao, J. Self-illuminating quantum dot conjugates for *in vivo* imaging. *Nat Biotechnol* **24**, 339–343 (2006).

92. Karthikeyan, K., Babu, A., Kim, S. J., Murugesan, R. & Jeyasubramanian, K. Enhanced photodynamic efficacy and efficient delivery of Rose Bengal using nanostructured poly(amidoamine) dendrimers: Potential application in photodynamic therapy of cancer. *Cancer Nanotechnol* **2**, 95–103 (2011).

93. Yang, Y. *et al.* Biodegradable Polymer Nanoparticles for Photodynamic Therapy by Bioluminescence Resonance Energy Transfer. *Biomacromolecules* **19**, 201–208 (2018).

94. Yeh, H. P. *et al.* A New Photosensitized Oxidation-Responsive Nanoplatform for Controlled Drug Release and Photodynamic Cancer Therapy. *ACS Appl Mater Interfaces* **10**, 21160–21172 (2018).

95. Qu, A. *et al.* timulation of neural stem cell differentiation by circularly polarized light transduced by chiral nanoassemblies. *Nat Biomed Eng* **5**, 103–113 (2021).

96. Geng, Y. *et al.* Differentiation of cancer stem cells through nanoparticle surface engineering. *ACS Nano* **14**, 15276–15285 (2020).

97. Huang, L. *et al.* Highly effective near-infrared activating tripleta-triplet annihilation upconversion for photoredox catalysis. *J Am Chem Soc* **142**, 18460–18470 (2020).

98. de Bruin, K. G. *et al.* Dynamics of photoinduced endosomal release of polyplexes. *Journal of Controlled Release* **130**, 175–182 (2008).

99. Tan, X., Bruchez, M. P. & Armitage, B. A. Efficient Cytoplasmic Delivery of Antisense Probes Assisted by Cyclized-Peptide-Mediated Photoinduced Endosomal Escape. *ChemBioChem* **20**, 727–733 (2019).

100. Yarani, R., Shiraishi, T. & Nielsen, P. E. Effective photo-enhancement of cellular activity of fluorophore-octaarginine antisense PNA conjugates correlates with singlet oxygen formation, endosomal escape and chromophore lipophilicity. *Sci Rep* **8**, (2018).

101. Miyoshi, Y. *et al.* Endosomal Escape of Peptide-Photosensitizer Conjugates Is Affected by Amino Acid Sequences near the Photosensitizer. *Bioconjug Chem* **31**, 916–922 (2020).

102. Schaible, P. Modifying enzyme replacement therapy – A perspective. *Journal of Cellular and Molecular Medicine* vol. 27 165–173 Preprint at https://doi.org/10.1111/jcmm.17653 (2023).

103. Li, M. Enzyme Replacement Therapy: A Review and Its Role in Treating Lysosomal Storage Diseases. *Pediatr Ann* 191–197 (2018).

104. Brady, R. O. & Schiffmann, R. Enzyme-replacement therapy for metabolic storage disorders. *Lancet Neurol* **3**, 752–756 (2004).

105. Concolino, D., Deodato, F. & Parini, R. Enzyme replacement therapy: Efficacy and l imitations. *Ital J Pediatr* **44**, (2018).

106. Vavilis, T. *et al.* mRNA in the Context of Protein Replacement Therapy. *Pharmaceutics* vol. 15 Preprint at https://doi.org/10.3390/pharmaceutics15010166 (2023).

107. Shaimardanova, A. A., Solovyeva, V. V., Issa, S. S. & Rizvanov, A. A. Gene Therapy of Sphingolipid Metabolic Disorders. *International Journal of Molecular Sciences* vol. 24 Preprint at https://doi.org/10.3390/ijms24043627 (2023).

108. Kido, J., Sugawara, K. & Nakamura, K. Gene therapy for lysosomal storage diseases: Current clinical trial prospects. *Frontiers in Genetics* vol. 14 Preprint at https://doi.org/10.3389/fgene.2023.1064924 (2023).

109. Hidai, C. & Kitano, H. Nonviral Gene Therapy for Cancer: A Review. *Diseases* **6**, 57 (2018).

110. Bulcha, J. T., Wang, Y., Ma, H., Tai, P. W. L. & Gao, G. Viral vector platforms within the gene therapy landscape. *Signal Transduction and Targeted Therapy* vol. 6 Preprint at https://doi.org/10.1038/s41392-021-00487-6 (2021).

111. Duan, L. *et al.* Nanoparticle Delivery of CRISPR/Cas9 for Genome Editing. *Frontiers in Genetics* vol. 12 Preprint at https://doi.org/10.3389/fgene.2021.673286 (2021).

112. Sharma, A. R. *et al.* Next generation delivery system for proteins and genes of therapeutic purpose: Why and how? *BioMed Research International* vol. 2014 Preprint at https://doi.org/10.1155/2014/327950 (2014).

113. Alden, T. D., Varady, P., Kallmes, D. F., Jane, J. A. & Helm, G. A. Bone Morphogenetic Protein Gene Therapy. *Number 16S* **27**, 87–93.

114. Kay, M. A. State-of-the-art gene-based therapies: the road ahead. *Nat Rev Genet* **12**, 316–328 (2011).

115. Rouatbi, N., McGlynn, T. & Al-Jamal, K. T. Pre-clinical non-viral vectors exploited for *in vivo* CRISPR/Cas9 gene editing: an overview. *Biomaterials Science* vol. 10 3410–3432 Preprint at https://doi.org/10.1039/d1bm01452h (2022).

116. Wei, T., Cheng, Q., Min, Y. L., Olson, E. N. & Siegwart, D. J. Systemic nanoparticle delivery of CRISPR-Cas9 ribonucleoproteins for effective tissue specific genome editing. *Nat Commun* **11**, (2020).

117. Zheng, Q. *et al.* Synthetic nanoparticles for the delivery of CRISPR/Cas9 gene editing system: classification and biomedical applications. *Biomater Sci* (2023) doi:10.1039/d3bm00788j.

118. Sinclair, F., Begum, A. A., Dai, C. C., Toth, I. & Moyle, P. M. Recent advances in the delivery and applications of nonviral CRISPR/Cas9 gene editing. *Drug Deliv Transl Res* **13**, 1500–1519 (2023).

119. Nagachinta, S., Bouzo, B. L., Vazquez-Rios, A. J., Lopez, R. & de la Fuente, M. Sphingomyelin-based nanosystems (SNs) for the development of anticancer miRNA therapeutics. *Pharmaceutics* **12**, (2020).

120. Bouzo, B. L. *et al.* Sphingomyelin nanosystems loaded with uroguanylin and etoposide for treating metastatic colorectal cancer. *Sci Rep* **11**, (2021).

121. Bouzo, B. L., Calvelo, M., Martín-Pastor, M., García-Fandiño, R. & De La Fuente, M. *In Vitro*- In Silico Modeling Approach to Rationally Designed Simple and Versatile Drug Delivery Systems. *Journal of Physical Chemistry B* **124**, 5788–5800 (2020).

122. Díez-Villares, S. *et al.* Quantitative PET tracking of intra-articularly administered 89Zr-peptide-decorated nanoemulsions. *Journal of Controlled Release* **356**, 702–713 (2023).

123. Nagachinta, S. *et al.* Radiolabelling of lipid-based nanocarriers with fluorine-18 for *in vivo* tracking by PET. *Colloids Surf B Biointerfaces* **188**, (2020).

124. Díez-Villares, S. *et al.* Biodistribution of 68/67Ga-radiolabeled sphingolipid nanoemulsions by pet and spect imaging. *Int J Nanomedicine* **16**, 5923–5935 (2021).

Hypotheses

HYPOTHESES

On the basis, this thesis is supported by the hypothesis that "It is possible to design and fine-tune nanosystems through the application of bioconjugation strategies to efficiently associate proteins, enhancing their stability and delivery and thereby promoting their use in therapeutics".

This main hypothesis can be divided in the following partial hypotheses (H):

H1. Proteins could be efficiently bioconjugated to preformed nanoparticles, upon incorporation of reactive functional groups onto the nanoparticle surface by selecting specific chemical reactions.

H2. Bioconjugation of bioluminescent proteins could prompt the development of self-illuminating nanosystems to explore innovative therapeutic approaches based on photodynamic therapy (PDT).

H3. The efficacy and biocompatibility of self-illuminating nanosystems could be tuned by careful selection of the type of nanoparticles used for their preparation.

H4. It is possible to bioconjugate therapeutic enzymes for the development of immunomodulatory therapies in pancreatic cancer.

H5. *[Confidential section]*

Objectives

OBJECTIVES

Based on the established hypotheses, the main aim of this research study is the development of novel protein nanotherapeutics by exploring several bioconjugation strategies to functionalized nanoparticles, providing evidence of the potential of this approach in cancer therapy and *[confidential section]*.

This main objective has been accomplished by establishing the following partial objectives (O):

O1. To associate the bioluminescent enzyme RLuc8 to quantum dots 705 to obtain self-illuminating RLuc8-QDots nanoconjugates (SI-NCs), and to SNs to obtain self-illuminating sphingomyelin nanosystems (SI-NS).

O2. To assess the capacity of RLuc8-QDots SI-NCs and of SI-NS to trigger PDT treatment in pancreatic cancer, using established pancreatic cancer cell lines and primary cultures (PDX).

O3. To assess the potential of biocompatible SI-NS for cell labelling and cell tracking analysis.

O4. To explore different bioconjugation strategies to expand the use of SNs to protein delivery for a variety of biomedical applications.

O5. To explore the potential of SNs for the delivery of the therapeutic protein Anakinra to modulate the tumor microenvironment (TME) in pancreatic cancer.

O6. *[Confidential section]*

Chapter I

Self-illuminating Nanoconjugates (SI-NCs) trigger an effective anti-tumor Photodynamic Therapy (PDT) response in Pancreatic Ductal Adenocarcinoma

Self-illuminating nanoconjugates (SI-NCs) trigger an effective anti-tumor Photodynamic Therapy (PDT) response in pancreatic ductal adenocarcinoma

ABSTRACT

Pancreatic ductal adenocarcinoma (PDAC) is projected to become the second leading cause of cancer-related deaths by 2030. Therefore, new strategies to combat this tumor are essential. Photodynamic Therapy (PDT) has proven to be efficient for treating superficial solid tumors. Nevertheless, due to the poor penetration of light, conventional laser-dependent PDT is not adequate for treating internal organs. For this particular purpose, we aimed i) to develop self-illuminating nanoconjugates (SI-NCs) that comprises a bioluminescent enzyme, *RLuc8*, associated to quantum dots (QDots 705), and ii) to determine their capacity to mediate a localized and controlled antitumoral response in PDAC through activation of the photosensitizer verteporfin, a FDA-approved drug. This study provides a full development and characterization of SI-NCs and their photodynamic properties. *In vitro* studies in immortalized pancreatic cancer cell lines and primary cultures, were performed to decipher the mechanism of action and highlight the anti-cancer potential of the proposed bioluminescent-activated (BioLight) PDT (BL-PDT). *In vivo* studies in patient-derived xenograft models (PDX), confirmed the clinical potential of SI-NCs for treating PDAC.

INTRODUCTION

Pancreatic ductal adenocarcinoma (PDAC), a highly devastating cancer of the pancreas, accounts for more than 90% of pancreatic cancer cases and is currently the fourth leading cause of death related to cancer worldwide [1,2], with a five-year survival rate of approximately 11% [1]. The particular anatomical location and pathological features of PDAC make it one of the most difficult to treat and diagnose. Even surgically resected patients present an average survival of only 10 to 20 months. Moreover, the incidence and mortality of pancreatic cancer are increasing each year, PDAC being projected the second leading cause of cancer-related deaths in the US and Europe by 2030 [3,4]. Therefore, the development of new therapies for this devasting tumor is a health-care priority [5,6].

Photodynamic therapy (PDT) is being proposed as a promising alternative to treat many different types of tumors [7,8]. PDT is based on a non-invasive approach, with the purpose of selectively killing cancer cells with minimal toxicity to normal tissues via light irradiation [9–11]. The fundamental principle of PDT is the generation of singlet oxygen ($^3O_2 \rightarrow {}^1O_2$) and other reactive oxygen species (ROS) upon activation of photosensitizing (PS) drugs when light is applied at a specific wavelength, thus oxidizing adjacent biomolecules and, consequently, inducing cell death[12–14]. The singlet oxygen formed during the PDT process can alter catalase activity. This prompts immunogenic modulation through Hypochlorous acid (HOCl), triggering the immune system to target cancer cells. Likewise, it can also induce apoptosis via extrinsic and intrinsic pathways. Both pathways initiate mechanisms such as caspases activation, oxidative stress, protein misfolding or unfolding, and p38 MAPK activation. The mechanism of induced cell death is determined by the localization of the organelles affected by the action of the PDT [6].

PDT is typically initiated with external light sources, which is a main limitation for treating internal organs, given the complex and low penetration of the laser light into deep tissues[15,16]. At shorter wavelengths, light penetrates less, and, at longer wavelengths, energy does not produce enough reactive oxygen species [7,16]. There is a region often called the "tissue optical window", which varies between 600 and 1200 nm, and is to a large extent used in PDT. Existing endogenous chromophores in tissues also compete with light absorption by the PS [17,18]. More recently, inner sources of light have also been explored for treating inner organs and deep tumors [19,20].

Nanoparticles, which can accumulate in the tumor and its microenvironment, can improve PDT in deep tumors such as PDAC [11,21].Quantum dots (QDots), are fluorescent nanometric particles with optical properties and photochemical stability. In addition, they present intrinsic sustained

light emission when they are excited from a light source [22]. More in detail, self-illuminating properties has been achieved by conjugating QDots to the bioluminescent protein Renilla luciferase (RLuc8) [23,24]. After addition of the substrate coelenterazine (CTZ), the light emitted by RLuc8 can be transferred to QDots via Bioluminescence energy resonance transfer (BRET) [23]. SI-NCs have already demonstrated their potential for *in vitro* and *in vivo* imaging of C6 glioma live cells[23]. *Hsu et Al.*[25] proposed the use of SI-NCs for treating A549 tumor cells, confirming improved tumor-death in comparison with the application of an external light source. The superiority of this approach with respect to external laser sources was also confirmed by *Kim et Al*[26]., using in this case CT26 murine colon cancer cells, Murine Lewis lung cancer (LLC) and B16F10 melanoma cells. SI-NCs have additionally been investigated for antimicrobial applications[27].

In this work, we propose the development of SI-NCs for the treatment of PDAC. For this, we optimized the conjugation of RLuc8 to QDots 705, which will allow using the PS drug verteporfin (commercially available under the name Visudyne®). The selection of verteporfin is supported by the fact that has the approval of the Food and Drug Administration (FDA) in age-related macular generation, damaging vascularization and inhibiting angiogenesis after excitation by external light sources [28–30]. Its application in PDAC and in other types of cancer is undergoing clinical trials with invasive protocols to allow the use of external light sources [31,32]. SI-NCs would provide a less invasive approach. Moreover, verteporfin similarly to conventional PS present red light that penetrates tissues more efficiently [7,16,28,33]. For instance, same family PS chlorin e6 (Ce6) achieved positive results in colon cancer SW480 cells via laser-PDT [34] and co-loaded with (ROS)-responsive nanoparticle (NP-sfb/ce6) improved antitumor responses by releasing sorafenib drug after PDT treatment [35].

We develop here a new type of SI-NCs specifically adapted to stimulate verteporfin to mediate bioluminescent-activated (BioLight) PDT (BL-PDT) in PDAC, as a versatile solution to overcome the limitations of conventional laser-dependent PDT. We also provide solid evidence of the potential of this approach to treat PDAC.

MATERIALS AND METHODS

Preparation of SI NCs (RLuc8-QDots 705 nanoconjugates)

To associate the purified RLuc8 protein (supp. Info.; "*Extraction, purification and characterization of RLuc8"*) to the QDots, a previously described protocol was followed with some modifications [24]. Ten pmol of QDots 705, 400 pmol of RLuc8, 40,000 pmol of EDC (N-(3-Dimethylaminopropyl)-N'-ethylcarbodiimide, Sigma-Aldrich, Spain) were combined, and the mixture was brought to a final volume of 20 μL in PBS buffer, 10 mM, pH 7.4 and incubated at room temperature (RT) for 1 hour. The purification of the SI-NCs was carried out using spin filters (Amicon® Ultra Centrifugal Filters, 0.5mL, Merck) in a refrigerated microcentrifuge (5417R; Eppendorf). The spin filters were first pre-washed with NTA buffer (N', N-bis-(carboximetil)-L-lisina, Sigma-Aldrich, Spain) at 6000×g for 5 min to reduce QDots loss during the process. Then the filters were flushed with PBS 10 mM buffer pH 7.4 at 6000×g for 5 min. Next, the conjugation reaction was transferred to the spin filters and 200 μL of PBS was added and centrifuged for 3 min, at 4°C and 3000×g. Then, four washes were made with 200 μL of PBS each, centrifuging as described above. Finally, SI-NCs were collected in 20 μL of PBS buffer, centrifuging for 2 min, at 4°C and at 1000×g. The reaction was escalated 5-fold to ease future experiments without compromising its physicochemical properties.

Characterization of SI-NCs

To determine the efficacy of the conjugation, different samples, namely i) free QDots, ii) a physical mixture of QDots and the EDC coupling reagent, and iii) the SI-NCs (RLuc8-QDots 705 nanoconjugates), prepared with 6X DNA orange loading buffer dye (Promega), were loaded in a 1% agarose gel (Fischer Scientific) in 1X TAE buffer. Electrophoresis was performed at 100V for 30 min, and the gel was visualized in a Chemidoc standard UV developer chamber (BioRad). In addition, a 12% acrylamide/bis-acrylamide (29:1) denaturing SDS-PAGE gel (BioRad®) was prepared, and additional samples were loaded, specifically i) the naked protein RLuc8, ii) free QDots, and iii) SI-NCs. Electrophoresis was performed at 150V for 90 minutes. The gel was developed using Coomassie® Brilliant Blue staining (ThermoFisher Scientific, USA).

BRET phenomenon was tested after its activation with 1µg of CTZ; ThermoFisher Scientific, USA) in a luminometer (SYNERGY H1, microplate reader, BioTek). The stability of the SI-NCs was determined by measuring their BRET kinetics at the time of production, as well as at day 4 and 7 after production. The kinetics of the reaction were determined in duplicate in a 96-well plate, monitoring the bioluminescence reaction from time 0 min (addition of the substrate) to 3 hours, and taking a measurement every 5 min.

Cell cultures maintenance

The L3.6pl cell line (RRID:CVCL_0384), is a highly metastatic PDAC cell line, originally described by Bruns et al. (PMID: 10935470). L3.6pl, MIA PaCa-2, PANC-1, PaTu 8988t and PaTu 8988s cells were cultured in RPMI 1640 media (Invitrogen, Cat no. 61870044) containing 10% fetal bovine serum and 50 units/ml penicillin/streptomycin in a humidified incubator (5%) at 37°C, and cultures were tested for Mycoplasma periodically.

Cellular internalization

For cellular internalization studies, 6 x10^4 L3.6pl, MIA PaCa-2, PANC-1, PaTu 8988t or PaTu 8988s cells/ well were seeded in 8-chamber slide plates and grown overnight. The following day, 2 pmol of SI-NCs were added to the wells and internalization was studied at different time points, 20 min, 1h and 3h. After incubation, treatments were removed, cell nuclei were stained with Hoechst 33342 (ThermoFisher, USA), cells were fixed with 4% PFA (ThermoFisher, USA), and cultures were observed by Confocal Laser Microscopy (CLM; Confocal Laser Microscopy Leica SP8®). Results were verified by Flow Cytometry (FACS Aria IIu de BD) in L3.6pl, MIA PaCa-2 and PANC-1 cells. 5 x10^5 cells/well were seeded in 6-multiwell plates and grown overnight. Next, 10 pmol of the nanoconjugate treatments were added to the cells, and after incubation, cells were washed with 2X DPBS and fixed with 2% PFA.

Cell viability assays

For cytotoxicity studies, L3.6pl, Mia PaCa-2 and PANC-1 were seeded into 96-well plates at a density of 25,000 cell/well and incubated for 24h. To determine the toxicity of the photosensitizer and the SI-NCs, each was tested in separate experiments. Both were applied in increasing order of

concentrations and incubated for 4 hours. Cell viability was determined using the MTT assay (3-(4,5-dimethylthiazol-2-yl)-2,5-diphenyltetrazolium bromide, Alfa Aesar) and the colorimetric assay was read using a scanning multi-well plate reader at 570 nm (Multiskan EX, ThermoLabsystems®).

Experiments to determine cell viability after BL-PDT treatment *[BL-PDT = verteporfin (PS) + SI-NCs + substrate (CTZ)]* were also performed. At 24h post-seeding, SI-NCs were added to the cells at 1 pmol. Next, verteporfin (4μM) was added and incubated for 2h. After treatments, cells were washed twice with 1X PBS. The photodynamic process was induced by adding 2 μg of CTZ to each well. After 12h, the cytotoxicity was determined using the aforementioned MTT assay. The negative controls (0% cell death) were cells growing in normal conditions and cells in which the vehicles were added. The positive control (100% cell death) consisted of the addition of a solution of Triton 0.1% in DPBS.

Measurement of ROS production and apoptosis induction

To determine the presence of intracellular ROS produced by the BL-PDT process, a fluorescence-based assay was performed, consisting in staining the cells with the fluorescent dye 2',7'-dichlorodihydrofluorescein diacetate (H_2DCFDA; ThermoFisher Scientific, USA) as per the manufacturer's instructions. Briefly, a 96-multiwell black wall plate with clear-bottoms was seeded with 25,000 cells /well and incubated for 24 h. Firstly, cells interacted with the dye at a final concentration of 5 μM for 60 min. Then, cells were treated with the same conditions and quantities of SI-NCs, verteporfin and coelenterazine, as mentioned in the previous section ("*cell viability"*) and were incubated at 37°C for the PDT process. As positive a control, Luperox® (Sigma Aldrich, USA) was added at a concentration of 100 μM and incubated for 2h at 37°C. ROS generation was measured with a fluorimeter at an excitation wavelength of 485nm and emission of 535 nm.

Laser-PDT culture conditions were the same as described before. After treatment, cells were washed twice with PBS and laser-PDT was performed at different energy ratios in J/cm^2. The optimal signal was used to compare to the BL-PDT.

Apoptosis after ROS production was evaluated by immunofluorescence-based detection of Annexin V. After BL-PDT treatment, cells were fixed with 4% PFA (15 min), incubated in 10% normal goat serum to block non-specific protein-protein interactions followed by mouse monoclonal anti-annexin V (Abcam, NL) staining overnight at 4°C. Annexin V was observed with

a Leica SP5 confocal laser microscope (Leica, Nussloch, Germany) using an excitation of 495 nm and an emission of 519 nm.

In vivo therapeutic efficacy of SI-NCs

PDAC patient-derived xenografts (PDAC PDX Panc354 and PancA6L) were obtained from Dr. Manuel Hidalgo under a Material Transfer Agreement with the Spanish National Cancer Centre (CNIO), Madrid, Spain (Reference no.I409181220BSMH). To establish low-passage primary PDAC PDX-derived *in vitro* cultures, xenograft tumors were minced, enzymatically digested with collagenase (Stem Cell Technologies) for 60 min at 37°C, clarified via multiple rounds of filter purification with 100µm and 40µM Fisherbrand™ Sterile Cell Strainers (FisherScientific, Cat no. 11517532 and 11587522), and after centrifugation for 5 min at 1800 rpm, the cell pellets were resuspended and cultured in RPMI (Invitrogen) supplemented with 10% FBS (Invitrogen), 50 units/mL penicillin/streptomycin and fungizone (Invitrogen). Primary cultures were tested for Mycoplasma at least every 4 weeks.

To perform PDT *in vivo*, 9-week-old 25 g male NOD.SCID (NOD.CB17-Prkdcscid/NCrHsd) mice (Janvier Labs, France), were orthotopically injected with 200,000 cells of the indicated PDX (resuspended in 50µl MatrigelTM, BD Cat no. 354234) to form tumors. Approximately two weeks post orthotopic injection, nanoconjugates (50 pmol) were administered intraperitoneally. Meanwhile, the photosensitizer (200 mg/kg) and substrate (20 µg) were retro-orbital sinus injected in isoflurane inhalation anesthetized mice. The succession of therapy was as followed; first, photosensitizer incubation for 1 h, then SI-NCs were injected and after 30 minutes the substrate (CTZ) was added to induce BL-PDT. Mice were treated twice a week for 3 weeks. For the control group, PBS was injected. The sham group consisted of mice treated with the photosensitizer and the SI-NCs without the substrate addition (no BL-PDT treatment) and the therapy group consisted of mice treated with the complete BL-PDT treatment *[BL-PDT = verteporfin (PS) + SI-NCs + substrate (CTZ)]*. *In vivo* experiments were conducted in collaboration with the group of Dr. Bruno Sainz Jr located in the Department of Cancer Biology, Instituto de Investigaciones Biomédicas Sols-Morreale (IIBM), CSIC-UAM, 28029 Madrid, Spain.

Immunohistochemistry

For histopathological analysis, 3 μm sections of FFPE blocks were stained with hematoxylin and eosin (H&E). Additional serial sections were used for immunohistochemical (IHC) analysis of pCNA using ImageJ software. Antigens were visualized using 3,3-diaminobenzidine tetrahydrochloride plus (DAB+). Counterstaining was performed with hematoxylin. Digital Images were obtained using an digital scanner "MOTIC EASY SCAN ONE" with a 20X Plan Apo objective (resolution of 0.22 microns/pixel). Digital images were analyzed and adjusted using ImageJ software.

TUNEL (TdT-mediated dUTP Nick-End Labeling) assay

Three-micron sections of formalin-fixed paraffin-embedded (FFPE) PDAC tumors were used for apoptosis detection by TUNEL assay (DeadEnd™ Fluorometric TUNEL System, PROMEGA), following the manufacturer's instructions. Briefly, tissues were de-paraffinized in fresh xylene, washed in 100% ethanol, rehydrated by sequentially immersing through graded ethanol washes (100%, 95%, 85%, 70% and 50%) and fixed using 4% methanol-free formaldehyde in PBS. Tumor sections were then treated with proteinase K and incubated with the transferase enzyme and the fluorescein-12-dUTPs, at 37 °C for 60 minutes, inside a humidified chamber. Slides were covered using an Anti-Fade solution (Molecular Probes) and the fluorescein-12-dUTP-labeled DNA was visualized using a Nikon Eclipse 200Ts fluorescence microscopy (Izasa S.A., Barcelona, Spain), images were captured with a microscope-associated camera and processed with a Nikon software package.

Statistical analysis

Error bars represent standard deviation (SD) from the mean (at least n = 3 per group). Statistical analyses were performed with a GraphPad Prism® Software (version 9.0). Data were analyzed by two-tailed, Student's t-test to compare two experimental groups and one- or two-way analysis of variance (ANOVA) with a Tukey correction was used to calculate differences among multiple populations. P-values <0.05 were considered statistically significant. Statistical analyses p > values meaning; * ($p < 0.05$), ** ($p < 0.005$), *** ($p < 0.0005$) and **** ($p < 0.0001$).

RESULTS AND DISCUSSION

Synthesis and characterization of SI-NCs

To develop a PDT triggered by BioLight (BL-PDT) and capable of inducing ROS to tumors *in vivo*, we proposed the development of SI-NCs based on fluorescent metallic quantum dots (QDots 705) as the core, and the bioluminescent protein RLuc8, assembled via an amine condensation reaction, to activate verteporfin (PS) **(Figure 1a-b)**. RLuc8, a mutant to *renilla* luciferase purified following a previously described protocol with minor modifications [24] (**Figure S1a-b**), was selected for this work due to its highly stability in serum and improved light irradiation properties[23]. The activity of RLuc8 was tested after substrate activation (colenterazine, CTZ), reaching its maximum emission at 490 nm (**Figure S1c**).

For the conjugation of RLuc8 to QDots 705, we tested different buffers (PBS, HEPES, MES, Tris-HCl buffer) for an optimal association. 10 mM PBS mixed with 0.1M NaCl was chosen to ensure that the ionic force of the protein would not be compromised, avoiding protein aggregation, and benefiting protein-protein interactions [36,37]. Compared to the So *et al.* study, Tris-base (tris(hydroxymethyl)aminomethane) was discarded as it is not adequate to perform reactions that involve amines, leading to poorer reaction yields [38,39].

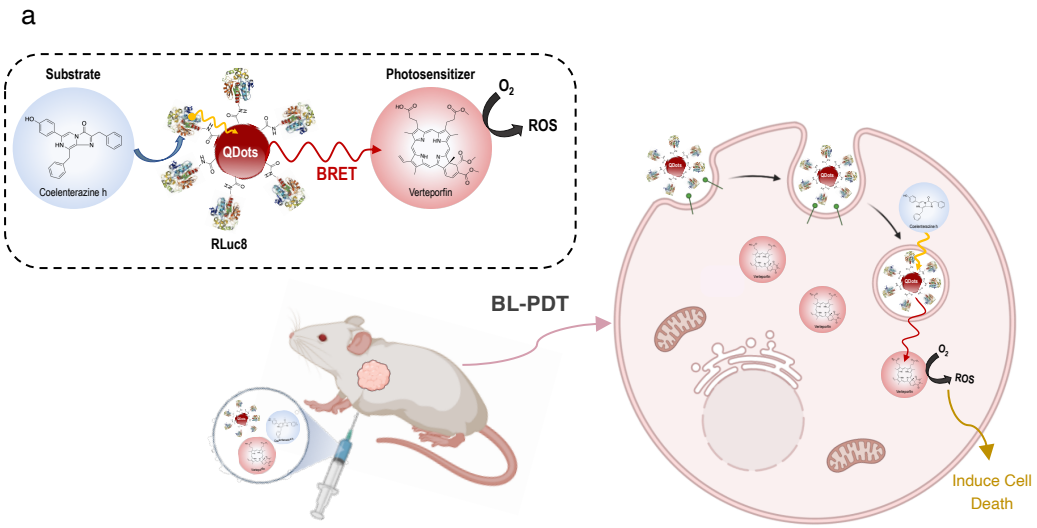

RLuc8: Luciferase enzyme; ***QDots:*** Quantum Dots; ***Substrate:*** Coelenterazine (CTZ); ***Photosensitizer:*** Verteporfin; ***BRET:*** Bioluminescence Resonance Energy Transfer; ***ROS:*** Reactive Oxygen Species; ***BL-PDT***: BioLight Photodynamic Therapy.

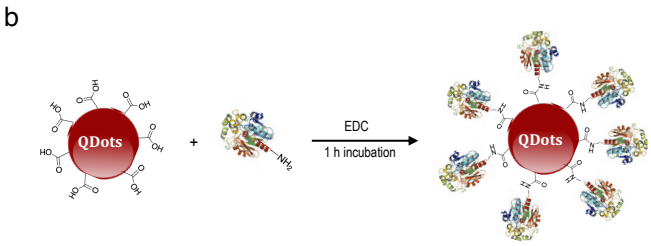

Figure 1. Preparation of SI-NCs (RLuc8-QDots 705 nanoconjugates). **(a)** Schematic representation of the proposed mechanism based on bioluminescent-activated (BioLight) photodynamic therapy (BL-PDT). In deep-tissue, SI-NCs BioLight source can excite a target photosensitive drug more effectively than external laser light. **(b)** SI-NCs coupling reaction undergoing a conversion of the carboxylic acid to amide using EDC (N-(3-Dimethylaminopropyl)-N'-ethylcarbodiimide) as activating agent.

After assembly, the success of the conjugation reaction was verified by agarose gel electrophoresis[24], observing a delay in the migration of the SI-NCs with respect to the free QDots (**Figure 2a**). This is in line with the work reported by Hsu *et al.* with QDots 655 nanoconjugates. A secondary validation of the efficacy of the conjugation was obtained by acrylamide denaturing SDS-PAGE gel, allowing us to observe that (i) free RLuc8 migrates according to its molecular weight (35 kDa), (ii) QDots hardly migrate in this type of gel, and (iii) the SI-NCs, due to their increased size, do not penetrate the gel and remain in the well (**Figure 2b**).

The morphology of the SI-NCs was observed by transmission electron microscopy (TEM) (**Figure 2c**-**S2a**). As can be appreciated, the conjugation of the protein does not lead to a big increase in the size of the QDots (average size of the conjugates is 20 nm, similar to the diameter of the free-QDots provided by the commercial company, which are about 15-21nm; included in **Figure S2b**). It can also be observed that samples are homogeneous, with a polydispersity index <0.3. The nanoconjugates were also characterized in terms of size and zeta potential (ZP) by Dynamic Light scattering (DLS) and Laser Doppler Anemometry (LDA). Results obtained with these two techniques correlate with the size determined by TEM. Moreover, nanoconjugates possess a negative superficial charge, which was expected due to QDots lipophilic surface coating. Protein loading to QDots was additionally calculated using a Bradford's assay, indicating that a mean loading efficiency of 88% was achieved [40] (**Table 1**).

Table 1. Physicochemical Characterization of SI-NCs measured by DLS and LDA. Percentage of RLuc8 loaded to QDots 705 quantified by Bradford's assay (Results are expressed as Mean ± Standard Deviation, n = 5). Abbreviations: nm: nanometer, PdI: polydispersity index, ZP: zeta potential in millivolts (mV), SI-NCs: Self-Illuminating Nanoconjugates (RLuc8-QDots 705).

Formulation	Size (nm)	PdI	ZP (mV)	% RLuc8
SI-NCs	22 ± 2	<0.3	- 6 ± 1	88 ± 2

To promote the activation of the photosensitizer verteporfin within the BL-PDT, it is necessary to achieve an optimal BRET signal between the light source (SI-NCs) and the photosensitizer [34–37]. RLuc8 energy by itself cannot promote the BRET phenomenon between the protein and the photosensitizer. This indicates that an intermediate step is necessary, which in this case is provided by the QDots. The BRET method is based on the Förster resonance energy transfer principle, which postulates that the efficiency of energy transfer between a donor and an acceptor is inversely proportional to the sixth power of the distance between them. However, the energy transfer process not only depends on the distance between the donor and the acceptor, but it is also based on their relative spatial orientation. Therefore, the absence of a BRET signal between two receptors does not necessarily mean that these receptors do not interact with each other [41–44]. Furthermore, the most important characteristic is the overlapping spectra between our nanoconjugates components [45–47]. In SI-NCs, the *RLuc8* acts as a donor and the QDots705 as an acceptor. Initial studies confirmed that both spectra (RLuc8 emission and QDots705 excitation) have a perfect match (**Figure 2d**), and therefore QDots can absorb the light emitted by RLuc8 and transfer it in the required range for the activation of the photosensitizer verteportin (QDots Ex/Em spectra, **Figure S2c**). In the BRET scanning spectrum, it is possible to observe that most of the light emitted by *RLuc8* is efficiently transferred to the QDots (**Figure S2d**). In **Figure 2e**, BRET ratio is calculated as the integral of the signal under the acceptor curve, divided by the integral under the donor curve, was estimated to be 5.05 [45,46], indicative of a superior capacity to produce BRET with respect to previously described conjugates (BRET ratio 5.05 > 1.32 reported by So *et al.,* [23] using RLuc8 and QDots 655). The highest BRET ratio occurs when the light intensity of the donor is closest to 0, indicating that almost all the bioluminescent activity is being transferred to the acceptor. Therefore, this difference in the obtained BRET ratio compared to the one reported by So *et al.*, might be due to the change in the buffer used to store the protein or to perform the coupling reaction to the QDots [48], or to the fact that *RLuc8* presents an enhanced activity and/or stability and probably an improved light output to perform BRET.

The quantum yield (or BRET yield), i.e., the energy transferred within the nanoconjugates, was calculated according to equation 1.

Eq.1

Qy = (*RLuc8* energy coupled to the QD/energy emitted by the QD)

The numerator was obtained by subtracting the emission of the free *RLuc8* (in the same wavelength range that the SI-NCs would then emit) from the emission of the *RLuc8* already coupled to the QDots (SI-NCs). If *RLuc8* emission within the SI-NCs were 0 or closest to it, ideally, this quotient would have a value of 1. SI-NCs achieved a BRET Qy of 0.64-0.72, slightly improved with respect to previous reports (0.60-0.65) with RLuc8-QDots 655 NCs [26].

Next, experiments were carried out to check the stability of the SI-NCs over time, by measuring the kinetics of the BRET on the day of the nanoconjugates synthesis (time 0) and after 4 and 7 days at 4°C storage. At day 4, we observed a loss of 50% in BioLight activity (**Figure 2f**) and after 7 days, BRET was no longer effective (**Figure 2g**). Compared to previous reports in the field using the same approach, total loss of BRET activity has been reported to occur at day 4 [23,24]. Although we observed a significant reduction in the light output of the SI-NCs at day 4, our overall results are encouraging as we provide improved stability.

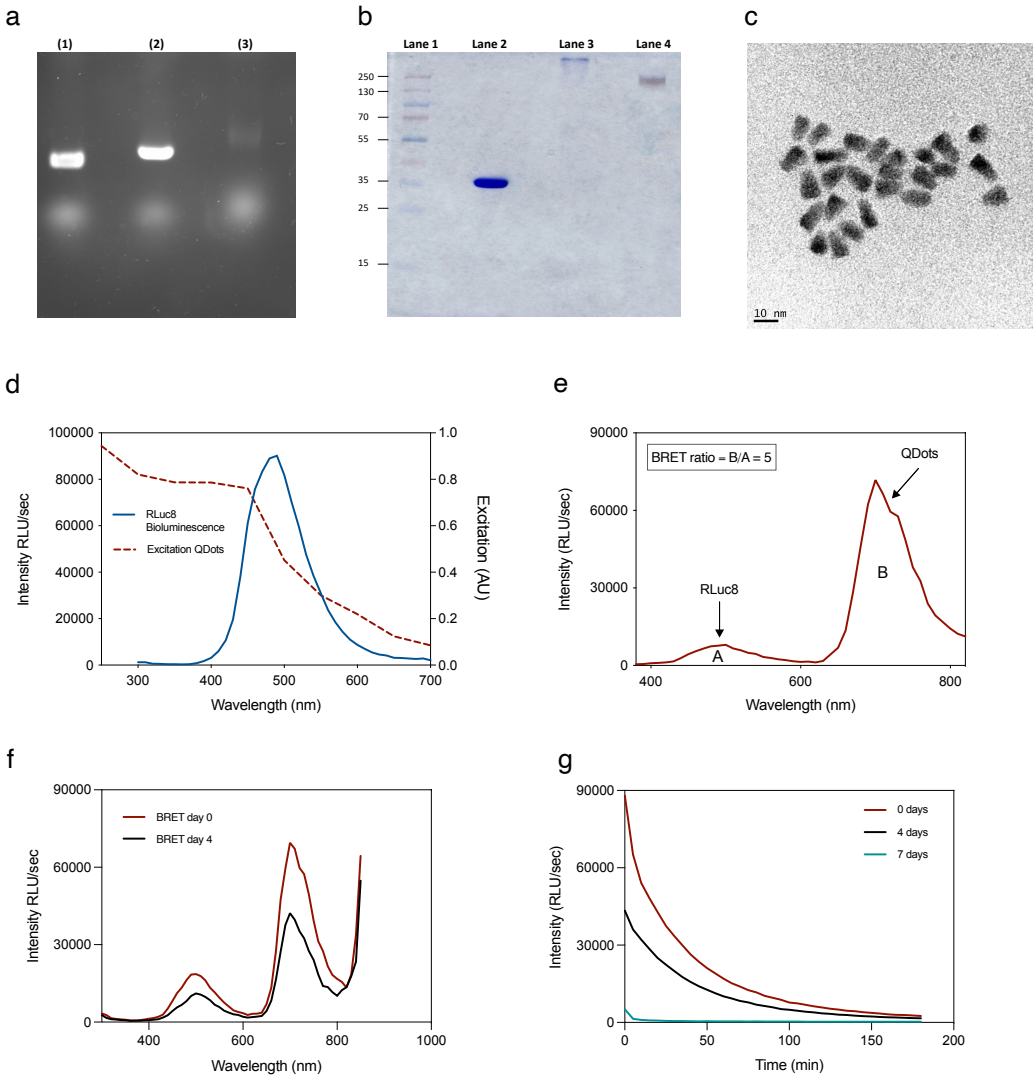

Figure 2. Characterization of SI-NCs. **(a)** 1% agarose gel of components [(1) free QDots; (2) free QDots + EDC physical mixture; (3) SI-NCs] respectively, confirming the successful nanoconjugates association. **(b)** 12% acrylamide electrophoresis gel [Lane 1: ladder; Lane 2: naked *RLuc8*; Lane 3: SI-NCs; Lane 4: free QDots] **(c)** TEM image of SI-NCs morphology and particle size. Scale bar: 10 nm. **(d)** QDots excitation spectra overlaps enzyme maximum RLuc8 emission peak. **(e)** SI-NCs emission spectrum (BRET spectral scanning) with CTZ (1 μg) adding. The BRET ratio was calculated from the ratio of the area under curve of RLuc8 (A) emission between 395 and 600 nm and that of QDots (B) emission between 650 and 760 nm. **(f)** BRET scanning at day 0 and 4. **(g)** Kinetics of SI-NCs emission at 0, 4 and 7 days after their coupling.

SI-NCs can efficiently internalize in pancreatic cancer cells

In vitro experiments were carried out to determine the ability of the SI-NCs to interact with different pancreatic cancer cell lines as showed in **Figure 3-S3**. To the best of our knowledge, this type of SI-NCs has not been previously evaluated for the treatment of pancreatic cancer [49]. First, we show internalization in L3.6pl cells, a pancreas to liver metastatic cancer cell line (**Figure 3a-b**) and PDAC cell line Mia PaCa-2 (**Figure 3c**). In both cell lines, it was possible to observe that the SI-NCs were efficiently internalized at short time-points (after only 30 min of incubation), and that the internalization efficiency reached a maximum at 3h. Similar data was obtained in PANC-1, PaTu8889t and PaTu8889s PDAC cell lines (**Figure S3a-c**). Cell uptake was additionally quantified by flow cytometry, showing around 93% of L3.6pl cells positive after 30 min of incubation (**Figure 3d**). The percentage of internalization slightly decreased after 4h and the maximum mean fluorescence was reached at 2h. In MIA PaCa-2 cells, 99% of cells were positive at all time points, with maximum fluorescence achieved at 1h post incubation (**Figure 3e**). Analogous results were obtained in PANC-1 cells (**Figure S3d**). The internalization of the photosensitizer was also assessed up to 2 hours at a dose of 2μM by confocal microscopy in L3.6pl and MiaPaCa2 cells (**Figure 4a-b**). In relation to other works, internalization rates vary from a few minutes to 3 hours in the case of the SI-NCs and an established 3 hour-incubation for the photosensitizer[25,26]. Importantly, SI-NCs also achieved an excellent uptake in c354 and A6L PDX cells (later tested). In general, the internalization of nanoparticles and nanoconjugates in primary cultures is less efficacious than in established cell lines.

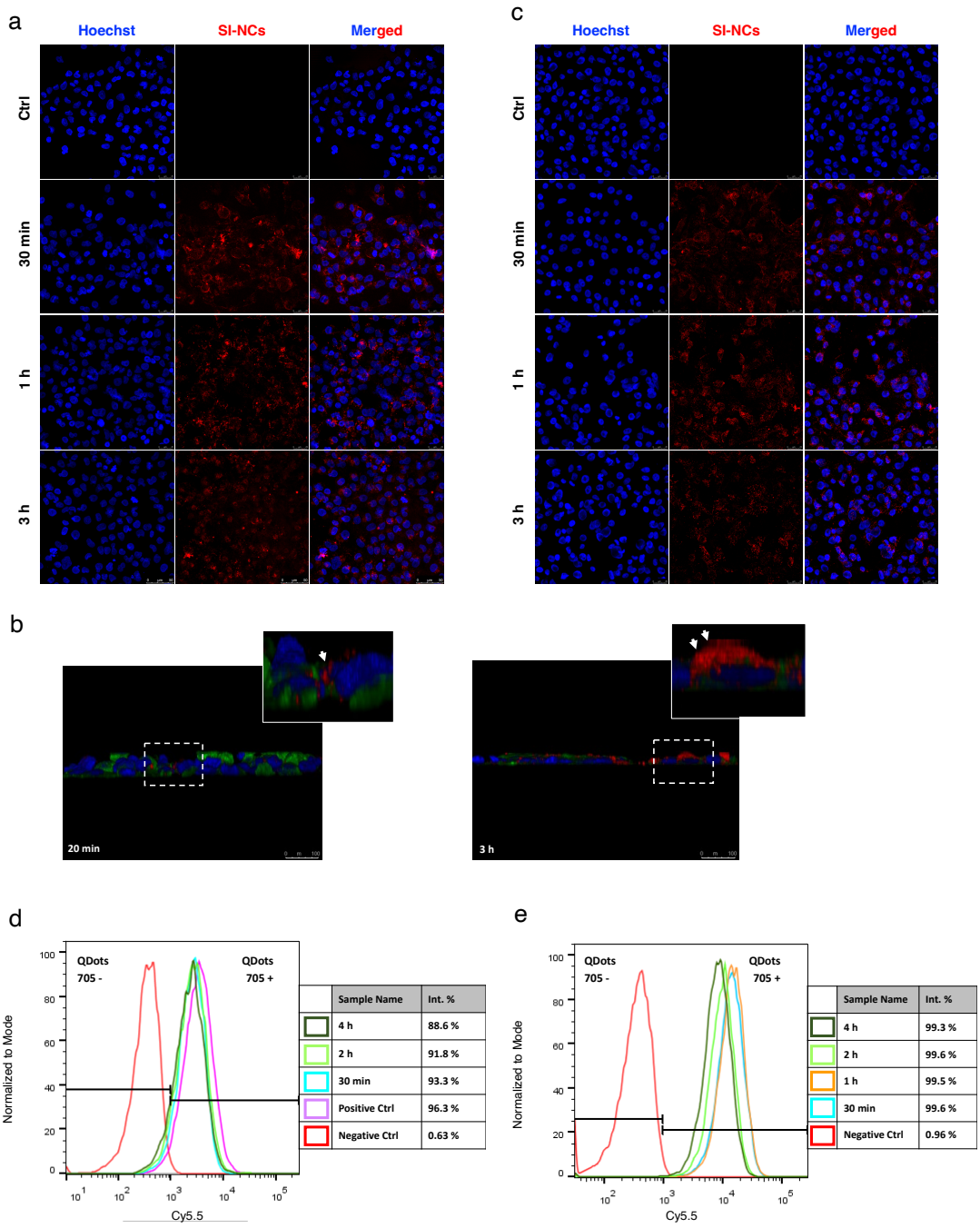

Figure 3. SI-NCs efficiently interact with pancreatic cancer cells. **(a)** Uptake experiments in metastatic pancreas to liver cancer cell line L3.6pl and **(b)** primary tumor cells Mia PaCa-2 of SI-NCs (red signal), incubated at increasing time points (30 min to 3h). Untreated cells were used as control. Cell Nuclei were stained with Hoechst 33342 (blue signal) observed by Confocal Laser Microscopy (CLM). **(c)** 3D projections of Confocal images in L3.6pl cells. SI-NCs (red) indicated with white arrows; cell nuclei (blue); cytoskeleton (green) stained with Alexa Fluor 488 Phalloidin™ (Invitrogen™). Evaluation of the internalization by Flow cytometry to calculate Cy5.5 positive cells (SI-NCs containing QDots 705 are observed by Cy5.5 laser line). % Internalization and mean fluorescence expressed in tables **(d)** for L3.6pl and **(e)** for Mia PaCa-2 cells.

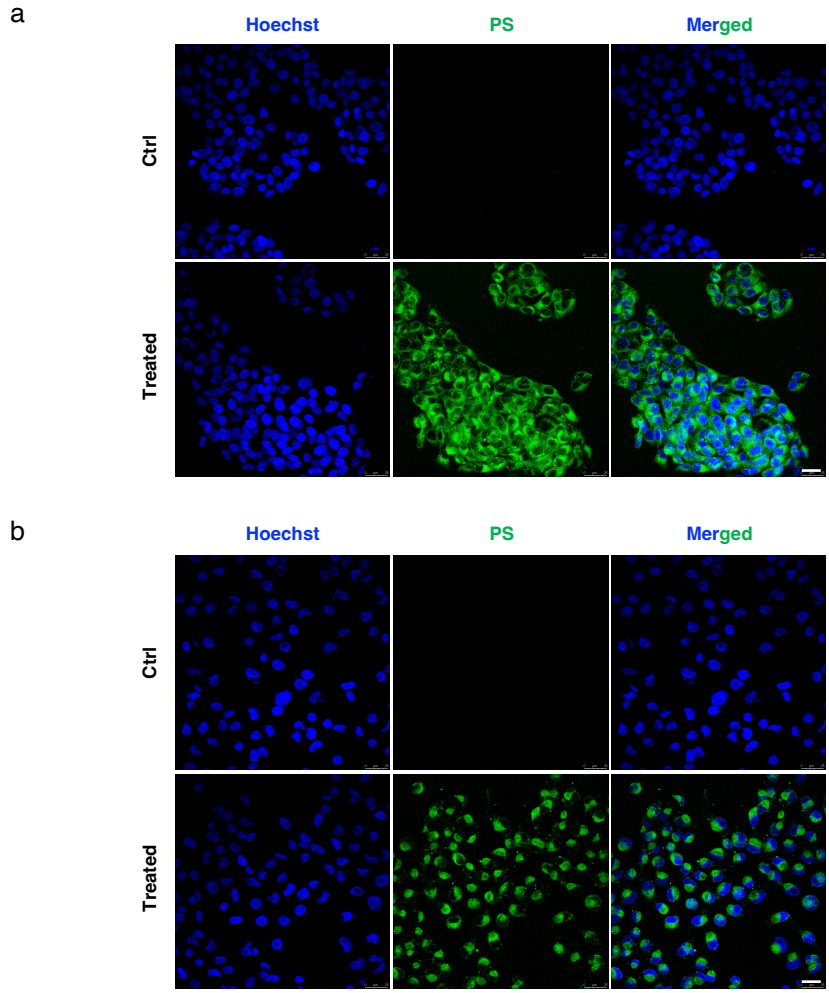

Figure 4. Photosensitizer verteporfin have an optimal cytosolic distribution *in vitro*. **(a)** L3.6pl and **(b)** Mia PaCa-2 cells cytosolic distribution of the photosensitizer acquired images by CLM after adding a dose of 2μM and after 2-hourincubation (Scale bar: 25 μm, white). Cell Nuclei were stained with Hoechst 33342 (blue signal) and fluorescent photosensitizer (green).

BioLight PDT (BL-PDT) effect in pancreatic cancer cells

Before investigating the BL-PDT effect in pancreatic cancer cells, preliminary studies were established with the photosensitizer, verteporfin, and the QDots705. We confirmed the excitation of verteporfin at 690 nm by performing an absorbance spectrum. Indeed, as observed in **Figure 5a**, QDots should theoretically excite the photosensitizer, since both spectra (excitation and emission) perfectly overlap, indicating that both components are suitable for our BL-PDT strategy.

Next, the cytotoxicity of the photosensitizer was determined in L3.6pl (**Figure 5b**), Mia PaCa-2 (**Figure 5c**) and in other pancreatic cell lines, PANC-1 (**Figure S4a**), after 4h of incubation to establish a working-dose. It was observed that, independent of the cell line, and as expected, an increase in cell death occurred as a function of concentration. There were no significant differences between the different cell lines. Therefore, a dosage of 4 μM was selected for further experiments (cell viability was closed to 90-95%). SI-NCs cytotoxicity was also evaluated in L3.6pl cells (**Figure 5d**). It was necessary to tightly adjust the dose due to the intrinsic toxicity of QDots' heavy metals core. An IC50 of 4.241[μM] was calculated (**Figure S4b**). While an IC50 range estimated between 10^2 – 10^3 nM has been reported in the literature, this result can be influenced by the QDots diameter, surface modification, metallic core and, of course, cell type used and exposure time [50]. There are studies using different metallic core compositions that obtained an IC50 in the range of 3 to 400 nM in cell lines such as HaCaT (Keratinocytes), MCF7 (Breast metastatic adenocarcinoma) and HT-29 (Human Colorectal Adenocarcinoma Cell Line) [51,52].

As reported by *Kim et al.,*[26], BL-PDT, via photosensitizer activation, induces a cytotoxic response into the tumor leading to cell death. Therefore, we monitored pancreatic cell viability after BL-PDT. Importantly, as shown for L3.6pl in **Figure 5e**, and Mia PaCa-2 cells in **Figure 5f**, at an optimal and low dose of SI-NCs (1 pmol) and verteporfin (4 μM), BL-PDT lead to cytotoxicity. In addition, no cell death was detected when cells were incubated with the SI-NCs, verteporfin, CTZ, or propylene glycol 1% (PG 1%; the vehicle for coelenterazine). Lastly, we evaluated the effect of a higher dose of SI-NCs on BL-PDT induced cytotoxicity, and while increasing concentrations (5 pmol) improved the efficacy of the therapy, it also increased toxicity in Mia PaCa-2, L3.6pl and PANC-1 cells (**Figure S4c-e**).

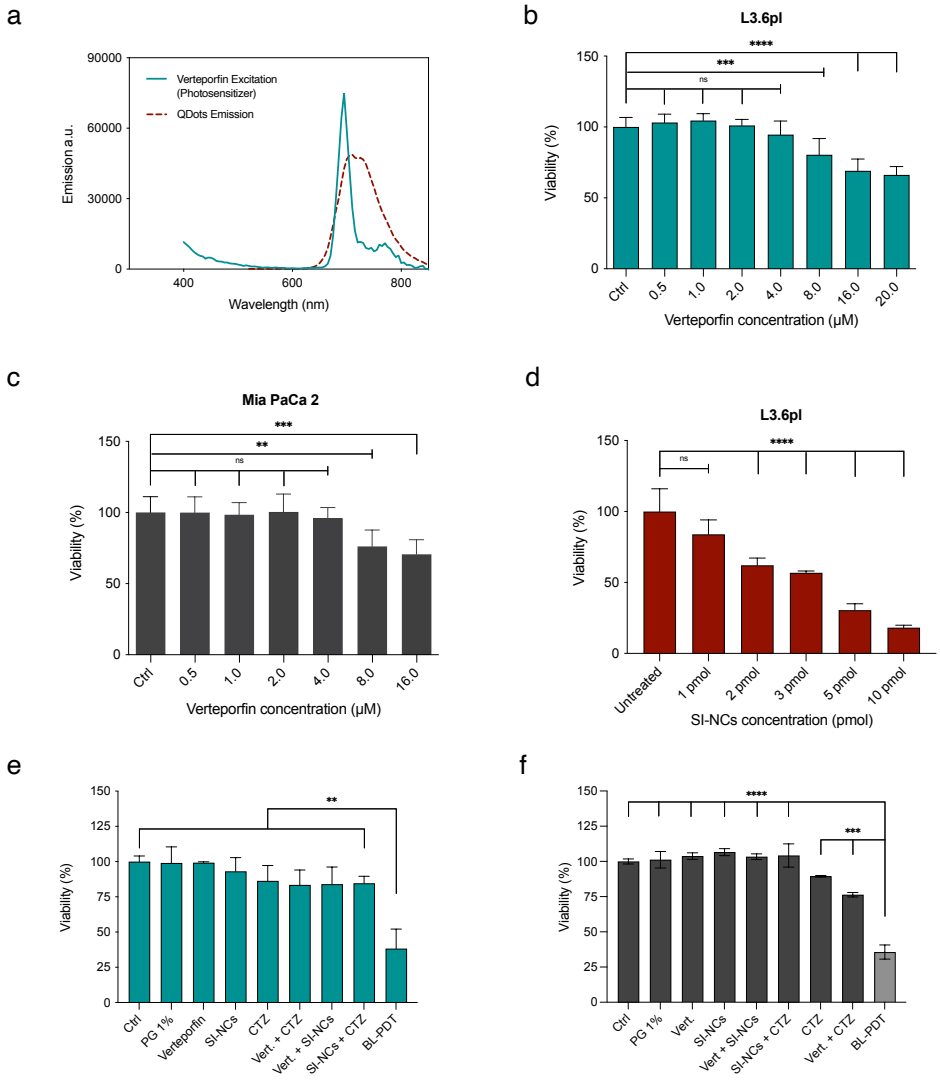

Figure 5. BL-PDT induces cell death in pancreatic cancer cells. **(a)** Excitation spectra of the photosensitizer matches the emission spectra of the QDots. Study of verteporfin cytotoxicity in **(b)** L3.pl6 and **(c)** Mia PaCa-2 cells after 4 hours of incubation at increasing concentrations (μM) of verteporfin. **(d)** SI-NCs cytotoxicity evaluated by MTT in L3.6pl cells after 4 hours of incubation with an IC50 calculated of 4.24. Statistical analyses ANOVA with a Dunnet's test. Cell viability analysis following BL-PDT in **(e)** L3.6pl and **(f)** Mia PaCa-2 cells. Doses: Verteporfin (4 μM); SI-NCs (1 pmol); CTZ (20 μg/mL). Bars representing: 1-8 controls and 9 BL-PDT treatment. All data are expressed in terms of dose-response and/or concentration/viability. Data are presented as mean ± SD (at least n = 3 per group). Statistical analyses p-value meaning; * ($p < 0.05$), ** ($p < 0.005$), *** ($p < 0.0005$) and **** ($p < 0.0001$).

BL-PDT generates intracellular ROS and induces apoptosis in pancreatic cancer cells.

It has been reported that cell death induced by BL-PDT is due to the production of ROS, in particular highly reactive and toxic singlet oxygen ($^1O_2$, SO) [6,14]. Consequently, several studies have concluded that after being activated, non-toxic photosensitizers generate ROS that induce apoptosis in cancer cells [6,16]. To validate the cell death mechanism produced in BL-PDT, intracellular ROS was measured using the fluorescent dye H_2DCFDA, and Luperox® (tert-butyl hydroperoxide; t-BHP) was included as an appropriate ROS-inducer positive control [53]. BL-PDT was performed exactly as described above, except L3.6pl cells were pre-incubated with the H_2DCFDA dye in order to detect ROS levels, and 12h after BL-PDT, significant ROS levels were detected. To determine the optimal dose at which SI-NCs induce ROS, a dose-response assay was performed (doses ranging from 1–5 pmol of SI-NCs per well). Maximum ROS production was achieved with 1 pmol of SI-NCs. Interestingly, ROS levels decreased as the concentration of the SI-NCs increased (**Figure 6a**), suggesting that at higher SI-NCs concentrations, the mechanism underlying BL-PDT cell death is ROS-independent. Indeed, the above-described cell viability assays showed reduced viability at higher doses of the SI-NCs, which can lead to the conclusion that other forms of regulated cell death, such as necroptosis or necrosis, could also be involved, as previously reported [54,55]. This was further explored in subsequent *in vivo* studies described in the next sections.

Quantification of ROS species was also measured in the c354 pancreatic PDX-derived primary culture, which was also used for subsequent *in vivo* experiments. ROS production was successfully achieved with 2 pmol of SI-NCs and 4 μM of photosensitizer as non-toxic effects were observed in controls (**Figure 6b**).

Finally, we compared the efficacy of the BL-PDT with conventional laser-PDT. For this and as described in the supporting information, we manufactured a laser that emits at 690 nm (photosensitizer's emission) and measured ROS after verteporfin was incubated with L3.6pl pancreatic cancer cells. To optimize laser-dependent PDT, preliminary experiments were performed in L3.6pl cells. A laser light dose of 0.36 J/cm^2 and 3 cycles of 30s, gave the greatest fluorescence signal and ROS production (**Figure S4f**). At higher laser irradiation, fluorescence related to ROS production was significantly reduced, suggesting that other cell death pathways could be activated, such as necrosis, and in agreement with our previous results for BL-PDT [31,54]. In light of these results in **Figure 6c**, we concluded that the BL-PDT mediated by the SI-NCs is

more efficient than laser-PDT as ROS formation was significantly lower for laser-PDT with respect to BL-PDT using bioluminescent SI-NCs.

Having confirmed that BL-PDT induces ROS, we next validated apoptosis induction. In **Figure 6d**, an immunofluorescence assay (IF) was performed to assess the levels of annexin V, a protein commonly used to detect apoptotic cells[56]. Confocal microscopy images revealed high levels of annexin V only in the positive control and BL-PDT treated cells, confirming an apoptosis-mediated cell death mechanism of action (**Figure S5**). Apoptosis was also confirmed by direct visualization of treated and non-treated L3.6pl cells by transmitted light microscopy. This experiment allows to visualize the morphology of the apoptotic cells as shown in **Figure 6e**. Herein, we provide extensive *in vitro* data that prove the successful efficacy of the develop SI-NCs to activate verteporfin, altogether working and perfectly integrated in BL-PDT.

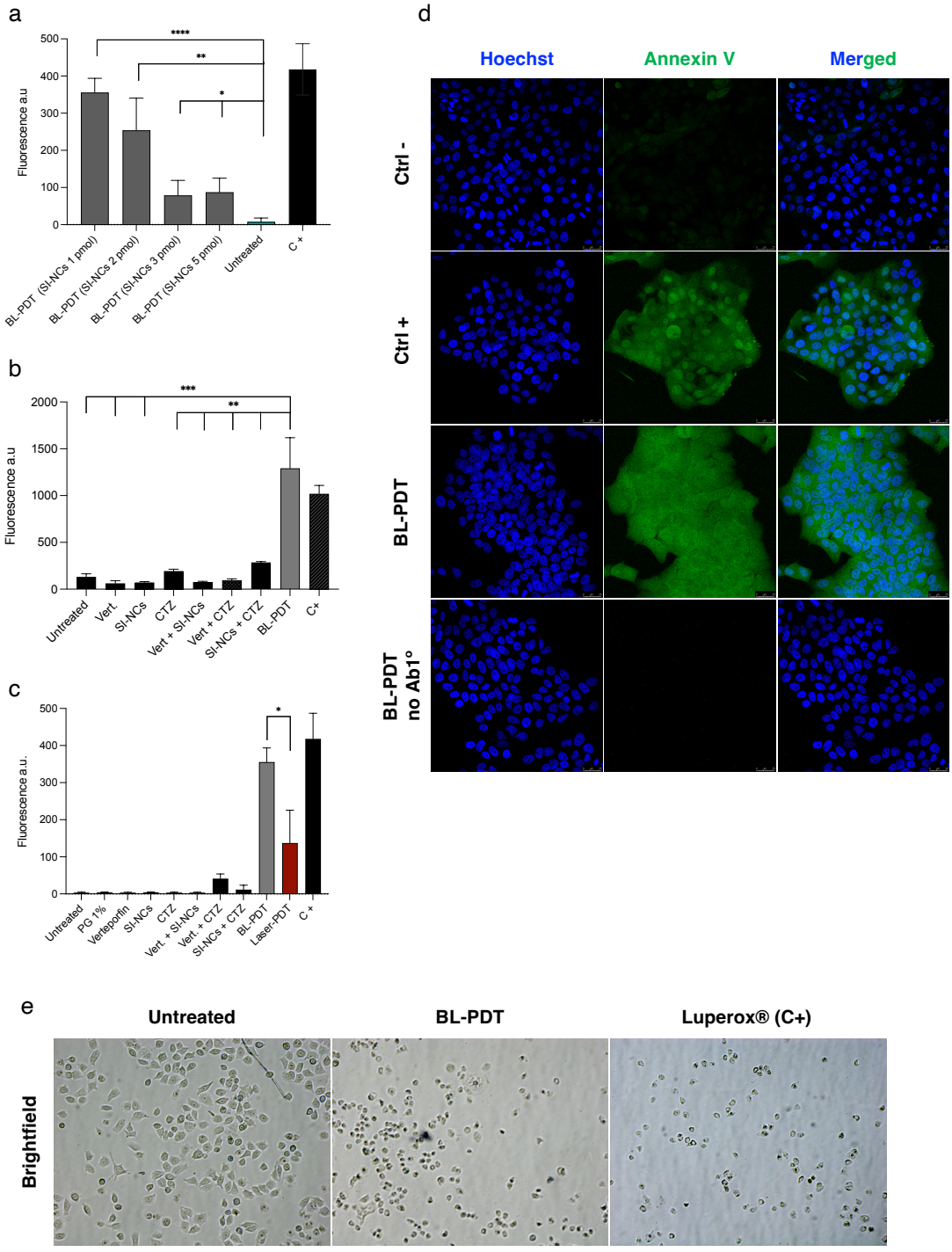
a
Fluorescence a.u
BL-PDT (Sl-NCs 1 pmol)
BL-PDT (Sl-NCs 2 pmol)
BL-PDT (Sl-NCs 3 pmol)
BL-PDT (Sl-NCs 5 pmol)
Untreated
C +
b
Fluorescence a.u
Untreated
Vert.
Sl-NCs
CTZ
Vert + Sl-NCs
Vert + CTZ
Sl-NCs + CTZ
BL-PDT
C+
c
Fluorescence a.u.
Untreated
PG 1%
Verteporfin
Sl-NCs
CTZ
Vert. + Sl-NCs
Vert. + CTZ
Sl-NCs + CTZ
BL-PDT
Laser-PDT
C +
d
Hoechst
Annexin V
Merged
Ctrl -
Ctrl +
BL-PDT
BL-PDT no Ab1°
e
Untreated
BL-PDT
Luperox® (C+)
Brightfield

Figure 6. Ability of the SI-NCs to induce a therapeutic response. **(a)** H_2DCFDA assay to measure intracellular ROS levels in L3.6pl cells at increasing SI-NCs (1-5 pmol) doses. Best performance determined at 1 pmol treatment. **(b)** Intracellular ROS production, measured with the H_2DCFDA assay, in pancreatic PDX-derived c354 primary culture that will be further used for *in vivo* experiments. **(c)** Comparison of ROS generated with BL-PDT versus laser-PDT treatment. BL-PDT achieved a significant difference compared to laser-PDT in L3.6pl cells. **(d)** CLM images of Annexin V levels assessed by immunofluorescence to confirm apoptosis cell-mediated killing mechanism after BL-PDT treatment. Appropriate negative controls and the positive control (Luperox®) were used to induce apoptosis. BL-PDT produced higher Annexin V signal. **(e)** Images of apoptotic cell morphology, observed by transmitted light microscopy after 16h BL-PDT treatment in L3.6pl cells. Data are presented as mean ± SD (at least n = 3 per group). a.u. = arbitrary units. Statistical analyses p-value meaning; * ($p < 0.05$), ** ($p < 0.005$), *** ($p < 0.0005$) and **** ($p < 0.0001$).

BL-PDT induces tumor cell death in two pancreatic PDX models.

First experiments were conducted to confirm the capacity of SI-NCs to produce BioLight *in vivo* after administration through different routes (supp. Info.; **Figure S6**). After confirmation of a successful emission of BioLight by the SI-NCs, experiments were designed to evaluate the efficacy of BL-PDT, using for that purpose pancreatic orthotopic tumors (c354PDX and A6LPDX in male NOD/SCID mice). C354PDX group was treated twice a week for 3 weeks. Considering that we recreated a pancreatic tumor in the target organ, SI-NCs and the photosensitizer (Verteporfin) were administered intraperitoneally to improve pancreas delivery. Meanwhile, substrate (CTZ) was systemically injected. The succession of therapy was followed as explained in previous section *"materials & methods"* and supporting information (**Figure S7**). Last treatment day, SI-NCs light emission was followed by IVIS observing how nanoconjugates reached tumor location. After that, mice were sacrificed, and BL-PDT efficacy analyzed. In c354PDX, SI-NCs reached the tumor 45 minutes after administration (30 min + 15 min) (**Figure 7a**). Tumor weight did not present a significant reduction. And, despite peritoneal metastasis weight was reduced in the treatment group, significant differences were not attained either (**Figure 7b**). However, histological sections clearly present a great necrotic area after BL-PDT treatment with SI-NCs compared to control and sham groups (**Figure 7c**). % Necrotic area was quantified as represented in **Figure 7d**, and statistical analysis concluded that BL-PDT significantly incremented the necrotic area in tumors. Cell proliferation marker PCNA, a nuclear protein synthesized in the late G1 and S phases of the cell cycle, was assessed for immunohistochemical (IHC) analysis. As shown in BL-PDT group

efficiently induced a reduction in cell proliferation in c354PDX. Although, it is observed a strong trend, cell proliferation was not significantly reduced in comparison to control and sham groups (**Figure 7e**). Next experiments were to evaluate the levels of apoptosis after BL-PDT as it is proposed as the cell death mechanism. TUNEL assays led us to affirm that our BL-PDT induced apoptosis in c354PDX tumor as observed by fluorescent microscopy (**Figure 7f**). Positive apoptotic cells were labeled in green, and nuclei was stained with Hoechst 33342 (blue) and acquired using a 405 nm laser line and excitation 488 nm. Thus, positive apoptotic cells were also quantified in both groups (control and BL-PDT) in which calculated positive events were much higher in BL-PDT group confirming apoptosis (**Figure 7g**).

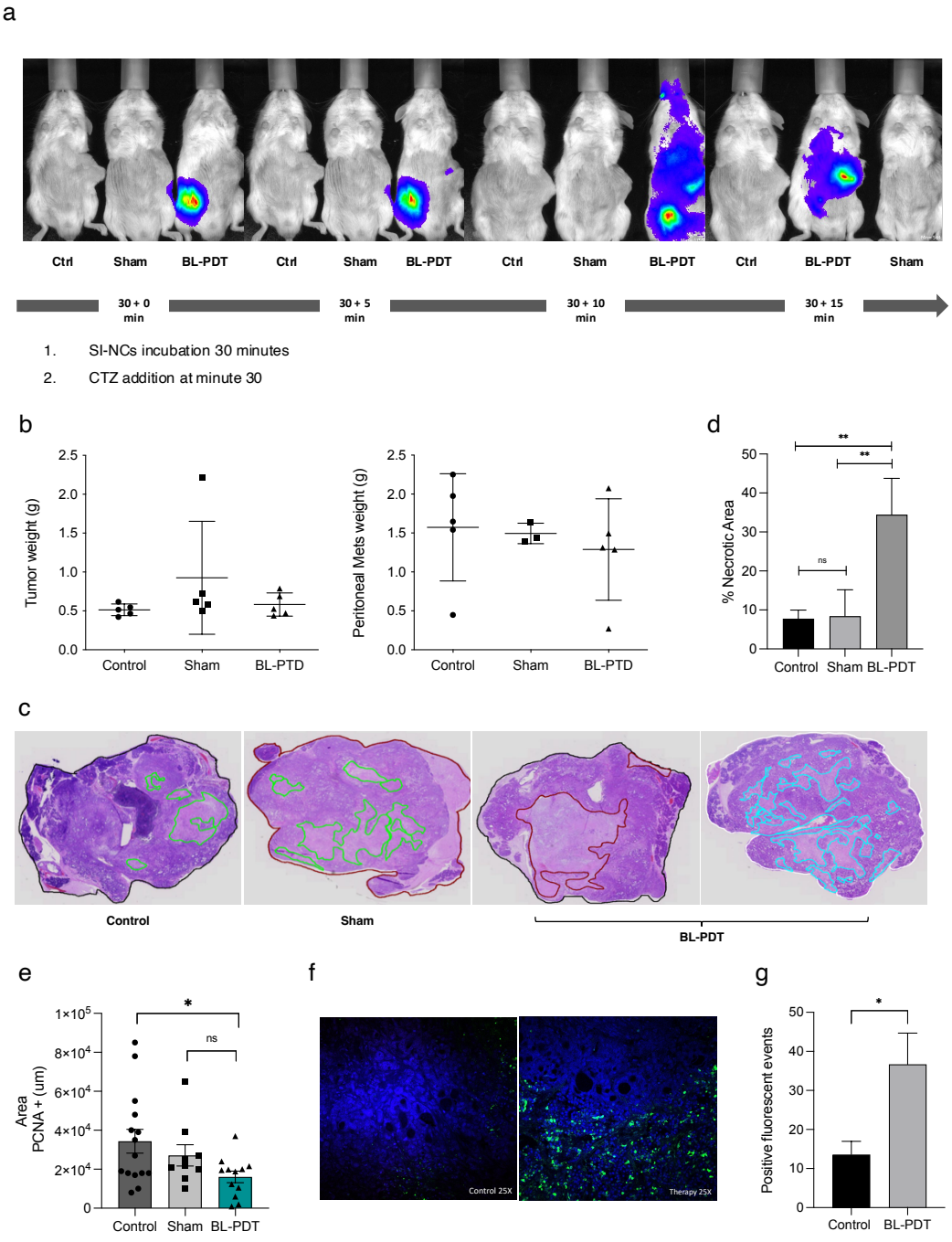

Figure 7. Photodynamic therapy (PDT) treatment efficiently induces necrosis and apoptosis in c354PDX orthotopic tumors. **(a)** By IVIS analysis, SI-NCs (50 pmol i.p.) bioluminescence was observed at the tumor site (pancreas) 15 minutes upon CTZ (5 nmol i.v.) injection. Shown are images for 4 mice. **(b)** Mean ± SD of tumor and peritoneal metastasis weights in control, sham and BL-PTD groups, observing a tendency for reduction in the BL-PDT group. **(c)** Representative images of hematoxylin and eosin (H&E)-stained histological sections of tumors (3 μm) from the three experimental groups (control, sham & BL-PDT). **(d)** H&E-stained sections for each mouse were prepared,

digitalized and used to evaluate the percentage of necrosis in the tumors. Data are presented as mean ± SD of the % necrotic area/total tumor area. **(e)** Additional serial sections were used for immunohistochemical (IHC) analysis of the number of PCNA-positive cells. Data are presented as mean ± SD of the area of PCNA+ cells in representative sections. **(f)** Apoptotic events in tumors were analyzed using the TUNEL assay where images were captured by fluorescence microscopy. Nuclei were stained with Hoechst 33342 (blue) and TUNEL staining is shown in green (Zoom: 25X). **(g)** Positive green-fluorescent events for TUNEL were quantified in control and BL-PDT groups. Data are presented as mean ± SD (at least n = 3 per group). Statistical analyses p-value meaning; * ($p < 0.05$), ** ($p < 0.005$).

Regarding A6LPDX orthotopic results led us to similar conclusions. SI-NCs reached A6LPDX after 35 minutes incubation observed by IVIS (**Figure 8a**). Concerning tumor weight, an apparent reduction in the primary tumor was not observed. Nevertheless, it was observed that peritoneal metastasis weight decreased in the BL-PDT group (**Figure 8b**). Cell proliferation marker in A6LPDX, did not give positive results as in the case of c354PDX orthotopic (**Figure 8c**). Therefore, we cannot conclude that BL-PDT reduce tumor cell proliferation in A6LPDX after the intraperitoneal injection of SI-NCs. In **Figure 8d-e**, we observed by fluorescent microscopy, TUNEL assays to evaluate the apoptosis generated after BL-PDT treatment, as well as in c354PDX. And the number of positive events were also quantified in control, sham, and BL-PDT groups. Quantification analysis resulted in a significant higher number of events of BL-PDT positive cells compared to control and sham groups.

Overall, *in vivo* results in orthotopic c354PDX and A6LPDX tumors suggest that BL-PDT treatment fulfills its goal by inducing tumor cell death. Although a significant tumor reduction was not achieved, a tendency to decrease in peritoneal metastasis weight hints the efficacy of BL-PDT in pancreatic tumors. It is true that a higher number of injections and an extended treatment, could probably had resulted in a reduced tumor and more efficiently tumor cell proliferation arrest in BL-PDT group. However, control mice tumor would not endure a longer treatment. Importantly, SI-NCs demonstrated the ability to induce cell death by generating BioLight in twain PDX. This work here presented opens the door for the use of self-illuminating RLuc8-QDots705 nanoconjugates, in combination with the approved drug verteporfin, as a promising tool to trigger an anti-tumoral response in PDAC and overcome the main limitations of laser-PDT for treatment of this solid and internal tumors.

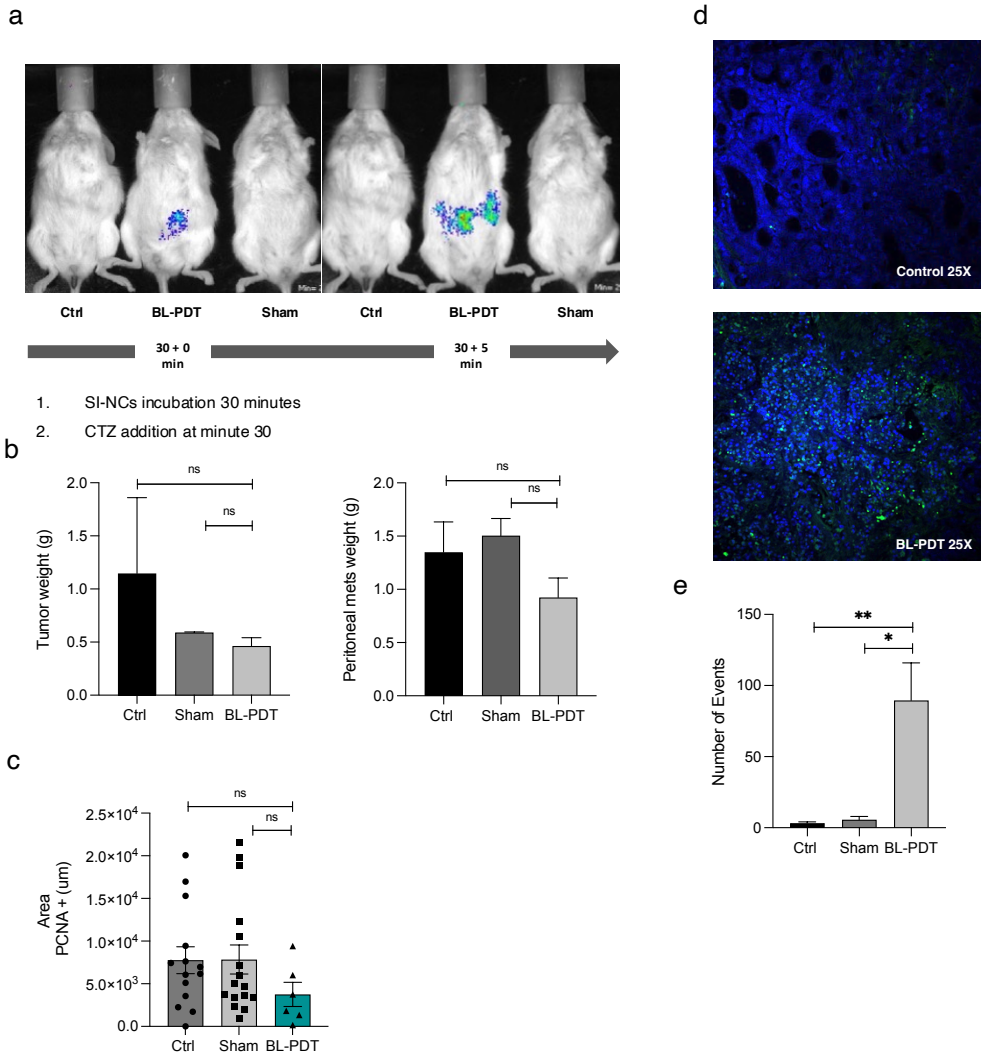

Figure 8. BL-PDT treatment triggers apoptosis in A6LPDX orthotopic tumors. **(a)** In A6L PDX orthotopic tumors, SI-NCs reached the tumors 5 minutes following CTZ injection, visualized using an IVIS system. **(b)** Mean ± SD of tumor and peritoneal metastasis weights in control, sham and BL-PTD groups, observing a tendency for reduction in the BL-PDT group. **(c)** Serial sections were used for immunohistochemical (IHC) analysis of the number of PCNA-positive cells. Data are presented as mean ± SD of the area of PCNA+ cells in representative sections. **(d)** Apoptotic events in tumors were analyzed using the TUNEL assay where images were captured by fluorescence microscopy. Nuclei were stained with Hoechst 33342 (blue) and TUNEL staining is shown in green (Zoom: 25X). **(e)** Positive green-fluorescent events for TUNEL were quantified in control and BL-PDT groups. Data are presented as mean ± SD (at least n = 3 per group). Statistical analyses p-value meaning; * ($p < 0.05$), ** ($p < 0.005$), *** ($p < 0.0005$) and **** ($p < 0.0001$).

CONCLUSIONS

As light tumor penetration is a great limitation treating deep-tissue tumors in clinical application of laser-PDT. In this study we have establish a possible alternative to solve this problem. SI-NCs based on RLuc8 and QDots705 were developed and fully characterized, to be used in combination with the approved drug verteporfin. Photosensitizer photocatalysis due to SI-NCs excitation source was stimulated by substrate (coelenterazine) activation. *In vitro* data revealed the potential of SI-NCs and verteporfin to activated ROS and induce apoptosis, without having to resort to the use of an external laser. This nanotechnology will enrich cancer nanomedicine in the way of treating alone deep cancer lesions by using BL-PDT therapy.

Furthermore, orthotopic c354PDX and A6LPDX *in vivo* experiments proved the real potential of this strategy for the treatment of pancreatic cancer.

Supporting Information

METHODS

Reagents. QDots™ 705 ITK™ Carboxyl Quantum Dots (Invitrogen, ThermoFisher Scientific, USA). Photosensitizer Verteporfin was provided by Sigma-Aldrich (Madrid, Spain) used in *in vitro* experiments and (Cayman Chemicals, USA, supplied by Vitro S.A., Spain) for *in vivo* studies. Coelenterazine h was purchased from Invitrogen (ThermoFisher Scientific, USA). Phosphate Buffer Saline (PBS) was acquired to Sigma-Aldrich (Madrid, Spain). HPLC-grade Ethanol (EtOH) and Water were obtained from Fisher Chemicals (Thermo Fisher Scientific, USA). All other chemicals used were HPLC or UPLC purity grade.

Extraction, purification and characterization of RLuc8. The plasmid (pBAD-RLuc8) expressing the bioluminescent protein RLuc8 was transformed into the E. coli LMG194 bacterial strain (deficient in arabinose metabolism). The protein expression was induced with the addition of arabinose for 12 hours. Then, it was purified using a disposable resin column containing Ni-NTA (HisPur™ Ni-NTA Superflow Agarose, Thermo Fisher Scientific, USA) thanks to the affinity of the polyhistidine tail that contains the plasmid to this nickel resin. The final concentration was determined by performing the Bradford's test (BioRad Protein Assay kit). RLuc8 activity was measured using a calibrated luminometer (SYNERGY H1, microplate reader, BioTek). For this, 1 μL of protein from a stock prepared at a concentration of 0.2 μg/μL (diluted in BSA 10mg/mL acting as a transporter protein) was mixed with 100 μL of 100 mM sodium phosphate buffer, pH=7.0. 0.5 μg of the substrate coelenterazine (from a 1mg/mL stock prepared in propylene glycol 1%) was added and the activity measured immediately in a 96-well plate (Corning® 96 well NBS™ Microplate, CLS3990).

Quantum Dots (QDots) characterization. Commercial QDots (Qdot™ 705 ITK™ Carboxyl Quantum Dots, Invitrogen, ThermoFisher Scientific) were characterized measuring its excitation and emission spectrum in a fluorimeter (SYNERGY H1, microplate reader, BioTek). Its molecular shape was also characterized by Transmission Electron Microscopy (TEM) (JEOL JEM-1011) by adding 10 pmol of QDots to 5 μL of ethanol 100%. The drug Verteporfin (Sigma-Aldrich) was also characterized by measuring its excitation spectrum using a 10 μg/mL sample in a fluorimeter.

Laser source. To be able to contrast the obtained results using internal bioluminescent light, a custom laser source has been specifically developed to activate the photosensitizer verteporfin. To offer a great flexibility during the experimental works, through a fiber optic cable equipped with a collimator at its end, the source can supply collimated light beams on any optical power up to 440 mW centred at an optimal wavelength of 690nm. To offer different collimated laser beam sizes, different collimators can be connected. The collimated beam (same transverse distribution at any distance) of photons is distributed following a "quasi-Gaussian" transverse function. It presents the maximum in the centre, its power decaying by half at points separated by a cross-sectional distance FWHM (mm). As reference, beam sizes (FWHM) can range from 2.05 mm to 2.50 mm, at average output powers of 100 mW and 400 mW respectively.

The source can supply an optical carrier of 434.78 THz (690nm wavelength) in continuous regimen (CR) or modulated regimen (MR) modes. In MR, the optical carrier is modulated with a sinusoidal modulating signal of variable amplitude and frequency ($0 \leq f \leq 25$Hz), frequency range that includes "natural human body frequencies " according to the expression:

$$P_O(t) = P_O\,(1 + m \cdot x(t)) \qquad [W]$$

Where Po is the mean power, m is the modulation index ($0 \leq m \leq 1$) and x(t) is the modulating function which in this case is cos ($2\pi ft$), whose frequency f can be of any value in the 0 to 25 Hz range. Any photonic dose (total energy supplied) can be obtained, automatically, just by selecting its average optical power (Po), and the exposure time t (s).

***In vivo* biodistribution in mice.** Mice were housed according to institutional guidelines and all experimental procedures were performed in compliance with the institutional guidelines for the welfare of experimental animals approved by the Universidad Autónoma de Madrid Ethics Committee (CEI 60-1057-A068 and CEI 103-1958-A337) and La Comunidad de Madrid (PROEX 335/14 and 294/19) and in accordance with the guidelines for Ethical Conduct in the Care and Use of Animals as stated in The International Guiding Principles for Biomedical Research involving Animals, developed by the Council for International Organizations of Medical Sciences (CIOMS). Briefly, mice were housed according to the following guidelines: a 12 h light/12 h dark cycle, with no access during the dark cycle; temperatures of 65-75°F (~18-23°C) with 40-60% humidity; a standard diet with fat content ranging from 4 to 11%; sterilized water was accessible at all times; for handling, mice were manipulated gently and as little as possible; noises, vibrations and odors were minimized to prevent stress and decreased breeding performance; and enrichment was always used per the facility's guidelines to help alleviate stress and improve breeding.

Eight-week-old 25 g C57Bl /6J female mice (Janvier Labs, France), under isoflurane inhalation anesthesia (Induction in a 3% vol chamber, maintenance in a 1.5% mask - XGI-8 anesthesia equipment) were retro-

orbital sinus injected with 100 μL of nanosystems. Bioluminescence was recorded with the IVIS-Lumina II *in vivo* optical imaging equipment and results analyzed with "spectral *in vivo*" software. Mice were sacrificed in a CO2 chamber and a complete organ necropsy was performed.

RESULTS

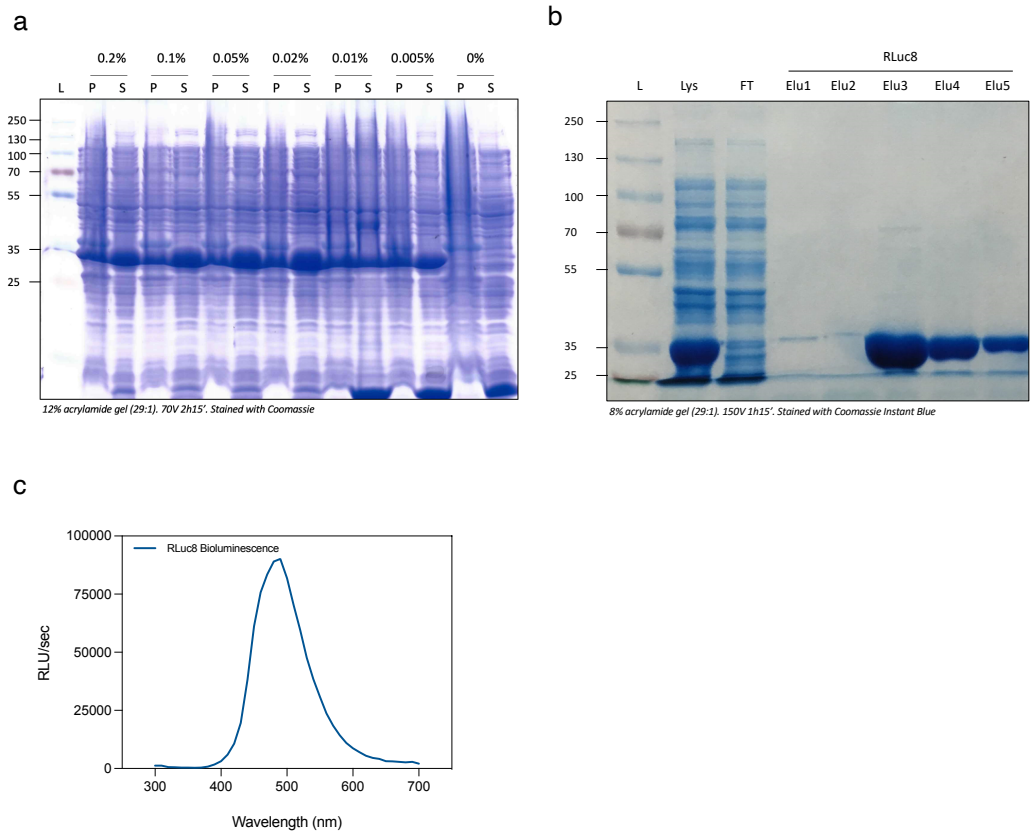

Figure S1. (a) 12% Acrylamide electrophoresis gel for plasmid induction optimization with different percentages of D-Arabinose (0-0.2%). 0.05% gave the best protein solubility and expression. **(b)** 12% Acrylamide electrophoresis gel to visualize each elution during RLuc8 purification. **(c)** Bioluminescence spectral scanning of RLuc8's activity after substrate (CTZ) addition (0.5 μg).

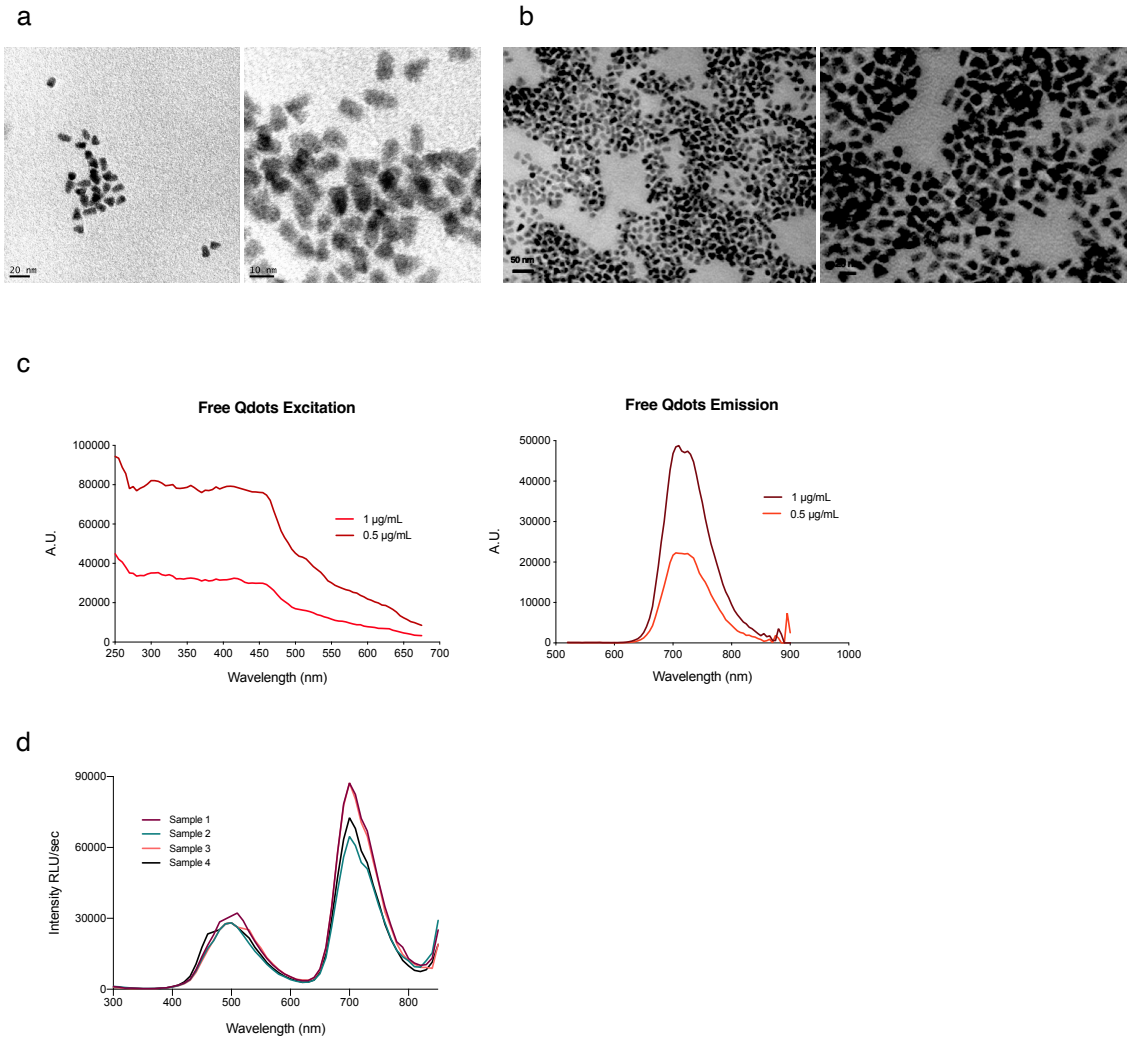

Figure S2. (a) Representative TEM images to confirm SI-NCs morphology and particle size. Scale bars: 20 and 10 nm, respectively. **(b)** Representative TEM images to observe commercial free QDots 705 morphology and particle size before nanoconjugates association. Scale bars: 50 and 20 nm, respectively. **(c)** Commercial QDots 705 excitation (left) and emission (right) spectra at lower and higher sample concentrations (0.5 and 1 µg/mL in EtOH). **(d)** BRET representation of 4 batch samples of SI-NCs on day 1 of their association. CTZ dose: 5 µg/mL.

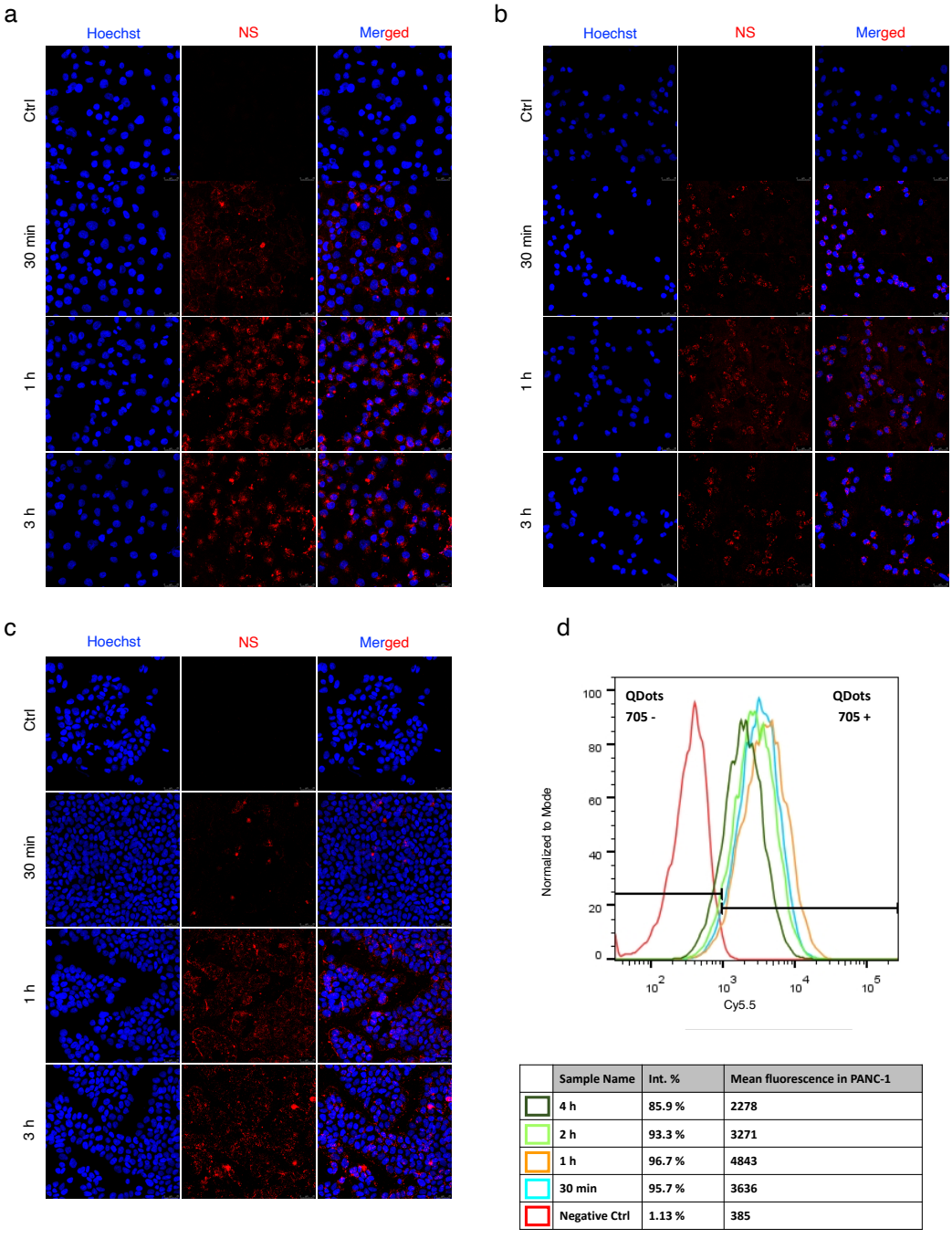

	Sample Name	Int. %	Mean fluorescence in PANC-1
	4 h	85.9 %	2278
	2 h	93.3 %	3271
	1 h	96.7 %	4843
	30 min	95.7 %	3636
	Negative Ctrl	1.13 %	385

Figure S3. Uptake experiments of nanoconjugates (red signal), incubated at increasing time points (30 min to 3h). Untreated cells were used as negative control. Cell Nuclei were stained with Hoechst 33342 (blue signal) observed by Confocal Laser Microscopy in **(a)** PANC-1, **(b)** PATU8889T, **(c)** PATU8889S cancer cell lines. **(d)** Evaluation of Cy5.5 positive cells by flow cytometry to determine the internalization of SI-NCs (SI-NCs containing QDots 705 are observed by Cy5.5 laser line). % Internalization and mean fluorescence are expressed in bottom table.

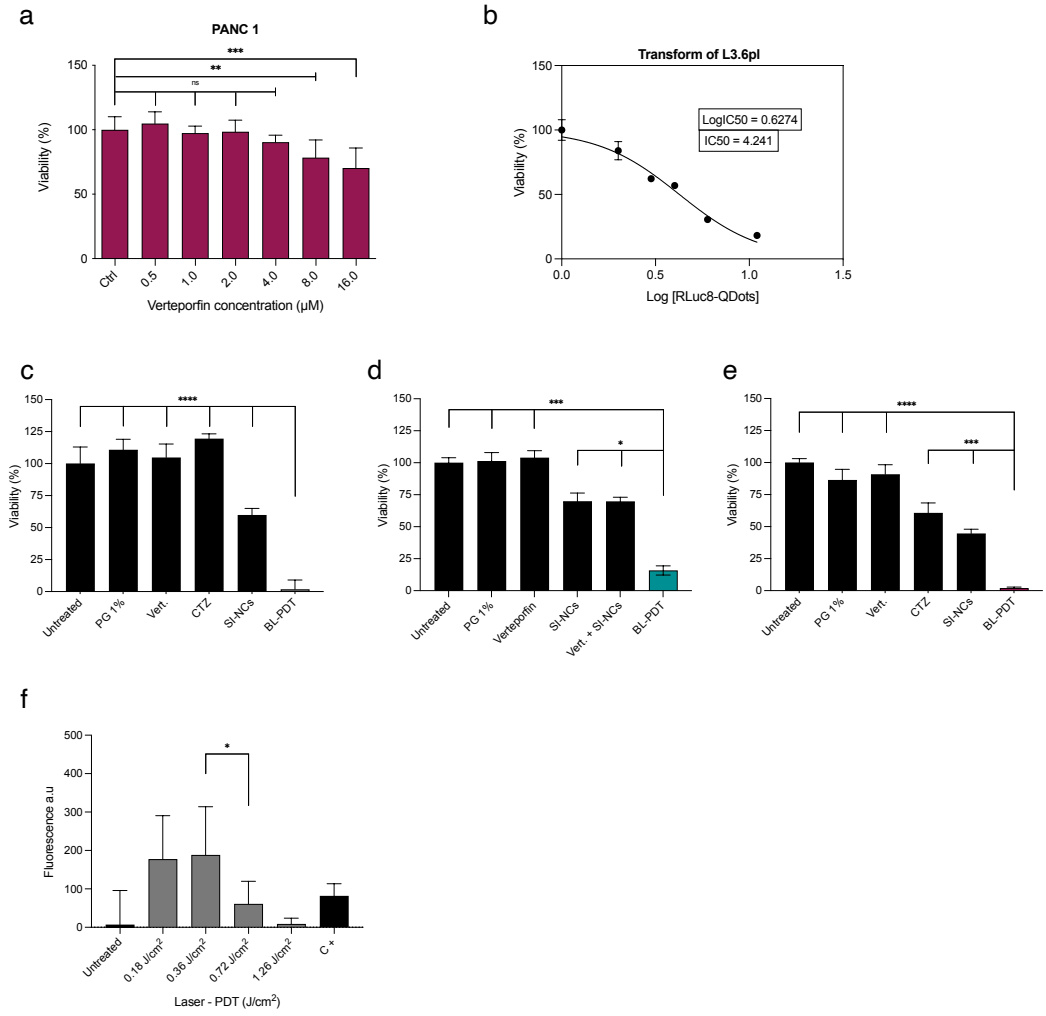

Figure S4. (a) Study of verteporfin cytotoxicity in PANC-1 cell line after 4 hours of incubation, at increasing concentrations. Data are presented as mean ± SD No IC50 is reached with the doses tested. **(b)** Viability of SI-NCs evaluated by MTT in L3.6pl cells with an IC50 calculated of 4.241μM. Cytotoxicity and first proof-of-concept of a BL-PDT. Bars 1-5: controls and Bar 6: BL-PDT treatment using a high SI-NCs dose (5 pmol) in **(c)** Mia PaCa-2, **(d)** L3.6pl and **(e)** PANC-1 cells. Data are presented as mean ± SD **(f)** H2DCFDA assay to measure ROS levels in L3.6pl cells at increasing laser irradiation doses. Best performance at 0.36 J/cm2 and 3 cycles of 30 s. Data are presented as mean ± SD (at least n = 3 per group). Statistical analyses p > values meaning; * ($p < 0.05$), *** ($p < 0.0005$) and **** ($p < 0.0001$).

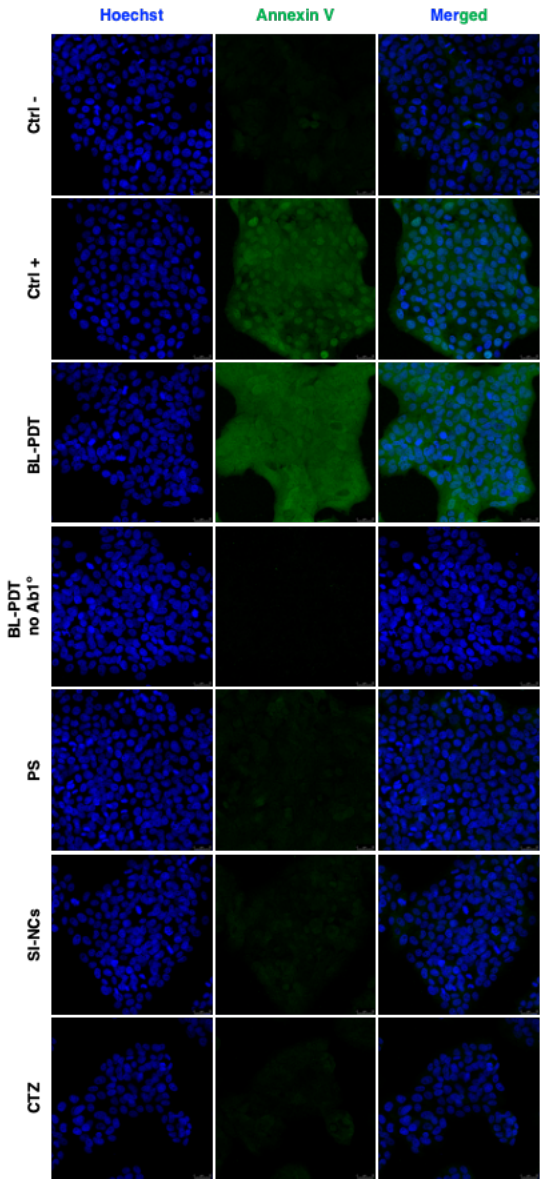

Figure S5. Confocal Laser Microscopy images of Annexin V levels assessed by Immunofluorescence to confirm apoptosis cell killing mechanism of action after 16 h BL-PDT treatment. Appropriate negative and positive controls to observe Annexin V were used. BL-PDT produced a better Annexin V signal. Shown are different captures from the principal figure to conclude that annexin V levels observed are similar in all fields examined from the wells.

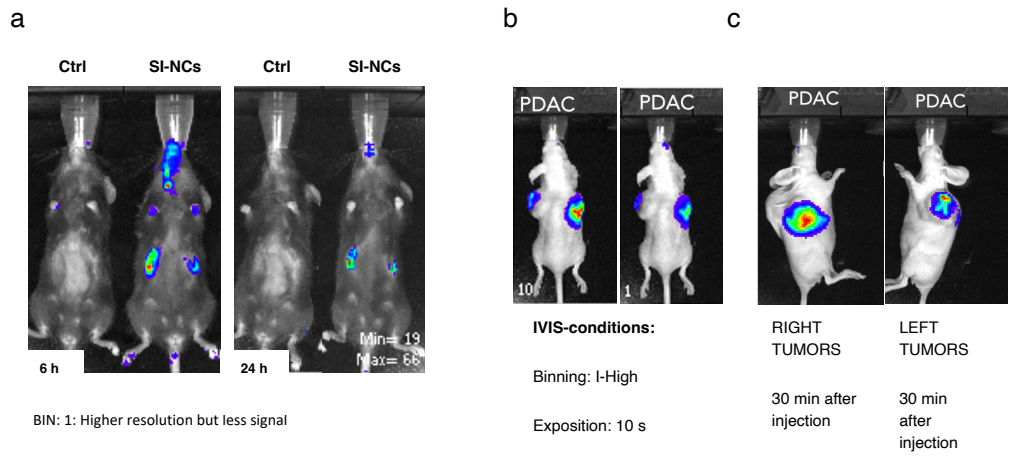

Figure S6. Self-illuminating nanoconjugates emit light *in vivo*. SI-NCs were administered via different administration routes. **(a)** SI-NCs were retroorbital administered in C57BL6 mice to observe systemically target organs. IVIS visualization after substrate addition at 6h and 24h. For intratumoral administration NU/NU nude mouses were used bearing PDAC tumor and different images were obtained **(b)** visualization of both tumors **(c)** right and left tumors exposition. Images acquired from different acquisition planes.

BioLight Photodynamic Therapy (BL-PDT) Analysis

(i) SI-NCs (RLuc8-QDots nanoconjugates) – Intraperitoneal injection

(ii) Photosensitizer (verteporfin) – Intraperitoneal injection

(iii) Substrate (Coelenterazine) – Retro-orbital injection (IV)

(iv) NOD.SCID male mice (7 weeks old; 25-27 g) with two Pancreas Orthotopic Implants:

(a) c354PdX; 200.000 cells, Matrigel 80%

(b) A6LPdX; 200.000 cells, Matrigel 80%

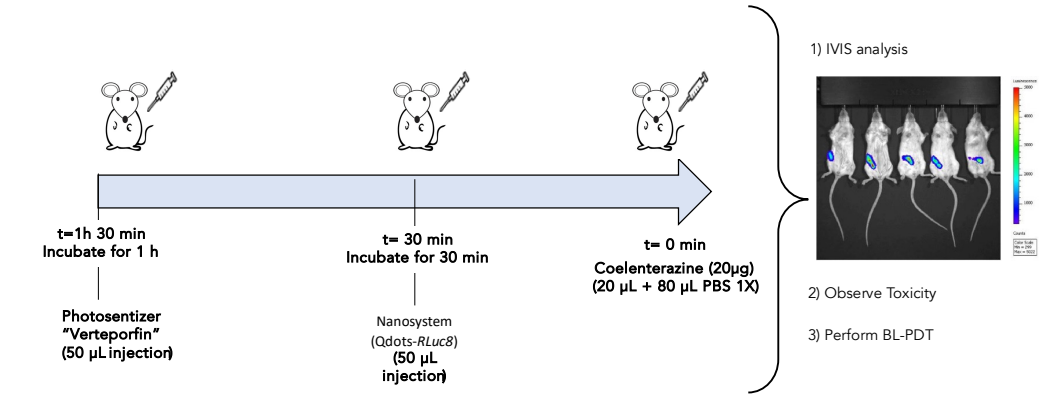

**Repeat treatment with 3 day interval for 21 days **

Figure S7. Scheme of the complete BL-PDT treatment. SI-NCs and photosensitizer (verteporfin) were intraperitoneal injected, and substrate (coelenterazine) was retro-orbital injected (IV). The goal of the PDT is to observe tumor suppression in NOS.SCID mice bearing two different orthotopic pancreatic tumors. In the graph it is showed the timeline of the BL-PDT treatment.

REFERENCES

1. NCI. https://seer.cancer.gov/statfacts/html/pancreas.html.

2. Sung, H. *et al.* Global Cancer Statistics 2020: GLOBOCAN Estimates of Incidence and Mortality Worldwide for 36 Cancers in 185 Countries. *CA Cancer J Clin* **71**, 209–249 (2021).

3. Hu, J. X. *et al.* Pancreatic cancer: A review of epidemiology, trend, and risk factors. *World Journal of Gastroenterology* vol. 27 4298–4321 Preprint at https://doi.org/10.3748/wjg.v27.i27.4298 (2021).

4. Chen, X., Zeh, H. J., Kang, R., Kroemer, G. & Tang, D. Cell death in pancreatic cancer: from pathogenesis to therapy. *Nature Reviews Gastroenterology and Hepatology* vol. 18 804–823 Preprint at https://doi.org/10.1038/s41575-021-00486-6 (2021).

5. Ackroyd, R., Kelty, C., Brown, N. & Reed, M. *The History of Photodetection and Photodynamic Therapy* ¶. *Photochemistry and Photobiology* vol. 74 (2001).

6. Maharjan, P. S. & Bhattarai, H. K. Singlet Oxygen, Photodynamic Therapy, and Mechanisms of Cancer Cell Death. *J Oncol* **2022**, 1–20 (2022).

7. Dos Santos, A. F., De Almeida, D. R. Q., Terra, L. F., Baptista, M. S. & Labriola, L. Photodynamic therapy in cancer treatment - an update review. *J Cancer Metastasis Treat* **2019**, (2019).

8. Lee, C. N., Hsu, R., Chen, H. & Wong, T. W. Daylight Photodynamic Therapy: An Update. *Molecules (Basel, Switzerland)* vol. 25 Preprint at https://doi.org/10.3390/molecules25215195 (2020).

9. Zhen, X., Cheng, P. & Pu, K. Recent Advances in Cell Membrane–Camouflaged Nanoparticles for Cancer Phototherapy. *Small* vol. 15 Preprint at https://doi.org/10.1002/smll.201804105 (2019).

10. Zhang, Y., Wang, B., Zhao, R., Zhang, Q. & Kong, X. Multifunctional nanoparticles as photosensitizer delivery carriers for enhanced photodynamic cancer therapy. *Materials*

Science and Engineering C vol. 115 Preprint at https://doi.org/10.1016/j.msec.2020.111099 (2020).

11. Chen, J. *et al.* Advances in nanomaterials for photodynamic therapy applications: Status and challenges. *Biomaterials* vol. 237 Preprint at https://doi.org/10.1016/j.biomaterials.2020.119827 (2020).

12. Apel, K. & Hirt, H. Reactive oxygen species: Metabolism, oxidative stress, and signal transduction. *Annual Review of Plant Biology* vol. 55 373–399 Preprint at https://doi.org/10.1146/annurev.arplant.55.031903.141701 (2004).

13. Steiling, H., Munz, B., Werner, S. & Brauchle, M. *Different Types of ROS-Scavenging Enzymes Are Expressed during Cutaneous Wound Repair*. http://www.idealibrary.com (1999).

14. Dąbrowski, J. M. Reactive Oxygen Species in Photodynamic Therapy: Mechanisms of Their Generation and Potentiation. in *Advances in Inorganic Chemistry* vol. 70 343–394 (Academic Press Inc., 2017).

15. Parasca, S. V., Calin, M. A. & Parasca, S. v. *Photodynamic therapy in oncology*. *Photodynamic therapy in oncology Article in Journal of Optoelectronics and Advanced Materials* vol. 8 https://www.researchgate.net/publication/228668607 (2006).

16. Correia, J. H., Rodrigues, J. A., Pimenta, S., Dong, T. & Yang, Z. Photodynamic therapy review: Principles, photosensitizers, applications, and future directions. *Pharmaceutics* **13**, (2021).

17. Yoon, I., Li, J. Z. & Shim, Y. K. Advance in photosensitizers and light delivery for photodynamic therapy. *Clin Endosc* **46**, 7–23 (2013).

18. Allison, R. R. & Sibata, C. H. Oncologic photodynamic therapy photosensitizers: A clinical review. *Photodiagnosis and Photodynamic Therapy* vol. 7 61–75 Preprint at https://doi.org/10.1016/j.pdpdt.2010.02.001 (2010).

19. Zhang, Y., Hao, Y., Chen, S. & Xu, M. Photodynamic Therapy of Cancers With Internal Light Sources: Chemiluminescence, Bioluminescence, and Cerenkov Radiation. *Frontiers in Chemistry* vol. 8 Preprint at https://doi.org/10.3389/fchem.2020.00770 (2020).

20. Algorri, J. F., Ochoa, M., Roldán-Varona, P., Rodríguez-Cobo, L. & López-Higuera, J. M. Light technology for efficient and effective photodynamic therapy: A critical review. *Cancers* vol. 13 Preprint at https://doi.org/10.3390/cancers13143484 (2021).

21. Grin, M. *et al.* Advantages of combined photodynamic therapy in the treatment of oncological diseases. *Biophysical Reviews* Preprint at https://doi.org/10.1007/s12551-022-00962-6 (2022).

22. Hong, E. J., Choi, D. G. & Shim, M. S. Targeted and effective photodynamic therapy for cancer using functionalized nanomaterials. *Acta Pharmaceutica Sinica B* vol. 6 297–307 Preprint at https://doi.org/10.1016/j.apsb.2016.01.007 (2016).

23. So, M. K., Xu, C., Loening, A. M., Gambhir, S. S. & Rao, J. Self-illuminating quantum dot conjugates for *in vivo* imaging. *Nat Biotechnol* **24**, 339–343 (2006).

24. So, M. K., Loening, A. M., Gambhir, S. S. & Rao, J. Creating self-illuminating quantum dot conjugates. *Nat Protoc* **1**, 1160–1164 (2006).

25. Hsu, C. Y., Chen, C. W., Yu, H. P., Lin, Y. F. & Lai, P. S. Bioluminescence resonance energy transfer using luciferase-immobilized quantum dots for self-illuminated photodynamic therapy. *Biomaterials* **34**, 1204–1212 (2013).

26. Kim, Y. R. *et al.* Bioluminescence-activated deep-tissue photodynamic therapy of cancer. *Theranostics* **5**, 805–817 (2015).

27. Hamblin, M. R. & Hasan, T. Photodynamic therapy: A new antimicrobial approach to infectious disease? *Photochemical and Photobiological Sciences* **3**, 436–450 (2004).

28. Abrahamse, H. & Hamblin, M. R. New photosensitizers for photodynamic therapy. *Biochemical Journal* vol. 473 347–364 Preprint at https://doi.org/10.1042/BJ20150942 (2016).

29. Visudyne.

30. Wei, H. *et al.* Verteporfin suppresses cell survival, angiogenesis and vasculogenic mimicry of pancreatic ductal adenocarcinoma via disrupting the YAP-TEAD complex. *Cancer Sci* **108**, 478–487 (2017).

31. Huggett, M. T. *et al.* Phase I/II study of verteporfin photodynamic therapy in locally advanced pancreatic cancer. *Br J Cancer* **110**, 1698–1704 (2014).

32. Lui, J. W. *et al.* The efficiency of verteporfin as a therapeutic option in pre-clinical models of melanoma. *J Cancer* **10**, 1–10 (2019).

33. Ormond, A. B. & Freeman, H. S. Dye sensitizers for photodynamic therapy. *Materials* vol. 6 817–840 Preprint at https://doi.org/10.3390/ma6030817 (2013).

34. Li, Y., Yu, Y., Kang, L. & Lu, Y. *Original Article Effects of chlorin e6-mediated photodynamic therapy on human colon cancer SW480 cells. Int J Clin Exp Med* vol. 7 www.ijcem.com/ (2014).

35. Sun, X. *et al.* Photodynamic therapy produces enhanced efficacy of antitumor immunotherapy by simultaneously inducing intratumoral release of sorafenib. *Biomaterials* **240**, (2020).

36. Möller, J. *et al.* The effect of ionic strength, temperature, and pressure on the interaction potential of dense protein solutions: From nonlinear pressure response to protein crystallization. *Biophys J* **102**, 2641–2648 (2012).

37. Mao, X. Y., Tong, P. S., Gualco, S. & Vink, S. Effect of NaCl addition during diafiltration on the solubility, hydrophobicity, and disulfide bonds of 80% milk protein concentrate powder. *J Dairy Sci* **95**, 3481–3488 (2012).

38. Koniev, O. & Wagner, A. Developments and recent advancements in the field of endogenous amino acid selective bond forming reactions for bioconjugation. *Chem Soc Rev* **44**, 5495–5551 (2015).

39. Burcham, P. C., Fontaine, F. R., Petersen, D. R. & Pyke, S. M. Reactivity with Tris(hydroxymethyl)aminomethane Confounds Immunodetection of Acrolein-Adducted Proteins. *Chem Res Toxicol* **16**, 1196–1201 (2003).

40. Ernst, O. & Zor, T. Linearization of the Bradford protein assay. *Journal of Visualized Experiments* (2010) doi:10.3791/1918.

41. Bhuckory, S., Kays, J. C. & Dennis, A. M. *In vivo* biosensing using resonance energy transfer. *Biosensors* vol. 9 Preprint at https://doi.org/10.3390/bios9020076 (2019).

42. Couturier, C. & Deprez, B. Setting up a bioluminescence resonance energy transfer high throughput screening assay to search for protein/protein interaction inhibitors in mammalian cells. *Frontiers in Endocrinology* vol. 3 Preprint at https://doi.org/10.3389/fendo.2012.00100 (2012).

43. Tyrosine, R. & Heteroreceptor, K. Bioluminiscence Resonance Energy Transfer (BRET) Methods to Study G Protein-Coupled Receptor Complexes. (2014) doi:10.1016/B978-0-12-408143-7.00008-6.BIOLUMINISCENCE.

44. Dacres, H., Michie, M. & Trowell, S. C. Comparison of enhanced bioluminescence energy transfer donors for protease biosensors. *Anal Biochem* **424**, 206–210 (2012).

45. Xing, Y., So, M. kyung, Koh, A. L., Sinclair, R. & Rao, J. Improved QD-BRET conjugates for detection and imaging. *Biochem Biophys Res Commun* **372**, 388–394 (2008).

46. Tiwari, D. K., Tiwari, M. & Jin, T. Near-infrared fluorescent protein and bioluminescence-based probes for high-resolution *in vivo* optical imaging. *Materials Advances* vol. 1 967–987 Preprint at https://doi.org/10.1039/d0ma00273a (2020).

47. Dragulescu-Andrasi, A., Chan, C. T., De, A., Massoud, T. F. & Gambhir, S. S. Bioluminescence resonance energy transfer (BRET) imaging of protein-protein interactions within deep tissues of living subjects. *Proc Natl Acad Sci U S A* **108**, 12060–12065 (2011).

48. Li, F. *et al.* Buffer enhanced bioluminescence resonance energy transfer sensor based on Gaussia luciferase for *in vitro* detection of protease. *Anal Chim Acta* **724**, 104–110 (2012).

49. Cai, W., Hsu, A. R., Li, Z. B. & Chen, X. Are quantum dots ready for *in vivo* imaging in human subjects? *Nanoscale Research Letters* vol. 2 265–281 Preprint at https://doi.org/10.1007/s11671-007-9061-9 (2007).

50. Oh, E. *et al.* Meta-analysis of cellular toxicity for cadmium-containing quantum dots. *Nat Nanotechnol* **11**, 479–486 (2016).

51. Pathakoti, K., Hwang, H. M., Xu, H., Aguilar, Z. P. & Wang, A. *In vitro* cytotoxicity of CdSe/ZnS quantum dots with different surface coatings to human keratinocytes HaCaT cells. *J Environ Sci (China)* **25**, 163–171 (2013).

52. Fakhroueian, Z., Dehshiri, A. M., Katouzian, F. & Esmaeilzadeh, P. *In vitro* cytotoxic effects of modified zinc oxide quantum dots on breast cancer cell lines (MCF7), colon cancer cell lines (HT29) and various fungi. *Journal of Nanoparticle Research* **16**, (2014).

53. Zhao, W. *et al.* Tert-butyl hydroperoxide (t-BHP) induced apoptosis and necroptosis in endothelial cells: Roles of NOX4 and mitochondrion. *Redox Biol* **11**, 524–534 (2017).

54. Galluzzi, L., Kepp, O., Chan, F. K. M. & Kroemer, G. Necroptosis: Mechanisms and Relevance to Disease. *Annual Review of Pathology: Mechanisms of Disease* vol. 12 103–130 Preprint at https://doi.org/10.1146/annurev-pathol-052016-100247 (2017).

55. Wang, Y. & Tang, M. Dysfunction of various organelles provokes multiple cell death after quantum dot exposure. *International Journal of Nanomedicine* vol. 13 2729–2742 Preprint at https://doi.org/10.2147/IJN.S157135 (2018).

56. Bastian, A. M., Yogesh, T. L. & Kumaraswamy, K. L. Various methods available for detection of apoptotic cells-A review. *Indian Journal of Cancer* vol. 50 274–283 Preprint at https://doi.org/10.4103/0019-509X.118720 (2013).

Chapter II

Biocompatible and Versatile Self-Illuminating Sphingomyelin Nanosystems (SI-NS) as a Potent Tool to Improve Cancer Therapies

Biocompatible and Versatile Self-Illuminating Sphingomyelin Nanosystems as a Potent Tool to Improve Cancer Therapies

ABSTRACT

In recent years, personalized medicine has emerged as a key approach to potentially treat numerous diseases, in particular cancer. Within this filed, nanotechnology has arisen as a promising tool with multiple biomedical applications, and organic nanoparticles stand out due to their improved translational prospects, primarily attributed to their biocompatibility and biodegradability. In this context, sphingomyelin nanosystems (NS) are promising carriers for the delivery of innovative therapeutics and the advancement of novel biomedical applications. This study focused on the development of self-illuminating (SI) sphingomyelin NS (SI-NS) by associating the bioluminescent protein RLuc8 with NS, exhibiting significant utility for a variety of applications such as photodynamic therapy (PDT), imaging and cell tracking, among others. Throughout this work, we provide extensive characterization and functional studies to support the versatility of the rationally designed SI-NS. *In vitro* and *in vivo* experiments are presented to provide solid proof of the potential of SI-NS for cell tracking, development of cell therapies and for PDT in pancreatic cancer.

INTRODUCTION

According to the World Health Organization (WHO), cancer accounted for 1 in 6 deaths in 2020, making it the leading cause of death worldwide [1]. Furthermore, it is estimated that cancer incidence will increase by up to 47% by 2040, with a likely parallel increase in mortality rates [2]. Various approaches to treating cancer include surgery and radiotherapy as first-line treatments for local and non-metastatic tumors [3]; however, despite advances in research, chemotherapeutic agents based on toxic drugs remain the primary choice for metastatic tumors [4]. Given this outlook, there is an urgent clinical need for the development of new strategies to address cancer therapies and combined treatments.

In recent years, personalized medicine has revolutionized treatment perspectives for many diseases through the development of new detection methods and novel therapeutic molecules, such as specific targeted therapies [5,6]. In this context, nanotechnology emerges as a promising tool for use in biomedicine, offering a rational design of multiple drug delivery systems (DDS). Nanomedicine presents several advantages, including enhanced drug solubility, increased drug loading, improved bioavailability, controlled drug release, and protection from chemical and enzymatic degradation, among others. Moreover, nanosystems have high potential for combination with drugs and/or biomolecules, either for individual use or alongside diagnostic agents, resulting in multifunctional nanoparticles known as nanotheranostics [7–10].

Additionally, nanosystems as DDS have been tested for administration via different routes, including parenteral, oral, topical/transdermal, intranasal, pulmonary, and ocular, depending on their composition and targeted tissue [11,12]. Nanosystems can overcome the limitation of poor drug accumulation at tumor sites through the Enhanced Permeability and Retention (EPR) effect, or passive targeting, promoted by leaky vasculature and pro-inflammatory processes within tumors [13,14]. This EPR effect has also been observed in other inflammatory diseases, such as arthritis, multiple sclerosis, or obesity [15].

Proteins, as biomacromolecules, regulate various biological processes such as coordination of cell signaling pathways, cell receptor recognition, biocatalysis and immune processes, making them perfect candidates for therapeutic agents due to their unique endogenous nature, ensuring biocompatibility and biodegradability. They offer an alternative to small molecule drugs with higher targeting specificity and activity, thus reducing side effects. Indeed, it is remarkable that their degradation products are well known and excreted by the body, being important to limit any

potential toxicity. Notably, protein engineering technologies allow the modification of their features, increasing their activity and biological stability [16–18]. Proteins for biomedical applications include therapeutic enzymes, antibodies, as well as bioluminescent and fluorescent proteins for imaging and reporting purposes. For example, ribonuclease A (RNAse A) has been studied for cancer treatment, while insulin remains the molecule of choice for diabetes treatment [19]. The application of luciferase for the development of self-illuminating nanosystems (SI-NS) has been proposed in the context of photodynamic therapy (PDT) triggered by bioluminescence (BioLight). *Firefly* luciferase (FLuc) loaded into PLGA nanoparticles achieved an antitumoral response in MCF-7 and HeLa cells [20]. *Renilla* luciferase (RLuc) associated with bovine serum albumin (BSA) and Rose Bengal (RB) in a protein conjugate was tested in PDT, but faced internalization problems [21]. Our previous work reported the development of SI nanoconjugates (SI-NCs) for pancreatic cancer treatment through BioLight-induced PDT (BL-PDT) (Chapter I). The BioLight produced by luciferase upon substrate (Coelenterazine; CTZ) activation could overcome the main limitation of light-penetration for the application of laser-PDT in the treatment of deep tissues (such as the pancreas). In addition, PDT can be minimally invasive and generates ROS, inducing apoptosis in cancer cells [22–24]. Inorganic nanoparticles, specifically quantum dots, have been proposed for this application [25–27], with limited reports on biodegradable PLGA organic nanoparticles [20]. However, there are reports delivering FLuc or RLuc in the form of plasmid DNA to express the protein directly in cells [28–31].

Another interesting application of SI-NS is cell tracking. Cell therapies based on T cells and menstrual mesenchymal stem cells (MenSCs) show promise in improving cancer treatment [32–36]. In this field, studies have demonstrated the therapeutic potential of MenSCs due to their immunoregulatory properties, ability to migrate into injury sites, differentiation into different cell lineages, and secretion of soluble factors [34,37]. T-cell therapies, including tumor-infiltrating lymphocyte (TIL) therapy and chimeric antigen receptor (CAR) T-cell therapy [35,36], have shown promise in treating blood cancers, such as lymphomas and certain forms of leukemia, and ongoing research explores their potential in treating solid tumors [38]. Cell tracking with SI-NS can decipher the *in vivo* fate of labeled T cells and MenSCs, reaching target tissues.

This study focuses on the development of novel and versatile SI-NS based on the efficient association of the bioluminescent protein RLuc8 with a new type of promising delivery system, NS. This provides a new technology for cell tracking in the development of cellular therapies and for use in cancer Photodynamic Therapy (PDT) upon encapsulation of the photosensitizer Rose

Bengal [39]. The incorporation of the bioluminescent enzyme RLuc8 is possible via orthogonal click chemistry reactions, specifically copper-free click chemistry, such as strain-promoted azide-alkyne cycloaddition (SPAAC). Click chemistry offers a range of conjugation reactions that are simple and high-yielding in mild aqueous conditions, orthogonal, and generate easily isolated products [40–42]. Particularly, copper-free click chemistry, including SPAAC and inverse-electron-demand Diels–Alder (iEDDA) reactions, enables fast and specific chemical conjugation without the need for toxic catalysts [43–46]. Click chemistry has evolved as a paradigm shift in the biomedical field, demonstrating that artificial chemical reactions can occur outside the laboratory in a controllable manner on live cell surfaces, in the cytosol, and in living bodies. It is an excellent technique for applications such as drug delivery, cell tracking, tissue engineering, as well as in multi-step organic synthesis [42,47–49].

This study provides a full development and characterization of novel SI-NS, probing their potential in different biomedical applications, including cell tracking. The study also aims to determine the potential of SI-NS to mediate a localized and controlled antitumoral response in pancreatic cancer, one of the most challenging to treat and diagnose due to its pathological features[3].

MATERIALS AND METHODS

Azide-modified protein (N3-RLuc8) preparation and characterization.

Protein RLuc8 (0.028 μmol) was modified with Azido-dPEG®8-NHS linker (0.58 μmol) (Sigma, Darmstadt, Germany) in phosphate buffer saline (PBS; 2mM, pH 7.4). The reaction was performed at room temperature (RT) for 6 hours with storage at 4ºC. Linker excess was eliminated using spin filters (Amicon® Ultra Centrifugal Filters, 10k, 0,5mL, Merck). Native RLuc8 and N3-RLuc8 bioluminescence was tested in two different calibrated luminometers (SYNERGY H1, microplate reader, BioTek; Victor Nivo™, multimode plate reader, PerkinElmer). Samples (0.1μM of enzyme) were mixed with the correspondent activating substrate (10 μM Coelenterazine, CTZ, ThermoFisher Scientific, USA) in 100 μL sodium phosphate dibasic and incubated for 5 minutes in the dark before measurement.

N3-RLuc8 modification was characterized by HPLC-MS (5 pmol) dissolved in ultrapure water. Equipment TimsTof Pro (Bruker) coupled to the ELUTE UHPLC. The analysis method used was positive ESI ionization, acquisition range 500-3000 m/z, chromatographic separation with column C4, mobile phases employed were A: Water/formic acid 0.1%, B: acetonitrile/formic acid 0.1%; and chromatographic separation time 17 minutes. MALDI Tof analysis was carried out in an Ultraflex III TOF/TOF (Bruker Daltonics, Bremen, Germany), and the analysis method chosen was MALDI linear mode ionization using a SA matrix (Sinapinic Acid).

Self-illuminating Sphingomyelin Nanosystems (SI-NS) preparation.

Briefly, vitamin E (5 mg, Sigma, Darmstadt, Germany), sphingomyelin (0.5 mg, Lipoid GmbH, Ludwigshafen, Germany) and the surfactant DSPE-PEG(2k)-DBCO (0.05 mg, Avanti Polar Lipids, Croda International Plc., Alabama, USA) with a lipid ratio 1:0.1:0.01 w/w were dissolved in 100 μL of absolute ethanol. DBCO-nanosystems (NS) were instantaneously formed by injecting the organic phase into 0.9 mL of ultrapure water, at RT.

To prepare self-illuminating NS (SI-NS), N3-RLuc8 was brought to a final volume of 500 μL in PBS buffer, 2 mM, pH 7.4, added dropwise to the NS and incubated at RT for 4 hours followed by an O/N incubation at 4ºC. The purification of the NS was carried out by spin filters (Amicon® Ultra Centrifugal Filters, 100k, 0.5mL, Merck) in a refrigerated microcentrifuge (5417R; Eppendorf). The spin filters were first pre-washed with 500 μL PBS 2 mM at 6000x*g* for 5 min to wet and hydrate the filter before initiating the process. SI-NS were transferred to the spin filters and 200 μL of PBS was added and centrifuged for 3 min, at 4°C and 3000x*g*. Four washes were

performed with 200 μL of PBS each, centrifuging as described above. Finally, SI-NS were collected with 50 μL of PBS buffer, centrifuging for 2 min, at 4°C and 1000x*g*.

Physicochemical and Morphological Characterization.

Particle size and polydispersity index (PdI) were determined by Dynamic Light Scattering (DLS), and Z-potential values by Laser Doppler Anemometry (LDA), using a Zetasizer NanoZS (Malvern Instruments, UK). Samples were diluted 1:10 with ultrapure water and the measurements were performed at 25ºC with a detection angle of 173º. All data are expressed as a mean value ± standard deviation (SD).

Both, NS and SI-NS formulations were evaluated in relevant biological media to ensure the maintenance of their properties during *in vitro* and *in vivo* assays. Formulations were incubated at 37ºC with 10% FBS supplemented DMEM, 0.9% physiological saline, 10% glucose w/v solution and filtered blood plasma under orbital shaking.

NS and SI-NS morphology was observed by Field Emission Scanning Electron Microscopy (FESEM) using a ZEISS FESEM ULTRA Plus microscope (Carl Zeiss Micro Imaging, GmbH, Germany) configured with InLens and STEM modes and operating at 20 kV. Briefly, 20 μL (0.55 mg/mL) of filtered NS were stained with phosphotungstic acid (2% w/v) at a ratio 1:1. Next, 10 μL were placed on a carbon-coated grids and left for 30s. The grids were allowed to dry and then washed repeatedly with filtered ultrapure water. Finally, grids were dried again until visualization.

Nanoparticle Tracking Analysis (NTA) characterization of NS and SI-NS.

Nanoparticle tracking analysis (NTA) measurements were performed to additionally characterize NS and SI-NS; a method based on visualizing each nanosystem individually. Samples were analyzed with a NanoSight NS3000 System (laser operating at λ = 488 nm) (Malvern Instruments, UK). Briefly, nanosystems were diluted 1000-fold in ultrapure water and injected in the sample chamber (sterile syringes; Omnifix®-F 1mL, Melsungen, Germany). All measurements were acquired at RT for 60 s in triplicate, and for each replicate, five captures were used to determine parameters such as average size, homogeneity, and particle concentration, and standard deviation values were obtained by the NTA 2.0 Build 127 software. Both shutter and gain were manually set up.

Nuclear magnetic resonance spectroscopy (NMR) and MALDI-Tof analysis.

NMR experiments were conducted at 25ºC on a Bruker NEO 17.6 T spectrometer (proton resonance 750 MHz), equipped with a 1H-19F /13C/ 15N triple resonance PA-TXI probe with

deuterium lock channel and shielded PFG z-gradient. The spectrometer control software was TopSpin 4.0. The chemical shifts reported are referenced to the lock deuterium solvent. Spectras were processed and analyzed with Mestrenova software v14.x (Mestrelab Inc.). NMR sample preparation: samples were prepared in 5 mm standard tubes and dissolved in DMSO-d6. The deuterium lock solvent was used for lock and chemical shift reference. For all sample, the 1D 1H spectra (sequence zg of the Bruker library) were measured with 128 scans, a relaxation delay of d1 2 s and a FID acquisition time (aq) of 2.75 s. The FID was acquired with 64k complex data points and was processed with zero-filling and Fourier Transformation (FT) to obtain a spectrum with 131k data points. The total measurement time was ~10 min. A 2D Diffusion-filtered TOCSY spectrum (2D Dfilter-TOCSY) was measured. The sequence was implemented by combination of an initial diffusion filter element (Dfilter) based on the Bipolar gradients-STimulated-Echo (BPP-STE) followed by a 2D TOCSY sequence with PFG gradients (sequence "dipsi2gpphpr" of the Bruker library). The purpose of the diffusion filter is to clean the Dfilter-TOCSY spectrum from the undesired peaks of low molecular weight impurities and the residual HDO solvent peak so as to obtain a clean spectrum of the sample under study. The conditions used for the Dfilter consisted in a diffusion delay Δ of 100 ms and bipolar gradient pulses (δ) of a total duration of 2 ms that were applied with the maximum gradient peak power of 50.2 G/cm. The TOCSY mixing time used DIPSI-2 and the duration was 80 ms. The center of the spectrum in both F1 and F2 dimensions was set at 4.7 ppm, and the spectral width in the two dimensions was 10 ppm. The interscan delay (d1) was 2 s, the number of scans was 24 and the number of complex points measured in the direct and indirect dimensions was 4k and 128, respectively. The total measurement time was ~2 h. A two-dimensional 2D symmetrized-ASAP-HSQC 1H-13C spectrum was measured. The spectrum includes optimal control broadband pulses in 13C for excitation/time-reversed excitation/inversion pulses from the BEBOP/BIBOP family and universal rotation pulses from the BURBOP family. The ASAP-like conditions were applied with the DIPSI-2 mixing sequence during 30 ms. The INEPTs transfers were optimized for a nominal value of 1JCH of 145 Hz with an effective Ernt angle excitation of 208º. The relaxation delay (d1) and the FID acquisition time (aq) were 0.4 and 0.087 s, respectively. The phase sensitivity in the indirect dimension uses Echo/Antiecho. During FID acquisition, 13C decoupling was applied with a garp-4 sequence with a field strength of 5 kHz. The spectrum was acquired with 2048 and 128 complex points in the t2 and t1 dimensions, respectively. The number of scans per t1 increment was 64 and the total measurement time was ~1 h 15min. Other NMR analyses are described in the supporting information section.

SI-NS were analyzed by MALDI-Tof as well. For that, analyses were conducted using an Ultraflex III TOF/TOF (Bruker) equipment, and the method used was MALDI linear mode ionization using a SA matrix (Sinapinic Acid) with previous sample ZipTip desalting.

Association of the Photosensitizer Rose Bengal.

For the use of SI-NS in PDT, a photosensitizer was encapsulated. Rose Bengal (0.82 μmol, 15% to total lipids; Sigma Aldrich, Darmstadt, Germany) was dissolved into the organic phase described in the previous "*Self-illuminating Sphingomyelin Nanosystems (SI-NS) preparation"* section. RB-NS (Rose Bengal DBCO-nanosystems) were instantly formed, and photosensitizer excess was removed by spin filters. N3-RLuc8 was incorporated to obtain SI-RB-NS (Self-illuminating- Rose Bengal-nanosystems) as introduced before in the previous "*Self-illuminating Sphingomyelin Nanosystems (SI-NS) preparation"* section.

Preparation of Cy5 and TopFluor® labelled NS.

Fluorescent-labelled NS were prepared as previously described section *"Self-illuminating Sphingomyelin Nanosystems (SI-NS) preparation"*. For *in vitro* assays TopFluor® (4.5 μg; Avanti Polar lipids, Sigma, Darmstadt, Germany) or C16 Cy5 SM (4.5 μg; Avanti Polar lipids, Sigma, Darmstadt, Germany) were mixed with the organic phase (final volume of 100 μL).

SI-NS bioluminescence kinetics and SI-RB-NS bioluminescence resonance energy transfer (BRET).

A kinetics assay for SI-NS was performed to assess the duration of the enzyme's biolight reaction. In a 96-multiwell plate, 0.8 and 1 μM of SI-NS were activated with 40 μM of CTZ in PBS 2mM, pH 7.4. The kinetic reaction was monitored for 2 and a half hours in a luminometer (Victor Nivo™, multimode plate reader, PerkinElmer).

The BRET phenomenon was determined in duplicate. Specifically, SI-RB-NS (1 μM) after its activation with CTZ (40 μM), luminescence was recorded in a Victor Nivo™ luminometer. A BRET kinetics assay was tested as well for 1 hour. Finally, the BRET ratio was calculated by performing a spectral scanning in a SYNERGY H1 microplate reader (BioTek).

Cellular internalization.

Cellular uptake was evaluated via different methods. $7x10^4$ cells per well were seeded in 24-multiwell plates and cultured O/N. Then, SI-NS (0.01 mg/mL) were added, and cell internalization

was studied after 2 hours of interaction with the cells. Afterwards, the treatment was removed, cells were lysed, and total protein was extracted. To detect the presence of SI-NS, bioluminescence was tested after enzyme activation and measured in a luminometer (SYNERGY H1, microplate reader, BioTek).

Cellular internalization was observed by Confocal Laser Microscopy (Confocal Laser Microscopy Leica SP5®). Briefly, $6x10^4$ cells per well were seeded in 8-chamber slide plate and cultured O/N. Then, labelled SI-NS (0.2 mg/mL) were added, and internalization was studied after 2 hours. After incubation, the treatment was removed, and an immunofluorescence assay was conducted to specifically detect the RLuc8 protein. Cells were fixed with 4% PFA for 15 min, permeabilized in PBS containing 0.2% Triton X-100 for 10 min, afterwards, cells were incubated in 10% normal goat serum to block non-specific protein-protein interactions followed by rabbit monoclonal anti-RLuc Alexa 647® (Abcam, NL) O/N at 4°C, and finally, cell nuclei were stained with Hoechst 33342 (ThermoFisher, USA).

Results were verified by Flow Cytometry (FACS Aria IIu de BD) in L3.6pl and HeLa cells at different time points (30 min and 2h). Briefly, $5x10^5$ cells per well were seeded in 6-multiwell plates and cultured O/N. Next, different types of fluorescently-labelled NS (0.5 mg/mL) treatments were added to cells, and after incubation, cells were washed with 3x DPBS and fixed with 2% PFA prior to flow cytometric analyses. Results were analysed with FlowJo v10 software.

Cell viability assays.

For cytotoxicity studies, L3.pl6 cells were seeded into a clear-bottom black wall 96-well multiwell plates at a density of $2.5x10^4$ cell/well and incubated for 24h. In separate assay, the toxicity of the photosensitizer, Rose Bengal vehicle (EtOH) and all nanosystems types were added in increasing order of concentration and incubated at different time points (see results section). Cell viability was determined using a 1:10 dilution of the Alamar Blue fluorescence assay and results were read using a Victor Nivo™ multimode plate reader at an excitation of 530 nm and emission of 590 nm. Data were normalized to negative controls (100% viability) and the reagent itself, used as a fluorescence background.

Measurement of ROS production and apoptosis assays.

To determine the presence of intracellular ROS provoked for the PDT process, a fluorescent assay was performed. This assay consisted in staining the cells with the fluorescent dye 2',7'-dichlorodihydrofluorescein diacetate (H_2DCFDA; ThermoFisher Scientific, USA). A a clear-

bottom black wall 96-well multiwell plate was seeded with $2.5x10^4$ cells per well and incubated for 24 h. First, cells interacted with the dye at a final concentration of 5 μM for 60 mins. Then, cells were treated with the optimal condition established for NS, SI-NS, SI-RB-NS and coelenterazine (2 μg/well) and were incubated at 37°C for the PDT process. As a positive control, Luperox® (Sigma Aldrich, USA) was loaded at concentrations of 100 μM and incubated for 2h at 37°C. Appropriate negative controls were also incorporated through this study. ROS generation was measured with a fluorimeter at an excitation wavelength of 485nm and emission of 535 nm.

Apoptosis after ROS production was evaluated by performing an immunofluorescence assay to detect Annexin V. After PDT treatment, cells were fixed with 4% PFA (15 min). The cells were then incubated in 10% normal goat serum to block non-specific protein-protein interactions followed by incubation with a mouse monoclonal anti-annexin V (Abcam, NL) staining O/N at 4°C. Annexin V was visualized with a Leica SP5 confocal microscopy (Leica, Nussloch, Germany) using an excitation of 495 nm and an emission of 519 nm.

Apoptosis was also confirmed by flow cytometry in L3.6pl, 185 PDX and A6L PDX pancreatic cancer cell lines. Once treatments were incubated and removed, PDT was initiated for 16 hours, and Annexin V-FITC binding protein (Cambridge bioscience, UK) was added and incubated with the samples. Appropriate controls (negative and positive) were included, and cells were also incubated with DAPI to stain nuclear DNA. Samples were analyzed with a 4-laser Attune NxT Acoustic Cytometer (ThermoFisher Scientific, USA), and results were processed with FlowJo v10 software.

Cell cycle studies after PDT.

6-multiwell plates were seeded with $5x10^5$ cells/well in triplicate for each condition (L3.6pl, 185 PDX and A6L PDX cell lines used). PDT process was carried out as in apoptosis studies described above. Subsequently, cells were stained with FxCycle™ Violet Ready Flow reagent (Invitrogen, USA) and incubated for 30 minutes at 25 ºC. Data were acquired with a 4-laser Attune NxT Acoustic Cytometer (ThermoFisher Scientific, USA) using 440/50 nm filters, and results were processed with FlowJo v10 software.

Adenovirus viral production assay.

MenSCs or SI-NS labelled MenSCs ($3.8x10^4$ cells per well in 24-well plates) were infected at a MOI of 100 TU/cell with the adenovirus ICOVIR15K [50]. Four hours after infection, medium was removed, and cells were washed three times with PBS and incubated with fresh medium. At the

indicated time points post-infection, a small fraction of the supernatant (SN) was collected, and total DNA was isolated using the QIAamp DNA Mini and QIAamp DNA Blood Mini Kits (QIAGEN, Valencia, CA), in triplicate, according to the manufacturer's protocol. A 10-fold serial dilution standard curve was generated by diluting ICOVIR5K with sterile phosphate buffered saline (PBS, Life Technologies, Carlsbad, CA, USA) and processed as SN samples. Four microliters of DNA were used to quantify genome copy number by Quantitative Real Time-PCR using ICOVIR15K specific primers. Real Time PCR consisting of 10 min at 95ºC and 40 cycles (95ºC, 15s; 60ºC, 30s; 72ºC, 10s) was performed on a LightCycler® 480 II (Roche, Basel, Switzerland), using LightCycler 480 SYBR Green I Master (Roche) and analyzed with LightCycler® 480 Software release 1.5.0 SP4 (Roche). A control PCR without DNA was included to monitor reagent contamination.

MenSCs and Tcells labelling with SI-NS.

MenSCs (passage 6) cells, resuspended in PBS at a concentration of $4x10^6$ cells/mL, were labelled with SI-NS (3.7 mg/mL) for two hours in agitation. After two washes with PBS, the majority of labelled-MenSCs were used for *in vivo* studies, whereas a small fraction was used to confirm proper RLuc8 cell incorporation and function. For the latter, a two-fold dilution a of labelled cells (ranging from $2x10^4$ to 625 cells) were seeded in triplicate into white opaque 96-well microplates (PerkinElmer, Waltham, MA, USA), and luciferase activity was measured by adding coelenterazine once a day per 6 days using a Multilabel Plate Reader Victor 5x (PerkinElmer).

T-cells in a DPBS suspension of $2x10^5$ cells/mL were labelled with TopFluor®-SI-NS for 2 hours in agitation. Labelled T-cells were then evaluated by flow cytometry every 24 h up to 120 h. Bioluminescence was also tested after CTZ addition with a Multilabel Plate Reader Victor 5x (PerkinElmer).

In vivo orthotopic implant and processing of the samples.

NOD-SCID males of 6-9 weeks (Janvier Labs, France) were implanted orthotopically in the pancreas with $3x10^5$ Panc185 PDX cells resuspended in 50 µL of a 3:2 ratio of Matrigel (Corning):RPMI. Treatments were initiated after tumor detection by abdominal palpation (3-4 weeks post-implant). Three weeks after treatment initiation, mice were sacrificed and tumor, liver and lung were weighed and photographed after animal perfusion with 25 mL of cold 1X PBS. For histopathological analyses, a section of each organ was fixed in formalin and paraffin embedded (FFPE) in blocks. Samples were serially sectioned (3 µm thick) and stained with hematoxylin and

eosin (H&E). Images were acquired with a Motic EasyScan One and analysed with Motic DS Assistant. The rest of the tumor was digested mechanically and enzymatically with collagenase P (Roche, Cat no. 11213857001) and dispase (Gibco, Cat no. 17105-041) for 30 min at 37ºC degrees, vortexing every 10 minutes. Samples were passed through a 40µM Fisherbrand™ Sterile Cell Strainer (FisherScientific, Cat no. 11587522) and cells were collected in a new tube. After a 1X PBS wash, cells were ready for flow cytometric analysis. *In vivo* experiments were conducted in collaboration with the group of Dr. Bruno Sainz Jr located in the Department of Cancer Biology, Instituto de Investigaciones Biomédicas Sols-Morreale (IIBM), CSIC-UAM, 28029 Madrid, Spain.

Flow cytometric analysis of tumors.

Cells from tumor digestions were resuspended in 1X PBS with 3mM EDTA and 2 mg/mL DAPI (Sigma) to exclude dead cells. The analysis of cells was performed with a 4-laser Attune NxT Acoustic Cytometer (Thermo Fisher Scientific) using the next filters: VL1 (Ex405nm/Em440/50) for DAPI and RL1 (Ex637nm/Em670/14) for Cy5.

Statistical analysis.

Data are expressed as mean ± standard deviation (SD). Statistical analyses were performed with a GraphPad Prism® Software (version 9.0). Significant differences were compared and analyzed by two-tailed, Student t-test to compare two experimental groups and one- or two-way analysis of variance (ANOVA) with a Tukey correction to calculate differences among multiple populations. *In vivo* data were analyzed using one-way ANOVA with Dunnett´s multiple comparisons statistical analysis was performed with Graph Pad Prism 8. P-values <0.05 were considered statistically significant. Statistical analyses p > values meaning; * ($p < 0.05$), ** ($p < 0.005$), *** ($p < 0.0005$) and **** ($p < 0.0001$). All experiments were performed at least in triplicate.

RESULTS AND DISCUSSION

Synthesis and characterization of SI-NS

To obtain SI-NS, first, the RLuc8 enzyme was modified with a linker containing an azide (N_3) functional group (NHS-PEG_8-N_3) for later incorporation into the sphingomyelin nanosystems (NS). The enzyme was placed in a PBS buffer solution pH 7.4, and the reaction was performed up to six hours at RT with a 20-fold dilution of the linker (**Fig. 1a**). Once the N_3-RLuc8 modified enzyme was obtained, it was characterized by several analytical methodologies. UHPLC-MS analyses evaluated the complete functionalization of native RLuc8 (**Fig. 1b**). We observed in both spectra the total ion count (TIC), meaning that the total MW of the biomolecule can be observed due to the positive ESI method, which allows the observation of protein profiles without fragmentation [51]. Mass spectrometry analyses concluded that the RLuc8 is completely modified, and any residue of unmodified enzyme is observed in N3-RLuc8. Matrix-assisted laser desorption/ionization time-of-flight mass spectrometry (MALDI-Tof) was also carried out to identify the successful modification of the N3-RLuc8 enzyme. Spectra analysis showed the disappearance of the peak intensity of the native enzyme and how the m/z increased. The successive peaks corresponding to the characteristic fragmentation pattern of PEG (44 g/mol separation between peaks) is clearly observed confirming the N3-RLuc8 formation (**Fig. 1c**). The MALDI method chosen was a linear mode ionization using a polar sinapinic acid (SA) matrix suitable for proteins [51]. Depending on the matrix and the ionization method used, some or other adducts that bind to the sample formed. This is the reason why the total mass of the sample can vary between MALDI and in HPLC-MS analyses.

After verification of enzyme modification, its BioLight activity was confirmed. Both native and modified N3-RLuc8 enzymes were activated with their corresponding substrate, coelenterazine (CTZ) in the presence of oxygen. The capacity of the enzymes to transform the substrate into coelenteramide with subsequent light emission was determined [52] (**Fig. 1d**). This enzymatic reaction follows the kinetics model described by Michaelis-Menten, taking the form of an equation describing the rate of enzymatic reactions as a function of substrate concentration (**Fig. S1**). Biochemical reactions involving a single substrate are often assumed to follow Michaelis–Menten kinetics, without regard for the model's underlying assumptions [53,54]. The native and N3-RLuc8 enzymes were incubated with CTZ for 5 min before measuring their bioluminescence, with no differences observed between samples (**Fig. 1e**). To further examine that the enzyme maintained its conformation and structure after modification, circular dichroism (CD), which analyzes the

interaction between light and matter involving circular polarized light, was performed to measure the protein's secondary structure based on the amide bonds disposition, specifically the π excited state [55]. It is worth mentioning that every protein's secondary conformation has associated to it a characteristic "fingerprint" of its α-helix and β-sheets. In our samples, we observed no changes between RLuc8 and N3-RLuc8 (**Fig. 1f**). Therefore, these results led us to conclude that azide-linker modification preserves the native RLu8 structure, and the modification reaction to add the azide ($-N_3$) group does not affect N3-RLuc8's bioluminescence activity. We have also monitored enzyme activity across time to confirm that light activity is maintained under long-term storage conditions (i.e., up to 360 days) at 4ºC (**Fig. 1g**).

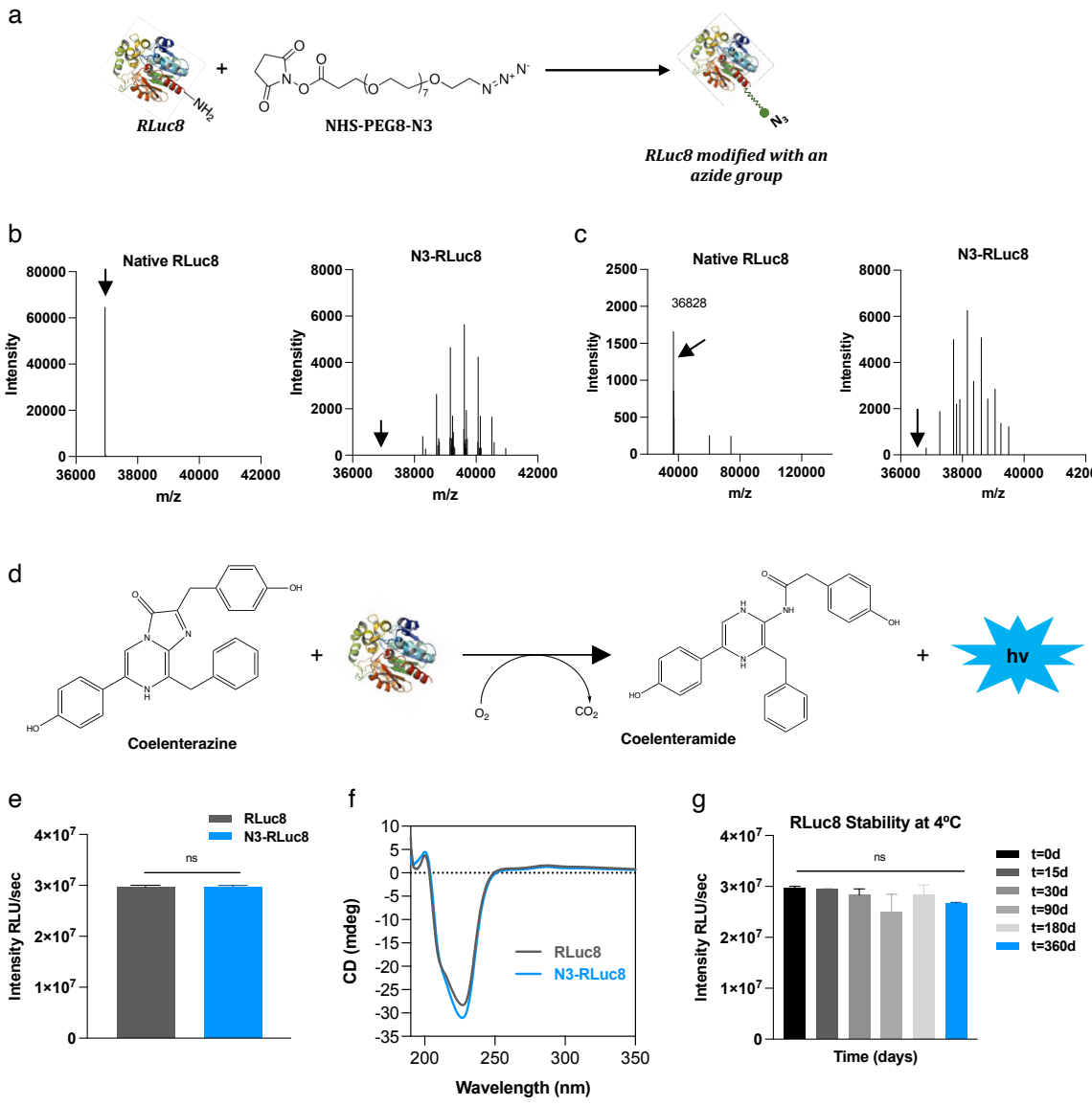

Figure 1. Preparation and characterization of the N3-RLuc8 modified enzyme. **(a)** Schematic representation of the N3-RLuc8 reaction. **(b)** HPLC-MS spectra of native RLuc8 (5 pmol) and modified N3-RLuc8 (5 pmol) showing enzyme modification. **(c)** MALDI-Tof analysis of native RLuc8, $[M+H]^+$ = 36828 and functionalized N3-RLuc8 $[M+H]^+$= ~38500. **(d)** Schematic representation of the enzymatic reaction produced between the RLuc8 enzyme upon substrate addition (CTZ), consuming oxygen to produce coelenteramide and light (of energy = hv). **(e)** Bioluminescence emission between native and N3-RLuc8 (1 μM) upon substrate activation (CTZ dose: 40 μM). ns=non-significance. Statistical analysis: t-test. **(f)** Circular dichroism (CD) of RLuc8 and N3-protein (both at 50 μM) to measure protein secondary structures (α-helix and β-sheets). **(g)** Bioluminescence emission from RLuc8 (1 μM) upon substrate addition (40 μM), assessed over a year to determine the preservation of its activity under storage conditions (4ºC), t=time, d=day. ns=non-significance. Statistical analysis: One-way ANOVA with Dunnett´s multiple comparisons against t=0 sample.

SI-NS, and the control (NS) formulation, were prepared by adapting the ethanol injection method previously optimized by our group[56–60] for the preparation of nanometric NS in a single step. Lipid PEG-DBCO, a functionalized polyethylene glycol (PEG) lipid conjugate, was included into the NS composition, allowing copper-free click chemistry reaction with the N3 group of the modified N3-RLuc8 enzyme [61,62]. Modified enzyme was added carefully, and dropwise, into the suspension of NS, as represented in **Figure 2a**. SPAAC click chemistry was selected to bind RLu8 to the NS for the formulation of SI-NS (**Fig. 2b**) as it allows selective biomolecule bioconjugation (biorthogonal), in a fast-reaction (30 min to 2 h), and independent of pH or specific solvents conditions [40]. As the alkyne contained in the DBCO group reacts specifically with azides, prescinding from catalysts, this reaction does not lead to undesired by-products (generally, other types of click chemistry generate minimal and inoffensive by-products). The triazole ring bond formed is highly stable and strong, characterized by a high thermodynamic driving force that leads it to quickly and irreversibly form a high yield single product with high reaction specificity (in some cases, with both regio- and stereo-specificity) [40,43,49]. Moreover, click reactions are not disturbed by water. These qualities make click reactions very useful to target specific molecules that can be modified with azides groups ($-N_3$) in complex biological environments, since in living systems products need to be physiologically stable, and by-products need to be null or non-toxic [44,45,47].

a

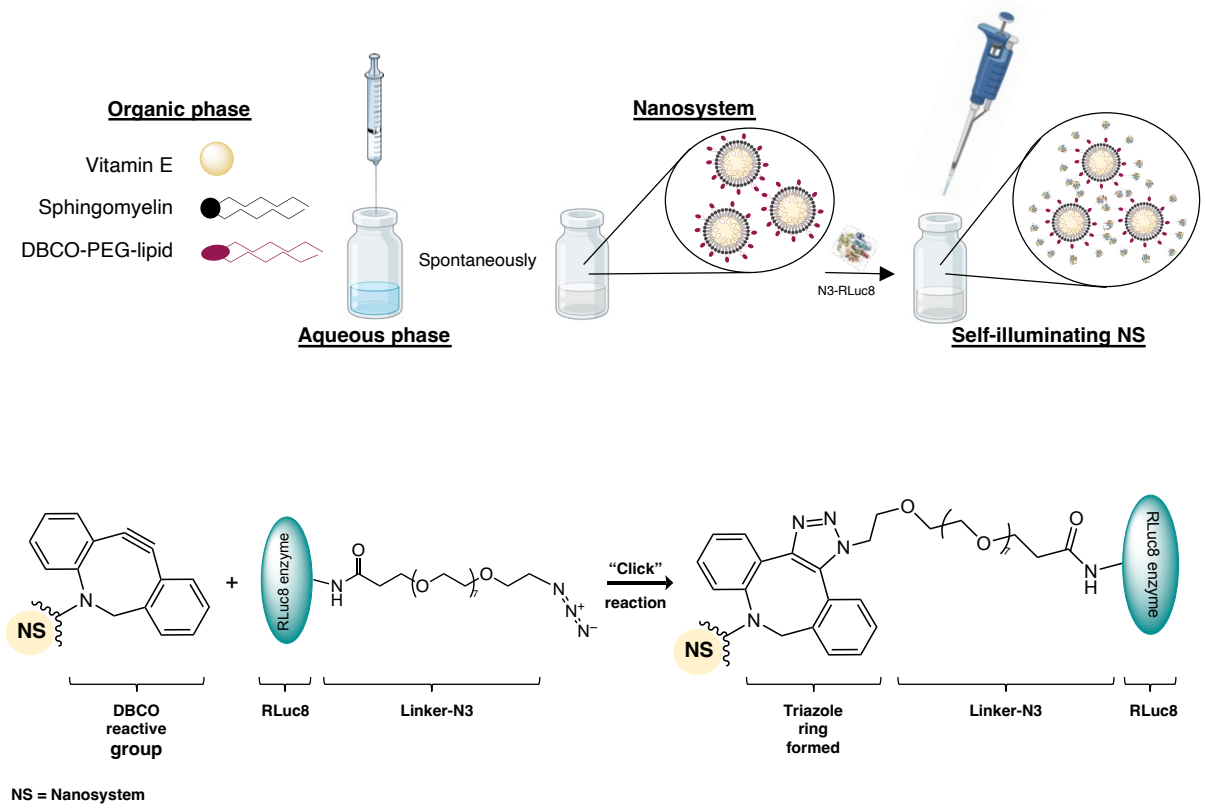

Figure 2. Schematic representation of **(a)** the formation of the sphingomyelin NS DBCO-nanosystems (NS) and further addition of the modified N3-RLuc8 protein to obtain self-illuminating nanosystems (SI-NS), and **(b)** SPAAC "click" chemistry reaction between N3-RLuc8 and the DBCO group of the NS.

The methodology described herein is highly reproducible, stable, and can be easily scaled-up. NS and SI-NS presented a small particle size, a monodisperse population, and a negative zeta potential, as determined by DLS and LDA (**Table 1)**. The successful association of N3-RLu8 enzyme was supported by the increment in size (SI-Ns ~165 nm) and a more homogeneous population resulting in a reduced PdI (<0.1). In addition, N3-RLuc8 loading was quantified by a microBCA assay, where a very high association via SPAAC "click" chemistry (~95%) was obtained. Colloidal stability at 4ºC storage was evaluated for up to one year for a minimum of 3 samples replicates for both NS and SI-Ns (**Fig. 3a, Fig. S2a**). Batch reproducibility for more than 25 replicates of NS and SI-NS were also measured in terms of size, with slight variability observed, within the range of the equipment's error (± 20 nm) (**Fig. S2b**).

Table 1. Physicochemical Characterization of the NS and SI-NS. Percentage of RLuc8 linked to the NS (Results are expressed as Mean ± Standard Deviation, n = 5). Abbreviations: nm: nanometer, PdI: polydispersity index, ZP: zeta potential in millivolts (mV), NS: Sphingomyelin DBCO-nanosystems, SI-NS: Self-Illuminating Nanosystems.

Formulation	Size (nm)	PdI	ZP (mV)	% RLuc8
NS	55 ± 3	<0.2	- 37 ± 2	-
SI-NS	165 ± 4	<0.1	- 34 ± 1	95 ± 3

NS and SI-NS were further characterized by nanoparticle tracking analysis (NTA), yielding a mean size of 88 ± 33 nm and a concentration of 5.42 x 10^{11} particles/mL for NS, and a mean size of 137 ± 33 nm and a concentration of 6.24 x 10^{11} particles/mL for SI-NS **(Table 2**). NTA analysis correlated with DLS data, confirming the size and the monodisperse distribution of the formulations, with NTA offering better resolution than DLS and allowing for visualization of peaks that are very close in size and cannot be detected by DLS [63,64]. Both, DLS and NTA results validated the efficient incorporation of N3-RLuc8 to the NS formulation, forming SI-NS. The ability of SI-NS to emit BioLight was monitored for up to one year under 4ºC storage conditions (**Fig. 3b**). Taken together, SI-NS self-illuminating properties are stable and protein integrity and functionality is fully maintained over time. This is very important, as many proteins and enzymes lose their functionality and properties if storage conditions are changed (i.e., standard storage conditions are typically -20 to -80ºC). In addition, enzymatic kinetics was monitored for 150 minutes to observe the maximum duration of SI-NS bioluminescence emission with a single-dose of CTZ (**Fig. 3c**). As described in *"materials and methods"*, 0.8 and 1 μM of SI-NS were activated with 40 μM of CTZ in PBS buffer and measurements were recorded every 5 minutes. During the first 10 minutes there was an increase in bioluminescence emission, which was sustained for 65 minutes with little variation. Afterwards, bioluminescence decreased until completely fading at approximately 90 to 105 minutes. Considering that the SI-NS enzymatic reaction follows the kinetics model described by Michaelis-Menten, the maximum dose (1 μM) tested reached a higher reaction rate consuming the substrate faster than the minimum dose (0.8 μM) [52,53].

Table 2. Physicochemical properties of NS and SI-NS determined by NTA. Mean particle size (diameter), D-values (D10, D50, D90), calculated SPAN value and sample concentration in particles per millilitre (particle/mL) (mean ± SD, n= 5).

Formulation	Mean size (nm)	D10	D50	D90	Span	Concentration (particles/mL)
NS	88.1 ± 1.8	47.4 ± 4.9	86.1 ± 1.1	130 ± 3.2	0.96	5.42×10^{11}
SI-NS	137.2 ± 1.6	96.9 ± 1.9	136.9 ± 1.4	177.7 ± 3	0.6	6.24×10^{11}

NS and SI-NS were subsequently examined by Field Emission Scanning Electron Microscopy (FESEM) to determine their morphology. Representative images were acquired by two detector modes, STEM and InLens showing a defined spherical and homogenous shape for both NS and SI-NS (**Fig. 3d**). Importantly, for SI-NS samples, a halo surrounding the nanosystems was observed, which could be due to the N3-RLuc8 displayed onto the surface of the NS, similar to protein corona affect that occurs with other nanosystems, as described [65–67]. SI-NS were also examined by MALDI-Tof to confirm the successful association of the N3-RLuc8 enzyme on the surface of the NS. An increase in enzyme mass corresponding to lipid-PEG-DBCO (~3 kDa; **Fig. S2c**), led us to conclude that the triazole ring, product of the SPAAC click chemistry reaction, was formed. With MALDI-Tof analysis, the enzyme and its chemical modifications were observed (**Fig. 3e**); however, the rest of the SI-NS components that formed were not observed due to the method used for sample ionization and crystallization disaggregates the oil and surfactants. In addition, in an enlarged capture of the spectrum, the characteristic fragmentation pattern peaks of PEG can be observed (**Fig. S2d**).

Finally, we evaluated the successful incorporation of the N3-RLuc8 enzyme to the NS by liquid ^{1}H-NMR spectroscopy [68–70], specifically on the different components in the SI-NS to obtain their characteristics peaks (**Fig. S3**). Thus, in **Figure 3f,** three ^{1}H-NMR spectra corresponding to native RLuc8, N3-RLuc8 and SI-NS are shown. The characteristic peaks of the native protein are highlighted in green, the PEG-linker in N3-RLuc8 is highlighted in orange, and the peaks corresponding to NS components (VitE, SM, PEG-DBCO) are shown in blue. In the SI-NS ^{1}H-NMR spectra, the peaks corresponding to PEG-linker in N3-RLuc8 and the aromatic groups of the RLuc8 can be observed, indicating satisfactory N3-RLuc8 association. Further analyses were conducted by solid NMR spectroscopy [71,72], in which ^{13}C-NMR and ^{1}H-NMR spectra (disclosed in

the supporting Info., **Fig. S3)** were analyzed, showing a good correlation with the liquid NMR analyses, and reaffirming the successful performance of the SPAAC "click" chemistry reaction to incorporate the N3-RLuc8 enzyme to the NS.

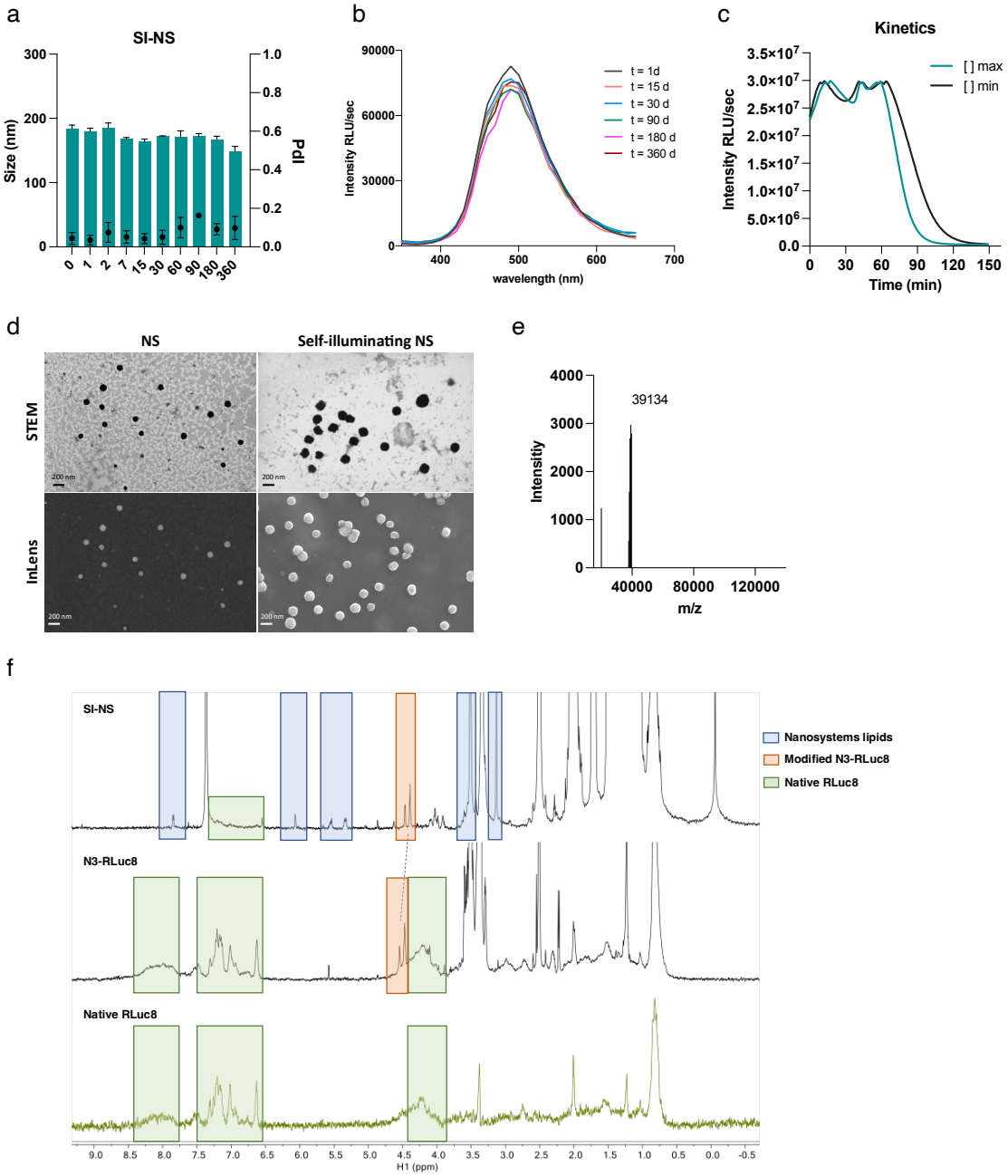

Figure 3. Characterization of the SI-SN. **(a)** Size and polydispersity index (PdI) determined for the SI-NS at stored at 4ºC for up to 360 days. **(b)** SI-NS bioluminescence emission tested for 360 days at storage conditions (4ºC). 1µM of SI-NS were activated with 40 µM of CTZ at each time point. **(c)** Bioluminescence emission kinetics for SI-NS after a single-dose of CTZ. SI-NS (0.8 and 1 µM) were activated with 40 µM of CTZ and RLuc intensity/sec was measured for up to 150 min. **(d)** FESEM images of NS and SI-NS captured using two detector modes, STEM and InLens; Scale bar: 200 nm. **(e)** MALDI-Tof analysis of SI-NS (50 µM). SI-NS: $[M+H]^+$= 39134 Da. **(f)** ^{1}H-NMR analysis of native RLuc8, N3-RLuc8 and SI-NS. Native RLuc8 spectra represent the characteristic pattern of NMR proteins (highlighted

in green). N3-RLuc8 spectra represent the incorporation of the PEG-linker (highlighted in orange). SI-NS, represent the peaks of NS lipids (VitE, SM and lipid-PEG-DBCO, highlighted in blue) and the before mentioned enzyme peaks. Additional details of the analysis are provided in the "supporting information" section.

Lastly, the stability of the NS and SI-NS in bio-relevant media (supplemented culture medium with 10% FBS, 0.9% physiological saline, 10% glucose w/v solution and filtered blood plasma) was assessed at 37ºC (under orbital shaking) for up to 4, 24 or 48 h, depending on each specific media and further experimental applications (**Fig. 4a-d**). Stability studies are key to determine the feasibility of these formulations for subsequent *in vitro* and *in vivo* usage. NS and SI-NS suffered little and insignificant variations in size, maintaining an overall optimal colloidal stability in all tested conditions [73]. When interacting with serum proteins (FBS and plasma), SI-NS decreased in size, likely due to protein-protein interactions (**Fig. 4a, 4d**). Size stability can be also related to the presence of the lipid-PEG derivative, known to avoid aggregation and stabilize the particles in medium by steric hydration repulsions [68,6]. Overall, NS and SI-NS remained stable in all the assays performed [74,75], validating their potential use in down-stream *in vitro* and *in vivo* studies.

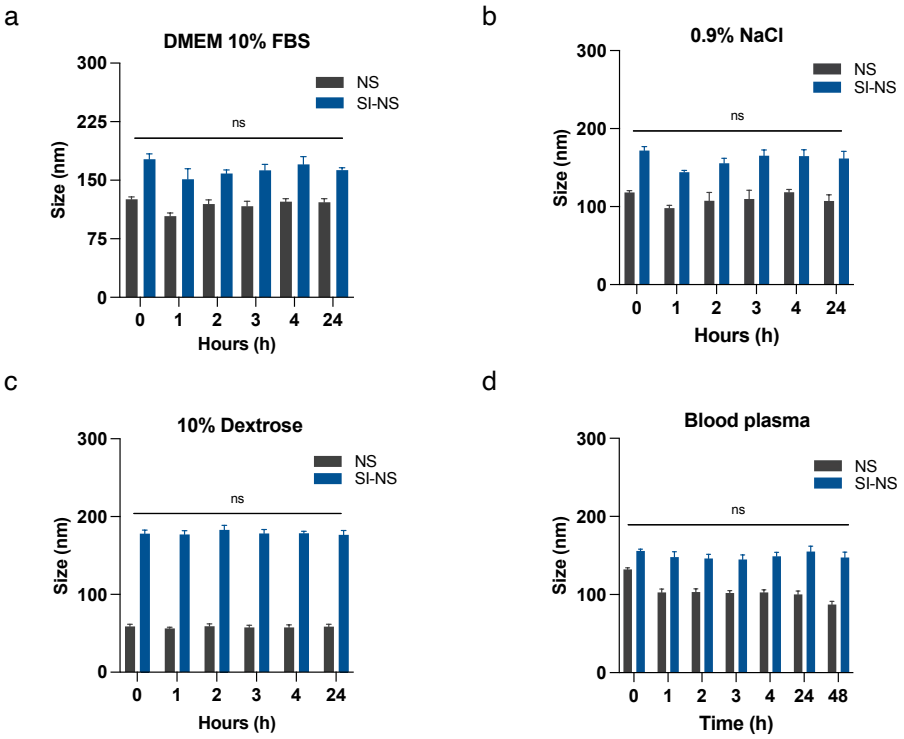

Figure 4. Stability studies of NS and SI-NS (1:10 dilution) in biorelevant media **(a)** 10% FBS supplemented cell culture medium, **(b)** 0.9% physiological saline, **(c)** 10% glucose w/v solution and **(d)** filtered blood plasma. All measurements were taken under the same conditions; incubation at 37ºC with orbital shaking (300 rpm) for up to 48h. ns=non-significance. Statistical analysis: One-way ANOVA with Dunnett´s multiple comparisons against t=0 for each condition NS and SI-NS samples.

In vitro studies of self-illuminating NS

Considering the extensive physicochemical and analytical characterization of the SI-NS, we next aimed to study their interactions *in vitro*. First, we assessed cytotoxicity using the Alamar Blue® assay in L3.6pl cells, a pancreas to liver metastatic cancer cell line, after 4 and 24h incubation with the NS and SI-NS at increasing concentrations. While the NS were non-toxic at the tested conditions (**Fig. S4a**), we observed lower toxicity at higher doses, independent of time, which may be due to the antioxidant effect of the oil core of vitamin E [76–78], but further studies along these lines are needed. Similar results were obtained with SI-NS, with almost 100 % viability at 10 mg/mL at 4 and 24 h incubations (**Fig. 5a**). We attribute this high-safety profile to the careful selection of the excipients for the formulation of the SI-NS, that is based on the combination of natural and antioxidant oils and lipids, which can be found in natural components such as cell membranes [79–81], and with a well-known safety record. In addition, the simple, spontaneous and low energy methodology used for its preparation, makes it advantageous in terms of a pharmaceutical industry point of view.

Since the efficient delivery of the bioluminescent enzyme is key for producing BioLight, cellular uptake was tested next. SI-NS containing 2 μg of the enzyme N3-RLuc8, control NS or naked N3-RLuc8 were added to L3.6pl cells. After 2 hours of incubation, cells were washed and lysed to extract total protein. Subsequently, the substrate (CTZ) was added to the lysate, and luminescence was quantified in a calibrated luminometer at enzyme wavelength emission (480 ± 20 nm), yielding high levels of luminescence emission only in the SI-NS-treated cells, confirming efficient entry. (**Fig.5b**). These results were confirmed by spectral scanning, with no luminescence obtained from the control NS or the naked enzyme as expected (**Fig S4b**). Confocal immunofluorescence analysis, using an Alexa-657-labelled monoclonal primary Ab against RLuc8, was performed on L3.6pl cells treated with TopFluor®-labelled SI-NS to directly visualize the SI-NS containing N3-Rluc8 (**Fig. 5c, Fig. S5a**). Co-localization of the enzyme (red) and labelled SI-NS (green) was

observed in treated L3.6pl cells, supporting the luminescence emission results (**Fig. 5b, S4b**) and the analytical results regarding the efficient binding of N3-RLuc8 to NS containing DBCO (as discussed in the previous section). Lastly, the internalization of the SI-NS after 30 min or 2h was also verified in L3.pl6 cells by flow cytometry using Cy5-labelled NS or SI-NS. Results confirmed that NS and SI-NS are efficiently internalized after only 30 min (**Fig. S5b**), and by 2h greater than 99% of the cells are Cy5-positive (**Fig. 5d**). Similar results were obtained using the HeLa cancer cell line after 2h incubation (**Fig S5c**). Importantly, the intracellular enzymatic activity of RLuc8 was measured up to 7 days post treatment in HEK293 cells, a faster cell division model, and c354 PDX, a slower cell division model. Strong luminescence emission was maintained for long periods (at least 7 days) irrespective of the cell model used (**Fig. 5e**).

Vitamin E is a fat-soluble antioxidant that regulates cell proliferation, expression of genes responsible for inflammation, oxidative damage, and apoptosis [77,78]. Use of antioxidant agents, such as vitamin E, can circumvent cellular damage mediated by free radicles produced by cytotoxic ROS, among other xenobiotics, or chemotherapeutics. These protective effects were previously studied in hepatotoxicity and nephrotoxicity studies using different chemotherapeutic agents [78]. Other studies have reported that lipid droplets do not protect against lipotoxicity induced by lipid overload/accumulation in tissues and organelles. Lipotoxicity in this context is produced by a variety of stressful conditions such as hypoxia, oxidative stress, and dysfunctional lipolysis [82–85]. For this reason, we next examined if lipotoxicity could occur by exposing cells to a high concentration of SI-NS (10 mg/mL). Although at 10 mg/mL we did not observe cytotoxicity (**Fig. 5a**), we wanted to study possible oxidative stress by evaluating apoptosis using an Alexa Fluor 488® annexin V/Dead cell apoptosis Kit in L3.6pl cells. Results showed no differences between non-SI-NS-treated and SI-NS-treated samples, suggesting that even with an overload concentration if NS, oxidative stress-induced apoptosis does not occur (**Fig. 5f**).

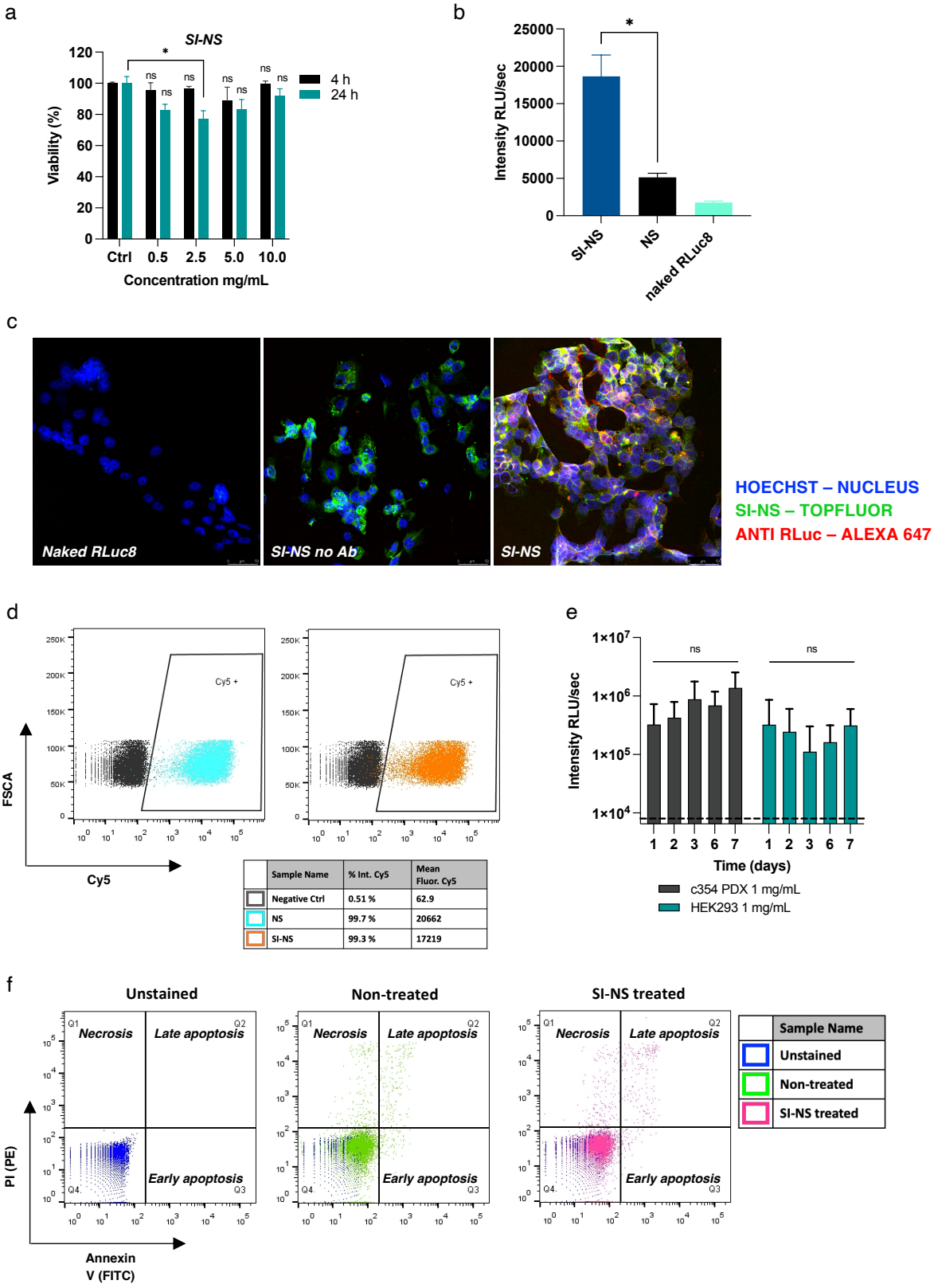
a
SI-NS
Viability (%)
Concentration mg/mL
Ctrl
0.5
2.5
5.0
10.0
4 h
24 h
b
Intensity RLU/sec
SI-NS
NS
naked RLuc8
c
Naked RLuc8
SI-NS no Ab
SI-NS
HOECHST – NUCLEUS
SI-NS – TOPFLUOR
ANTI RLuc – ALEXA 647
d
FSCA
Cy5
Cy5 +
Sample Name
% Int. Cy5
Mean Fluor. Cy5
Negative Ctrl
0.51 %
62.9
NS
99.7 %
20662
SI-NS
99.3 %
17219
e
Intensity RLU/sec
Time (days)
c354 PDX 1 mg/mL
HEK293 1 mg/mL
f
Unstained
Non-treated
SI-NS treated
PI (PE)
Annexin V (FITC)
Necrosis
Late apoptosis
Early apoptosis
Sample Name
Unstained
Non-treated
SI-NS treated

Figure 5. *In vitro* evaluation of SI-NS. **(a)** Mean % viability ± SD determined by Alamar Blue® assay, in L3.6pl cells treated for 4 or 24 hours with increasing concentrations (mg/mL) of SI-NS. ns=non-significance, *<0.05. Statistical analysis: One-way ANOVA with Dunnett´s multiple comparisons against t=0 for each condition 4h and 24h samples. **(b)** Cellular uptake evaluated after SI-NS (correspondent dose: 2 μg of RLuc8) internalization for 2 hours in L3.6pl cells by protein extraction and RLuc8 activated with CTZ (40 μM). *<0.05. Statistical analysis: t-test. **(c)** Immunofluorescence using a mAb to RLuc to confirm the uptake of TopFluor® labelled-SI-NS observed by confocal microscopy in L3.6pl cells. RLuc8 (red signal), fluorescent labelled SI-NS (green) and cell Nuclei were stained with Hoechst 33342. Left panel: naked RLuc8; Centre panel: SI-NS without anti-RLuc; Right panel: SI-NS incubated with anti-RLuc. **(d)** Evaluation of the internalization by Flow cytometry to calculate Cy5 positive cells (Cy5-labelled SI-NS; 1 mg/mL). % Internalization and mean fluorescence expressed in tables for L3.6pl, >99% positive cells after 2 h. Left panel: NS; Right panel: SI-NS. **(e)** Bioluminescence evaluation *in vitro* after 2 h incubation of SI-NS (1 mg/mL) and measured up to 7 days in HEK293 (fast metabolism) and c354 PDX (slower metabolism) cell lines to compare duration of BioLight upon CTZ activation (40 μM). ns=non-significance. Statistical analysis: One-way ANOVA with Dunnett´s multiple comparisons against t=1 for each condition c354 PDX and HEK293 samples **(f)** Alexa Fluor 488® annexin V/Dead cell apoptosis Kit to evaluate apoptosis (oxidative stress) in L3.6pl cells at maximum dose 10 mg/mL of SI-NS for its further use in PDT treatment experiments. Left panel: untreated cells; Centre panel: untreated cells stained with the kit; Right panel: SI-NS stained with the kit. No differences were observed between treated and non-treated.

In vivo activity and biodistribution of SI-NS

To determine the potential translational applicability of the SI-NS, an *in vivo* bioluminescent analysis was performed with TopFluor®-labeled SI-NS. Female C57BL/6J mice were retro-orbitally injected twice (0 and 24h) with 25 mg/Kg of SI-NS and 24 or 48 h post treatment initiation, mice were retro-orbitally injected with the substrate CTZ (1 mg/Kg) and luminescence was visualized by IVIS (Supp. Info: *"Animal models"*). SI-NS mainly accumulated in lungs and liver (**Fig. 6a-b**), as expected and confirming the use of the SI-NS to generate BioLight *in vivo*. After 48h, mice were sacrificed, organs extracted and digested, and cells were analyzed by flow cytometry to detect the presence of TopFluor®-SI-NS. FACS analysis confirmed our IVIS data, showing a strong accumulation of TopFluor®-SI-NS in lungs and liver, which is well aligned with previous results obtained with this type of NS [86,87]. TopFluor® signal was also detected in the kidneys, suggesting clearance [86] and in the brain, which could be indicative of a minimum blood-brain barrier (BBB) penetrance (**Fig. 6c**).

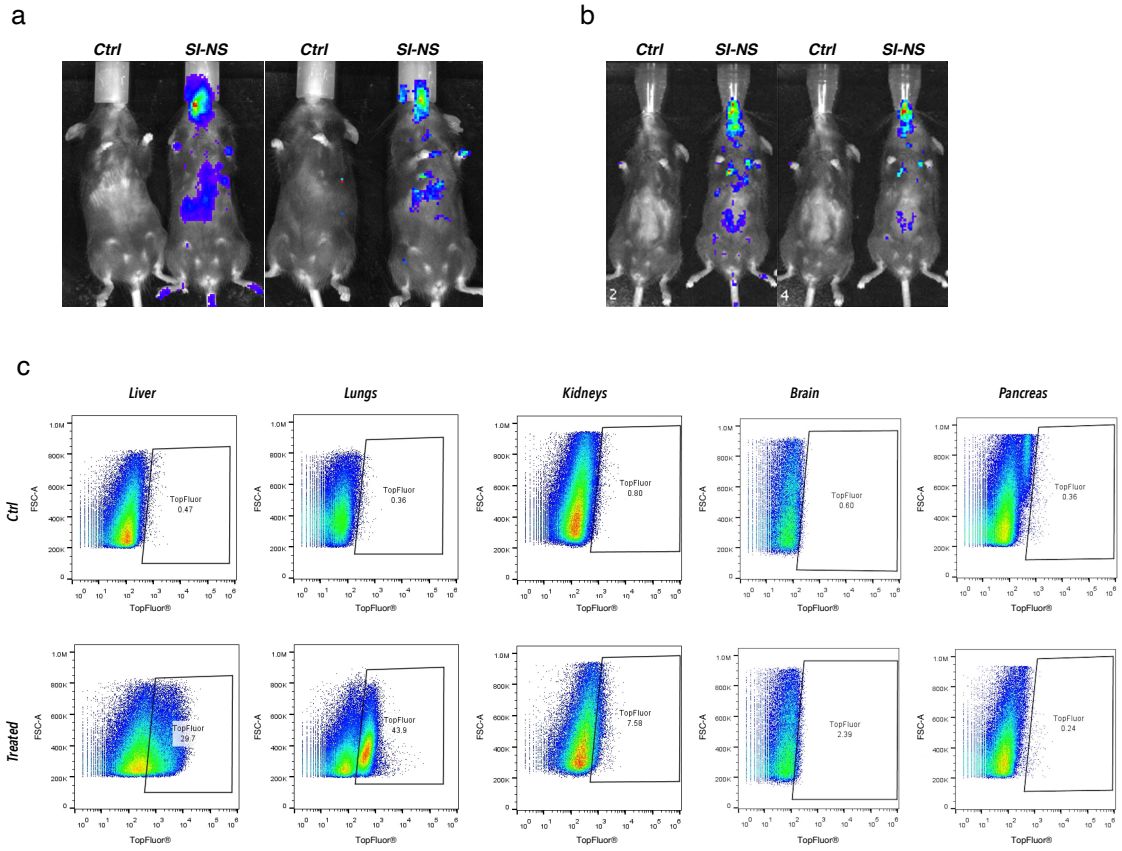

Figure 6. SI-NS ability to emit BioLight *in vivo*. Biodistribution of SI-NS in female C57BL/6J healthy mice after 100 µL retro-orbital sinus injection of TopFluor®-SI-NS (25 mg/kg per mouse) (n=5). Light emission acquired by IVIS at **(a)** 24 h and **(b)** 48 h post-treatment. SI-NS activated after retro-orbital injection of the substrate CTZ (1 mg/kg per mouse). Different experiments acquisition by IVIS. **(c)** 48 hours post-treatment, mice were sacrificed, main organs extracted, and cells isolated. Cells were then evaluated by flow cytometry to quantify positive TopFluor®-labelled SI-NS cells.

SI-NS for cell tracking

Considering the robustness of the developed SI-NS and the versatile bioluminescent features it offers for various biomedical applications, we further tested the SI-NS in imaging and cell-tracking *in vitro* and *in vivo* assays. Given the growing interest in T-cell therapeutics development, particularly to target the tumor microenvironment to counter tumor immune escape mechanisms for enhanced outcomes in solid tumors [35,36], we first focused on cell labeling. T-cells were incubated with Top-Fluor®-SI-NS and their fluorescence and bioluminescence were assessed by flow cytometry and luminometry, respectively, at increasing incubation times. This approach aimed to gauge the

potential of SI-NS for improving immunotherapies in the context of T-cell therapeutics. Results showed good internalization of Top-Fluor®-SI-NS, validated by flow cytometry (**Fig. S6a-b**). Finally, we evaluated labelling efficacy of T-cells and NS degradation for further *in vivo* tracking experiments, and future applications in immunotherapy assays by measuring RLuc8 luminescence by substrate activation up to 120 h (**Fig. S6c**).

A second experiment was conducted to investigate the application of SI-NS for labeling and tracking MenSCs *in vivo,* specifically for tumor delivery of adenoviruses for therapeutic purposes [34]. Towards this end, MenSCs were co-infected with SI-NS and an ICOVIR15K adenovirus [50]. Subsequently, labelled MenSCs were analyzed over a span of 6 days (144 h in total). Serial dilutions of the cells were cultured, and luciferase activity was measured and detected using a luminometer. As shown in **Figure 7a**, the light emission relative to the number of cells remained linear over time, albeit the intensity progressively decreased, as anticipated. This decrease in intensity was in line with expectations, considering cellular mechanisms for protein degradation. These mechanisms may vary depending on the cell type; for instance, we previously demonstrated the maintenance of RLuc8 signal up to a week in c354 PDX and HEK293 cells. The morphology of MenSCs containing SI-NS, infected with ICOVIR15K (along with control MenSCs that were not infected with ICOVIR15K and that did not receive SI-NS treatment) was observed for 144h (**Fig. 7b**). The images revealed that SI-NS did not induce toxicity to MenSCs-untreated cells, and cells treated with SI-Ns exhibited similar morphology. Moreover, the experiment demonstrated that the labelling of MenSCs with SI-NS did not compromise their function, as evidenced by the correct production of adenoviruses by the labelled cells (**Fig. 7c**). Recognizing that the *in vitro* scenario does not fully mirror the complexity found *in vivo*, subsequent experiments were designed to the toxicity, biodistribution, and tracking of the SI-NS labelled MenSCs *in vivo.* Labelled MenSCs were intraperitoneally administered to mice bearing A549 tumors (the oncolytic adenovirus ICOVIR15K was engineered to express an EGFR-targeting bispecific T-cell-engager), and bioluminescence was monitored at 24, 48 and 72h post substrate administration. This approach allowed for the determination of MenSC-tumor homing using IVIS (**Fig. S7**). Finally, we confirmed that labelled MenSCs successfully reached tumors in mice following injection (**Fig. 7d**).

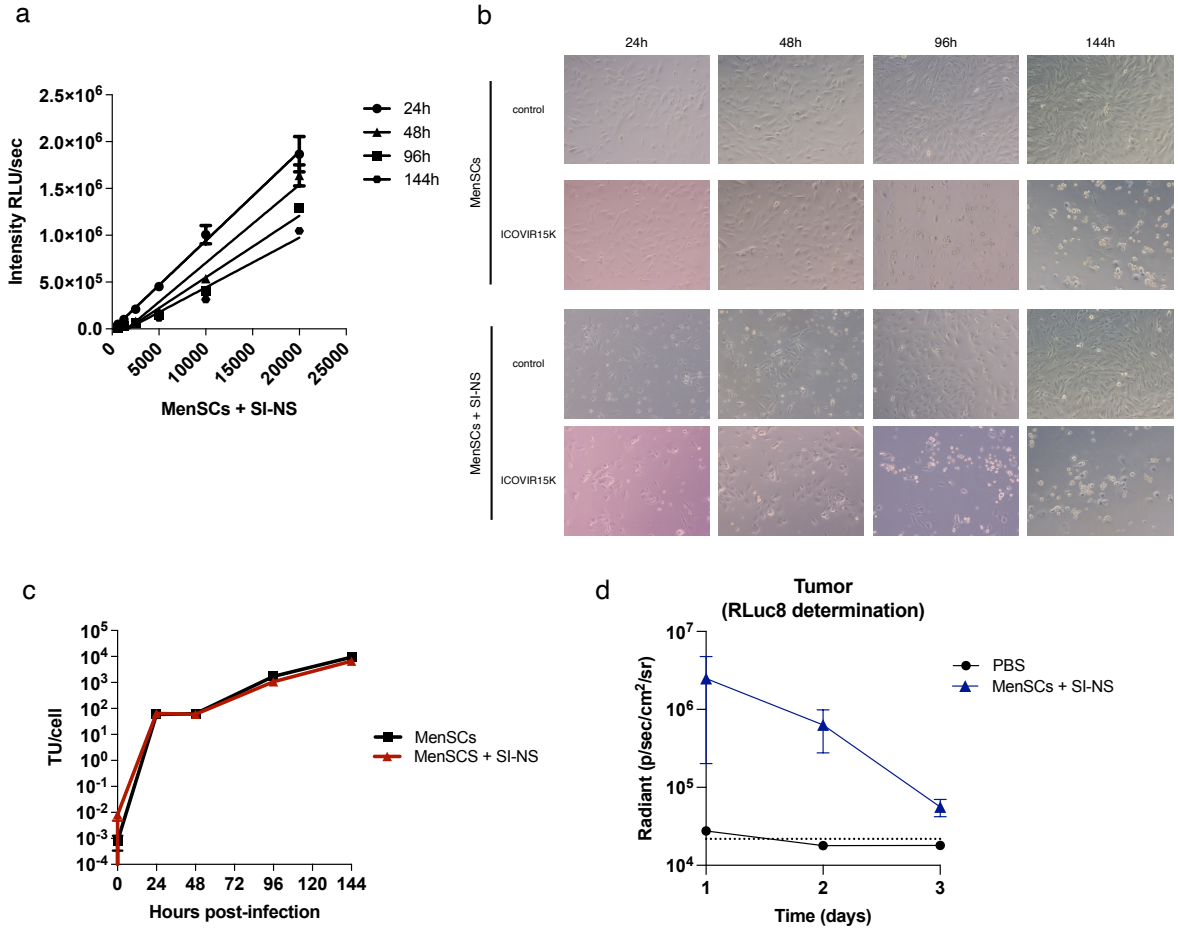

Figure 7. Application of SI-NS for cell tracking. Co-infected MenSCs with ICOVIR15K adenovirus and SI-NS. **(a)** Bioluminescence of RLuc8 MenSCs treated with SI-NS and infected with ICOVIR15K adenovirus over time (24, 48, 96 and 144h). **(b)** MenSCs morphology after adenovirus transfection and SI-NS co-incubation to evaluate possible SI-NS toxicity over time (24, 48, 96 and 144h). **(c)** Evaluation of MenSCs capacity to produce adenoviruses after SI-NS transfection over time (24, 48, 96 and 144h) (TU/cell: Transducing units per cel.). **(d)** Quantification of the bioluminescence at different time points (24, 48 and 72 h) in mice xenotransplanted with A549 cancer cells, that received an intraperitoneal injection of MenSCs cells infected with ICOVIR15K adenovirus and labelled with SI-NS. The substrate CTZ was administered intraperitoneally at each time point (Dose: 10 μg per mouse).

SI-NS for PDT in pancreatic cancer

Thus far, we have characterized an optimal nanotechnology for protein (i.e., RLuc8) delivery, based on a biodegradable NS. We propose to extend the application of the SI-NS to BioLight-induced

PDT for the treatment of pancreatic cancer. For this purpose, we introduced the photosensitizer Rose Bengal (RB), with a close absorbance wavelength to RLuc8 enzyme emission (**Fig. S8a)** into the SI-NS. Importantly, RB is FDA-approved for the treatment of eye macular degeneration, melanoma or breast cancer using laser-PDT. First, the SI-NS preparation protocol was adapted to incorporate the RB photosensitizer into the organic phase (**Fig. 8a**). RB-loaded NS (RB-NS) and SI-NS (SI-RB-NS) were characterized in terms of their physicochemical properties (**Table 3**) and batch reproducibility (**Fig. S8b**). After preparation, the encapsulation efficiency (%EE) of RB was determined by HPLC, as well as the percentage of RB loaded into the SI-NS (**Table S1**).

Table 3. Physicochemical Characterization of RB-NS and SI-RB-NS. Percentage of RLuc8 linked to RB-NS (Results are expressed as Mean ± SD, n = 5). Abbreviations: nm: nanometer, PdI: polydispersity index, ZP: zeta potential in millivolts (mV), RB-NS: Rose Bengal/DBCO-Nanosystems, SI-RB-NS: Self-Illuminating/Rose Bengal/Nanosystems.

Formulation	%RB in NS	Size (nm)	PdI	ZP (mV)	RB %EE	% RLuc8
RB-NS	15 %	76 ± 2	<0.2	- 41 ± 1	80 %	-
SI-RB-NS	15 %	200 ± 5	<0.1	- 40 ± 2	80 %	95 ± 3 %

Next, we verified bioluminescence resonance energy transfer (BRET) generated with the SI-RB-NS. The BRET method is based on the Förster resonance energy transfer principle, which postulates that the efficiency of energy transfer between a donor (RLuc8 enzyme) and an acceptor (photosensitizer) is inversely proportional to the sixth power of the distance between them. However, the energy transfer process not only depends on the distance between the donor and the acceptor, but it is also based on their relative spatial orientation. Therefore, the absence of a BRET signal between two receptors does not necessarily mean that these receptors do not interact with each other [88,89]. Moreover, the most important aspect of the BRET method is the matching spectra between the components. After CTZ substrate addition to SI-RB-NS, BRET was monitored in a luminometer, using a mix of 3 different batches of SI-RB-NS prepared on two different days (N=1 and N=2), in triplicate (**Fig. 8b**). The BRET ratio was calculated as the integral of the signal under the acceptor curve, divided by the integral under the donor curve and estimated to be 15 (**Fig. S8c**). The best BRET ratio occurs when the bioluminescence emission intensity of the donor is

closest to 0, which would indicate that most of its bioluminescence is being transferred to the acceptor [90].

Having confirmed BRET, cytotoxicity experiments were performed in L3.6pl cells treated with SI-RB-NS or RB alone in solution for 4h. RB alone, dissolved in EtOH, was more toxic than RB encapsulated in SI-RB-NS. The EtOH diluent control did not compromise cell viability (**Fig. 8c**), leading to the conclusion that high concentrations of the RB photosensitizer are toxic; however, its encapsulation into SI-NS decreases its associated toxicity. Next, cellular uptake of Cy5-labelled SI-RB-NS in L3.6pl cells was evaluated by flow cytometry after 2 h of incubation. Efficient internalization of Cy5-labelled SI-RB-NS, superior to 99%, and with high fluorescence intensities were observed (**Fig. 8d**). Co-localization of RB fluorescence with Cy5 confirmed that RB was internalized together with SI-NS, a result that was verified in a complementary confocal microscopy-based study (**Fig. S9**).

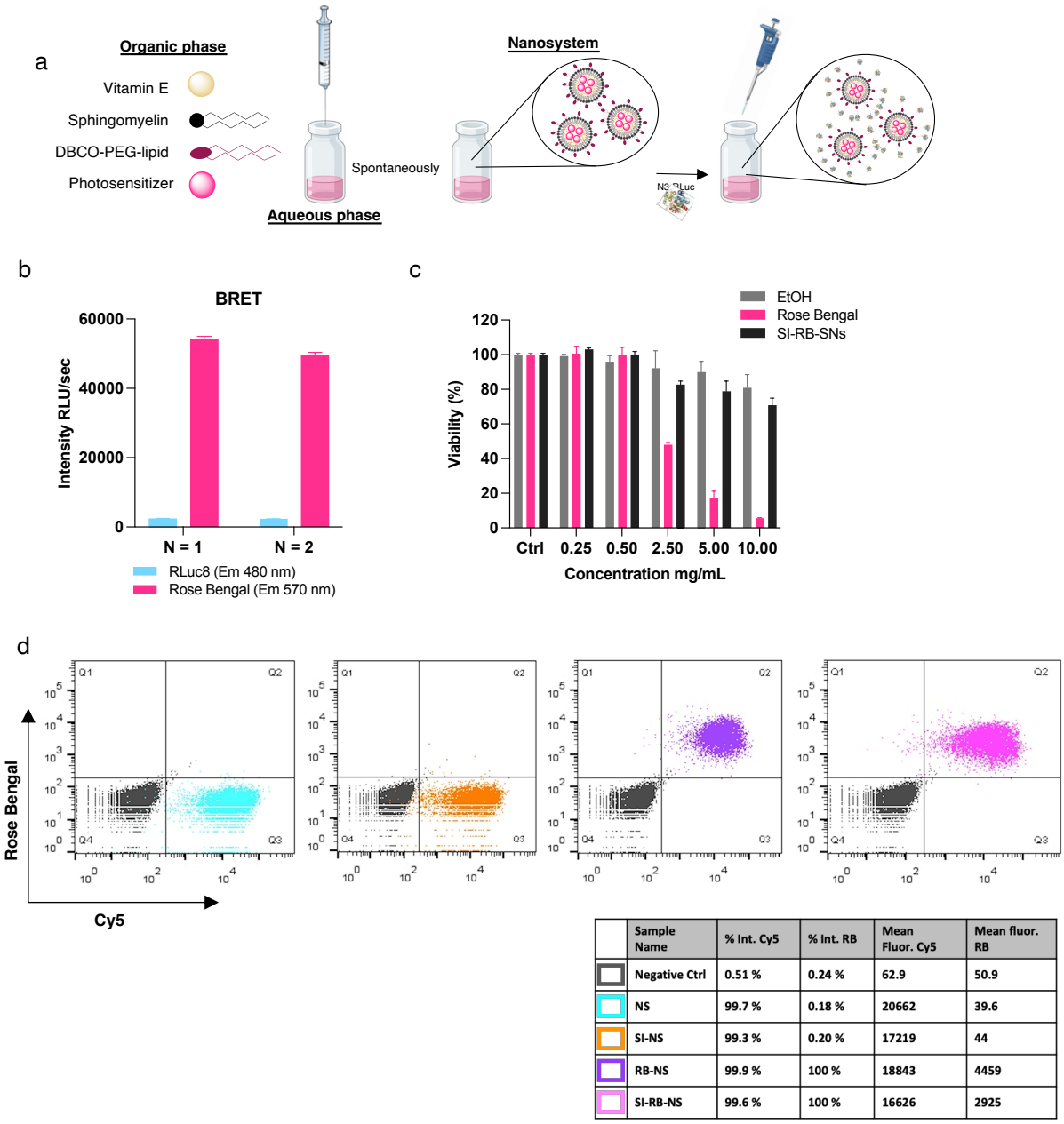

	Sample Name	% Int. Cy5	% Int. RB	Mean Fluor. Cy5	Mean fluor. RB
	Negative Ctrl	0.51 %	0.24 %	62.9	50.9
	NS	99.7 %	0.18 %	20662	39.6
	SI-NS	99.3 %	0.20 %	17219	44
	RB-NS	99.9 %	100 %	18843	4459
	SI-RB-NS	99.6 %	100 %	16626	2925

Figure 8. *In vitro* evaluation of SI-RB-NS. **(a)** Schematic representation of self-illuminating rose Bengal nanosystems (SI-RB-NS) preparation. **(b)** BRET phenomenon within nanosystems. Three batches prepared two different days (N=1 and N=2) of SI-RB-NS (1 μM) were activated upon CTZ addition (40 μM). **(c)** Cytotoxicity determined in L3.6pl cell line after 4 hours of incubation with Alamar Blue® assay for SI-RB-NS, EtOH (RB solvent) and Rose Bengal solution at increasing concentrations. **(d)** Evaluation of the internalization by Flow cytometry to calculate Cy5 (Cy5-labelled SI-RB-NS) and PE channel (photosensitizer Rose Bengal emission = 570 nm) positive cells. % Internalization and mean fluorescence expressed in the table for L3.6pl cells where is observed >99% positive cells in both channels. Left panel: NS; Centre left panel: SI-NS; Centre right panel: RB-NS; Right panel: SI-RB-NS.

Several studies have concluded that after being activated, non-toxic photosensitizers used in PDT eliminate target cells by generating ROS, which induces cellular apoptosis [22]. Thus, to test the efficacy of our SI-RB-NS-based PDT in PDAC cell lines, we first performed viability assays in L3.6pl cells and in 185 PDX cells, a pancreatic patient-derived xenograft (PDX) primary culture, where a strong cytotoxic effect was observed only in the PDT group (PDT = 10 mg/mL of SI-RB-NS + 0.02 mg/mL of CTZ) compared with untreated cells and all appropriate controls in both cell lines after 16h (**Fig. 9a**). To evaluate intracellular ROS, the fluorescent H_2DCFDA probe was used, and Luperox® (tert-butyl hydroperoxide; t-BHP) was included as an appropriate ROS-inducer (positive control) [91]. L3.6pl and 185 PDX cells were pre-incubated with the H_2DCFDA dye to detect ROS levels, followed by the indicated treatments and subsequent activation with CTZ, if indicated. After 12h, intracellular ROS was measured with a fluorimeter, observing significant H_2DCFDA levels (i.e., ROS levels) only for the PDT group and no significant fluorescence for untreated cells and in all the appropriate control groups (**Fig. 9b**). To further evaluate apoptosis, an immunofluorescence assay (IF) was carried out to visualize the levels of annexin V produced after PDT. High levels of annexin V were observed only in the PDT and positive control samples (**Fig. 9c, Fig. S10**). Finally, total apoptosis was also measured by flow cytometry in a variety of pancreatic cancer cell lines (immortalized cell lines and primary cultures): L3.6pl, 185 PDX and A6L PDX, confirming that apoptosis is efficiently achieved in all of the cultures tested following PDT (**Fig 9d**). Finally, a cell cycle analysis was performed in treated cultures to determine if PDT arrests cells in a specific phase (G1, G2-M or S) (**Fig. 9e**). Indeed, PDT arrested 185 PDX and A6L PDX cells in S phase, which is an interesting result as Gemcitabine, the first-line chemotherapeutic for pancreatic cancer, also arrests tumor cells in the S phase [92,93]. For L3.6pl cells, however, PDT arrested cells in the G2-M phase.

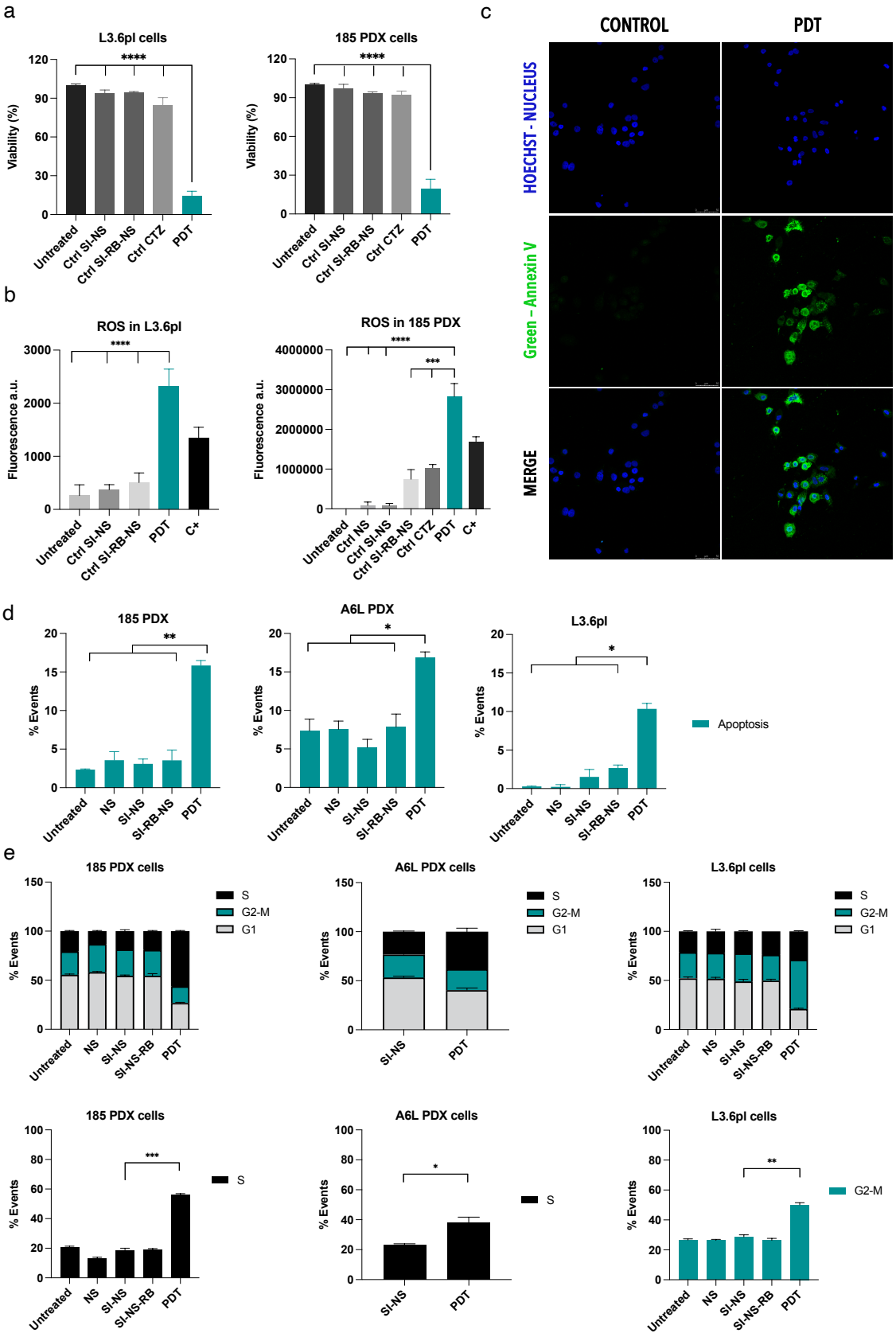
a
L3.6pl cells
185 PDX cells
Viability (%)
Untreated
Ctrl SI-NS
Ctrl SI-RB-NS
Ctrl CTZ
PDT
b
ROS in L3.6pl
ROS in 185 PDX
Fluorescence a.u.
Ctrl NS
C+
c
CONTROL
PDT
HOECHST - NUCLEUS
Green – Annexin V
MERGE
d
185 PDX
A6L PDX
L3.6pl
% Events
NS
SI-NS
SI-RB-NS
Apoptosis
e
185 PDX cells
A6L PDX cells
L3.6pl cells
S
G2-M
G1
SI-NS-RB

Figure 9. Ability of the SI-RB-nanosystems to provide a therapeutic response after PDT process. **(a)** Viability studies conducted in highly metastatic pancreatic cancer cells L3.6pl and primary culture 185 PDX cells 16 hours after PDT treatment with Alamar Blue® reagent. **(b)** ROS evaluation by H_2DCFDA staining (5 μM) in L3.6pl and 185 PDX cells 12 hours post-PDT treatment. **(c)** Representative Confocal Laser Microscopy images of Annexin V levels assessed by Immunofluorescence (Annexin V: green; Nuclei: blue, stained with Hoechst 33342) (more detailed in supporting information). **(d)** Annexin V-FITC binding protein evaluation by flow cytometry in 185 PDX, A6L PDX and L3.6pl pancreatic cancer cells after PDT process. **(e)** Cell cycle experiments in 185 PDX, A6L PDX and L3.6pl cells to assess cell cycle after PDT treatment by flow cytometry. Cells were stained with FxCycle™ Violet Ready Flow reagent (Invitrogen, USA). In all experiments represented doses: SI-NS 10 mg/mL, SI-RB-NS 10 mg/mL, CTZ 0.02 mg/mL. Data are presented as mean ± SD (at least n = 3 per group). Statistical analyses p > values meaning; * ($p < 0.05$), ** ($p < 0.005$), *** ($p < 0.0005$) and **** ($p < 0.0001$).

Finally, we investigated the effects of SI-RB-NS *in vivo*. First, mice were orthotopically implanted in the pancreas with 185 PDX cells and 3-4 weeks post tumor formation, two routes of SI-RB-NS administration were evaluated: intravenous delivery via retroorbital (RO) injection versus intraperitoneal (IP) (**Fig. 10a**). Following injection with 125 mg/kg of Cy5-labeled SI-RB-NS, no differences in the overall state of the animals nor at the level of macroscopic evaluation of organs were observed across Ctrl, RO or IP groups (**Fig. 10b**), and no differences in tumor weight were observed between control and treated mice (**Fig. 10c**). Flow cytometric analysis of the liver and tumor to detect the percentage of Cy5+ cells following injection showed that although RO administration was better for liver delivery, IP administration was better for reaching the tumor (**Fig. 10d**). Therefore, IP administration was used in subsequent experiments. Moreover, once versus twice dosing of SI-RB-NS before the administration of the substrate CTZ was also evaluated (**Fig. 10e**). As in the previous experiment, we evaluated by flow cytometry the percentage of Cy5+ cells in the tumor, concluding that in mice treated twice with SI-RB-NS, the accumulation of NS in the tumor was almost 2-fold greater (**Fig. 10f**).

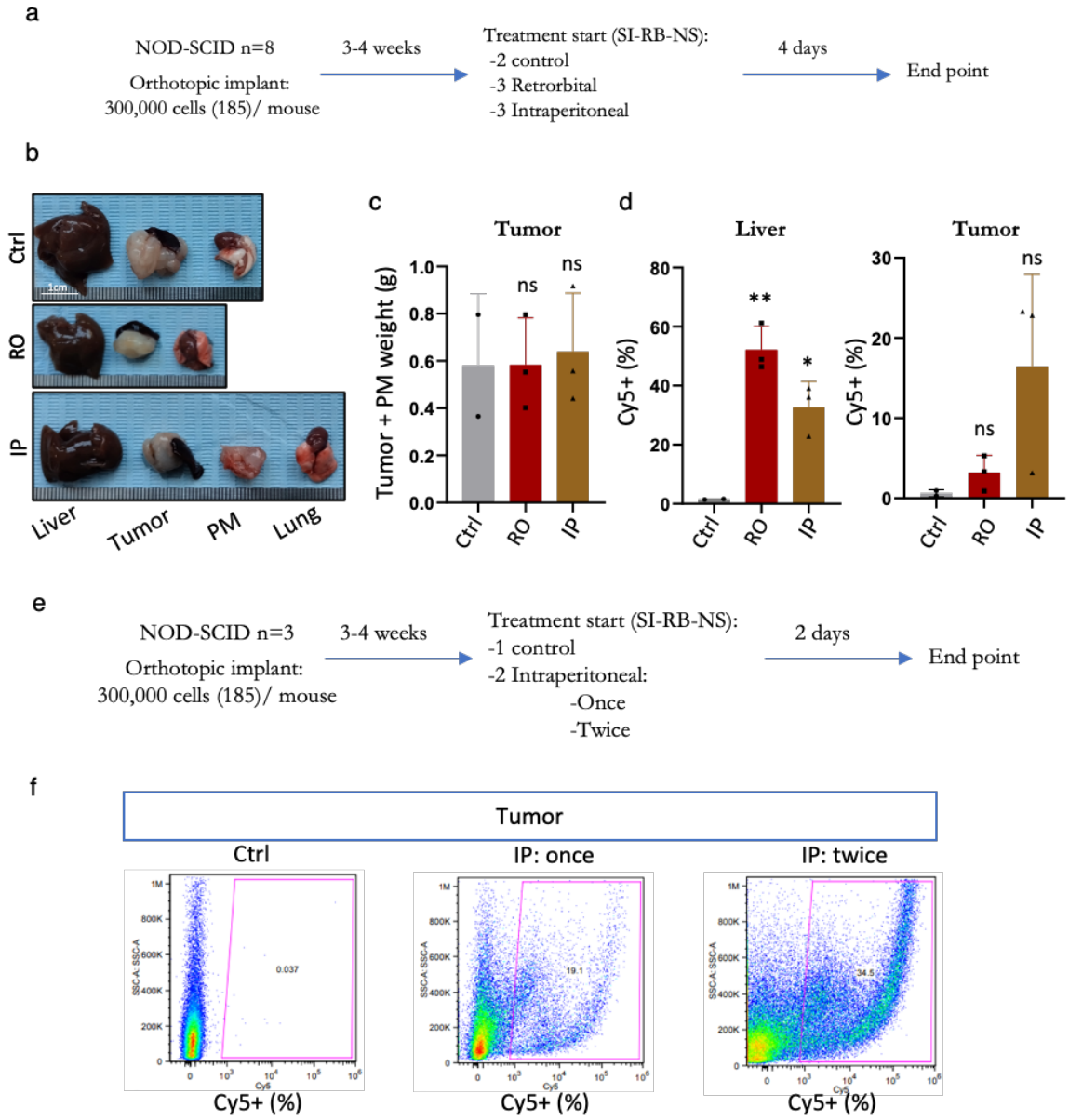

Figure 10. Evaluation of SI-RB-NS fate *in vivo*. **(a)** Scheme of the *in vivo* model pilot experiment to evaluate the optimal route of administration. **(b)** Representative macroscopic images of the organs (Liver, Tumor, PM: peritoneum metastasis and Lung). Scale: 1cm. **(c)** Mean weight (g) ± SD of tumor (and peritoneum metastasis, if observed). **(d)** Mean percentage (%) ± SD of Cy5+ cells observed by flow cytometry after tumor and liver digestion. **(e)** Scheme of the *in vivo* model pilot experiment to evaluate the treatment approach. **(f)** Representative dot plots showing the percentage of Cy5 positive cells after one or two consecutive days of treatment. PM: peritoneum metastasis, Ctrl: Control, RO: Retroorbital, IP: Intraperitoneal. ns=non-significance, *<0.05, **<0.01. Statistical analysis: One-way ANOVA with Dunnett´s multiple comparisons against "Ctrl" sample.

Having determined the optimal administration route and treatment approach, 15 mice were orthotopically implanted in the pancreas with 185 PDX cells. Three-four weeks post-implantation, treatment (i.e., three weeks) was initiated: control, SI-RB-NS, and SI-RB-NS with substrate administration (+ CTZ) (**Fig. 11a-b**). At the conclusion of the experiment, similarities in tumor weight were reported between control, SI-RB-NS and three of the five mice treated with SI-RB-NS + CTZ (**Figure 11c, c'-d**), while in the other two mice a marked reduction in tumor weight compared to the untreated controls was observed (**Fig. 11c"-d**). After digestion of the tumors, flow cytometric analysis showed the presence of the Cy5+ nanoparticles in 50% of the cells (**Fig. 11e**), confirming delivery. H&E staining was also performed allowing for the quantification of the ratio of tumor area vs healthy pancreas area in these samples, with equivalent results as shown in **Figure 11d**. In control, SI-RB-NS, and three of five mice in the SI-RB-NS + CTZ group, essentially all of the tissue was tumoral (**Fig. 11f, f'-g**), while in the other two mice from the SI-RB-NS + CTZ group, the totality of the tissue was healthy pancreas (**Fig. 11f, f"-g**).

a

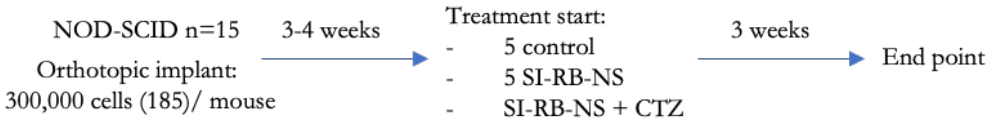

b

	Monday	Tuesday	Wednesday	Thursday	Friday
Control	Lactate	Lactate	Lactate	Lactate	Lactate
SI-RB-NS	SI-RB-NS	SI-RB-NS	SI-RB-NS	SI-RB-NS	Lactate
SI-RB-NS + CTZ	SI-RB-NS	SI-RB-NS	CTZ (morning) SI-RB-NS (afternoon)	SI-RB-NS	CTZ

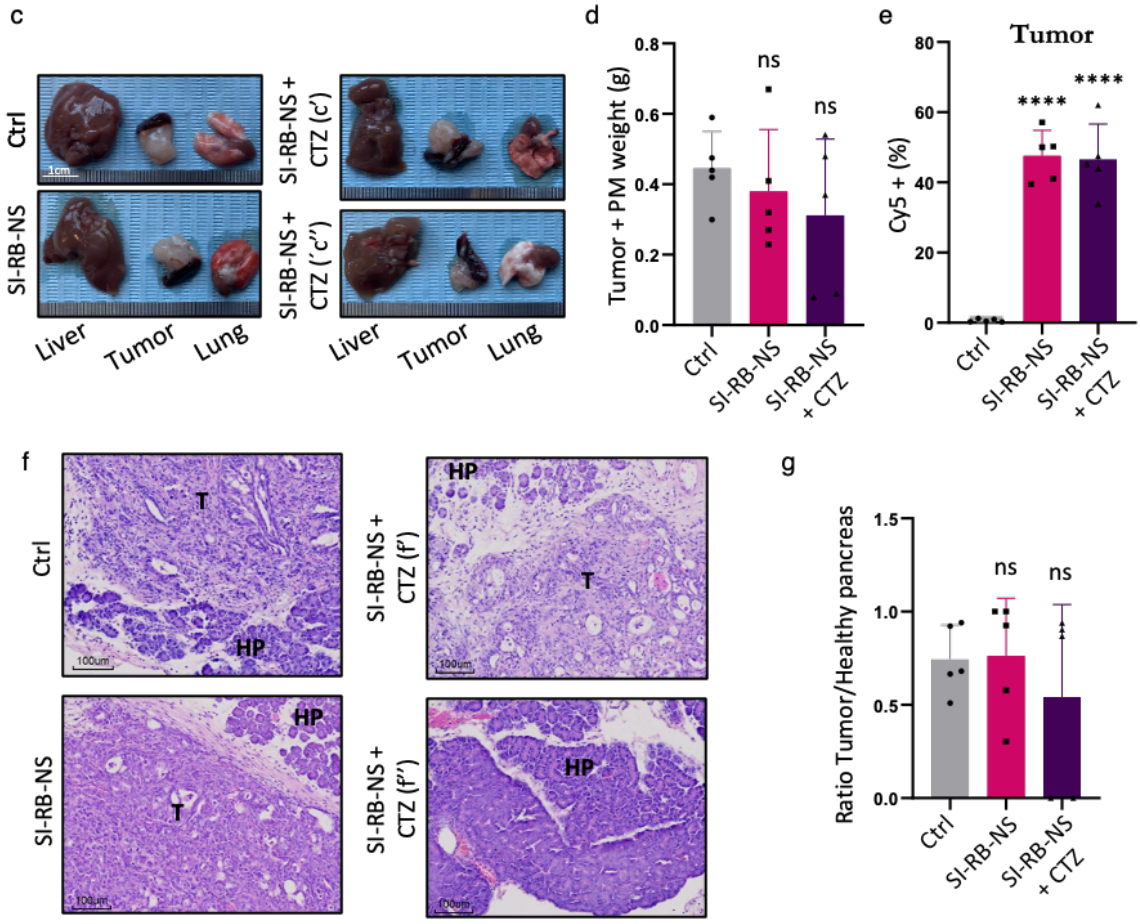

Figure 11. The effects of SI-RB-NS *in vivo*. **(a)** Scheme of the *in vivo* experiment to evaluate PDT efficacy. **(b)** Table summarizing the weekly treatment approach with two cycles of two consecutive days of SI-RB-NS before substrate (CTZ) administration. **(c)** Representative macroscopic images of the tumor and the two principal organs susceptible to metastasis: Liver and Lung. **c'**: representative image of the three mice treated with SI-RB-NS + CTZ, which were similar to controls. **c''**: representative image of the two mice treated with SI-RB-NS + CTZ, showing a reduction in

tumor weight. Scale: 1cm. **(d)** Mean tumor and peritoneum metastasis weight (g) ± SD across the different study groups. **(e)** Histogram representing the mean percentage of Cy5+ cells ± SD detected by flow cytometry in tumor digests. **(f)** H&E staining of tumors. The images (40X) are the equivalent of those from *figure 11c*. T: Tumor, HP: Healthy pancreas. **(g)** Ratio of the area of the tumor vs healthy tissue ± SD quantified in the H&E slides from *figure 11f*. CTZ: Coelenterazine. ns=non-significance, *<0.05, **<0.01, ***<0.001, ****<0.0001. Statistical analysis: One-way ANOVA with Dunnett´s multiple comparisons against "Ctrl" sample.

CONCLUSIONS

In summary, we have established the potential of a versatile and biodegradable nanoplatform, based on the efficient integration of a bioluminescent protein into a biocompatible lipid-based NS, suitable for *in vitro* and *in vivo* cell tracking, imaging, and PDT treatment. Initially, we successfully developed SI-NS, which underwent comprehensive physicochemical characterization, including size, monodisperse population and surface charge analyses. In addition, analytical methods such as NTA, NMR, MALDI-Tof, and FESEM were employed to further characterize SI-NS, confirming the association of RLuc8 and revealing SI-NS morphology and disposition. Secondly, SI-NS effectively labelled T-cells and MenSCs. MenSCs labeled with SI-NS were infected with an adenovirus and administered *in vivo* to track targeted tumor accumulation. Thirdly, the encapsulation of the photosensitizer enhanced drug bioavailability in cells, improving its disposition as an energy source for the PDT process compared to alternative approaches. Notably, the encapsulation of hydrophobic molecules into nanocarriers provided protection during i.v. delivery by preventing aggregation caused by strong interactions with blood proteins. Consequently, SI-RB-NS demonstrated tumor reduction and induced cell death in pancreatic cancer in both *in vitro* and *in vivo* models. Furthermore, the bioluminescent feature of SI-NS offers a wide range of applications, including endosomal escape and catalytic up-conversion for prodrugs.

It is essential to highlight the robustness facilitated by copper-free SPAAC click chemistry union in our SI-NS. This reaction involved incorporating a DBCO ring structure to our lipid-based NS. Although SPAAC may not exhibit the fastest reaction rate compared to iEEDA using Tz and TCO, its smaller azide group size provides an advantage in certain macromolecules or NPs, avoiding steric hindrance. Consequently, we consider click chemistry a valuable technique in this field with expectations for its broader application in the future. In conclusion, this study suggests that the combination of lipid surfactants and oil to form nanocarriers, in association with the RLuc8 bioluminescent enzyme, represents a powerful tool for drug delivery systems with a wide range of potential uses.

Supporting Information

MATERIALS AND METHODS

Reagents

Vitamin E (DL-α-Tocopherol) was purchased from Sigma Aldrich (Merck-Millipore, Darmstadt, Germany). Sphingomyelin (Lipoid E SM) was kindly provided by Lipoid GmbH (Ludwigshafen, Germany). DSPE-PEG(2k)-DBCO, C11 TopFluor® Sphingomyelin and C16 Cy5 SM, were acquired in Avanti Polar Lipids (Croda International Plc., Alabama, USA). Rose Bengal was provided by Sigma-Aldrich (Darmstadt, Germany). Azido-dPEG®8-NHS lipid was purchased in Sigma-Aldrich (Darmstadt, Germany). HPLC-grade Acetonitrile (ACN), Ethanol (EtOH), Isopropanol (IPA) and Water were obtained from Fisher Chemicals (Thermo Fisher Scientific, USA). Trifluoroacetic acid (TFA) was provided by Sigma-Aldrich (Darmstadt, Germany). All other chemicals used were HPLC or UPLC purity grade.

Photosensitizer characterization

The photosensitizer Rose Bengal was characterized to observe its maximum absorbance peak in a SYNERGY H1 microplate reader (BioTek). For that, 0.5 μg Rose Bengal was dissolved in 1 mL EtOH and 100 μL were placed in a 96-multiwell white plate and a measure was recorded every 10 nm to outline a spectral scanning.

Maldi-Tof of DSPE-PEG(2k)-DBCO lipid

DSPE-PEG(2k)-DBCO lipid mass spectra analysis was carried out in an ULTRAFLEX III MALDI TOF/TOF mass spectrometer (Bruker Daltonics, Bremen, Germany) equipped with a 200-Hz smartbeam laser. Samples were set onto a DCTB matrix (trans-2-[3-(4-tert-Butylphenyl)-2-methyl-2-propenylidene] malononitrile). MS spectra were acquired in the linear, positive ionization mode within a mass range from 800 to 5200 Da and voltage settled at 25kV.

Circular dichroism of native RLuc8 and N3-RLuc8

Studies were performed to ensure that enzyme's structure and function is maintained after modification. Circular dichroism measurements of both samples (RLuc8 and N3-RLuc8) were carried at a 50 μM concentration on a Jasco J-710 CD spectrometer.

Nuclear magnetic resonance spectroscopy (NMR)

i) Liquid NMR analysis

For, SI-NS, native RLuc8 and N3-RLuc8 samples, the 1D 1H diffusion-filtered spectrum (1D 1H PE-Dfilter-wg) was measured with the Perfect-Echo-Stimulated-Echo-LED method with bipolar PFG gradients. The diffusion delay Δ was set to 100 ms. The bipolar gradient pulses (δ) used to encode/decode diffusion have a total duration of 2 ms and were applied at the maximum gradient peak power of 50.2 G/cm. The interscan delay (d1) was set to 2 s and the number of scans was 128. The total measurement time was ~10 min. A 1D Waterlogsy spectrum (pulse sequence WaterLOGSY of the Bruker library) was measured with a 180o inversion pulse applied over signal at ~3.4 ppm of the residual protonated fraction of DMSO by means of a gaussian shaped selective pulse of 7.5 ms covering a band-width of 118 Hz. The strong water peak was suppressed before detection with a pair of excitation-sculpting echoes based in a selective 180o sinc pulse of 2 ms and PFG gradients of duration 1 ms and power levels of 31 and 11 G/cm. The inter-scan relaxation delay (d1) was 4 s, the acquisition time (aq) was 1.38 s and the spectrum was acquired with 256 scans. Three WaterLOGSY spectra were acquired for each sample with a NOE mixing time of 50 ms.

For SI-NS sample, a two-dimensional 2D TOCSY spectrum with zero-quantum filtration was measured (pulse sequence "dipsi2gpphzs" of Bruker library). The TOCSY mixing time used DIPSI-2 and the duration was 80 ms. The center of the spectrum in both F1 and F2 dimensions was set at 4.7 ppm and the spectral width in the two dimensions was 11 ppm. The interscan delay (d1) was 1.4 s, the number of scans was 24 and the number of complex points measured in the direct and indirect dimensions was 4k and 160, respectively. The total measurement time was ~2 h. A Diffusion-Ordered SpectroscopY (DOSY) spectrum (pulse sequence "ledbpgp2s" of the Bruker library) was measured with the based in the Oneshot experiment based in the bipolar gradients-stimulated echo-longitudinal experiment with eddy current delay (BPP-STE-LED). The gradient pulses that encode diffusion were varied linearly between 1 and 50 G cm-1 along 32 points in the diffusion dimension. The duration of each pair of bipolar gradients δ was 3 ms (1.5 and 1.5

ms) and the diffusion time Δ was 200 ms. The spectrum was acquired with a relaxation delay (d1) of 2 s, an acquisition time of 2.75 s and 32 scans per each point in the diffusion dimension. After Fourier transformation in the 1H dimension with zero-filling to 8 k points, the points along the diffusion dimension were processed with the exponential peak-fitting algorithm implemented in MestreNova to generate the DOSY representation of the spectrum with one dimension of chemical shifts (ppm) and the other with self-diffusion coefficients (m2 s-1). A two-dimensional 2D HSQC 1H-13C spectra was measured (pulse sequence "invigpphps" of the Bruker library. The spectrum was acquired with 2048 and 180 complex points in the t2 and t1 dimensions, respectively. The phase sensitivity in the indirect dimension uses States-TPPI. The INEPT's transfers of HSQC were optimized for a nominal value of 1JCH of 145 Hz. The relaxation delay (d1) and the FID acquisition time (aq) were 1.4 and 0.146 s, respectively. During FID acquisition 13C decoupling was applied with a garp sequence with a field strength of 5 kHz. The center of the spectrum in the 1H dimension (F2) was set at 4.7 ppm and the spectral width was 16 ppm. The center of the spectrum in the 13C dimension (F1) was set at 75 ppm and the spectral width was 160 ppm. The spectrum was acquired with 16 scans per t1 increment and the total measurement time was 1 h 18 min.

ii) Solid NMR analysys

Solid NMR spectra were measured at 298K in a Bruker NEO-750 spectrometer (750 MHz proton frequency) equipped with a Varian T3 solid triple resonance probe 1H/X/Y that uses zirconia rotor of an outer diameter of 3.2 mm with an effective sample capacity of 22 μL which corresponds to approximately 30 mg of the powder sample. The probe was adapted to the Bruker spectrometer by a A2B conversion kit (Revolution NMR, LLC). The spectrometer control software was TopSpin 4.x. All the spectra were measured under MAS of 20 kHz and processed with MestreNova software v14.0 (Mestrelab Research Inc.). Carbon-13 chemical shifts were referenced externally to the methylene signal of crystalline α-form of glycine at 43.5 ppm. Proton chemical shifts were referenced externally to the amide NH proton of the crystalline glycine that resonates at 8.5 ppm.

All samples SI-NS, native RLuc8 and N3-RLuc8 were measured by this technique. The 1D 1H MAS spectrum was acquired (sequence “zg” of the Bruker library). The inter-scan delay was set to 1.5 s, the number of scans was 64. The excitation proton pulse was applied with a tilt angle of thirty degrees at a field strength of 71.4 kHz.

The 1D 1H T2-filter-MAS spectrum was acquired at MAS 20 kHz with the Perfect-Echo MAS sequence [Paruzzo18]. The total duration of the Perfect-Echo was 2 ms. Each one of the two spin-

echoes in the sequence was synchronized to an integer number of rotor periods. The inter-scan delay was set to 1.5 s, the number of scans was 128. The proton pulses were applied with a field strength of 71.4 kHz.

The 1D 13C spectrum was measured under MAS with the Phase Alternated Recoupling Irradiation Schemes scheme (13C PARIS) [Purusottam13]. A train of PARIS-xy irradiating pulses was applied on 1H at a B1 field strength of 6 kHz and a duration of 50 us corresponding to half the MAS rotation frequency (0.5·νr). The total duration of PARIS-xy pulses train was 2 s. The irradiation was followed by a 13C hard excitation of tilt angle 90 degrees applied with a B1 field strength of 63.1 kHz. Heteronuclear decoupling during acquisition of the FID was performed with SPINAL-64 with a proton field strength of 79.4 kHz. The spectrum was acquired with 1800 scans.

The 1D 13C-CP-MAS spectra (sequence "hC.cp" of the Bruker library) were measured with an inter-scan delay (d1) of 2 s. -polarization was applied during 2 ms with a constant carbon field strength and with a linear ramped for 1H from 70% to 100%. Heteronuclear decoupling during the FID acquisition was performed with Spinal-64 with a proton field strength of 79.4 kHz. The spectrum was acquired with 1000 scans.

Rose Bengal % EE calculation by HPLC in SI-RB-NS

HPLC analyses were performed in a HPLC system 1260 Infinity II (Agilent, USA) equipped with a pump G7111A, an autosampler G7129A and UV-Vis detector G7114A set at 254nm. A LUNA C18 column (5µm, 100Å pore size, 4.6 mm × 150 mm) (Phenomenex Inc., US) operating at 40 ºC was used for separation. The mobile phases used were solvent A (10% ammonium phosphate pH 7, constant), solvent B (85-25% ultrapure water) and solvent C (5-65% acetonitrile). Flow rate was set at 0.3 mL/min. Separation was achieved by mobile phase gradient; at minute 6, 25% solvent B and 65% solvent C held for 5 minutes. Total run 18 minutes.

Cell culture conditions

The L3.6pl cell line (RRID:CVCL_0384), is a highly metastatic PDAC cell line, originally described by *Bruns et al,*. L3.6pl cells and pancreatic cancer primary cell cultures c354 PDX, A6L PDX, 185 PDX were cultured in RPMI 1640 media (Invitrogen, Cat no. 61870044) containing 10% fetal bovine serum and 50 units/mL penicillin/streptomycin in a humidified incubator (5%) at 37°C. Human cervical carcinoma HeLa cells (ATCC® CCL-2™) and human embryonic kidney, HEK-

293 cells (CRL-1573, ATCC) were acquired from ATCC and were maintained in Dulbecco's Modified Eagle Medium (DMEM; Sigma). Cell cultures were tested for Mycoplasma periodically.

In vivo Panc185 cells (185 PDX) were derived from PDAC 185 patient-derived xenograft (PDAC PDX) and were culture in RPMI (Invitrogen) supplemented with 10% FBS (Invitrogen), 50 units/mL penicillin/streptomycin and fungizone (Invitrogen) and tested for Mycoplasma before injected in mice. The PDAC 185 PDX was obtained from Dr. Manuel Hidalgo under a Material Transfer Agreement with the Spanish National Cancer Centre (CNIO), Madrid, Spain (Reference no. I409181220BSMH).

Apoptosis measurement in SI-NS

An Alexa Fluor 488® annexin V/Dead cell apoptosis Kit (ThermoFisher, USA) for flow cytometry was conducted in L3.6pl cells to evaluate if the highest dose of SI-NS tested in viability assays promote any type of apoptosis. $5x10^5$ cells per well were seeded in a 6-multiwell plate and let grow O/N. After treatments were incubated and removed, kit was applied. Appropriate controls (negative and positive) were included, and stained cells were analyzed measuring fluorescence emission at 530 nm using an excitation laser line at 488 nm.

Isolation of human menstrual blood-derived mesenchymal stem cells (MenSCs)

Menstrual blood (1-5 mL) was collected from healthy female donors, on the first 3 days of the menstrual phase using a menstrual cup (Mooncup, Brighton, UK). The protocol and cell donation for research purposes was approved by the Institutional Ethics Committee and written consent was signed for each donor. Blood samples were transferred to a sterile 50 mL centrifuge tube with conical bottom, filled with sterile phosphate buffered saline (PBS, Life Technologies, Carlsbad, CA, USA), and centrifuged at 1500 rpm for 5 minutes. The pellet was resuspended in a-MEM (Life Technologies) containing 20% Fetal Bovine Serum, 1% penicillin/streptomycin, and 1% gentamicin/amphotericin B (all from Life Technologies), and seeded overnight in culture flasks (Corning Inc., Corning, NY) at 37ºC in a 5% CO_2 atmosphere. Next day, cell monolayer was washed once with PBS to remove non-adherent cells and cellular debris and replaced with fresh medium. Finally, MenSCs were amplified for 7-24 days (passage 0), substituting the culture medium every 3-4 days, until 75%-90% confluent, and then passaged periodically by detachment (0.25% trypsin-1mM EDTA in PBS (Life Technologies)) after achieving a subconfluent monolayer.

Animal models

For *in vivo* biodistribution studies, mice were housed according to institutional guidelines and all experimental procedures were performed in compliance with the institutional guidelines for the welfare of experimental animals approved by the Universidad Autónoma de Madrid Ethics Committee (CEI 60-1057-A068 and CEI 103-1958-A337) and La Comunidad de Madrid (PROEX 335/14 and 294/19) and in accordance with the guidelines for Ethical Conduct in the Care and Use of Animals as stated in The International Guiding Principles for Biomedical Research involving Animals, developed by the Council for International Organizations of Medical Sciences (CIOMS). Briefly, mice were housed according to the following guidelines: a 12 h light/12 h dark cycle, with no access during the dark cycle; temperatures of 65-75°F (~18-23°C) with 40-60% humidity; a standard diet with fat content ranging from 4 to 11%; sterilized water was accessible at all times; for handling, mice were manipulated gently and as little as possible; noises, vibrations and odors were minimized to prevent stress and decreased breeding performance; and enrichment was always used per the facility's guidelines to help alleviate stress and improve breeding.

Female C57Bl/6J mice (Janvier Labs, France), 17 weeks old, 25 g, under isoflurane inhalation anesthesia (Induction in a 3% vol chamber, maintenance in a 1.5% mask - XGI-8 anesthesia equipment) were retro-orbital sinus injected with 100 µL of nanosystems twice with 24h difference. Bioluminescence was recorded by *in vivo* optical imaging equipment IVIS-Lumina II and results analyzed with "spectral *in vivo*" software. Mice were sacrificed in a CO_2 chamber and performed a complete organ necropsy to isolate cells and evaluate them by flow cytometry.

In vivo studies involving MenSCs were performed at the ICO-IDIBELL facility (Barcelona, Spain) AAALAC unit 1155 and approved by IDIBELL's Ethical Committee for Animal Experimentation. Subcutaneous xenograft tumors were established by injection of 5×10^6 A549 cells into the flanks of 8-week-old NOD/SCID gamma (NSG) mice. When tumors reached 400 mm^3, 4×10^6 SI-NS-labelled MenSCs (passage 6) were administered intraperitoneally in mice (n = 4). Briefly, MenSCs were incubated with formulation for two hours in agitation before animal administration. IP administration of 10 µL Coelenterazine 1mg/mL was used to monitored SI-NS-labelled MenSCs at 24 h, 48 h and 72h post administration which allowed MenSC-homing determination using IVIS Lumina bioimaging system (PerkinElmer). Images were analyzed with IVIS Living Image (PerkinElmer) software. Regions were manually drawn around the tumors.

RESULTS

$$V_0 = \frac{V_{max}[S]}{K_m + [S]} \qquad E + S \leftrightarrows ES \rightarrow E + P$$

E = enzyme
S = substrate
P = product

Figure S1. Michaelis-Menten equation and reaction describing the kinetic model of RLuc8 (enzyme) + CTZ (substrate).

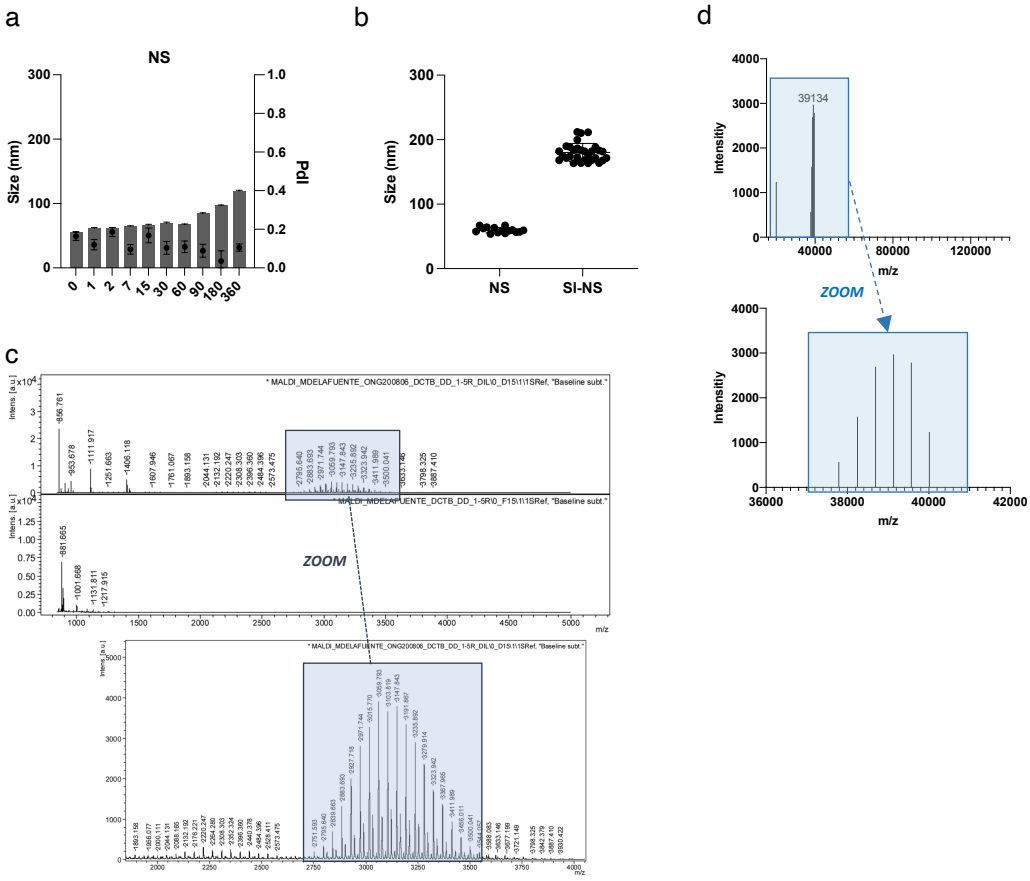

Figure S2. (a) Size and polydispersity index (PdI) determined for the NS at stored at 4ºC for up to 360 days. At least 3 batches tested (n>3). **(b)** NS and SI-NS batch reproducibility measured in terms of size after preparation (n>25). **(c)** MALDI-TOF signals of DSPE-PEG(2k)-DBCO (blue area) calculated mass ~3kDa. **(d)** MALDI-TOF analysis of SI-NS and zoomed MS spectra (blue area). Calculated mass ~39kDa.

a

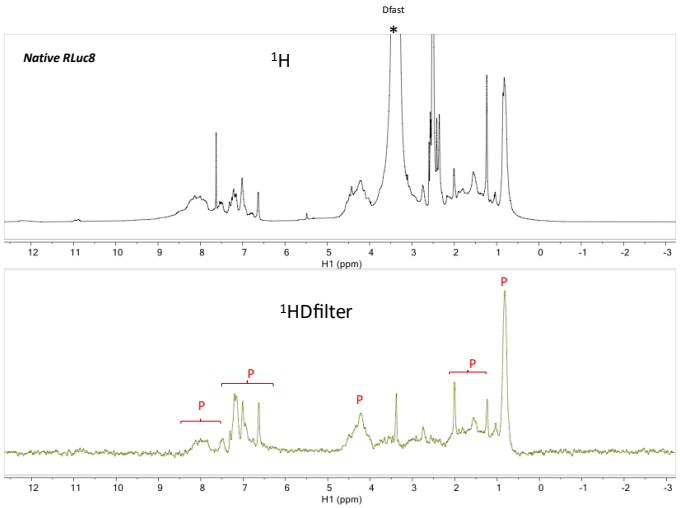
Dfast
Native RLuc8
1H
*Impurity
H1 (ppm)
1HDfilter
P
Dfast = Fast diffusion coefficient
Dslow = Slow diffusion coefficient

b

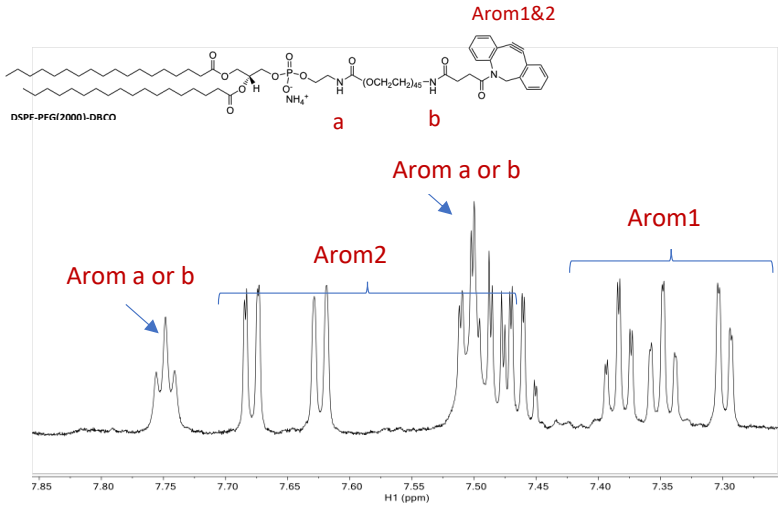
Arom1&2
DSPE-PEG(2000)-DBCO
a
b
Arom a or b
Arom1
Arom2
Arom a or b
H1 (ppm)

c

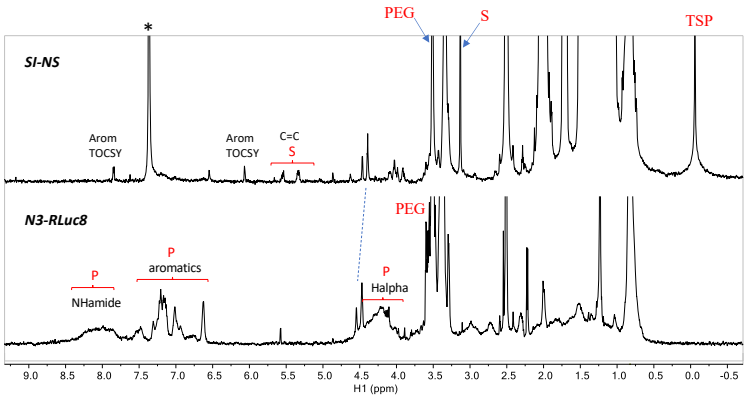
PEG
S
TSP
*
SI-NS
Arom TOCSY
Arom TOCSY
C=C
S
*Impurity
P = protein
S = Sphingomyelin
Arom = aromatic groups DBCO
N3-RLuc8
PEG
P
aromatics
P
NHamide
P
Halpha
H1 (ppm)

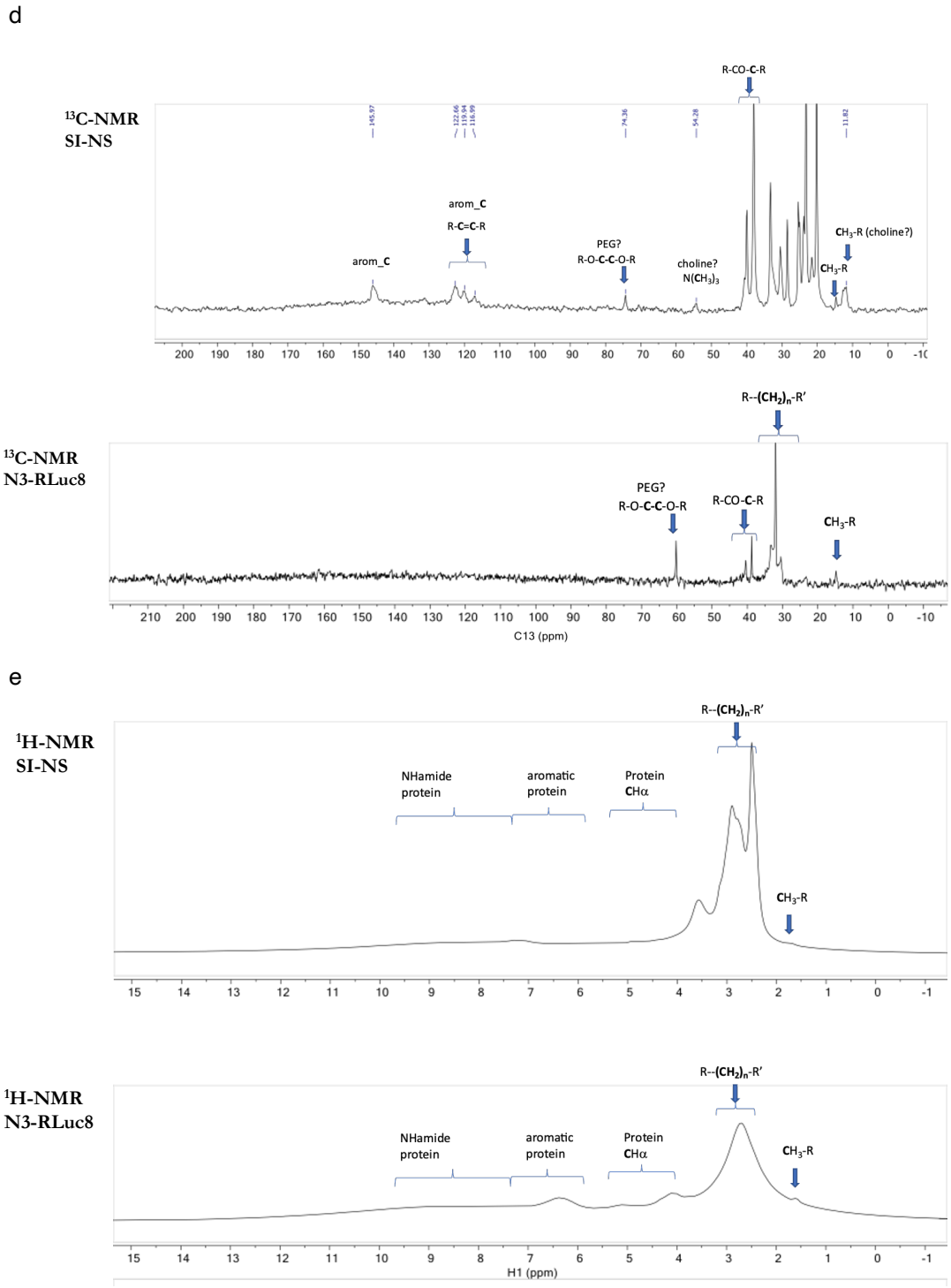

Figure S3. Liquid NMR analysis of SI-NS and components. (a) ^{1}H-NMR and ^{1}HDfilter-NMR spectra of the native RLuc8 to identify its characteristics H-proton peaks of the proteins functional groups. **(b)** DSPE-PEG(2k)-DBCO lipid ^{1}H-NMR spectra to observe the shift of the H-proton of its components. **(c)** ^{1}H-NMR spectra of N3-RLuc8 to confirm the incorporation of the PEGylated moiety to the native RLuc8.

Solid NMR analysis of SI-NS and components. (d) ^{13}C-NMR spectra of SI-NS and N3-RLuc8. N3-RLuc8 spectra represents the shift of the peaks corresponding to chemical sequences of the amino acids in proteins (e.g., R-$(CH_2)_n$-R' and R-CH_3) and the PEG moiety (R-O-C-C-O-R'). SI-NS analysis represents the shift of the peaks of N3-RLuc8 and lipid components in NS (VitE, SM and PEG-DBCO). **(e)** SI-NS and N3 RLuc8 ^{1}H-NMR analysis spectra.

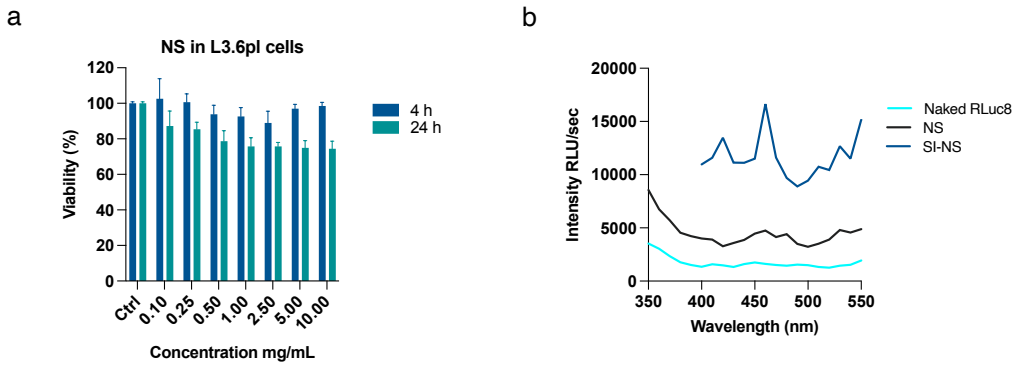

Figure S4. (a) Nanosystems cytotoxicity in L3.6pl cell line after 4 and 24 hours of incubation determined with Alamar Blue® assay. Represented %viability. **(b)** Cellular uptake was analyzed after SI-NS (0.01mg/mL; correspondent dose: 2 μg of RLuc8) internalization for 2 hours in L3.6pl cells with subsequent cell lysis and upon CTZ activation (40 μM). Here it is represented bioluminescent activity spectral scanning of the samples, naked RLuc8 (control), NS (control) and SI-NS (treatment).

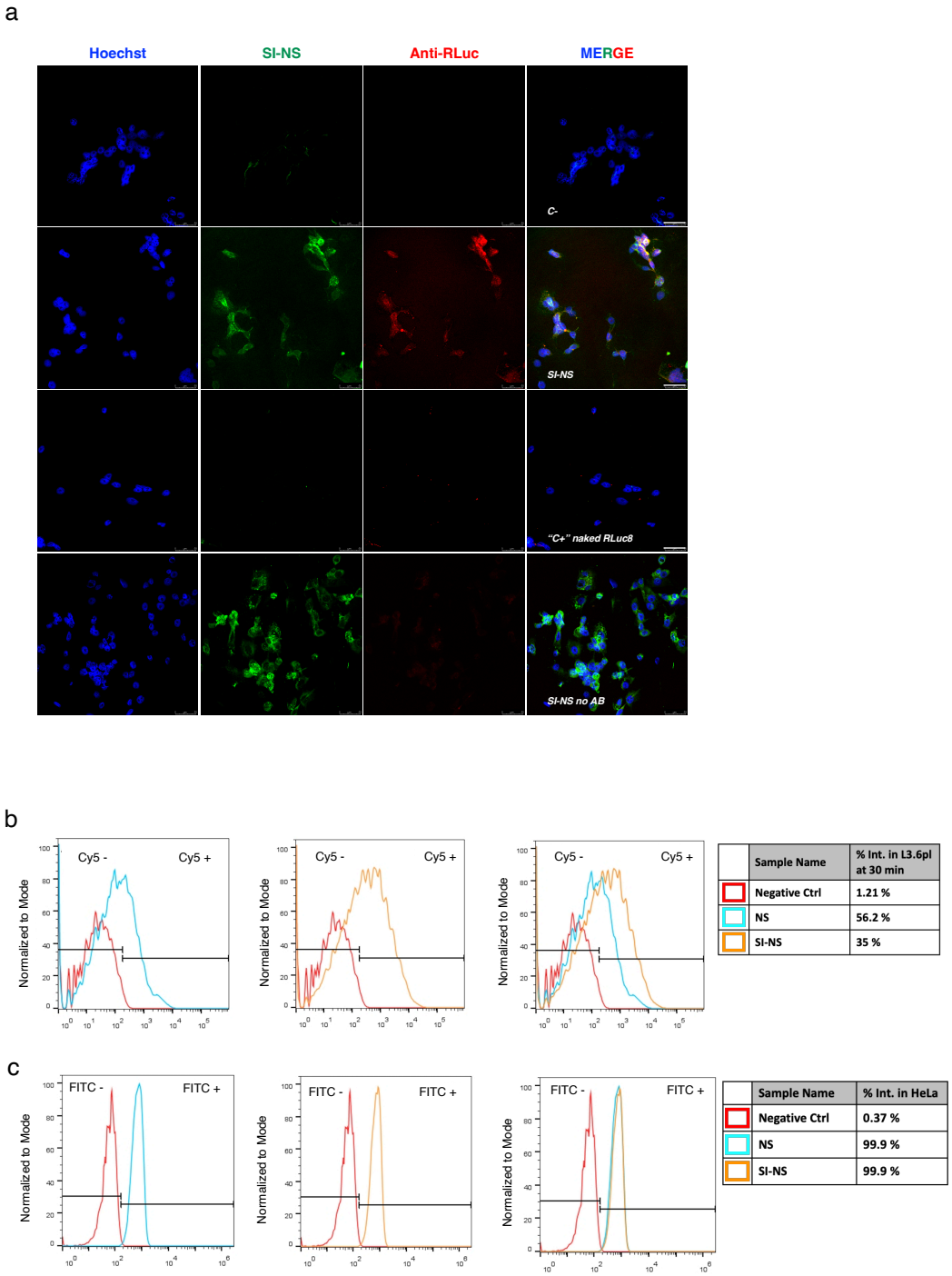

Figure S5. (a) Uptake experiment of TopFluor®-SI-NS to visualize internalization of NS and the enzyme (Merge: Yellow signal). Untreated cells with mAb-anti-RLuc Alexa 647® were used as control. Cell Nuclei were stained with Hoechst 33342 (blue signal), TopFluor® labelled NS in green and mAb-anti-RLuc Alexa 647® in red observed by Confocal Microscopy (Scale bar: 50 μm). Evaluation of SI-NS internalization by Flow cytometry to calculate Cy5 positive cells. SI-NS incubated for **(b)** 30 minutes in L3.6pl and **(c)** 2 hours in HeLa cells. Untreated cells were used as control. % Internalization and mean fluorescence expressed in tables.

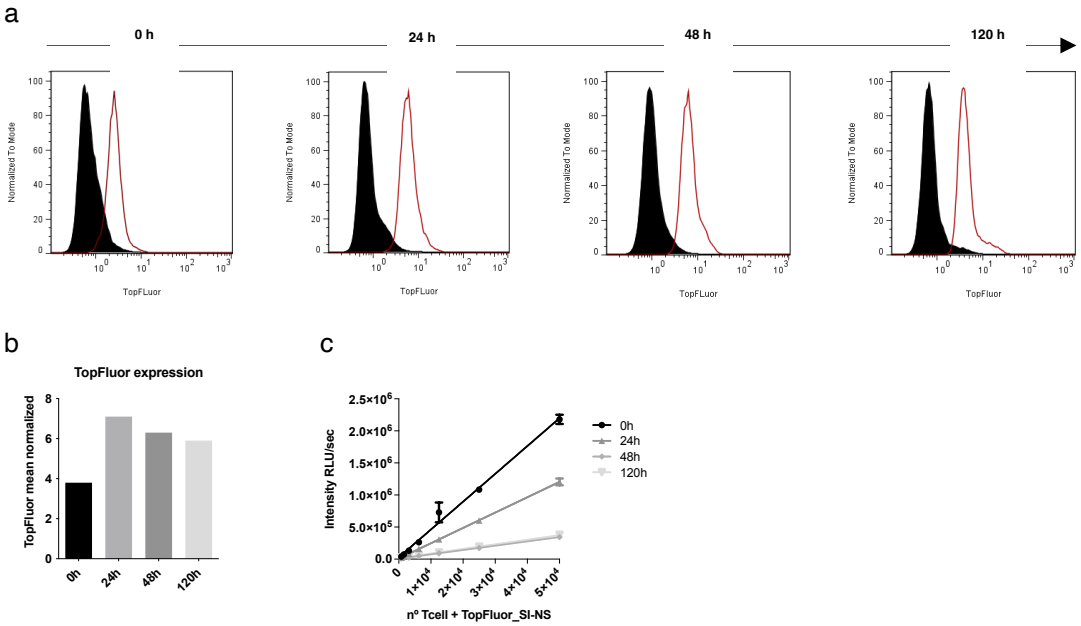

Figure S6. Tcells labelling with TopFuor®-SI-NS. **(a)** Evaluation of the labelled Tcells by flow cytometry measuring TopFluor®'s fluorescence up to 120 hours. **(b)** Quantification of the fluorescence by flow cytometry. **(c)** SI-NS bioluminescence evaluation upon CTZ (40 µM) activation over time (0, 24, 48 and 120h).

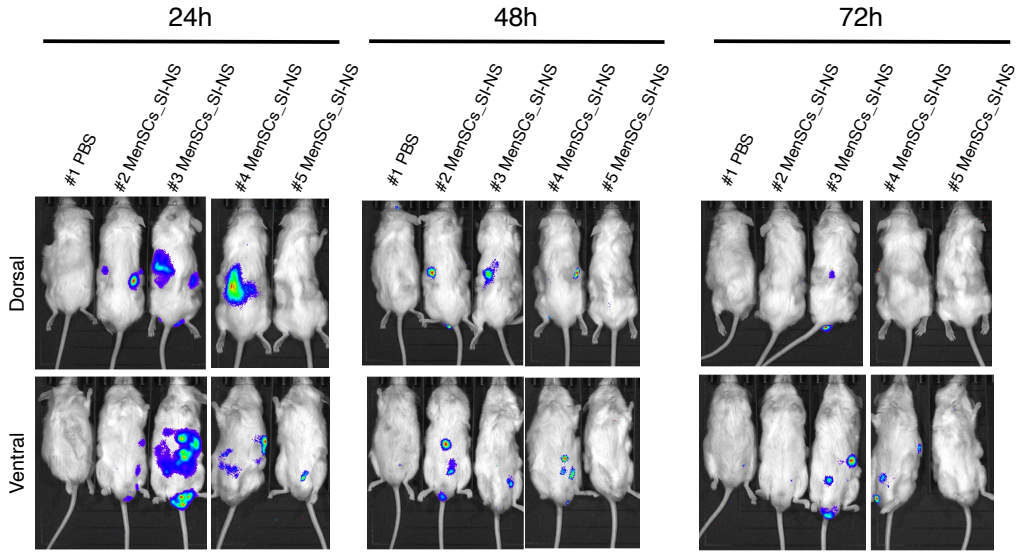

Figure S7. Quantification of the bioluminescence at different time points (24, 48 and 72 h) in mice xenotransplanted with A549 cells, that received an intraperitoneal injection of MenSCs cells infected with ICOVIR15K adenovirus and labelled with SI-NS. The substrate CTZ was administered intraperitoneally at each time point (Dose CTZ: 1 mg/kg per mouse).

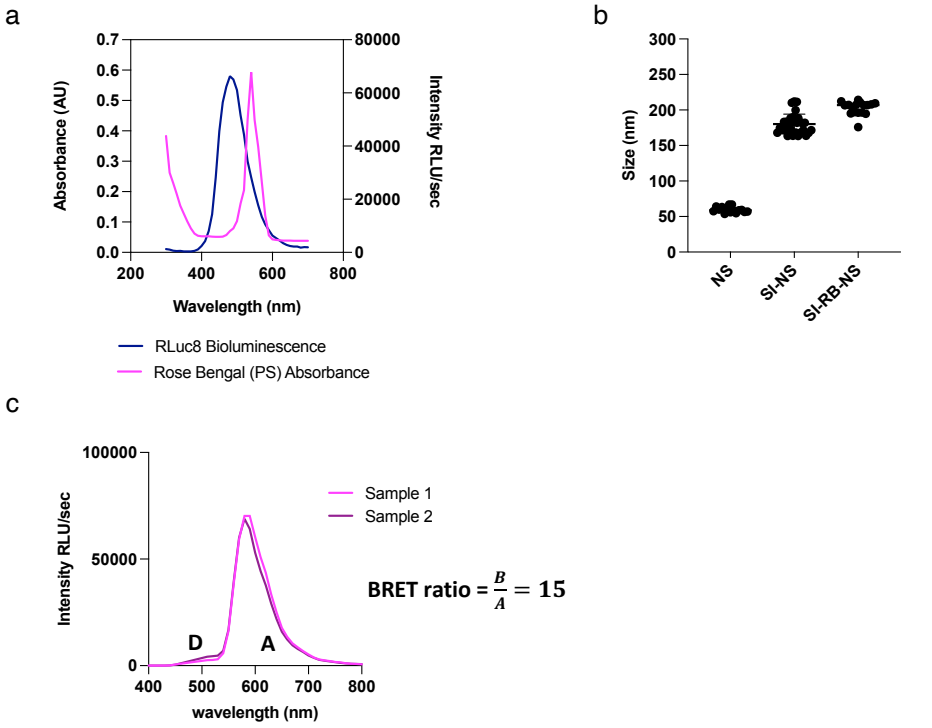

Figure S8. (a) Matching spectra of RLuc8 emission and Rose Bengal absorption. **(b)** Batches reproducibility of the 3 different nanosystems; NS, SI-NS and SI-RB-NS (n>25). **(c)** BRET spectral scanning of 3 different batches each sample (samples corresponding to 2 days of preparation N=1 and N=2) of SI-RB-NS upon CTZ activation. BRET ratio calculation was shown.

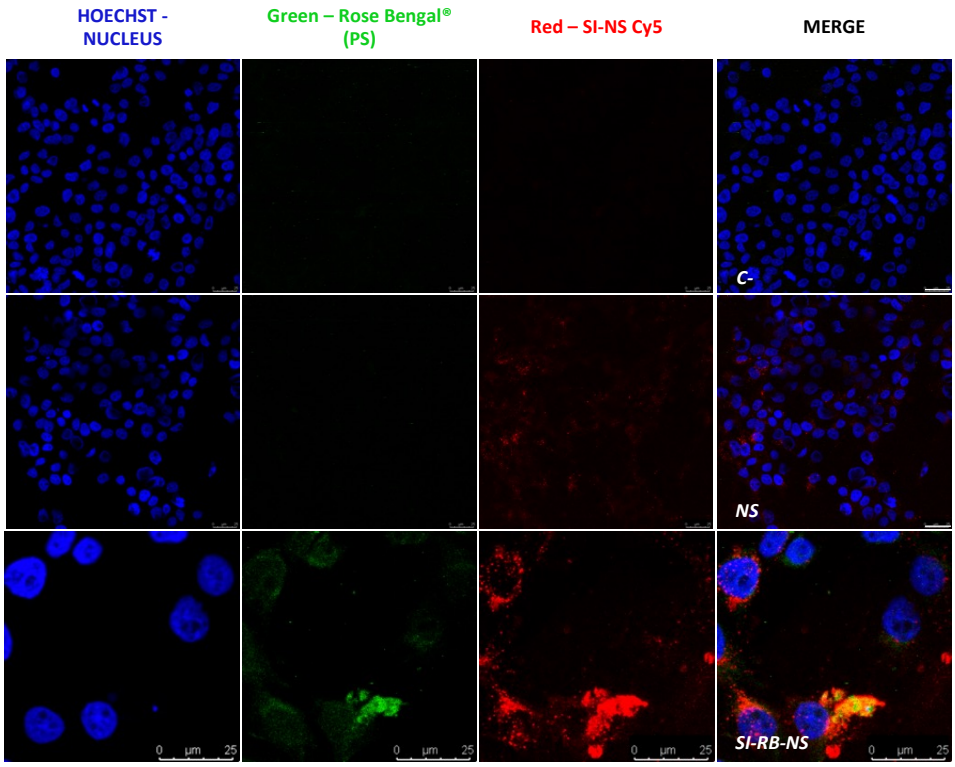

Figure S9. Uptake experiments of Cy5 labelled SI-RB-NS observed by confocal microscopy. SI-NS signal in red (Cy5), RB in green, cell nuclei stained with Hoechst 33342 (blue signal), merge in yellow. Scale bar: 25 µm.

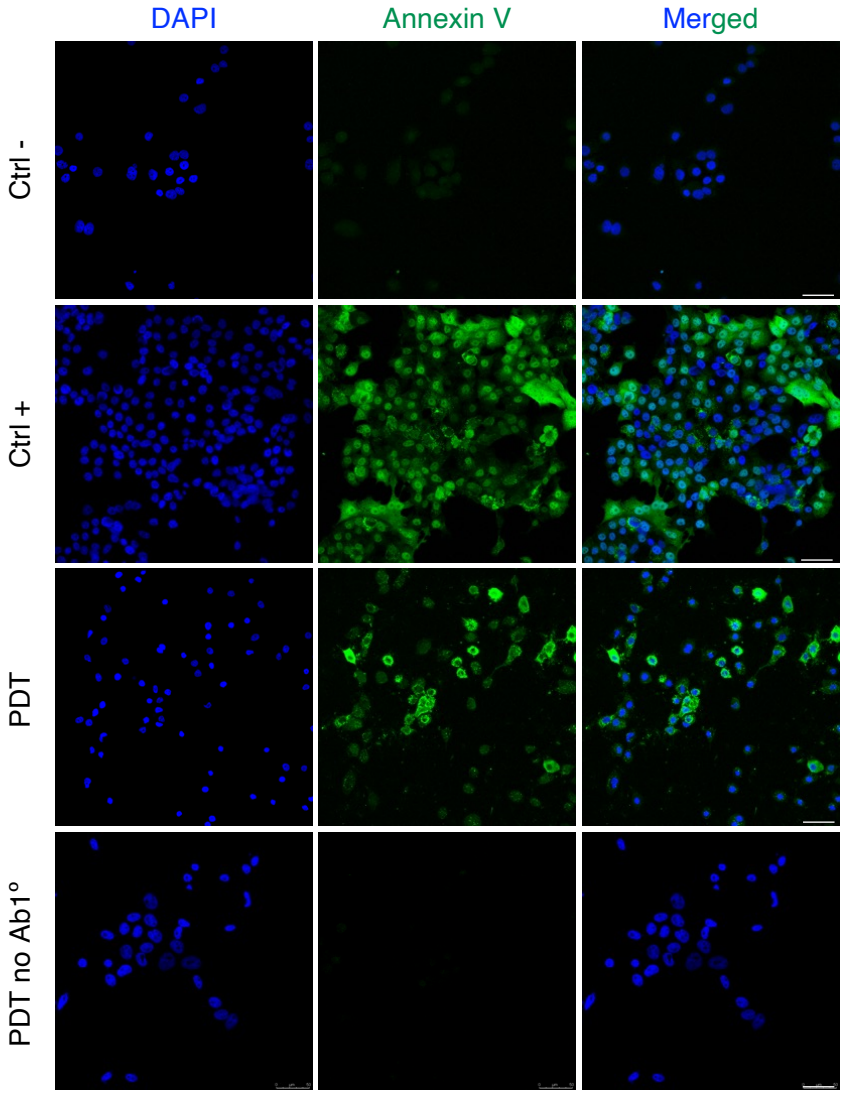

Figure S10. Confocal Microscopy images of Annexin V levels assessed by Immunofluorescence to confirm apoptosis cell killing mechanism pathway after 16 h PDT treatment. Appropriate negative controls were used and positive control to observe Annexin V. Here are shown different captures of principal figure to conclude that annexin V levels observed are similar in any field of the well treated. Scale bar: 50 μm.

Table S1. Physicochemical Characterization of NS and RB-NS. Percentage of RLuc8 linked to RB-NS (Results are expressed as Mean ± SD, n = 5). Abbreviations: nm: nanometer, PdI: polydispersity index, ZP: zeta potential in millivolts (mV), NS: DBCO-Nanosystems, RB-NS: Rose Bengal/DBCO-Nanosystems.

Formulation	%RB in NS	Size (nm)	PdI	ZP (mV)	RB %EE
NS	-	57 ± 3	<0.2	- 37 ± 2	-
RB-NS	10 %	84 ± 3	<0.2	- 37 ± 5	83 %
RB-NS	15 %	76 ± 2	<0.2	- 41 ± 1	80 %
RB-NS	20 %	71 ± 4	<0.2	- 44 ± 2	66 %

REFERENCES

1. Siegel, R. L., Miller, K. D., Fuchs, H. E. & Jemal, A. Cancer Statistics, 2021. *CA Cancer J Clin* **71**, 7–33 (2021).

2. Sung, H. *et al.* Global Cancer Statistics 2020: GLOBOCAN Estimates of Incidence and Mortality Worldwide for 36 Cancers in 185 Countries. *CA Cancer J Clin* **71**, 209–249 (2021).

3. Hu, J. X. *et al.* Pancreatic cancer: A review of epidemiology, trend, and risk factors. *World Journal of Gastroenterology* vol. 27 4298–4321 Preprint at https://doi.org/10.3748/wjg.v27.i27.4298 (2021).

4. Tuveson, D. A. & Neoptolemos, J. P. Understanding metastasis in pancreatic cancer: A call for new clinical approaches. *Cell* **148**, 21–23 (2012).

5. SLIWKOWSKI, M. X. & MELLMAN, I. Antibody Therapeutics in Cancer. *Science (1979)* **341**, 1192–1198 (2013).

6. Cheng, L., Yang, L., Meng, F. & Zhong, Z. Protein Nanotherapeutics as an Emerging Modality for Cancer Therapy. *Adv Healthc Mater* **7**, (2018).

7. Dessale, M., Mengistu, G. & Mengist, H. M. Nanotechnology: A Promising Approach for Cancer Diagnosis, Therapeutics and Theragnosis. *International Journal of Nanomedicine* vol. 17 3735–3749 Preprint at https://doi.org/10.2147/IJN.S378074 (2022).

8. Friberg, S. & Nyström, A. M. NANOMEDICINE: Will it offer possibilities to overcome multiple drug resistance in cancer? *J Nanobiotechnology* **14**, 1–17 (2016).

9. Mitchell, M. J. *et al.* Engineering precision nanoparticles for drug delivery. *Nature Reviews Drug Discovery* vol. 20 101–124 Preprint at https://doi.org/10.1038/s41573-020-0090-8 (2021).

10. Rosenblum, D., Joshi, N., Tao, W., Karp, J. M. & Peer, D. Progress and challenges towards targeted delivery of cancer therapeutics. *Nature Communications* vol. 9 Preprint at https://doi.org/10.1038/s41467-018-03705-y (2018).

11. Chenthamara, D. *et al.* Therapeutic efficacy of nanoparticles and routes of administration. *Biomaterials Research* vol. 23 Preprint at https://doi.org/10.1186/s40824-019-0166-x (2019).

12. Graván, P., Aguilera-Garrido, A., Marchal, J. A., Navarro-Marchal, S. A. & Galisteo-González, F. Lipid-core nanoparticles: Classification, preparation methods, routes of administration and recent advances in cancer treatment. *Advances in Colloid and Interface Science* vol. 314 Preprint at https://doi.org/10.1016/j.cis.2023.102871 (2023).

13. Kalyane, D. *et al.* Employment of enhanced permeability and retention effect (EPR): Nanoparticle-based precision tools for targeting of therapeutic and diagnostic agent in cancer. *Materials Science and Engineering C* vol. 98 1252–1276 Preprint at https://doi.org/10.1016/j.msec.2019.01.066 (2019).

14. Nel, A., Ruoslahti, E. & Meng, H. New Insights into 'permeability' as in the Enhanced Permeability and Retention Effect of Cancer Nanotherapeutics. *ACS Nano* vol. 11 9567–9569 Preprint at https://doi.org/10.1021/acsnano.7b07214 (2017).

15. Fang, J., Nakamura, H. & Maeda, H. The EPR effect: Unique features of tumor blood vessels for drug delivery, factors involved, and limitations and augmentation of the effect. *Advanced Drug Delivery Reviews* vol. 63 136–151 Preprint at https://doi.org/10.1016/j.addr.2010.04.009 (2011).

16. Kianfar, E. Protein nanoparticles in drug delivery: animal protein, plant proteins and protein cages, albumin nanoparticles. *Journal of Nanobiotechnology* vol. 19 Preprint at https://doi.org/10.1186/s12951-021-00896-3 (2021).

17. Pisal, D. S., Kosloski, M. P. & Balu-Iyer, S. V. Delivery of therapeutic proteins. *Journal of Pharmaceutical Sciences* vol. 99 2557–2575 Preprint at https://doi.org/10.1002/jps.22054 (2010).

18. Berdan, V. Y., Klauser, P. C. & Wang, L. Covalent peptides and proteins for therapeutics. *Bioorg Med Chem* **29**, (2021).

19. Bizeau, J. & Mertz, D. Design and applications of protein delivery systems in nanomedicine and tissue engineering. *Advances in Colloid and Interface Science* vol. 287 Preprint at https://doi.org/10.1016/j.cis.2020.102334 (2021).

20. Yang, Y. *et al.* Biodegradable Polymer Nanoparticles for Photodynamic Therapy by Bioluminescence Resonance Energy Transfer. *Biomacromolecules* **19**, 201–208 (2018).

21. Kim, S. *et al.* Luciferase-Rose Bengal conjugates for singlet oxygen generation by bioluminescence resonance energy transfer. *Chemical Communications* **53**, 4569–4572 (2017).

22. Correia, J. H., Rodrigues, J. A., Pimenta, S., Dong, T. & Yang, Z. Photodynamic therapy review: Principles, photosensitizers, applications, and future directions. *Pharmaceutics* **13**, (2021).

23. Dos Santos, A. F., De Almeida, D. R. Q., Terra, L. F., Baptista, M. S. & Labriola, L. Photodynamic therapy in cancer treatment - an update review. *J Cancer Metastasis Treat* **2019**, (2019).

24. Agostinis, P. *et al.* Photodynamic therapy of cancer: An update. *CA Cancer J Clin* **61**, 250–281 (2011).

25. Kim, Y. R. *et al.* Bioluminescence-activated deep-tissue photodynamic therapy of cancer. *Theranostics* **5**, 805–817 (2015).

26. So, M. K., Loening, A. M., Gambhir, S. S. & Rao, J. Creating self-illuminating quantum dot conjugates. *Nat Protoc* **1**, 1160–1164 (2006).

27. Hsu, C. Y., Chen, C. W., Yu, H. P., Lin, Y. F. & Lai, P. S. Bioluminescence resonance energy transfer using luciferase-immobilized quantum dots for self-illuminated photodynamic therapy. *Biomaterials* **34**, 1204–1212 (2013).

28. Shramova, E. I. *et al.* Genetically encoded BRET-activated photodynamic therapy for the treatment of deep-seated tumors. *Light Sci Appl* **11**, (2022).

29. Theodossiou, T. *et al. Firefly Luciferin-Activated Rose Bengal: In Vitro Photodynamic Therapy by Intracellular Chemiluminescence in Transgenic NIH 3T3 Cells 1*. *CANCER RESEARCH* vol. 63 http://aacrjournals.org/cancerres/article-pdf/63/8/1818/2513447/ch0803001818.pdf (2003).

30. Al-Ani, A. W. *et al.* Listeria innocua Dps as a nanoplatform for bioluminescence based photodynamic therapy utilizing Gaussia princeps luciferase and zinc protoporphyrin IX. *Nanomedicine* **20**, (2019).

31. Hye Kim, E. *et al. A P P L I E D S C I E N C E S A N D E N G I N E E R I N G Self-Luminescent Photodynamic Therapy Using Breast Cancer Targeted Proteins*. *Sci. Adv* vol. 6 https://www.science.org (2020).

32. Guedan, S., Ruella, M. & June, C. H. Downloaded from www.annualreviews.org Access provided by 94.73.40.35 on 11/28/23. For personal use only. *Annu. Rev. Immunol* **37**, 145–171 (2019).

33. Song, N., Scholtemeijer, M. & Shah, K. Mesenchymal Stem Cell Immunomodulation: Mechanisms and Therapeutic Potential. *Trends in Pharmacological Sciences* vol. 41 653–664 Preprint at https://doi.org/10.1016/j.tips.2020.06.009 (2020).

34. Hmadcha, A., Martin-Montalvo, A., Gauthier, B. R., Soria, B. & Capilla-Gonzalez, V. Therapeutic Potential of Mesenchymal Stem Cells for Cancer Therapy. *Frontiers in Bioengineering and Biotechnology* vol. 8 Preprint at https://doi.org/10.3389/fbioe.2020.00043 (2020).

35. Ferreira, L. M. R., Muller, Y. D., Bluestone, J. A. & Tang, Q. Next-generation regulatory T cell therapy. *Nature Reviews Drug Discovery* vol. 18 749–769 Preprint at https://doi.org/10.1038/s41573-019-0041-4 (2019).

36. Magalhaes, I. *et al.* Facing the future: challenges and opportunities in adoptive T cell therapy in cancer. *Expert Opinion on Biological Therapy* vol. 19 811–827 Preprint at https://doi.org/10.1080/14712598.2019.1608179 (2019).

37. Chen, L., Qu, J. & Xiang, C. The multi-functional roles of menstrual blood-derived stem cells in regenerative medicine. *Stem Cell Res Ther* **10**, (2019).

38. Rohit Reddy, S. *et al.* The Role of Chimeric Antigen Receptor-T Cell Therapy in the Treatment of Hematological Malignancies: Advantages, Trials, and Tribulations, and the Road Ahead. *Cureus* (2021) doi:10.7759/cureus.13552.

39. Karthikeyan, K., Babu, A., Kim, S. J., Murugesan, R. & Jeyasubramanian, K. Enhanced photodynamic efficacy and efficient delivery of Rose Bengal using nanostructured poly(amidoamine) dendrimers: Potential application in photodynamic therapy of cancer. *Cancer Nanotechnol* **2**, 95–103 (2011).

40. Dommerholt, J., Rutjes, F. P. J. T. & van Delft, F. L. Strain-Promoted 1,3-Dipolar Cycloaddition of Cycloalkynes and Organic Azides. *Topics in Current Chemistry* vol. 374 Preprint at https://doi.org/10.1007/s41061-016-0016-4 (2016).

41. Dommerholt, J., Rutjes, F. P. J. T. & van Delft, F. L. Strain-Promoted 1,3-Dipolar Cycloaddition of Cycloalkynes and Organic Azides. *Topics in Current Chemistry* vol. 374 Preprint at https://doi.org/10.1007/s41061-016-0016-4 (2016).

42. Agard, N. J., Prescher, J. A. & Bertozzi, C. R. A strain-promoted [3 + 2] azide-alkyne cycloaddition for covalent modification of biomolecules in living systems. *J Am Chem Soc* **126**, 15046–15047 (2004).

43. Wu, D. *et al.* Metal-free bioorthogonal click chemistry in cancer theranostics. *Chemical Society Reviews* vol. 51 1336–1373 Preprint at https://doi.org/10.1039/d1cs00451d (2022).

44. Yoon, H. Y., Lee, D., Lim, D. K., Koo, H. & Kim, K. Copper-Free Click Chemistry: Applications in Drug Delivery, Cell Tracking, and Tissue Engineering. *Advanced Materials* vol. 34 Preprint at https://doi.org/10.1002/adma.202107192 (2022).

45. Werengowska-Ciećwierz, K., Wiśniewski, M., Terzyk, A. P. & Furmaniak, S. The chemistry of bioconjugation in nanoparticles-based drug delivery system. *Advances in Condensed Matter Physics* vol. 2015 Preprint at https://doi.org/10.1155/2015/198175 (2015).

46. Shi, S. *et al.* Combination of Click Chemistry and Enzymatic Ligation for Stable and Efficient Protein Immobilization for Single-Molecule Force Spectroscopy. *CCS Chemistry* **4**, 598–604 (2022).

47. Kim, E. & Koo, H. Biomedical applications of copper-free click chemistry:: *In vitro*, *in vivo*, and ex vivo. *Chem Sci* **10**, 7835–7851 (2019).

48. Werengowska-Ciećwierz, K., Wiśniewski, M., Terzyk, A. P. & Furmaniak, S. The chemistry of bioconjugation in nanoparticles-based drug delivery system. *Advances in Condensed Matter Physics* vol. 2015 Preprint at https://doi.org/10.1155/2015/198175 (2015).

49. Fantoni, N. Z., El-Sagheer, A. H. & Brown, T. A Hitchhiker's Guide to Click-Chemistry with Nucleic Acids. *Chemical Reviews* vol. 121 7122–7154 Preprint at https://doi.org/10.1021/acs.chemrev.0c00928 (2021).

50. Fajardo, C. A. *et al.* Oncolytic adenoviral delivery of an EGFR-targeting t-cell engager improves antitumor efficacy. *Cancer Res* **77**, 2052–2063 (2017).

51. Blumer, M. R. *et al.* Mass Spectrometry Adduct Calculator. *J Chem Inf Model* **61**, 5721–5725 (2021).

52. Krasitskaya, V. V., Bashmakova, E. E. & Frank, L. A. Coelenterazine-dependent luciferases as a powerful analytical tool for research and biomedical applications. *International Journal of Molecular Sciences* vol. 21 1–31 Preprint at https://doi.org/10.3390/ijms21207465 (2020).

53. Woo, J. & Von Arnim, A. G. Mutational optimization of the coelenterazine-dependent luciferase from Renilla. *Plant Methods* **4**, (2008).

54. Lyons, S. K., Patrick, P. S. & Brindle, K. M. Imaging mouse cancer models *in vivo* using reporter transgenes. *Cold Spring Harbor Protocols* vol. 2013 685–699 Preprint at https://doi.org/10.1101/pdb.top069864 (2013).

55. Miles, A. J., Janes, R. W. & Wallace, B. A. Tools and methods for circular dichroism spectroscopy of proteins: A tutorial review. *Chemical Society Reviews* vol. 50 8400–8413 Preprint at https://doi.org/10.1039/d0cs00558d (2021).

56. Bouzo, B. L. *et al.* Sphingomyelin nanosystems loaded with uroguanylin and etoposide for treating metastatic colorectal cancer. *Sci Rep* **11**, (2021).

57. Nagachinta, S., Bouzo, B. L., Vazquez-Rios, A. J., Lopez, R. & de la Fuente, M. Sphingomyelin-based nanosystems (SNs) for the development of anticancer miRNA therapeutics. *Pharmaceutics* **12**, (2020).

58. Bouzo, B. L., Calvelo, M., Martín-Pastor, M., García-Fandiño, R. & De La Fuente, M. *In Vitro*- In Silico Modeling Approach to Rationally Designed Simple and Versatile Drug Delivery Systems. *Journal of Physical Chemistry B* **124**, 5788–5800 (2020).

59. Díez-Villares, S. *et al.* Quantitative PET tracking of intra-articularly administered 89Zr-peptide-decorated nanoemulsions. *Journal of Controlled Release* **356**, 702–713 (2023).

60. Saraiva, S. M. *et al.* Edelfosine nanoemulsions inhibit tumor growth of triple negative breast cancer in zebrafish xenograft model. *Sci Rep* **11**, (2021).

61. Wang, L., Jiang, R., Wang, L., Liu, Y. & Sun, X. L. Preparation of chain-end clickable recombinant protein and its bio-orthogonal modification. *Bioorg Chem* **65**, 159–166 (2016).

62. Weber, C. *et al.* Functionalization of Liposomes with Hydrophilic Polymers Results in Macrophage Uptake Independent of the Protein Corona. *Biomacromolecules* **20**, 2989–2999 (2019).

63. Kim, A., Ng, W. B., Bernt, W. & Cho, N. J. Validation of Size Estimation of Nanoparticle Tracking Analysis on Polydisperse Macromolecule Assembly. *Sci Rep* **9**, (2019).

64. Filipe, V., Hawe, A. & Jiskoot, W. Critical evaluation of nanoparticle tracking analysis (NTA) by NanoSight for the measurement of nanoparticles and protein aggregates. *Pharm Res* **27**, 796–810 (2010).

65. Galdino, F. E., Picco, A. S., Capeletti, L. B., Bettini, J. & Cardoso, M. B. Inside the Protein Corona: From Binding Parameters to Unstained Hard and Soft Coronas Visualization. *Nano Lett* **21**, 8250–8257 (2021).

66. Kokkinopoulou, M., Simon, J., Landfester, K., Mailänder, V. & Lieberwirth, I. Visualization of the protein corona: Towards a biomolecular understanding of nanoparticle-cell-interactions. *Nanoscale* **9**, 8858–8870 (2017).

67. Chantada-Vázquez, M. D. P. *et al.* Protein corona gold nanoparticles fingerprinting reveals a profile of blood coagulation proteins in the serum of her2-overexpressing breast cancer patients. *Int J Mol Sci* **21**, 1–18 (2020).

68. Ilgen, J., Kaltschnee, L. & Thiele, C. M. A pure shift experiment with increased sensitivity and superior performance for strongly coupled systems. *Journal of Magnetic Resonance* **286**, 18–29 (2018).

69. Pelta, M. D., Morris, G. A., Stchedroff, M. J. & Hammond, S. J. A one-shot sequence for high-resolution diffusion-ordered spectroscopy. *Magnetic Resonance in Chemistry* **40**, (2002).

70. Schulze-Sünninghausen, D., Becker, J., Koos, M. R. M. & Luy, B. Improvements, extensions, and practical aspects of rapid ASAP-HSQC and ALSOFAST-HSQC pulse sequences for studying small molecules at natural abundance. *Journal of Magnetic Resonance* **281**, 151–161 (2017).

71. Purusottam, R. N., Bodenhausen, G. & Tekely, P. Quantitative one- and two-dimensional 13C spectra of microcrystalline proteins with enhanced intensity. *J Biomol NMR* **57**, 11–19 (2013).

72. Paruzzo, F. M. & Emsley, L. High-resolution 1H NMR of powdered solids by homonuclear dipolar decoupling. *Journal of Magnetic Resonance* **309**, (2019).

73. Moore, T. L. *et al.* Nanoparticle colloidal stability in cell culture media and impact on cellular interactions. *Chem Soc Rev* **44**, 6287–6305 (2015).

74. Milton Harris, J. & Chess, R. B. Effect of pegylation on pharmaceuticals. *Nature Reviews Drug Discovery* vol. 2 214–221 Preprint at https://doi.org/10.1038/nrd1033 (2003).

75. Veronese, F. M. & Mero, A. *The Impact of PEGylation on Biological Therapies. Biodrugs* vol. 22 (2008).

76. Lee, G. Y. & Han, S. N. The role of vitamin E in immunity. *Nutrients* vol. 10 Preprint at https://doi.org/10.3390/nu10111614 (2018).

77. Welson, N. N. *et al.* Vitamin E protects against gabapentin-induced chronic hepatic and renal damage associated with the inhibition of apoptosis and tissue injury in rats. *Life Sci* **267**, (2021).

78. Villalón-García, I. *et al.* Vitamin E prevents lipid peroxidation and iron accumulation in PLA2G6-Associated Neurodegeneration. *Neurobiol Dis* **165**, (2022).

79. Neophytou, C. M. & Constantinou, A. I. Drug delivery innovations for enhancing the anticancer potential of vitamin e isoforms and their derivatives. *BioMed Research International* vol. 2015 Preprint at https://doi.org/10.1155/2015/584862 (2015).

80. Abu-Fayyad, A. & Nazzal, S. Gemcitabine-vitamin E conjugates: Synthesis, characterization, entrapment into nanoemulsions, and in-vitro deamination and antitumor activity. *Int J Pharm* **528**, 463–470 (2017).

81. Slotte, J. P. & Ramstedt, B. The functional role of sphingomyelin in cell membranes. in *European Journal of Lipid Science and Technology* vol. 109 977–981 (2007).

82. Jarc, E. & Petan, T. *Lipid Droplets and the Management of Cellular Stress. YALE JOURNAL OF BIOLOGY AND MEDICINE* vol. 92 (2019).

83. Jaishy, B. & Abel, E. D. Thematic review series: Lipotoxicity: Many roads to cell dysfunction and cell death lipids, lysosomes, and autophagy. *Journal of Lipid Research* vol. 57 1619–1635 Preprint at https://doi.org/10.1194/jlr.R067520 (2016).

84. Su, L. J. *et al.* Reactive Oxygen Species-Induced Lipid Peroxidation in Apoptosis, Autophagy, and Ferroptosis. *Oxidative Medicine and Cellular Longevity* vol. 2019 Preprint at https://doi.org/10.1155/2019/5080843 (2019).

85. Scha. Lipotoxicity: when tissues overeat. *Curr Opin Lipidol* 281–287 (2003) doi:10.1097/01.mol.0000073508.41685.7f.

86. Nagachinta, S. *et al.* Radiolabelling of lipid-based nanocarriers with fluorine-18 for *in vivo* tracking by PET. *Colloids Surf B Biointerfaces* **188**, (2020).

87. Díez-Villares, S. *et al.* Biodistribution of 68/67Ga-radiolabeled sphingolipid nanoemulsions by pet and spect imaging. *Int J Nanomedicine* **16**, 5923–5935 (2021).

88. Dragulescu-Andrasi, A., Chan, C. T., De, A., Massoud, T. F. & Gambhir, S. S. Bioluminescence resonance energy transfer (BRET) imaging of protein-protein interactions within deep tissues of living subjects. *Proc Natl Acad Sci U S A* **108**, 12060–12065 (2011).

89. Couturier, C. & Deprez, B. Setting up a bioluminescence resonance energy transfer high throughput screening assay to search for protein/protein interaction inhibitors in mammalian cells. *Front Endocrinol (Lausanne)* **3**, 1–13 (2012).

90. Bhuckory, S., Kays, J. C. & Dennis, A. M. *In vivo* biosensing using resonance energy transfer. *Biosensors* vol. 9 Preprint at https://doi.org/10.3390/bios9020076 (2019).

91. Zhao, W. *et al.* Tert-butyl hydroperoxide (t-BHP) induced apoptosis and necroptosis in endothelial cells: Roles of NOX4 and mitochondrion. *Redox Biol* **11**, 524–534 (2017).

92. Montano, R. *et al. Cell Cycle Perturbation Induced by Gemcitabine in Human Tumor Cells in Cell Culture, Xenografts and Bladder Cancer Patients: Implications for Clinical Trial Designs Combining Gemcitabine with a Chk1 Inhibitor*. www.impactjournals.com/oncotarget (2017).

93. Namima, D. *et al.* The Effect of Gemcitabine on Cell Cycle Arrest and microRNA Signatures in Pancreatic Cancer Cells. *In Vivo (Brooklyn)* **34**, 3195–3203 (2020).

Chapter III

Versatile and efficient protein association through chemically modified Sphingomyelin Nanosystems (SNs) for enhanced delivery

Versatile and efficient protein association through chemically modified Sphingomyelin Nanosystems (SNs) for enhanced delivery

ABSTRACT

Proteins are biological macromolecules well known to regulate many cellular signaling mechanisms. For instance, they seem to be very appealing for its application as therapeutics agents presenting high specificity and activity. Nonetheless, they suffer from unfolding, instability and low bioavailability that make their administration through systemically and other routes very tough. To overcome these drawbacks, drug delivery systems and nanotechnology has arisen to deliver biomolecules in a sustained manner and, at the same time increasing dose availability, protecting the cargo without compromising proteins bioactivity, and enhancing intracellular delivery. In this work, we proposed the optimization of sphingomyelin nanosystems (SNs) for the delivery of a wide collection of proteins (ranging 10-500 kDa and pI) using diverse chemical association strategies. We have further characterized SNs by varied analytical methodologies. We have also carried out *in vitro* experiments to validate the potential of the developed formulations. As the final goal, we aim to obtain evidence of the potential use of SNs for the development of protein therapeutics.

INTRODUCTION

Proteins are biomacromolecules that exist in a broad range of biological processes such as activation/inhibition of signaling pathways, molecular recognition, biocatalysis and protection, features that make them promising therapeutic agents. Indeed, their higher affinity and targeting specificity compared to small molecule drugs is presented as a perfect alternative treatment choice. In addition, proteins endogenous nature ensures biocompatibility and biodegradability, as their degradation products (amino acids) are well known and excreted by the body, reducing potential toxicity. Furthermore, the appearance of engineering technologies enables the modification of their properties improving their functional activity and biological stability [1–4]. So, proteins seem to be very attractive pharmaceutical therapeutics. However, problems related to protein unfolding, enzymatic degradation in biological systems, short half-life, poor or no membrane permeability and low bioavailability in parenteral and non-parenteral routes, hampers their efficient administration and exploitation in therapeutics [5]. For instance, more than 130 protein therapeutics have been approved by the Food and Drug Administration (FDA), but most of them are based in naked enzymes or mAb depending on a continuous administration and mainly used in immunotherapies or metabolic disorders [6]. Such challenges make drug delivery systems an urgent and needed tool. Since the 70's to date, much research has arisen on the field of drug delivery and nanotechnology to overcome these drawbacks. Thus, nano-vehicles have emerged to protect, carry, deliver, and release these biomolecules in a controlled manner, increasing bioavailability and without compromising their bioactivity [7–9].

Liposomes were proposed as the first nanocarriers for protein delivery, specifically for albumin and *Aspergillus niger* amyloglucosidase [8,10]. Subsequent developments in the 90's included polyalkylcyanoacrylate nanocapsules as carriers for orally administering insulin [11], and peptide-loaded solid lipid nanoparticles for delivering thymopentin and D-Trp-6-LHRH (Triptorelin) [12,13]. There has also been progress in the development of polymeric nanoparticles made of PLGA, PLA-PEG, and chitosan for delivering proteins and antigens [14,15]. Nevertheless, the current trend has shifted towards employing less complex formulations and easily scalable production techniques to revolutionize the translational potential of these delivery vehicles for clinical use. Indeed, the challenge persists in developing efficient nanostructures for protein delivery, as evidenced by the limited number of therapies that have been successfully brought into market to date [16–19].

In this context, this study is focused on the optimization of biodegradable and versatile SNs for the delivery of a variety of proteins. SNs are non-toxic and biocompatible nanocarriers [20] that have proved their potential for the delivery of anticancer drugs [21], oligos[22] and peptides[23], but the delivery of proteins has not been attempted to date.

The aim of this approach is to provide a novel type of nanocarrier with potential to formulate protein therapeutics following a versatile and translatable approach. The versatility of SNs for protein delivery will be investigated by associating proteins with a wide range of MW (10-500 kDa) and diverse isoelectric points (pI) and therapeutic activities.

The composition of SNs will be adapted to incorporate functional groups exposed to the nanoparticle surface, to allow establishing different chemical linking strategies. For that, a set of chemical reactions will be explored, such as SPAAC and Thiol-maleimide copper-free "click chemistry" reactions, active ester, and amide condensation [24,25]. Click chemistry has evolved as a change of paradigm in the biomedical field, showing that artificial chemical reactions can occur outside of the laboratory in a controllable manner in living systems. Indeed, it is an excellent technique for its application in drug delivery systems and multi-step organic synthesis since it offers fast, simple, and highly selective reactions that are well-suited for the modification of the drug delivery systems and the capture and release of payloads [26,27]. Association by electrostatic interactions will also be attempted upon inclusion positive or negative charged lipids into SNs composition. Functionalized SNs and protein-loaded SNs (P-SNs) will be fully characterized. In addition, cell culture experiments will allow determining intracellular delivery and cytotoxicity, as a first step for validation of the technology for the development of innovative protein therapeutics

MATERIALS AND METHODS

Materials

Vitamin E (DL-α-Tocopherol) was purchased from Sigma (Merck, Darmstadt, Germany). Sphingomyelin (Lipoid E SM) was kindly provided by Lipoid GmbH (Ludwigshafen, Germany). Surfactant lipids DSPE-PEG(2k)-X (X = DBCO; Maleimide; NHS), 18:1 TAP (DOTAP) cationic lipid, 16:0 PG (DPPG) anionic lipid and fluorescent labelling lipids, C11 TopFluor® Sphingomyelin and C16 Cy5 SM were acquired in Avanti Polar Lipids (Croda International Plc., Alabama, USA). Azido-dPEG®$_8$-NHS ester and TFP-dPEG$_{13}$-DSPE lipid were purchased in Merck (Darmstadt, Germany). HPLC-grade Acetonitrile (ACN), Ethanol (EtOH), Isopropanol (IPA) and Water were obtained from Fisher Chemicals (Thermo Fisher Scientific, USA). All other chemicals used were HPLC or UPLC purity grade.

Azide-modified protein (N3-protein) preparation and characterization, for SPAAC click chemistry reaction

Proteins (0.03 μmol) were modified with Azido-dPEG®$_8$-NHS linker (0.6 μmol) (Sigma, Darmstadt, Germany) in phosphate buffer saline (PBS; 2mM, pH 7.4). Reaction was performed at room temperature (RT) for 6 hours and storage at 4ºC. Linker excess was eliminated using spin filters (Amicon® Ultra Centrifugal Filters, 10k, 0,5mL, Merck). For bioluminescent and fluorescent naked proteins and N3-proteins (RLuc8, FLuc, GFP and R-PE) activities were tested in different calibrated luminometer and fluorimeter (SYNERGY H1, microplate reader, BioTek; Victor NivoTM, multimode plate reader, PerkinElmer). Samples of RLuc8 (0.1μM of enzyme) were mixed with the correspondent activating substrate (10 μM Coelenterazine, CTZ, ThermoFisher Scientific, USA) in 100 μL sodium phosphate dibasic and incubated 5 minutes in the dark before measurement. In the case of FLuc, samples were mixed with ATP (15 nmol) and D-Luciferin (40 pmol) per enzyme unit. For fluorescent proteins, 0.5 μg/100μL buffer were placed in a black bottomed and walls multiwell 96 plate and measured by triplicate.

N3-protein modification was characterized by HPLC-MS (5 pmol) dissolved in ultrapure water. Equipment TimsTof Pro (Bruker) coupled to the ELUTE UHPLC. Analysis method used was positive ESI ionization, acquisition range 500-3000 m/z, chromatographic separation with column C4, mobile phases employed were A: Water/formic acid 0.1%, B: acetonitrile/formic acid 0.1%;

and chromatographic separation time 17 minutes. MALDI-Tof analysis was carried out in Ultraflex III TOF/TOF (Bruker Daltonics, Bremen, Germany), analysis method chosen was MALDI linear mode ionization using a SA matrix (Sinapinic Acid). Naked proteins were also tested.

Protein-loaded sphingomyelin nanoemulsions (P-SNs) preparation and purification method

Briefly, vitamin E (5 mg, Sigma, Darmstadt, Germany), sphingomyelin (0.5 mg, Lipoid GmbH, Ludwigshafen, Germany) and surfactants DSPE-PEG(2000)-X (0.05 mg, Avanti Polar Lipids, Croda International Plc., Alabama, USA; X=functional reactive group, i.e. DBCO, maleimide, or NHS) having a lipid ratio 1:0.1:0.01 w/w were dissolved in 100 μL of absolute ethanol. SNs were instantaneously formed by injecting the organic phase into 0.9 mL of ultrapure water, at RT.

- For SPAAC and Thiol-maleimide click chemistry (DBCO, MAL) and active ester (NHS, TFP) reactions, protein solution (naked or N3-proteins) was brought to a final volume of 500 μL in PBS buffer, 2 mM, pH 7.4, added dropwise to SNs and incubated at RT for 4-6 hours followed by an overnight (O/N) incubation at 4ºC.
- In the case of amide condensation (COOH), the reaction was incubated for 2 hours via EDC coupling and subsequently purified.
- For electrostatic interactions (DOTAP, DPPG), upon protein addition, solution was led to interact for 20-30 minutes prior to characterization and later use.

The purification of P-SNs was carried out by spin filters (Amicon® Ultra Centrifugal Filters, 100k, 0.5mL, Merck) in a refrigerated microcentrifuge (5417R; Eppendorf). The spin filters were first pre-washed with 500 μL PBS 2 mM at 6000g for 5 min to wet and hydrate the filter before starting the process. P-SNs were transferred to the spin filters and 200 μL of PBS was added and centrifuged for 3 min, at 4°C and 3000g. Four washes were made with 200 μL of PBS each, centrifuging as described above. Finally, P-SNs were collected with 50 μL of PBS buffer, centrifuged 2 min, at 4°C and 1000*xg*. This method was applied to proteins whose MW ranged among 10-60 kDa.

Physicochemical and Morphological Characterization

Particle size and polydispersity index (PdI) were determined by Dynamic Light Scattering (DLS), and Z-potential values by Laser Doppler Anemometry (LDA), using a Zetasizer NanoZS (Malvern Instruments, UK). Samples were diluted to 1:10 with ultrapure water and the measurements were performed at 25ºC with a detection angle of 173º. All data is expressed as a mean value ± standard deviation (SD). Formulations were evaluated for their stability in relevant biological media to ensure the maintenance of their properties during *in vitro* and *in vivo* assays. Formulations were incubated at 37ºC with 10% FBS supplemented DMEM and RPMI under orbital shaking.

SNs and P-SNs morphology was observed by Field Emission Scanning Electron Microscopy (FESEM) using a ZEISS FESEM ULTRA Plus, microscope (Carl Zeiss Micro Imaging, GmbH, Germany) configured with InLens and STEM modes and operating at 20 kV. So, 20 μL (0.55 mg/mL) of filtered nanosystems were stained with phosphotungstic acid (2% w/v) ratio 1:1. Next, 10 μL were placed on a carbon coated grid and left for 30s, twice. The grid was allowed to dry and then, washed repeatedly with filtered ultrapure water. Finally, it was let dry until its visualization.

Preparation of Cy5 and TopFluor® labelled P-SNs

Fluorescent labelled SNs and P-SNs were prepared as previously described in the previous section "Protein-loaded sphingomyelin nanoemulsions (P-SNs) preparation and purification method", upon inclusion of TopFluor®SM (4,5 μg; Avanti Polar lipids, Sigma, Darmstadt, Germany) or C16 Cy5 SM (4,5 μg; Avanti Polar lipids, Sigma, Darmstadt, Germany) in the lipid mixture (final volume of 100 μL) prior formulation.

Cell culture conditions

Pancreatic adenosquamous carcinoma derived from metastatic liver L3.6pl (RRID: CVCL_0384), were maintained in DMEM HG medium (Dulbecco's Modified Eagle's Medium-High glucose, Sigma-Aldrich) supplemented with 10% fetal bovine serum (Gibco®, LifeTecnologies) and 1% with antibiotic (penicillin and streptomycin, Sigma-Aldrich). L3.6pl Cells were provided by Dr. Bruno Sainz (UAM-CSIC). Human cervical carcinoma HeLa cells (ATCC® CCL-2™) were acquired from ATCC. Cell lines were kept in an atmosphere at 5% CO2, 37°C, in high relative humidity. All were tested for Mycoplasma, giving negative results.

Cellular internalization

Cellular uptake was evaluated through different methods.

For evaluation of RLu8-SNs, $7x10^4$ L3.6pl cells per well were seeded in 24-multiwell plates and growth O/N. Then, SNs (0.01 mg/mL) were added and incubated for 2 hours. Treatment was then removed, cells were lysed, and total protein was extracted. To detect the presence of RLuc8-SNs, bioluminescence was tested after RLuc8 activation with colenterazine (40 μM per well of a solution of 1mg/mL in propylene glycol) and measured in a luminometer (SYNERGY H1, microplate reader, BioTek).

For evaluation of GFP-SNs internalization, cells were observed by Confocal Microscopy (Confocal Laser Microscopy Leica SP5®), $6x10^4$ cells per well were seeded in 8-chamber slide plate and growth O/N. Then, labelled SNs (0.2 mg/mL) were added, and internalization was studied after 2 hours. After incubation, treatment was removed. Cells were visualized in fresh DPBS.

Results were verified by Flow Cytometry (FACS Aria IIu de BD) in L3.6pl and HeLa cells at 2h. For that, $5x10^5$ cells per well were seeded in 6-multiwell plates and growth O/N. Next, different type of labelled nanosystems (0.5 mg/mL) treatment were added to cells, and after incubation, cells were washed with 3x DPBS and fixed with 2% PFA.

X-GAL assay

L3.6pl at a density of $7x10^4$ cells per well were seeded in 24-multiwell plates and growth O/N. Next, B-GAL-SNs (0,15 mg/mL SNs; 2 μg B-GAL) were added and incubated for 2 hours. Treatment was removed, cells were washed twice with 1X DPBS and fixed with 2% v/v PFA; 0,2% v/v Glutaraldehyde (15 min). Add X-GAL staining solution and incubate O/N at 37ºC in darkness. Cells were then washed twice with 1X DPBS and stored at 4ºC.

Cell viability assays

For cytotoxicity studies, L3.pl6 cells were seeded into a clear-bottomed and black walls at a density of $2.5x10^4$ cell/well and incubated for 24h. Different prototypes of SNs were incubated at increasing concentrations at different time points. Cell viability was determined using a 1:10 dilution Alamar blue fluorescence assay and results were read using a Victor Nivo™ multimode plate reader at an excitation of 530 nm and emission of 590 nm. Data were normalized to negative control 100% viability and reagent itself used as fluorescence background.

Statistical analysis

Data are expressed as mean ± standard deviation (SD). Statistical analyses were performed with a GraphPad Prism® Software (version 9.0). Significant differences were compared and analyzed by two-tailed, Student t-test. P-values <0.05 were considered statistically significant. Statistical analyses p > values meaning; * ($p < 0.05$), ** ($p < 0.005$), *** ($p < 0.0005$) and **** ($p < 0.0001$). All experiments were performed at least in triplicate.

RESULTS AND DISCUSSION

Synthesis and characterization of SNs and P-SNs

SNs were prepared by adapting the ethanol injection method previously optimized by our group for the preparation of nanometric emulsions on a single step [20,22,23,28–31] allowing the straightforward formation of the SNs (**Fig. 1a**) containing either lipid-PEG derivatives (**Table 1**) or charged lipids (**Table 1**), necessary for the different protein-binding strategies (**Fig. 1b**). The functional reactive groups (**Table 1**) will be exposed onto the surface of the SNs and will react with the proteins of interest. PEG-lipids were analyzed by MALDI-Tof to perfectly calculate their mass to react to proteins and if they were properly preserved at storage (**Fig. S1a-c**). SNs were characterized physicochemically in terms of their size, polydispersity index and surface charge by Dynamic Light Scattering (DLS) and Laser Doppler Anemometry (LDA) (**Table S1**).

To perform SPAAC "click chemistry" reaction, native proteins had to be previously functionalized with an azide-linker, to obtain N3-proteins (**Fig. S2**). Then, several proteins (and N3-proteins) as represented in **figure 2,** were added carefully and dropwise onto preformed SNs. The resulting P-SNs were further characterized.

Table 1. Disclosure of lipid-PEG derivatives and charged lipids employed to prepared P-SNs. Abbreviations: P-SNs: Protein-loaded sphingomyelin nanoemulsions.

Lipid	Name	Active group	Chemical association
PEG-derivative	DSPE-PEG(2k)-DBCO	DBCO	SPAAC click chemistry
PEG-derivative	DSPE-PEG(2k)-Maleimide	MAL	Thiol-maleimide click chem.
PEG-derivative	DSPE-PEG(2k)-NHS	NHS	Active ester
PEG-derivative	TFP-dPEG$_{13}$-DSPE	TFP	Active ester
PEG-derivative	DSPE-PEG(2k)-COOH	COOH	Amide condensation
Charged (cationic)	18:1 TAP	DOTAP	Electrostatic interactions
Charged (anionic)	16:0 PG	DPPG	Electrostatic interactions

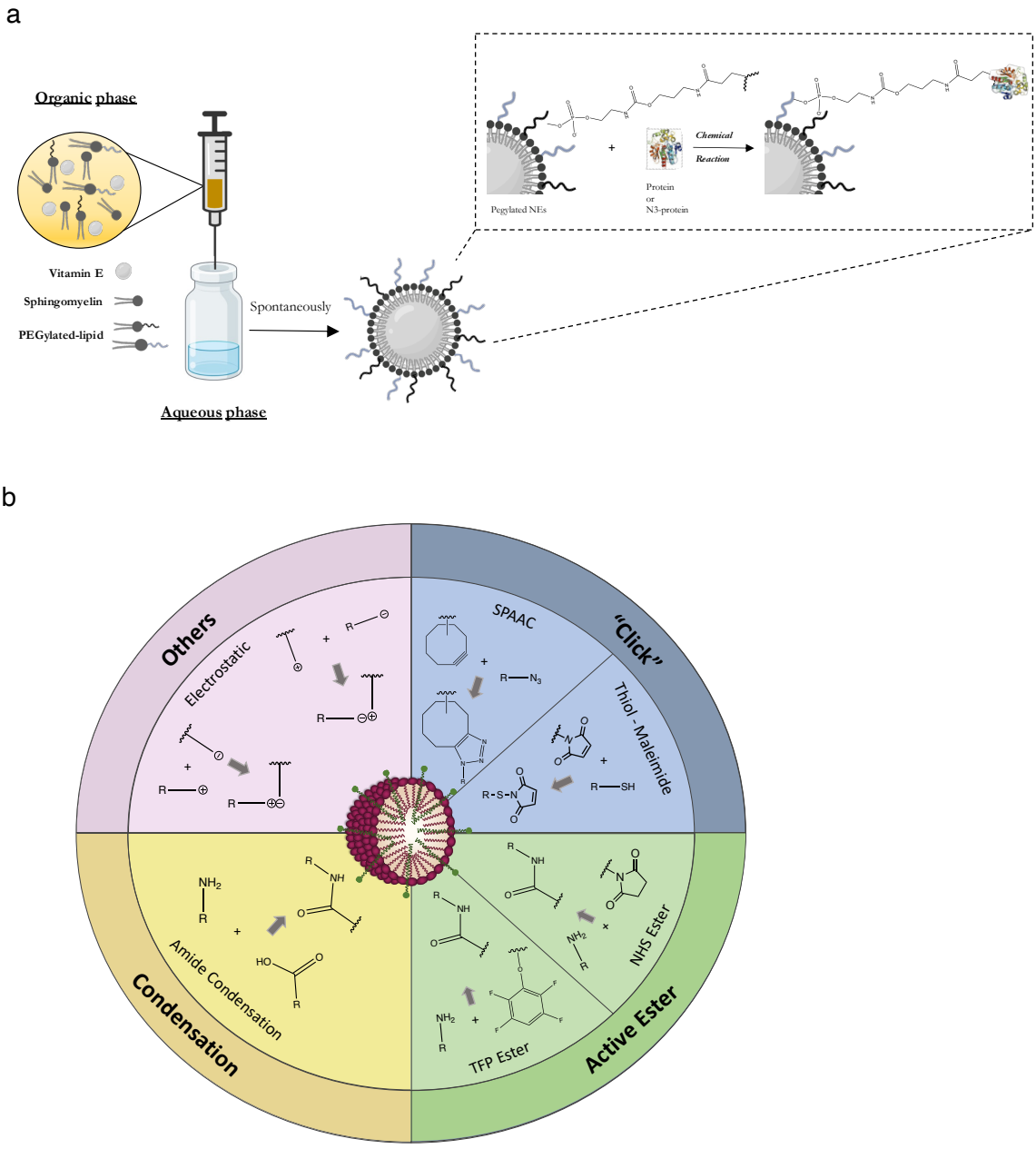

Figure 1. (a) Representation of the preparation methodology of SNs, and subsequent chemical association of proteins. **(b)** Detailed scheme describing the chemical toolbox employed to perform the different chemical strategies, namely, "click" chemistry, active ester, condensation, and electrostatic interactions, proposed to associate the proteins to SNs and form P-SNs.

Protein	Representation	MW (kDa)	pI
Anakinra (Ank)		17.3	5.46
GFP		28.7	~6.00
RLuc8		36.9	8.26
Ovalbumin (OVA)	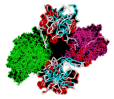	44.2	4.50
FLuc	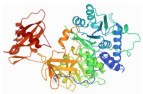	62.0	6.42
R-Phycoerythrin	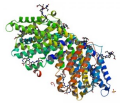	250	5.60
β-Galactosidase (β-Gal)	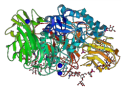	465	4.60

Figure 2. Scheme of the different proteins linked to SNs organized by increasing MW. The isoelectric point (pI) varied depending on each protein. We propose the association of enzymes (ANK and β-Gal), bioluminescent enzymes (RLuc8 and FLuc) and fluorescent proteins (GFP and PE), and immunogenic proteins (OVA), to evaluate the versatility of SNs and the formulation process to efficiently deliver P-SNs (protein-loaded SNs).

Association of the enzymes RLuc8, FLuc and β-galactosidase

(i) RLuc8 and FLuc

First, activity measurements were carried out to native RLuc8 and N3-RLuc8. Thus, HPLC-MS and MALDI-Tof analysis were performed to both forms of the enzyme showing complete functionalization and the exact enzyme mass was calculated (**Fig. 3a**). Bioluminescence was measured for native- and N3-protein to ensure that modification and association to SNs did not affect activity (**Fig. 3b**). Structure and activity were also evaluated by circular dichroism (CD) for native- and N3-RLuc8, observing conserved features as explained in "Chapter II". RLuc8-SNs

were characterized for their physicochemical properties in terms of size, surface charge, and polydispersity index (**Table 2)**. Colloidal stability was assessed at storage conditions through time (**Fig. 3c**). The most promising formulation in terms of size stability was RLuc8-SNs(DBCO), which maintained a constant size up to a year. The rest of the formulations were not stable as size was increased to values higher than 300 nm at time point measured at 12 months. Stability in cell culture medium supplemented with 10% FBS was also carried out for later cellular experiments (**Fig. S3a**). RLu8-SNs remained stable for the evaluated time in all formulations tested.

Table 2. Physicochemical Characterization of RLuc8-SNs prepared by different chemical associations. Percentage of RLuc8 linked to SNs (Results are expressed as Mean ± Standard Deviation, n = 5). Abbreviations: nm: nanometer, PdI: polydispersity index, ZP: zeta potential in millivolts (mV).

Formulation	Ratio	Size (nm)	PdI	ZP (mV)	RLuc8 % Associated
VitE:SM:DBCO	1:0.1:0.01	165 ± 4	<0.1	- 26 ± 1	95 ± 3
VitE:SM:MAL	1:0.1:0.01	196 ± 9	0.2	- 25 ± 2	87 ± 2
VitE:SM:NHS	1:0.1:0.01	179 ± 2	0.2	- 20 ± 1	86 ± 1
VitE:SM:TFP	1:0.1:0.01	191 ± 6	0.1	- 26 ± 3	89 ± 2
VitE:SM:COOH	1:0.1:0.01	211 ± 6	0.1	- 26 ± 2	86 ± 2
VitE:SM:DPPG	1:0.1:0.01	198 ± 8	<0.3	- 13 ± 5	20 ± 4

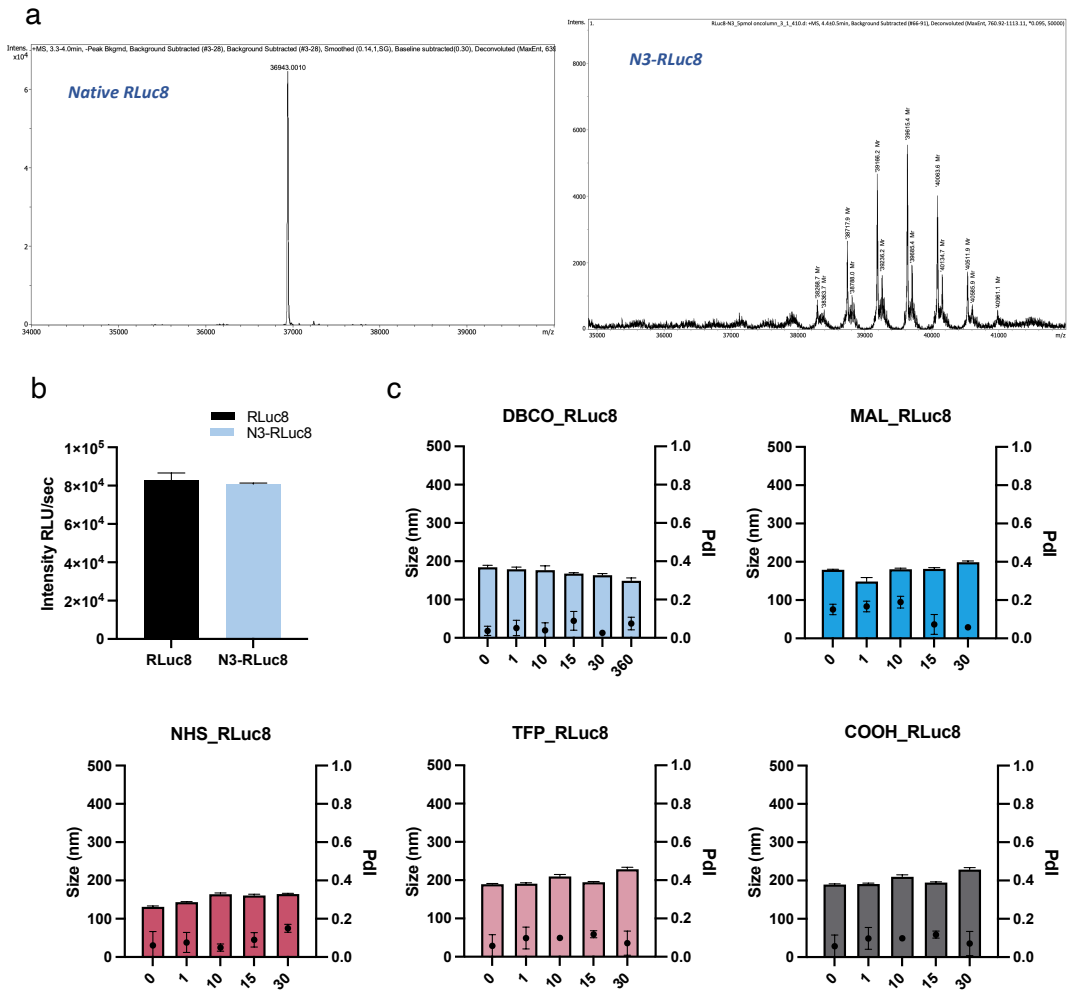

Figure 3. RLuc8-SNs. **(a)** HPLC-MS of native and N3-RLuc8 to evaluate the functionalization with the azide-linker. **(b)** RLuc8 bioluminescent activity measured in Intenstity/sec of RLuc8 and N3-RLuc8 (1 μg) after coelenterazine activation (0.5 μg). **(c)** Colloidal stability of the different P-SNs formulations that associate RLuc8 by different strategies, DBCO-RLuc8 measured over a year and the rest of the RLuc8-SNs (MAL; NHS; TFP; COOH) upon 30 days at storage conditions (4ºC). (n=5, data expressed as mean ± SD).

RLuc8-SNs were purified by spin filters, to allow direct determination of the percentage of protein efficiently associated to SNs. The efficacy of the purification method was assessed by SDS-PAGE electrophoresis gel; at day 0, no free RLuc8 remained in the preparations (**Fig. 4a**). The absence of free RLuc8, was confirmed after one year of storage at 4ºC (**Fig. S3b**). The bioluminescence of purified RLuc8-SNs was measured at different time points, from 0 to 6 months, except in the case of RLuc8-SNs(DBCO). Results show that the SNs that linked the protein through the SPAAC click chemistry reaction, i.e. RLuc8-SNs(DBCO), rendered the best

results, and light emission was maintained with comparable intensity for up to a year (**Fig. 4b**). This can be explained by the type of bond formed that it is very stable and difficult to alter. For the other formulations, light fainted at 6 months, being this the end-point for evaluation. This could be related to their poorest colloidal stability (as mentioned, aggregation occurred over time with an increase in size above > 300 nm). Overall, RLuc8-SNs presented good colloidal stabilities over time and light activity. RLuc8-SNs have demonstrated to protect RLuc8 from degradation processes and to preserve protein structures, conformation, and activity. However, RLuc8-SNs(DBCO) have shown more promising results compared to the other prototypes (a year vs 6 months).

RLuc8-SNs were next tested *in vitro*. RLuc8-SNs were incubated with L3.6pl to test internalization. Total protein content was then extracted, and internalized RLuc8 activated with the CTZ substrate to observe luminescence (**Fig. 4c**). RLuc8-SNs(DBCO). Results have shown that RLuc8-SNs(DBCO) achieved a higher internalization rate compared to the other prototypes after 2h incubation in L3.6pl cells. Although, other prototypes (COOH, MAL and NHS) also obtained a considered internalization. Cellular internalization images of fluorescently labelled empty SNs(DBCO) and RLuc8-SNs(DBCO) (labelled with TopFluor®SM) in L3.6pl were acquired by Confocal Laser Microscopy (CLM) to observe possible interferences in cell uptake due to the linked protein located at the nanoparticle surface. Two hours post-treatment, all samples were successfully internalized, and slightly enhanced uptake was reached in RLuc8-SNs(DBCO) (**Fig. S4**). Interestingly, the superior behavior of RLuc8-SNs(DBCO) confirmed the potential of this strategy for the development of innovative therapeutics as described and discussed in the "Chapter II" of this thesis. So, RLuc8-SNs(DBCO) in general rendered the most promising results over P-SNs formulations prepared with the alternative binding strategies, Importantly, RLuc8 linked by electrostatic interactions did not show great results being excluded. Notably, it must be remarked that activity and glycosylation patterns of the protein were preserved.

In the literature, we could not find published reports with the same approach of lipid-based nanoparticles with its surface decorated with proteins. In the field of inorganic nanoparticles, AuNPs have arisen as a tool to associate antibodies or peptides onto their surface for targeting purposes. Other example are the metallic quantum dots linked to RLuc8 used in the "chapter I". However, the clinical translation of inorganic nanoparticles has been limited due to establishment of safety and efficacy investigation of reliable scale-up methods [32]. Regarding organic nanoparticles, most of the published reports are based on the entrapment of proteins in hydrogels, polymeric

nanocapsules and nanoparticles, polymersome and liposomes. In the context of surface-decoration, most of the research is moving towards antibodies or peptides ligation or the formation of nanocapsules [33–35]. However, in our approach we have efficiently incorporated proteins to the SNs surface without compromising their structure and activity. In addition, the oil core of SNs can be loaded with other molecules such as small drugs (chapter II) and *[confidential section]* (chapter V).

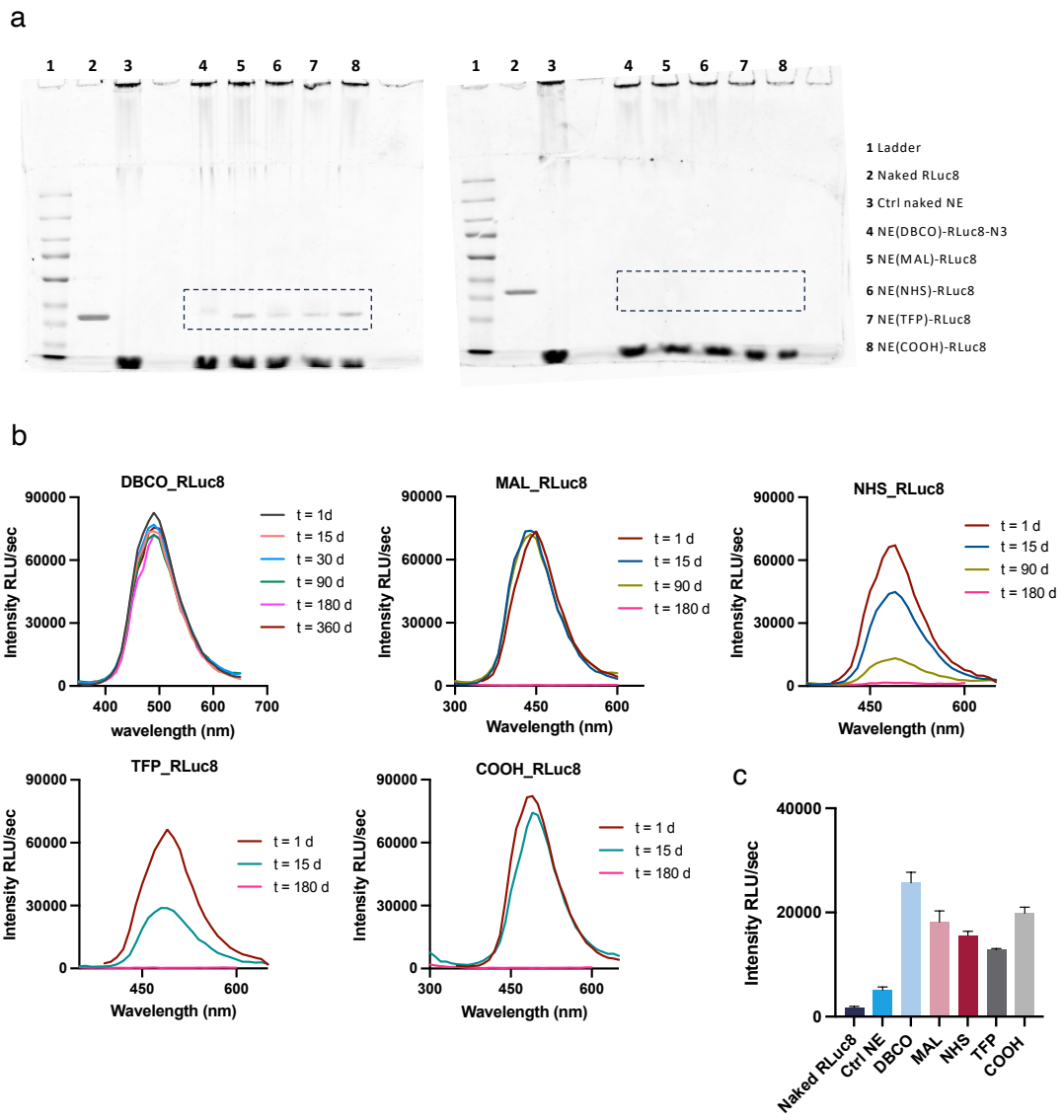

Figure 4. (a) Evaluation of the purification method by SDS-PAGE electrophoresis at day 0 pre- and post- purification. **(b)** Evaluation of SNs light activity at different times points at storage conditions (4ºC) since day 0 until day 180 (except for SNs(DBCO), which was determined until day 360). **(c)** RLuc8 luminescence intensity after cellular uptake

of RLuc8-loaded SNs (2h incubation at 37ºC in L3p cells), evaluated in the cell lysate after activation with the substrate coelenterazine (40 μM), (n=5, data expressed as mean ± SD).

To confirm the obtained results, a second bioluminescent enzyme, FLuc, was also linked to SNs(DBCO). Briefly, we tested its activity and physicochemical properties. N3-FLuc modification was evaluated by HPLC-MS. Colloidal stability at storage was measured upon 15 days for FLuc-SNs(DBCO) maintaining size and PdI (**Table S2**). Bioluminescent activity of native FLuc, N3-FLuc and FLuc-SNs(DBCO) was assessed after FLuc activation with D-Luciferin in the presence of ATP and O_2. Finally, % of FLuc associated to SNs(DBCO) was quantified in 94% by microBCA assay. Overall, results were comparable to previous data with the RLuc8 formulations in terms of physicochemical properties and activity, thus offering a bioluminescent formulation with a different wavelength emission for a versatile use (**Figure S5**).

Results have shown the great potential of this strategy for enzyme association. RLuc8-SNs was in-depth characterized and studied for its application in photodynamic therapy (Chapter II). This opens the doors not only to its application in PDT (Chapter II), but also to enzyme replacement therapies.

(ii) Beta-galactosidase (β-GAL).

β-galactosidase is a big enzyme with a MW of 465 kDa that catalyzes the hydrolysis of β-D-galactose into β-D-galactosidase substrates, such as lactose, keratin sulfates, sphingolipids, etc [36]. Deficiency of β-galactosidase can lead to galactosialidosis, or Morquio B syndrome. Lysosomal proteases regulate transition of 86-kDa precursor form of β-galactosidase to a 64-kDa mature enzyme [37,38]. This enzyme is also known to be a classic marker of senescence in cellular biology. Furthermore, cellular senescence, a stable cell cycle arrest, is often compared to apoptosis as an intrinsic tumor suppression mechanism. Thus, high levels of senescence-associated β-galactosidase can be found in tumors. These findings led to investigate the use of B-GAL to induce senescence as a promising therapeutic strategy [38]. We here propose to explore the association and delivery of B-GAL *in vitro* as a second proof of concept of the potential of P-SNs for the development of protein replacement therapies, as well as for a possible strategy to induce cellular senescence to cancer cells [39].

Thus, a vary set of B-GAL-SNs were formed and characterized (**Table 1**). Colloidal stability was measured upon a month at storage conditions (**Fig. 5a**; **Fig. S6a**). Two association strategies performed (SNs(DBCO) and SNs(NHS)) showed lower size and narrow polydisperse population, characteristics that were maintained through the testing time. For later *in vitro* experiments, stability in cell culture medium was also monitored at different time points for up to 24 hours (**Fig. 5b**). We successfully confirm by the X-GAL staining assay[40], the efficiency of the B-GAL internalization when it was associated to SNs (**Fig. 6**). Additionally, the behavior of B-GAL-SNs was compared with two commercial preparations for protein delivery, BioPORTER® (cationic lipid mixture) and PULSin® (cationic amphiphile molecule). Our B-GAL-SNs presented a better cellular uptake. In addition, B-GAL-SNs did not cause cytotoxic effects as observed for the commercial preparations. BioPORTER® and PULSin® modify the morphology of L3.6pl cells. As observed in **figure 6**, cell membranes seemed to be disaggregated and cell compartments released. Overall, B-GAL-SNs offer an enhanced uptake in both supplemented and non-supplemented culture medium (**Fig. S6b**) compared to BioPORTER® and PULSin® that only work in non-supplemented ones (manufacture's instructions). Regarding our data, all SNs resulted in an efficacious internalization, being probably the most suitable B-GAL-SNs(DBCO), B-GAL-SNs(DOTAP) and B-GAL-SNs(NHS). What's more, if we directly compare cationic B-GAL-SNs(DOTAP) to cationic commercial preparations, BioPORTER® and PULSin®, SNs(DOTAP) did not exhibit associated cytotoxicity.

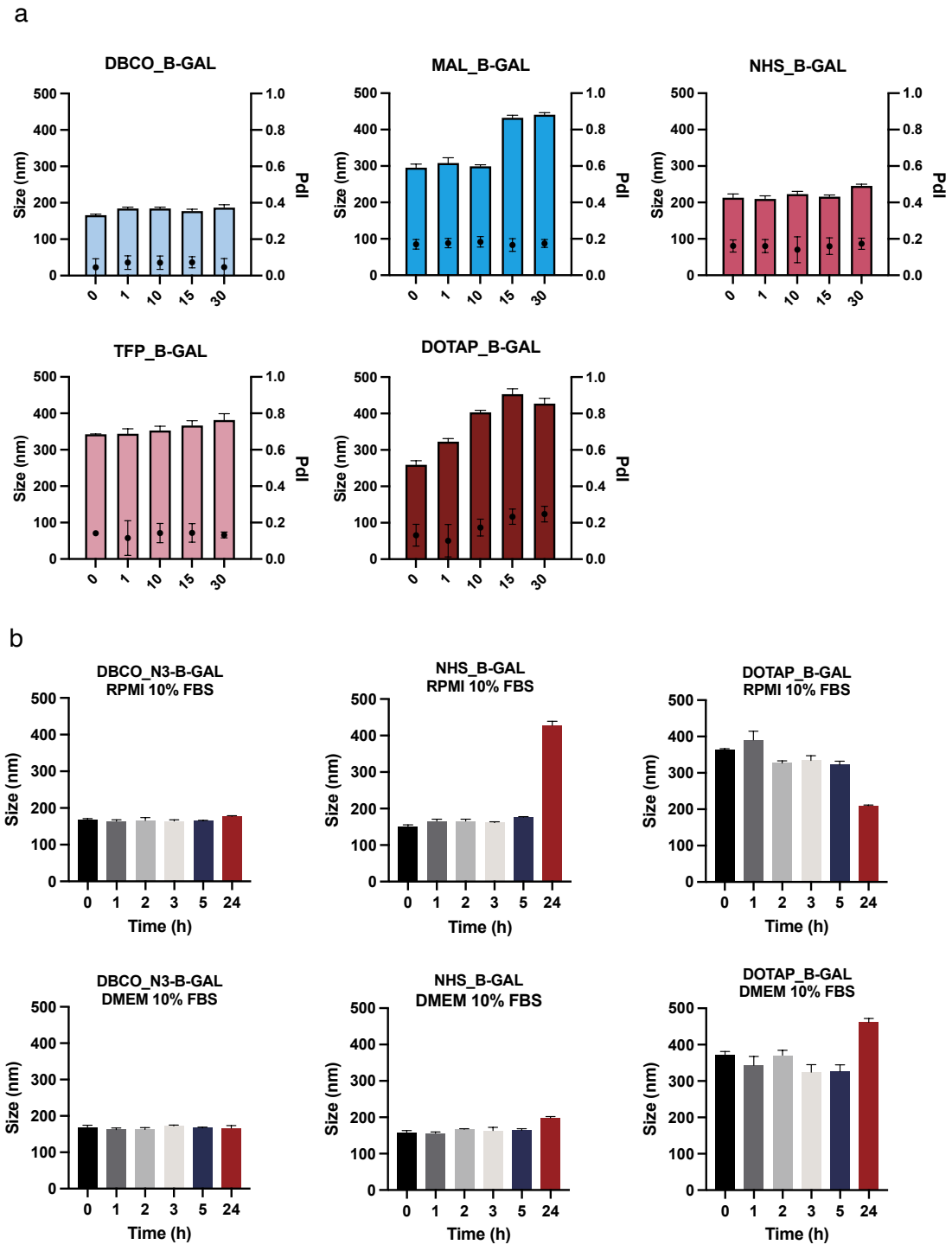

Figure 5. β-GAL-SNs. **(a)** Colloidal stability of the different strategies measured up to one-month at storage conditions (4ºC). **(b)** Stability in cell culture medium evaluated up to 24 h in supplemented cell culture medium, at 37ºC under orbital shaking (300 r.p.m.). (n=5, data expressed as mean ± SD).

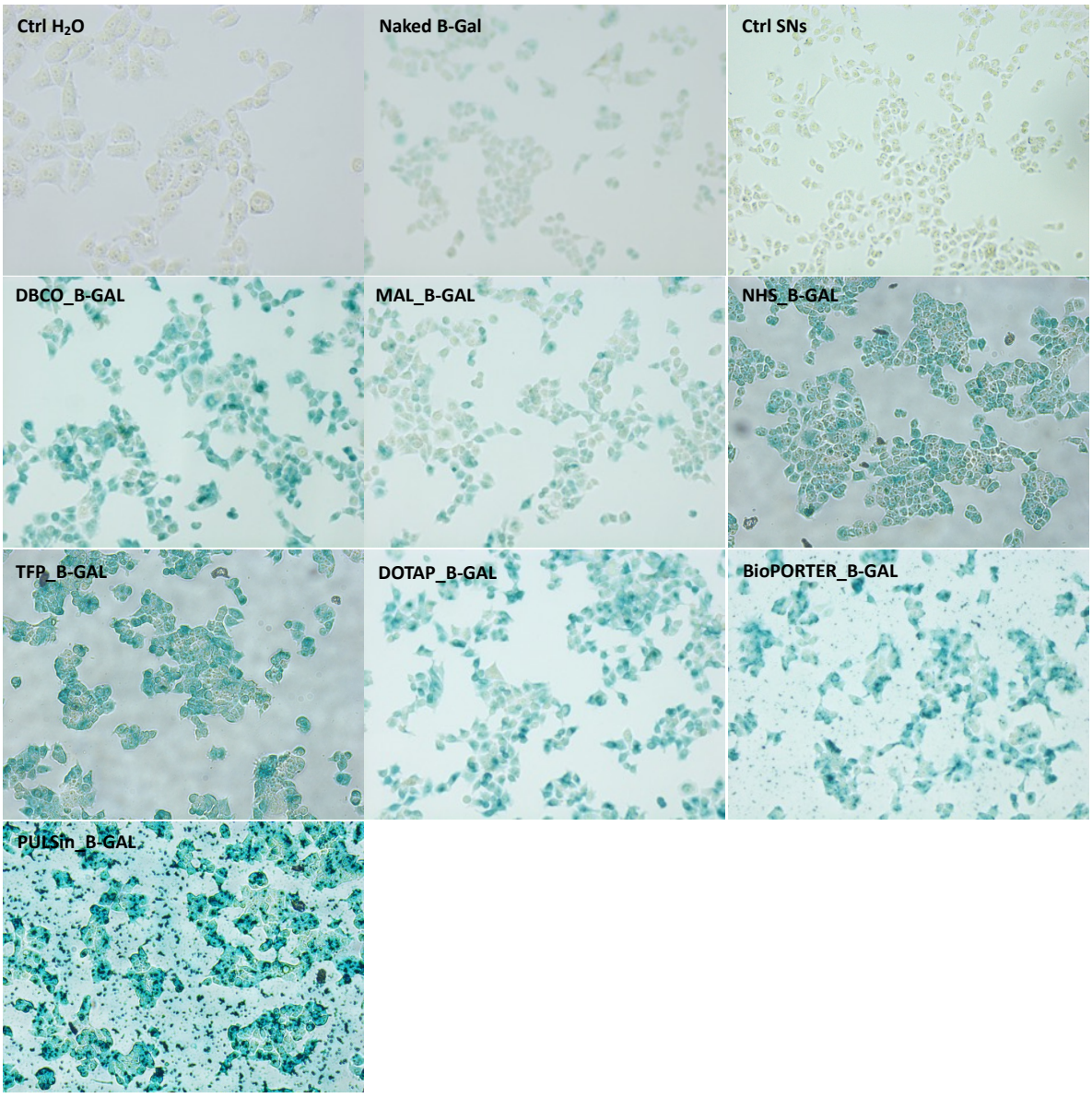

Figure 6. X-GAL assay to evaluate the internalization of B-GAL-SNs formulations (names as described in Table 1). in comparison, with commercially available protein delivery kits BioPORTER® and PULSin®. As negative controls for the detection of B-GAL, we have added (i) H_2O; (ii) naked enzyme B-GAL (does not trespass cell membranes); (iii) SNs without B-GAL. B-GAL-SNs formulations were added in non-supplemented cell culture RMPI medium (Dose corresponding to 2μg of B-Gal in all conditions; incubation time 2h; expression of B-Gal was performed by X-Gal staining at 12h post incubation).

GFP and R-Phycoerythrin (PE) as models of reporter fluorescent proteins

We prepared P-SNs that associate two fluorescent proteins (GFP; PE) with the purpose of using them *in vitro* cell tracking analysis. These P-SNs could also be loaded with other cargoes (small drugs, oligos, peptides, etc) as previously reported [22,23,41]. SNs are here presented as a tool to follow up colocalization of fluorescent nanoparticles (SNs) and cargo, thanks to this dual labelling, other mechanisms such as endosomal escape can be deeply studied in future research studies [42–44]. Concerning N3-GFP, complete functionalization was observed by HPLC-MS and MALDI-Tof analysis (**Fig. 7a-b**). Once formed, GFP-SNs we examined their physicochemical characteristics, which are collected in **Table 3,** and their colloidal stability (**Fig. 7c**).

Table 3. Physicochemical Characterization of GFP-SNs measured by DLS and LDA. Percentage of GFP linked to SNs (Results are expressed as Mean ± Standard Deviation, n = 5). Abbreviations: nm: nanometer, PdI: polydispersity index, ZP: zeta potential in millivolts (mV).

Formulation	Ratio	Size (nm)	PdI	ZP (mV)	GFP % Associated
VitE:SM:DBCO	1:0.1:0.01	177 ± 5	<0.1	- 29 ± 3	91 ± 3
VitE:SM:MAL	1:0.1:0.01	191 ± 4	0.2	- 33 ± 1	79 ± 4
VitE:SM:NHS	1:0.1:0.01	171 ± 3	0.2	- 25 ± 2	70 ± 1
VitE:SM:TFP	1:0.1:0.01	229 ± 7	0.1	- 34 ± 3	83 ± 4
VitE:SM:COOH	1:0.1:0.01	193 ± 3	0.1	- 35 ± 1	84 ± 2

GFP-SNs were purified, and SNs fluorescence was next measured and compared to native- and N3-GFP proteins. GFP-SNs(DBCO) gave the best results in terms of relative fluorescence levels (**Fig. 7d, S7**). These results are well aligned with the higher GFP association in GFP-SNs(DBCO), but also in relation to the performance of SNs(DBCO) with the other enzymes tested (bioluminescent activity of RLuc8-SNs(DBCO)).

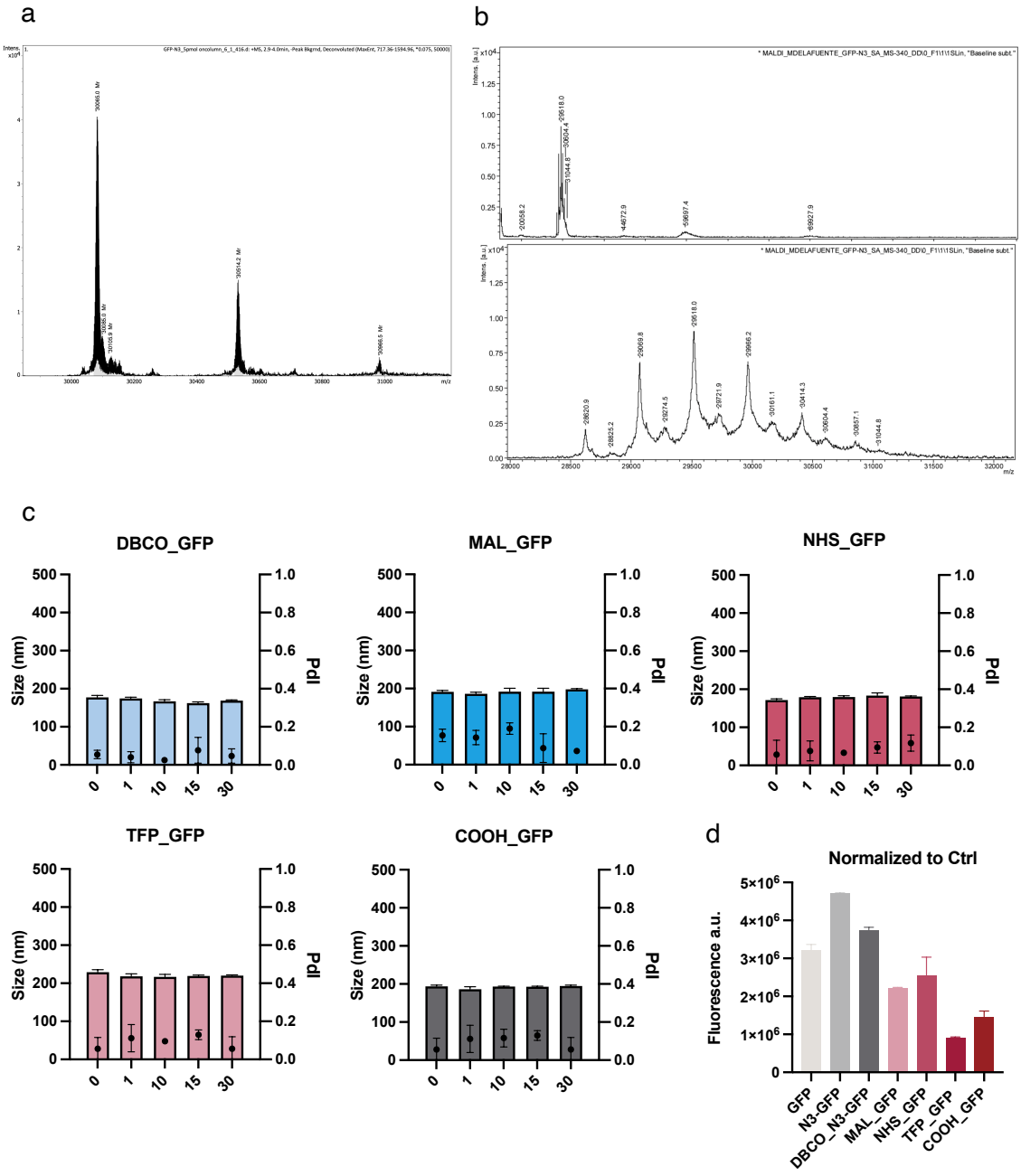

Figure 7. GFP-SNs. **(a)** HPLC-MS and **(b)** MALDI-Tof to evaluate complete functionalization of N3-B-Gal. **(c)** Colloidal stability of the P-SNs formulations prepared by different binding strategies (**Table 1**) measured over time for up to 30 days at storage conditions (4ºC). **(d)** Fluorescence measures of GFP by a fluorimeter; samples tested naked GFP, GFP-N3 and purified GFP-SNs (corresponding dose of 0.5 µg of GFP per condition). (n=5, data expressed as mean ± SD).

Next, GFP-SNs were added to L3.6pl cells, incubated for 2 hours and examined by flow cytometry. GFP-SNs(DBCO) and GFP-SNs(NHS) were more efficiently internalized (**Fig. 8a**). This correlates well with the higher uptake in SNs(DBCO) with RLuc8 and B-Gal. Furthermore, delivery of GFP using the commercial kit PULSin® led to minimal internalization (26%). This is logical considering that PULSin® is a cationic molecule and the fact that the isoelectric point (pI) of GFP is ~6.0 at physiological pH, rendering a practically neutral /slightly negative charge and therefore to the absence of electrostatic interactions. P-SNs based on the establishment of covalent bonds (as the ones mediated by DBCO, MAL, NHS, TFP and COOH), had the advantage of providing a binding strategy that do not depend on charges. Thus, SNs(DBCO) was selected for a later experiment to test cellular uptake by CLM observed in fresh L3.6pl cells (**Fig. 8b**), because it is reported that fixation methods and cell culture medium may interfere with fluorescence signal[45]. Bearing these results in mind, we must remark that we have achieved the efficient delivery of GFP first described using nanoemulsions. Generally, in the literature it is mainly reported GFP delivery by linking the protein to CPPs [46–48] to facilitate its cellular membrane trespassing, and to silica nanoparticles [49]. But the simplicity of our developed strategy, makes it more advantageous in terms of translational aspects.

a

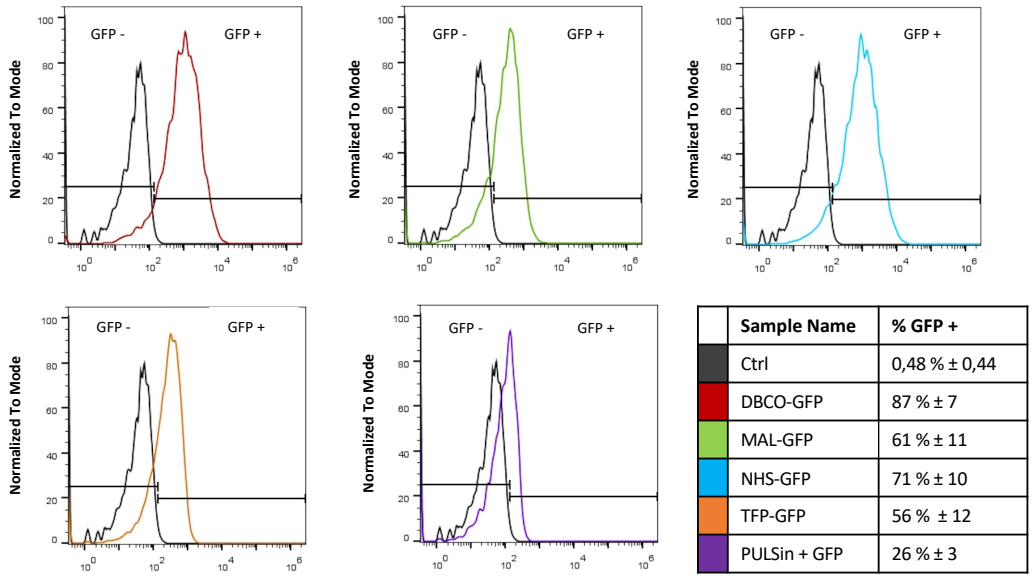

	Sample Name	% GFP +
	Ctrl	0,48 % ± 0,44
	DBCO-GFP	87 % ± 7
	MAL-GFP	61 % ± 11
	NHS-GFP	71 % ± 10
	TFP-GFP	56 % ± 12
	PULSin + GFP	26 % ± 3

b

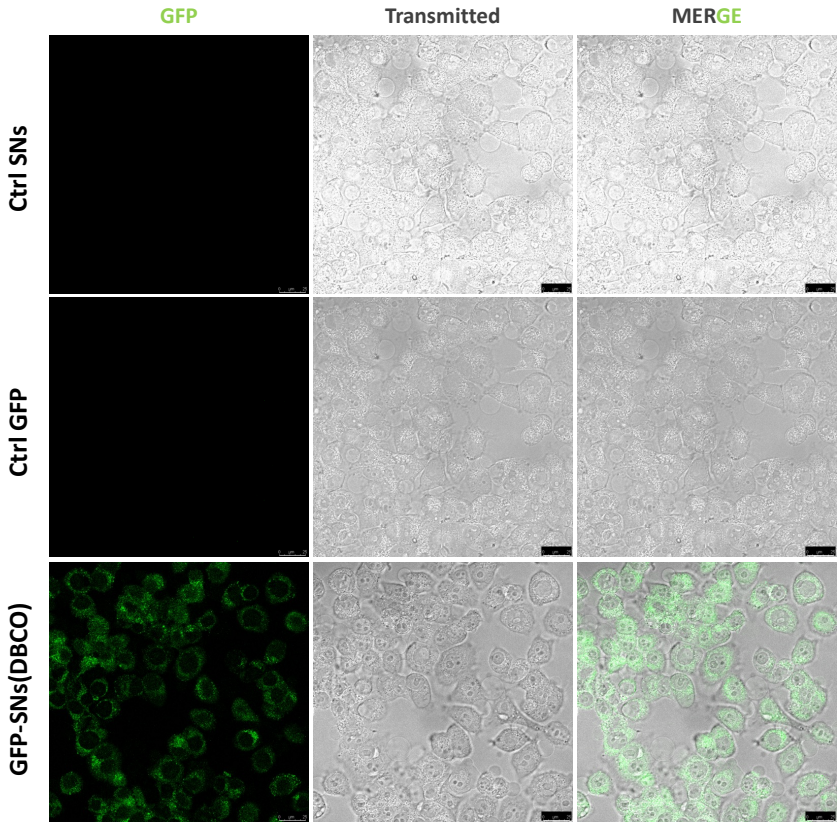

Figure 8. (a) Flow cytometry (FACS) analysis of the internalization of GFP-SNs to evaluate differences in efficacy depending on the SNs prototypes. Incubation time in L3.6pl 2 hours at 37ºC. SNs names and % internalization expressed in the table (right panel). **(b)** Confocal microscopy images of GFP-SNs(DBCO) (green signal) and controls (naked GFP and plain SNs) observed in fresh non-fixed cells upon 2 hours incubation at 37ºC in DPBS 1X. (n=5, data expressed as mean ± SD).

Regarding PE-SNs, colloidal stability was measured up to 30 days (**Fig. 9a**). PE has a MW of 250 kDa, making difficult purification by ultrafiltration or dialysis. To remove unreacted protein, it is necessary filters with a MW at least 3 to 10-fold higher. We could not find a simply and successful purification method to separate PE-SNs from unreacted PE without PE-SNs loss. So, we performed SDS-PAGE electrophoresis gel to elucidate the percentage of association of PE to SNs. SNs are not expected, as well as the bound protein, to migrate in the gel. Unreacted PE is observed in the gel, and we concluded that PE-SNs(DBCO) presented a higher PE association efficacy (**Fig. 9b**). Then, PE-SNs were further tested *in vitro*. Cellular uptake was monitored by flow cytometry. For that, PE-SNs were added to L3.6pl cells and PE fluorescence within cells calculated by flow cytometry analysis after 2 hours of treatment. All PE-SNs get internalized by the cells but the best results were obtained by PE-SNs(DBCO) and PE-SNs(DOTAP). As reported for B-GAL-SNs and GFP-SNs, our formulations showed improved internalization rates than the commercial formulation PULSin® (**Fig. 9c**). Furthermore, P-SNs offer a better protein delivery system as it can be loaded with negative and positive charged proteins (wide range of pI tested) compared to commercial protein delivery kits based on cationic molecules or lipid mixture. Also, we achieved the delivery of active and functional proteins. This is very important because successful nanoparticle uptake of a labelled protein (and other cargo molecules) does not necessarily mean that the protein is still functional [50].

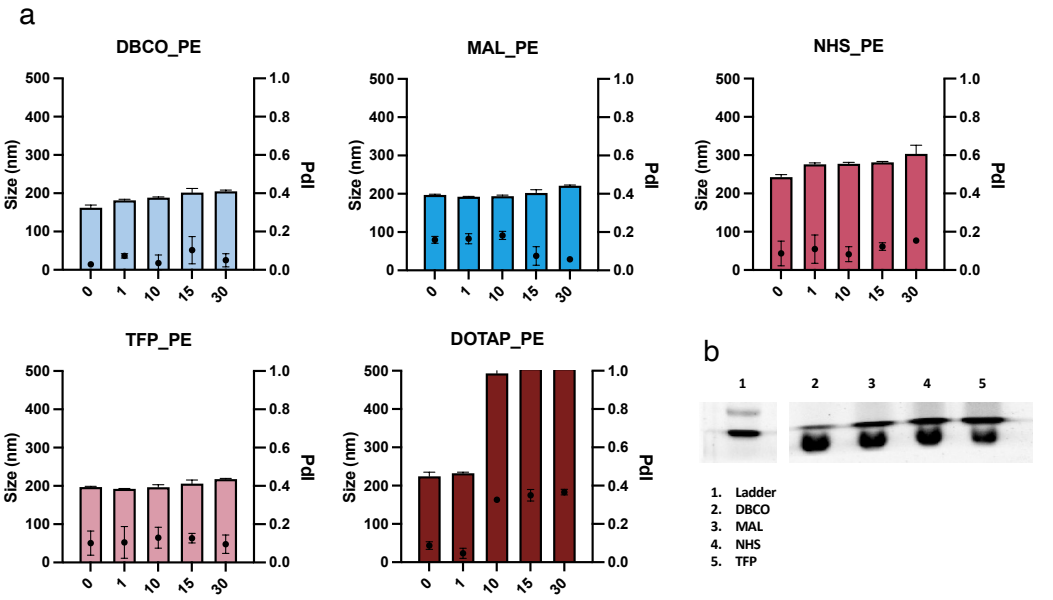

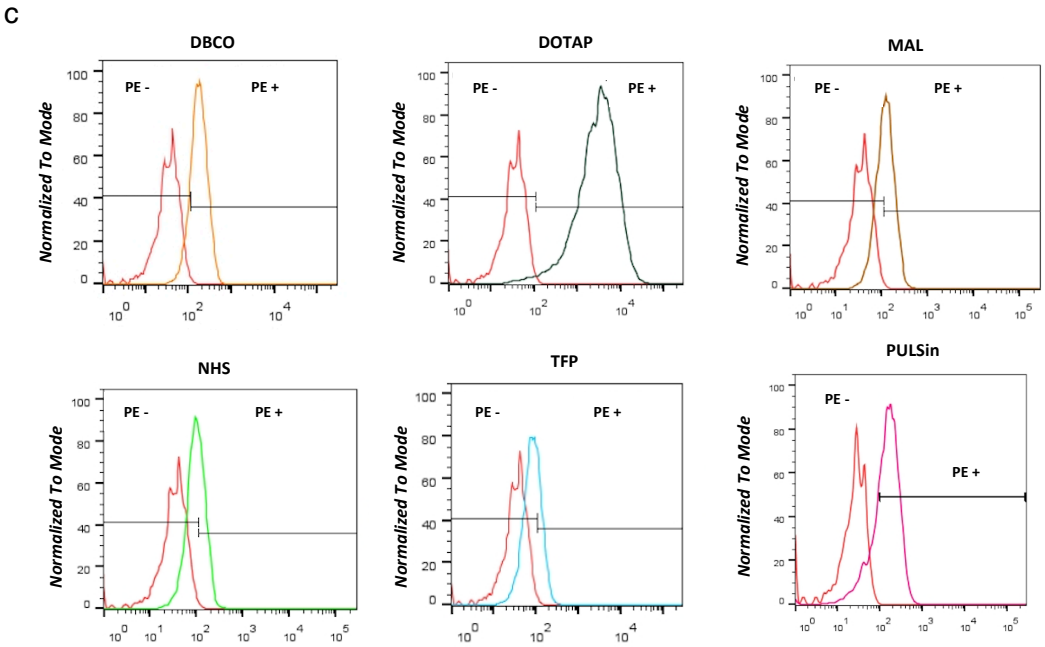

	Sample Name	% PE +
	Ctrl	0,06 % ± 0,06
	DBCO-PE	87 % ± 2
	DOTAP-PE	74 % ± 4
	MAL-PE	40 % ± 7
	NHS-PE	43 % ± 3
	TFP-PE	31 % ± 3
	PULSin + PE	63 % ± 2

Figure 9. PE-SNs. **(a)** Colloidal stability of the different strategies measured over 30 days at storage conditions (4ºC). **(b)** SDS-PAGE electrophoresis gel to observe unreacted PE to SNs, (PE loading 0.5 μg per condition, SDS-PAGE stained with Coomassie blue) . **(c)** Flow cytometry (FACS) analysis of the internalization of PE-SNs to evaluate differences in efficacy depending on the SNs prototypes. Incubation time in L3.6pl 2 hours. SNs names and % internalization expressed in the table (lower panel). (n=5, data expressed as mean ± SD).

Ovalbumin (OVA) as a model of immunogenic protein

Ovalbumin is the predominant protein in chicken egg white. It is commonly used to sensitize immune reactions. OVA leads to the development of some skin diseases such as dermatitis due to the increase of the expression of total and OVA-specific serum IgE and other immune system cells[51,52]. OVA is also the most widely used to induce experimental allergic asthma models in mice alongside house dust mite extract to trigger Th2 type allergic immune responses in mice [53,54]. In these studies, OVA strongly augmented serum levels of OVA-specific IgE. Thus, in this research work we exploited the delivery of OVA-SNs as a future model for nanovaccines to induce an immune system response to Tcells. OVA was associated to SNs by following different binding strategies (**Table 1**). But first, and as previously described, to perform SPAAC reaction, OVA has to be linked to a N3-moiety, and the correct functionalization was monitored by HPLC-MS [55] (**Fig. 10a**). Then, native- and N3-OVA were bound to SNs, and their physicochemical properties determined (**Table 4**). Purified OVA-SNs were then quantified to calculate % of OVA that was efficiently loaded into SNs. % of OVA loading was consistently with the other evaluated proteins (DBCO>TFP>MAL>NHS). Results correlates as well with the type of reactive group hydrophilicity and disposition on the SNs surface.

Table 4. Physicochemical Characterization of OVA-SNs measured by DLS and LDA. Percentage of OVA linked to SNs (Results are expressed as Mean ± Standard Deviation, n = 5). Abbreviations: nm: nanometer, PdI: polydispersity index, ZP: zeta potential in millivolts (mV).

Formulation	Ratio	Size (nm)	PdI	ZP (mV)	OVA % Associated
VitE:SM:DBCO	1:0.1:0.01	85 ± 2	<0.1	- 24 ± 1	92 ± 2
VitE:SM:MAL	1:0.1:0.01	218 ± 1	0.2	- 38 ± 1	80 ± 6
VitE:SM:NHS	1:0.1:0.01	231 ± 4	0.2	- 23 ± 1	65 ± 5
VitE:SM:TFP	1:0.1:0.01	217 ± 1	0.2	- 28 ± 8	84 ± 3
VitE:SM:DOTAP	1:0.1:0.01	90 ± 2	0.1	+ 22 ± 2	-

OVA-SNs colloidal stability was evaluated up to 30 days (**Fig. 10b**). Accordingly, to other tested proteins (B-GAL and PE; negatively charged), SNs(DBCO) and SNs(DOTAP) exhibited a superior % of internalization in L3.6pl cell line (%>75). OVA-SNs(DBCO) and OVA-SNs(DOTAP) were selected for *in vitro* testing. So, labelled OVA-TF-SNs(DBCO) and OVA-TF-SNs(DOTAP) were added to HeLa cells for 2 hours. Treatment was removed and internalization assessed by flow cytometry. Both OVA-SNs attained a 99% positive cells (**Fig. 10c**). Next, cytotoxicity of SNs(DOTAP) + OVA-SNs(DOTAP) was carried out on HeLa cells at 4- and 24-hours. SNs(DOTAP) has an intrinsic toxicity associated to cationic lipid DOTAP, but it seems that linked OVA slightly increases viability (**Fig. 10d**). In future studies, we aim to elucidate the mechanism of action of OVA-SNs to stimulate the activation of Tcells in blood samples.

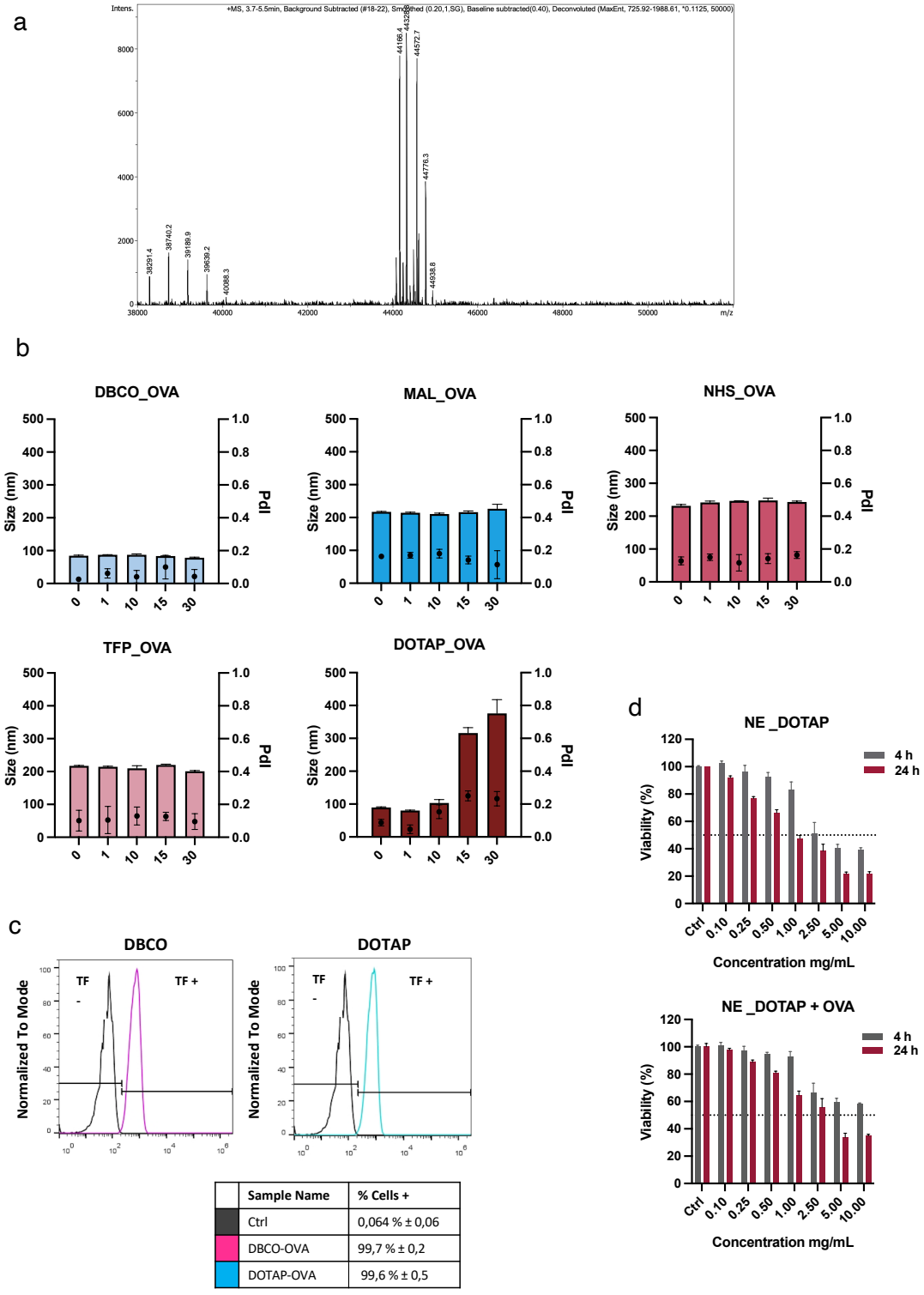
a
Intens.
+MS, 3.7-5.5min, Background Subtracted (#18-22), Smoothed (0.20,1,SG), Baseline subtracted(0.40), Deconvoluted (MaxEnt, 725.92-1988.61, *0.1125, 50000)
38291.4
38740.2
39189.9
39639.2
40088.3
44166.4
44328.6
44572.7
44776.3
44938.8
m/z
b
DBCO_OVA
MAL_OVA
NHS_OVA
TFP_OVA
DOTAP_OVA
Size (nm)
PdI
c
DBCO
DOTAP
TF -
TF +
Normalized To Mode
Sample Name
% Cells +
Ctrl
0,064 % ± 0,06
DBCO-OVA
99,7 % ± 0,2
DOTAP-OVA
99,6 % ± 0,5
d
NE _DOTAP
NE _DOTAP + OVA
4 h
24 h
Viability (%)
Concentration mg/mL
Ctrl
0.10
0.25
0.50
1.00
2.50
5.00
10.00

Figure 10. OVA-SNs. **(a)** HPLC-MS of N3-OVA to evaluate complete functionalization. **(b)** Colloidal stability of the different strategies measured over 30 days at storage conditions (4ºC). **(c)** Flow cytometry (FACS) analysis of the internalization of OVA-SNs(DBCO) and OVA-SNs(DOTAP) in HeLa cells after 2 hours of incubation. SNs names and % internalization expressed in the table (lower panel). **(d)** Cytotoxicity assays of SNs(DOTAP) and OVA-SNs(DOTAP) tested at increasing concentrations (0.1 mg/mL to 10 mg/mL) at 4h and 24h interaction with HeLa cancer cells. %Viability measured with Alamar Blue™ reagent. (n=5, data expressed as mean ± SD).

CONCLUSIONS

In this study, we have developed a nanoplatform for the delivery of a versatile range of different proteins such as reporter proteins, functional and therapeutic enzymes, based on a sphingomyelin lipid nanosystem. We proved the successfully association of all the proteins independently of their MW (10 – 500 kDa) and pI at the pH used. This is very important due to the limitation that commercial cationic formulations present at surface charge complexation and related toxicity. We have carried out different chemical strategies based on covalent linking reactions and electrostatic interactions between SNs and proteins. All in all, different strategies gave good results. However, we should remark the performance of SNs(DBCO). This type of reaction rendered the best percentage of protein loading across all experiments with different proteins, irrespective of MW and net charge (pI), and the best internalization rates without causing cell damage or inducing cytotoxicity in L3.6pl at the doses tested (including high dose of 10 mg/mL). Also, it is important to highlight the potential of SNs(NHS) and SNs(DOTAP) formulations, which achieved a good internalization in two cell lines (L3.6pl and HeLa) with the different proteins. In general, our P-SNs perfectly trespassed cellular membrane barriers in different cells lines and did not induce toxic effects (except for SNs(DOTAP) at 24h incubation at maximum doses). Overall, this work presents for the first time a simple and versatile methodology to associate proteins to a biocompatible lipid formulation, SNs. The fact that proteins are stable and efficiently delivered to target cells, improve the potential of the approach described here for the development of protein therapeutics.

Supporting Information

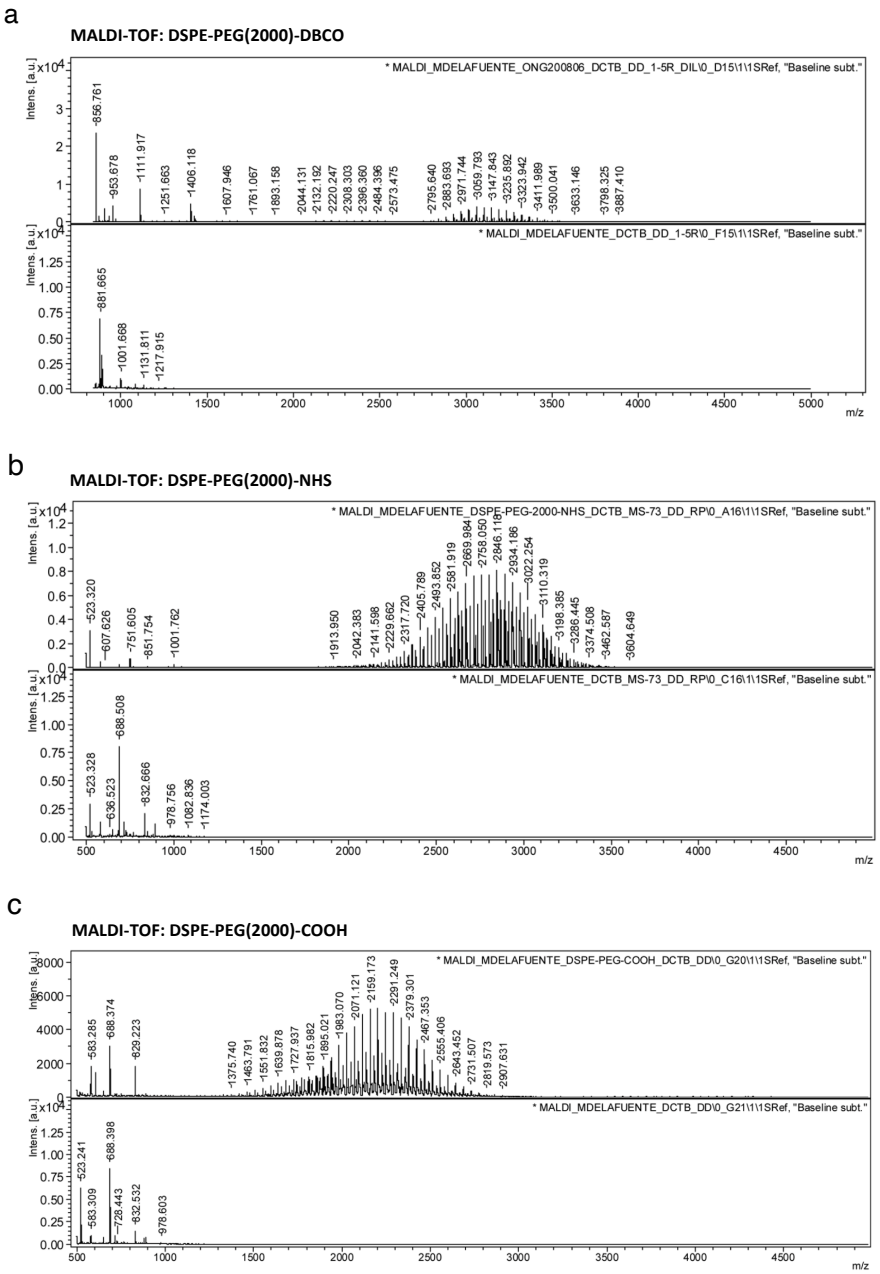

Figure S1. MALDI-Tof analysis of **(a)** DSPE-PEG(2000)-DBCO, **(b)** DSPE-PEG(2000)-NHS, **(c)** DSPE-PEG(2000)-COOH lipids that constitute SNs.

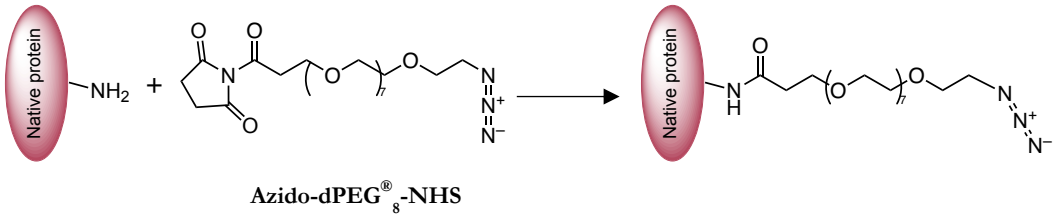

Figure S2. Azide-linker modification of the proteins for further SPAAC "click chemistry" reaction to SNs.

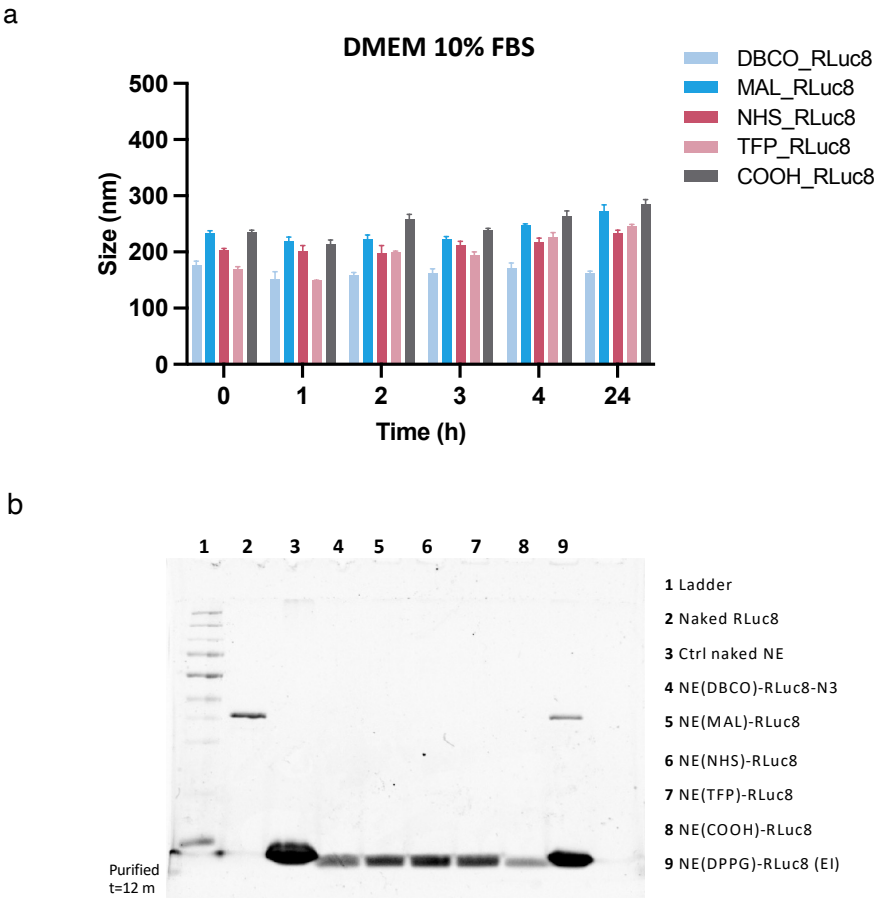

Figure S3. (a) Stability in cell culture medium (DMEM) supplemented with 10% FBS incubated at 37ºC under orbital stirring (300 r.p.m.) measured up to 24 h of RLuc8-SNs. **(b)** SDS-PAGE electrophoresis gel to confirm no protein release from SNs under storage conditions (4ºC). (n=5, data expressed as mean ± SD).

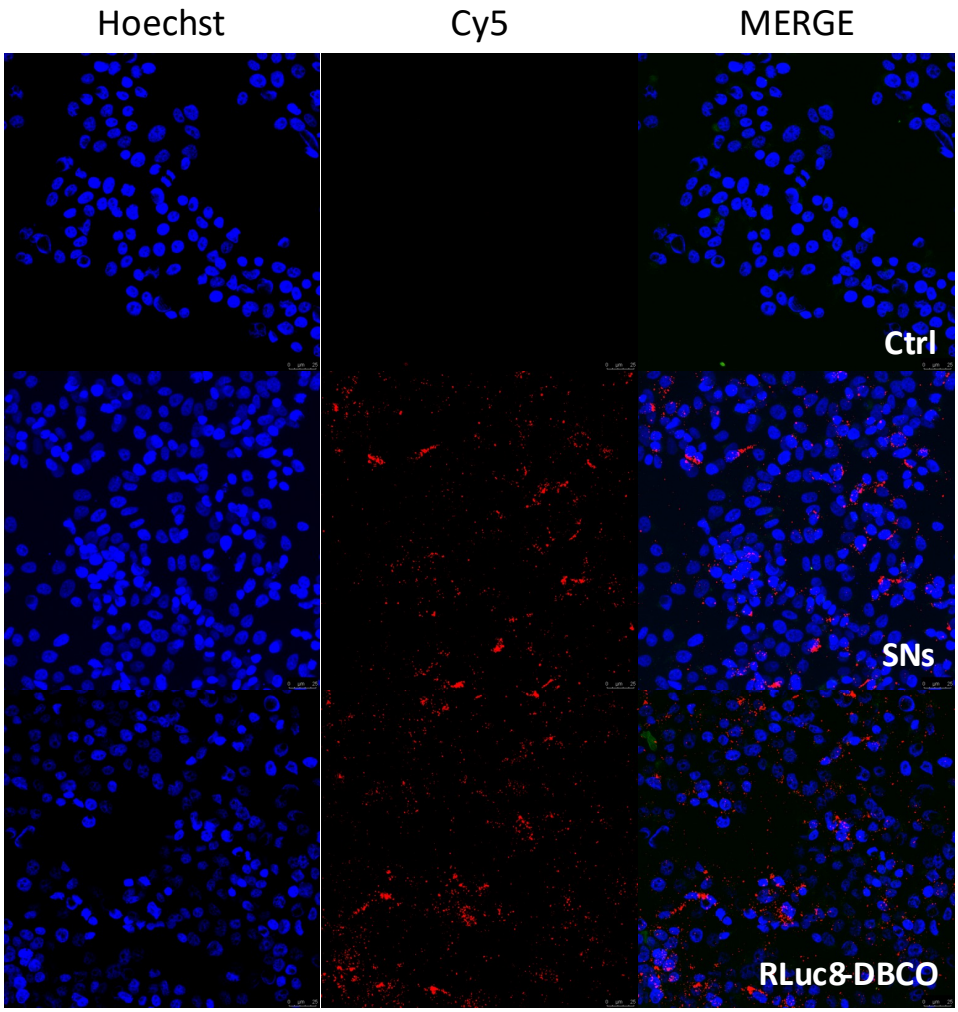

Figure S4. Confocal Laser Microscopy (CLM) images of Cy5-SNs(DBCO) and RLuc8-Cy5-SNs(DBCO) after 2 hours of incubation in L3.6pl cells. Red: Cy5, Blue: nucleus (cell nuclei stained with Hoechst 33342).

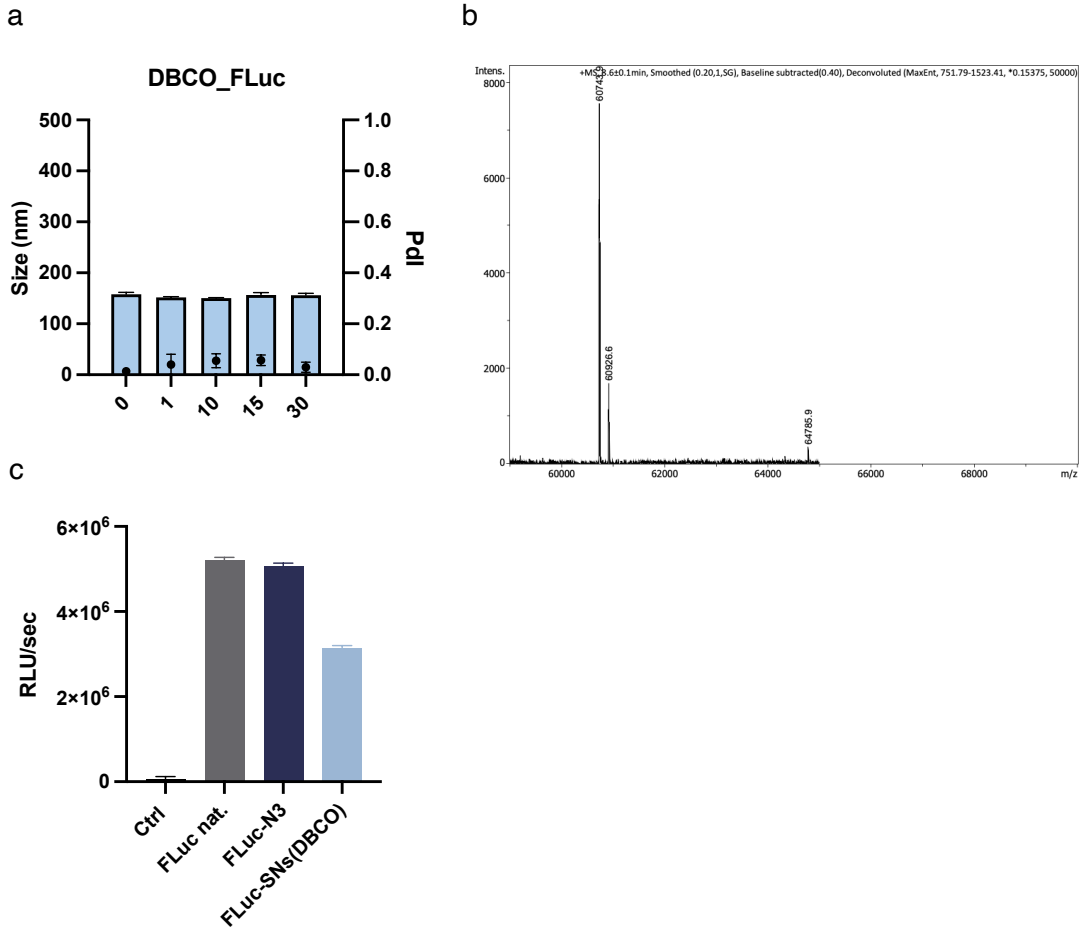

Figure S5. FLuc-SNs. **(a)** Colloidal stability of FLuc-SNs(DBCO) through time (30 days) at storage conditions. **(b)** HPLC-MS analysis of N3-FLuc to observe complete functionalization with the azide-linker. **(c)** Evaluation of the bioluminescent activity of FLuc, N3-FLuc and FLuc-SNs(DBCO). (n=5, data expressed as mean ± SD).

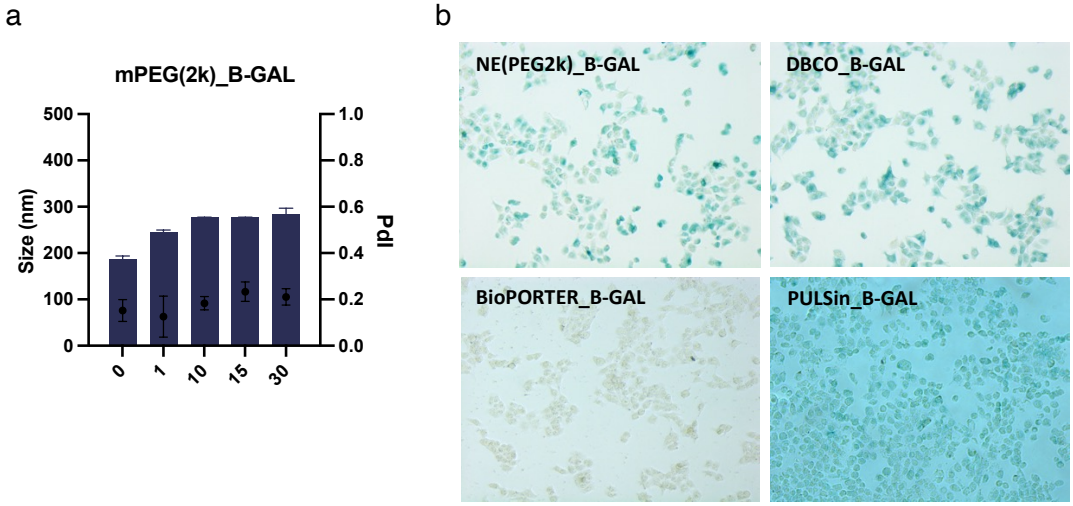

Figure S6. β-GAL-SNs. **(a)** Colloidal stability of mPEG(2k)_B-GAL upon a month at storage conditions (4ºC). **(b)** X-GAL assay to evaluate the internalization of B-GAL-SNs(mPEG 2k) and in comparison, with commercially available protein delivery kits. B-GAL-SNs formulations were added in plain cell culture RMPI medium supplemented with 10% FBS (Dose corresponding to 2µg of B-Gal in all conditions; incubation time 2h; expression of B-Gal was performed by X-Gal staining at 12h post incubation). (n=5, data expressed as mean ± SD).

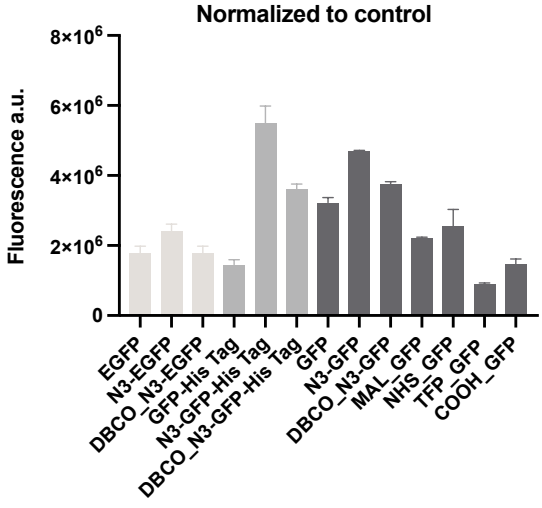

Figure S7. Fluorescence measures of GFP; GFP-N3; EGFP; EGFP-N3; GFP-HisTag; GFP-HisTag-N3 and purified -SNsGFP to observe differences within prototypes. (n=5, data expressed as mean ± SD).

Table S1. Physicochemical Characterization of SNs prepared with different lipids (results are expressed as Mean ± SD, n = 5). Abbreviations: nm: nanometer, PdI: polydispersity index, ZP: zeta potential in millivolts (mV).

Formulation	Ratio*	Size (nm)	PdI	ZP (mV)
VitE:SM:DBCO	1:0.1:0.01	56 ± 3	<0.2	- 28 ± 1
VitE:SM:Maleimide	1:0.1:0.01	60 ± 4	<0.2	- 27 ± 2
VitE:SM:NHS	1:0.1:0.01	59 ± 3	0.2	- 23 ± 1
VitE:SM:TFP	1:0.1:0.01	74 ± 4	0.2	- 29 ± 3
VitE:SM:COOH	1:0.1:0.01	73 ± 2	0.1	- 38 ± 1
VitE:SM:DPPG	1:0.1:0.01	92 ± 5	0.2	- 22 ± 3
VitE:SM:DOTAP	1:0.1:0.01	50 ± 4	0.1	+ 36 ± 5

*The amount of Vit E and SM remained constant, 5mg/mL and 0.5mg/mL respectively. Formulation batch size: 1mL.

Table S2. Physicochemical Characterization of FLuc-SNs(DBCO) measured by DLS and LDA. % of Associated FLuc quantified by microBCA assay (results are expressed as Mean ± SD, n = 5). Abbreviations: nm: nanometer, PdI: polydispersity index, ZP: zeta potential in millivolts (mV).

Formulation	Ratio	Size (nm)	PdI	ZP (mV)	FLuc % Associated
VitE:SM:DBCO	1:0.1:0.01	158 ± 5	<0.1	- 28 ± 2	94 ± 3

REFERENCES

1. Vermonden, T., Censi, R. & Hennink, W. E. Hydrogels for protein delivery. *Chemical Reviews* vol. 112 2853–2888 Preprint at https://doi.org/10.1021/cr200157d (2012).

2. Yu, M., Wu, J., Shi, J. & Farokhzad, O. C. Nanotechnology for protein delivery: Overview and perspectives. *Journal of Controlled Release* **240**, 24–37 (2016).

3. Lu, Y., Sun, W. & Gu, Z. Stimuli-responsive nanomaterials for therapeutic protein delivery. *Journal of Controlled Release* vol. 194 1–19 Preprint at https://doi.org/10.1016/j.jconrel.2014.08.015 (2014).

4. Sinha, V. R. & Trehan, A. Biodegradable microspheres for protein delivery. *Journal of Controlled Release* vol. 90 261–280 Preprint at https://doi.org/10.1016/S0168-3659(03)00194-9 (2003).

5. Bizeau, J. & Mertz, D. Design and applications of protein delivery systems in nanomedicine and tissue engineering. *Advances in Colloid and Interface Science* vol. 287 Preprint at https://doi.org/10.1016/j.cis.2020.102334 (2021).

6. Sauna, Z. E. *et al.* Recent advances in (therapeutic protein) drug development. *F1000Research* vol. 6 Preprint at https://doi.org/10.12688/f1000research.9970.1 (2017).

7. Santalices, I., Gonella, A., Torres, D. & Alonso, M. J. Advances on the formulation of proteins using nanotechnologies. *Journal of Drug Delivery Science and Technology* vol. 42 155–180 Preprint at https://doi.org/10.1016/j.jddst.2017.06.018 (2017).

8. Gregoriadis, G., Leathwood, P. D. & Ryman, B. E. Enzyme entrapment in liposomes. *FEBS Lett* **14**, 95–99 (1971).

9. MG, K., V, K. & F, H. History and Possible Uses of Nanomedicine Based on Nanoparticles and Nanotechnological Progress. *J Nanomed Nanotechnol* **06**, (2015).

10. Gregoriadis, G. & Ryman, B. E. Fate of Protein-Containing Liposomes Injected into Rats: An Approach to the Treatment of Storage Diseases. *Eur J Biochem* **24**, 485–491 (1972).

11. Damge, C., Michel, C., Aprahamian, M. & Couvreur, P. *New Approach for Oral Administration of Insulin With Polyalkylcyanoacrylate Nanocapsules as Drug Carrier*. http://diabetesjournals.org/diabetes/article-pdf/37/2/246/512899/37-2-246.pdf.

12. Morel, S., Gasco, M. R. & Cavalli, R. *international journal of pharmaceutics Rapid Communication Incorporation in lipospheres of [D-Trp-6]LHRH*. *International Journal of Pharmaceutics* vol. 105 (1994).

13. Morel, S., Ugazio, E., Cavalli, R. & Rosa Gasco, M. *international journal of pharmaceutics Notes Thymopentin in solid lipid nanoparticles*. *International Journal of Pharmaceutics* vol. 132 (1996).

14. S~nchez, A., Vila-Jato, L. & Alonso, M. J. *Development of biodegradable microspheres and nanospheres for the controlled release of cyclosporin A*. (1993).

15. Calvo, P., Remuñán-López, C., Vila-Jato, J. L. & Alonso, M. J. Novel hydrophilic chitosan-polyethylene oxide nanoparticles as protein carriers. *J Appl Polym Sci* **63**, 125–132 (1997).

16. *Nanomedicine Drugs Approved and in Development Product Disease Area Active Pharmaceutical Ingredient(s) Stage of Development Company (Innovator) Technology Description Indications Approval Year* Last Update (m/d/y) Update Reference*. http://ir.ceruleanrx.com/releasedetail.cfm?ReleaseID=968534.

17. Hafner, A., Lovrić, J., Lakŏ, G. P. & Pepić, I. Nanotherapeutics in the EU: An overview on current state and future directions. *International Journal of Nanomedicine* vol. 9 1005–1023 Preprint at https://doi.org/10.2147/IJN.S55359 (2014).

18. Weissig, V., Pettinger, T. K. & Murdock, N. Nanopharmaceuticals (part 1): products on the market. *International journal of nanomedicine* vol. 9 4357–4373 Preprint at https://doi.org/10.2147/IJN.S46900 (2014).

19. Kianfar, E. Protein nanoparticles in drug delivery: animal protein, plant proteins and protein cages, albumin nanoparticles. *Journal of Nanobiotechnology* vol. 19 Preprint at https://doi.org/10.1186/s12951-021-00896-3 (2021).

20. Bouzo, B. L., Calvelo, M., Martín-Pastor, M., García-Fandiño, R. & De La Fuente, M. *In Vitro*- In Silico Modeling Approach to Rationally Designed Simple and Versatile Drug Delivery Systems. *Journal of Physical Chemistry B* **124**, 5788–5800 (2020).

21. Bidan, N. *et al.* Before *in vivo* studies: *In vitro* screening of sphingomyelin nanosystems using a relevant 3D multicellular pancreatic tumor spheroid model. *Int J Pharm* **617**, (2022).

22. Nagachinta, S., Bouzo, B. L., Vazquez-Rios, A. J., Lopez, R. & de la Fuente, M. Sphingomyelin-based nanosystems (SNs) for the development of anticancer miRNA therapeutics. *Pharmaceutics* **12**, (2020).

23. Bouzo, B. L. *et al.* Sphingomyelin nanosystems loaded with uroguanylin and etoposide for treating metastatic colorectal cancer. *Sci Rep* **11**, (2021).

24. Werengowska-Ciećwierz, K., Wiśniewski, M., Terzyk, A. P. & Furmaniak, S. The chemistry of bioconjugation in nanoparticles-based drug delivery system. *Advances in Condensed Matter Physics* vol. 2015 Preprint at https://doi.org/10.1155/2015/198175 (2015).

25. Baldwin, A. D. & Kiick, K. L. Reversible maleimide-thiol adducts yield glutathione-sensitive poly(ethylene glycol)-heparin hydrogels. *Polym Chem* **4**, 133–143 (2013).

26. Wang, L., Jiang, R., Wang, L., Liu, Y. & Sun, X. L. Preparation of chain-end clickable recombinant protein and its bio-orthogonal modification. *Bioorg Chem* **65**, 159–166 (2016).

27. Kim, E. & Koo, H. Biomedical applications of copper-free click chemistry:: *In vitro*, *in vivo*, and *ex vivo*. *Chem Sci* **10**, 7835–7851 (2019).

28. Nagachinta, S. *et al.* Radiolabelling of lipid-based nanocarriers with fluorine-18 for *in vivo* tracking by PET. *Colloids Surf B Biointerfaces* **188**, (2020).

29. Saraiva, S. M. *et al.* Edelfosine nanoemulsions inhibit tumor growth of triple negative breast cancer in zebrafish xenograft model. *Sci Rep* **11**, (2021).

30. Díez-Villares, S. *et al.* Manganese Ferrite Nanoparticles Encapsulated into Vitamin E/Sphingomyelin Nanoemulsions as Contrast Agents for High-Sensitive Magnetic Resonance Imaging. *Adv Healthc Mater* **10**, (2021).

31. Díez-Villares, S. *et al.* Biodistribution of 68/67Ga-radiolabeled sphingolipid nanoemulsions by pet and spect imaging. *Int J Nanomedicine* **16**, 5923–5935 (2021).

32. Huang, H., Feng, W., Chen, Y. & Shi, J. Inorganic nanoparticles in clinical trials and translations. *Nano Today* vol. 35 Preprint at https://doi.org/10.1016/j.nantod.2020.100972 (2020).

33. Huo, Q. *et al.* Nanoparticle surface decoration mediated efficient protein and peptide co-encapsulation with precise ratiometric control for self-regulated drug release. *Nanoscale* **15**, 5063–5073 (2023).

34. Heinz, H. *et al.* Nanoparticle decoration with surfactants: Molecular interactions, assembly, and applications. *Surface Science Reports* vol. 72 1–58 Preprint at https://doi.org/10.1016/j.surfrep.2017.02.001 (2017).

35. Ding, H. M. & Ma, Y. Q. Design strategy of surface decoration for efficient delivery of nanoparticles by computer simulation. *Sci Rep* **6**, (2016).

36. Saqib, S., Akram, A., Halim, S. A. & Tassaduq, R. Sources of β-galactosidase and its applications in food industry. *3 Biotech* vol. 7 Preprint at https://doi.org/10.1007/s13205-017-0645-5 (2017).

37. Okada, S. Lysosomal storage disease. *Nippon rinsho. Japanese journal of clinical medicine* vol. 53 2911–2914 Preprint at https://doi.org/10.3233/trd-160005 (1995).

38. Valieva, Y., Ivanova, E., Fayzullin, A., Kurkov, A. & Igrunkova, A. Senescence-Associated β-Galactosidase Detection in Pathology. *Diagnostics* vol. 12 Preprint at https://doi.org/10.3390/diagnostics12102309 (2022).

39. Lozano-Torres, B., Blandez, J. F., Sancenón, F. & Ramón Martínez-Máñez, &. Chromo-fluorogenic probes for β-galactosidase detection. doi:10.1007/s00216-020-03111-8/Published.

40. Debacq-Chainiaux, F., Erusalimsky, J. D., Campisi, J. & Toussaint, O. Protocols to detect senescence-associated beta-galactosidase (SA-βgal) activity, a biomarker of senescent cells in culture and *in vivo*. *Nat Protoc* **4**, 1798–1806 (2009).

41. Díez-Villares, S. *et al.* Quantitative PET tracking of intra-articularly administered 89Zr-peptide-decorated nanoemulsions. *Journal of Controlled Release* **356**, 702–713 (2023).

42. Andrian, T., Riera, R., Pujals, S. & Albertazzi, L. Nanoscopy for endosomal escape quantification. *Nanoscale Advances* vol. 3 10–23 Preprint at https://doi.org/10.1039/d0na00454e (2021).

43. Miyoshi, Y. *et al.* Endosomal Escape of Peptide-Photosensitizer Conjugates Is Affected by Amino Acid Sequences near the Photosensitizer. *Bioconjug Chem* **31**, 916–922 (2020).

44. Tan, X., Bruchez, M. P. & Armitage, B. A. Efficient Cytoplasmic Delivery of Antisense Probes Assisted by Cyclized-Peptide-Mediated Photoinduced Endosomal Escape. *ChemBioChem* **20**, 727–733 (2019).

45. Bogdanov, A. M. *et al.* Cell culture medium affects GFP photostability: A solution. *Nature Methods* vol. 6 859–860 Preprint at https://doi.org/10.1038/nmeth1209-859 (2009).

46. Patel, S. G. *et al.* Cell-penetrating peptide sequence and modification dependent uptake and subcellular distribution of green florescent protein in different cell lines. *Sci Rep* **9**, (2019).

47. Schneider, A. F. L., Kithil, M., Cardoso, M. C., Lehmann, M. & Hackenberger, C. P. R. Cellular uptake of large biomolecules enabled by cell-surface-reactive cell-penetrating peptide additives. *Nat Chem* **13**, 530–539 (2021).

48. Pesce, D., Wu, Y., Kolbe, A., Weil, T. & Herrmann, A. Enhancing cellular uptake of GFP via unfolded supercharged protein tags. *Biomaterials* **34**, 4360–4367 (2013).

49. Schmidt, S. *et al.* Silica Nanoparticles for Intracellular Protein Delivery: a Novel Synthesis Approach Using Green Fluorescent Protein. *Nanoscale Res Lett* **12**, (2017).

50. Kopp, M. *et al.* Delivery of the autofluorescent protein Rphycoerythrin by calcium phosphate nanoparticles into four different eukaryotic cell lines (HeLa, HEK293T, MG-63, MC3T3): Highly efficient, but leading to endolysosomal proteolysis in HeLa and MC3T3 cells. *PLoS One* **12**, (2017).

51. Spergel, J. M. *et al.* Epicutaneous sensitization with protein antigen induces localized allergic dermatitis and hyperresponsiveness to methacholine after single exposure to aerosolized antigen in mice. *Journal of Clinical Investigation* **101**, 1614–1622 (1998).

52. Kim, W. H. *et al.* Beneficial effects of melittin on ovalbumin-induced atopic dermatitis in mouse. *Sci Rep* **7**, (2017).

53. Park, S. C. *et al.* An alternative dendritic cell-induced murine model of asthma exhibiting a robust Th2/Th17-skewed response. *Allergy Asthma Immunol Res* **12**, 537–555 (2020).

54. Lan, F. *et al. Th17 response is augmented in OVA-induced asthmatic mice exposed to HDM*. http://www.medscimonit.com/fulltxt.php?ICID=881759.

55. Tu, J. *et al.* Stable, Reactive, and Orthogonal Tetrazines: Dispersion Forces Promote the Cycloaddition with Isonitriles. *Angewandte Chemie - International Edition* **58**, 9043–9048 (2019).

Chapter IV

Anakinra-loaded Sphingomyelin Nanosystems (ANK-SNs) to Immunomodulate the Tumor Microenvironment (TME) in Pancreatic Ductal Adenocarcinoma (PDAC)

Anakinra-loaded Sphingomyelin Nanosystems (ANK-SNs) to Immunomodulate the Tumor Microenvironment (TME) in Pancreatic Ductal Adenocarcinoma (PDAC)

ABSTRACT

In pancreatic ductal adenocarcinoma (PDAC), tumor microenvironment (TME) exerts an immunosuppressive activity, which triggers tumor cell growth, invasion, and metastases. In addition, *Kras* activation promotes production of inflammatory cytokines, among which IL-1, indirectly activated by CAFs, secretes several tumor-promoting cytokines and directly by activation of IL-1R expressing immune effectors. On the other hand, Th17 require IL-1 for their differentiation, high levels of IL-17 and Th17 cells correlated with worse survival in PDAC patients. In the regard of the role of IL-1 in tumor-promoting inflammation in PDAC, IL-1 inhibition by the use of an IL-1R antagonist (IL-1RA) (anakinra, ANK) has been previously reported in several works. In this study, we have developed sphingomyelin nanosystems (SNs) loaded with ANK (ANK-SNs), and *in vitro* tested their capacity to inhibit IL-1-induced CAF activation and pro-inflammatory cytokine secretion (TSLP, IL-6 and IL-8), and Th17 cell differentiation (inhibition of IL-17 secretion) in comparison to free drug ANK.

INTRODUCTION

Pancreatic ductal adenocarcinoma (PDAC) is a very aggressive disease with dismal prognosis (expected to become the 2nd cause of cancer mortality by 2030) [1,2]. The tumor microenvironment exerts an immunosuppressive activity, which supports tumor cell growth, invasion and metastases, and it is sustained by a complex crosstalk among tumor, stromal and immune cells within the tumor microenvironment [3].

The cytokines of the IL-1 group are inflammatory mediators frequently upregulated in a variety of cancer and their production is associated with poor prognosis, with several mechanisms accounting for their pro-tumorigenic effects [4,5].

In PDAC the activation *of Kras* promotes production of inflammatory cytokines, among which IL-1 that activates NF-κB to promote tumor cell survival and proliferation, angiogenesis and increased invasive and metastatic behavior of pancreatic cancer cells [6–8]. In addition, IL-1 exert also important immunomodulatory functions within the tumor microenvironment, where IL-1α and IL-1β derived from both tumor cells and tumor associated macrophages act both indirectly by activation of cancer associated fibroblasts (CAFs) with secretion of several tumor-promoting cytokines and directly by activation of IL-1R expressing immune effectors.

In the context of PDAC, we previously reported that the ratio of Th2/Th1 cells is a predictor of poor prognosis after surgery in patients underwent surgery for primary PDAC [9]. We found that Th2 cell polarization was due to activation of myeloid dendritic cells with Th2 polarizing capability that was dependent on the thymic stromal lymphopoietin (TSLP) secreted by tumor-derived IL-1-activated CAFs [9–11], pointing to a relevant role for IL-1 in driving Th2 cell polarization in PDAC. Th17 cells also require IL-1 for their differentiation, and in PDAC Th17 cells were increased in the tumor compared to normal pancreatic tissue, and high levels of IL-17 and Th17 cells in the tumor correlated with worse survival in PDAC patients [12–16]. These data highlight the relevance in PDAC for an indirect as well as a direct role of IL-1 in the differentiation of protumor Th2 and Th17 cells, respectively.

Considering the key role of IL-1 in tumor-promoting inflammation in PDAC, IL-1 inhibition by the use of an IL-1R antagonist (IL-1RA) (anakinra, ANK) has been tested in *in vitro* and *in vivo* preclinical studies demonstrating that indeed anakinra is an effective anti-tumor agent [11,17–20]. Based on these results, clinical trials in PDAC patients with metastatic disease as well as in the neoadjuvant

setting using anakinra in combination with chemotherapy are ongoing/ have been planned (NCT02021422, NCT02550327, NCT04926467). A preliminary report demonstrated feasibility of the therapeutic approach with toxicities expected from the combination regimen [21]. As increased toxicity due to anakinra may constitute a problem in these combination regimens, targeting of anakinra to the tumor might highly impact on reducing systemic toxicities and/or effective concentrations of ANK to use in this combination settings.

Here, we prepare sphingomyelin nanosystems (SNs), composed by sphingomyelin and vitamin E, as described in *Bouzo et al.*[22], loaded with ANK (ANK-SNs), and used them in *in vitro* testing for their capacity to inhibit IL-1-induced CAF activation and pro-inflammatory cytokine secretion, and Th17 cell differentiation. We found that ANK-SNs highly inhibited TSLP, IL-6 and IL-8 secretion by CAF at levels similar to the free drug. Importantly, IL-17 secretion by Th17 cells differentiated in the presence of ANK-SNs was highly inhibited, and at levels significantly superior to the free drug.

MATERIALS AND METHODS

Materials

Vitamin E (VitE, DL-α-Tocopherol) was purchased from Sigma (Merck, Darmstadt, Germany). Sphingomyelin (SM, Lipoid E SM) was kindly provided by Lipoid GmbH (Ludwigshafen, Germany). Surfactants lipids being DSPE-PEG(2k)-X (X = DBCO; Maleimide; NHS) and 18:1 TAP (DOTAP) cationic lipid were obtained from Avanti Polar Lipids. Fluorescent labelling lipid, C11 TopFluor® Sphingomyelin was also acquired from Avanti Polar Lipids. Azido-dPEG®$_8$-NHS ester and TFP-dPEG$_{13}$-DSPE were provided by Merck (Darmstadt, Germany). HPLC grade Ethanol (EtOH) and Dimethyl sulfoxide (DMSO) were purchased from Thermo Fisher Scientific. Dulbecco's Modified Eagle Medium (DMEM) was obtained from Sigma, RPMI 1640 Medium, Fetal Bovine Serum (FBS) and penicillin–streptomycin from Thermo Fisher Scientific.

Isolation of Anakinra

The recombinant protein Anakinra was isolated from its other components present in its pharmaceutical form Kineret®, namely salts, using a desalting column (CentriPure 10, emp Biotech

GmbH, Berlin, Germany), and eluted with Phosphate buffer saline (PBS, 2 mM, pH 7.4) following the manufacturer instructions. Afterwards, the obtained concentration of anakinra was determined by BCA Protein Assay Kit (Thermo Scientific, Rockford, USA).

Anakinra-loaded Nanosystems (ANK-SNs) preparation

ANK-SNs composed by VitE, SM and surfactants lipids were prepared by adapting the straightforward and very simple ethanol injection method previously described by our group[22]. In short, 5 mg of VitE, 0.5 mg of SM and 0.05 mg of surfactants lipids were dissolved in 100 μL of ethanol. Blank-SNs were instantaneously formed by injecting the organic phase into 0.9 mL of ultrapure water, at room temperature (RT). ANK-SNs was then formed by dropwise adding ANK solution (14 μM) in PBS under magnetic stirring up to 5 minutes and incubated at RT for 6 hours followed by O/N at 4ºC. In the case of the cationic lipid, after adding ANK solution it was interacted with SNs for 30 minutes. ANK-SNs were stored at 4ºC until further use.

The purification of the ANK-SNs was carried out by spin filters (Amicon® Ultra Centrifugal Filters, 100K, 0.5mL, Merck) in a refrigerated microcentrifuge (5417R; Eppendorf) as previous reported by our group.

Preparation of TopFluor®-SM labelled ANK-SNs

Fluorescent labelled SNs were prepared as previously described in the section "Anakinra-loaded Nanosystems (ANK-SNs) preparation". Briefly, for subsequent *in vitro* assays TopFluor®-SM (4.5 μg) was mixed with the other compounds of the organic phase (final volume of 100 μL), The organic phase was then injected in 0.9 mL of ultrapure water and immediately formed at RT.

Physicochemical Characterization of the nanosystems

Particle size and polydispersity index (PdI) were determined by Dynamic Light Scattering (DLS), and Z-potential values by Laser Doppler Anemometry (LDA), using a Zetasizer NanoZS® (Malvern Instruments, Worcestershire, UK). Samples were diluted to 1:10 with ultrapure water and

the measurements were performed at 25ºC with a detection angle of 173º. All data is expressed as a mean value ± standard deviation (SD).

Both, SNs and ANK-SNs formulations were evaluated in relevant biological media to ensure the maintenance of their properties during *in vitro* assays. Formulations were incubated at 37ºC with 10% FBS (Fetal Bovine Serum) supplemented DMEM (Dulbecco's Modified Eagle Medium) and RPMI 1640 (Roswell Park Memorial Institute) under orbital shaking.

Additionally, extended characterization was performed by Nanoparticle Tracking Analysis (NTA). For NTA, the nanosystems were diluted at 1:1000 (v/v) in ultrapure water using a NanoSight NS3000 sytem (Malvern Instrument, UK) with laser operating at λ = 488 nm and 200 mW power. Data collection was settled with 3 repeats/60s capture time, with both shutter and gain manually determined for each sample. NTA 2.0 Build 127 software was used for measurement and subsequent data analysis.

ANK-SNs was analyzed by Matrix-Assisted Laser Desorption/Ionization (MALDI). For that, analysis was conducted in Ultraflex III TOF/TOF (Bruker) equipment, method used was MALDI linear mode ionization using a SA matrix (Sinapinic Acid) with previous sample ZipTip desalting.

Blank SNs and ANK-SNs particle size and morphology distribution was observed by Field Emission Scanning Electron Microscopy (FESEM) using a ZEISS FESEM ULTRA Plus, microscope (Carl Zeiss Micro Imaging, GmbH, Germany) configured with InLens and STEM modes and operating at 20 kV. 20 μL (0.55 mg/mL) of filtered nanosystems were stained with phosphotungstic acid (2% w/v) ratio 1:1. Next, 10 μL were placed on a carbon coated grid and left for 30s, twice. The grid was allowed to dry and then, repeatedly washed with filtered ultrapure water. Finally, it was let dry until its visualization.

In vitro studies in a PDAC cell line

The L3.6pl cell line (RRID:CVCL_0384), is a highly metastatic PDAC cell line, originally described by Bruns et al. (PMID: 10935470). L3.6pl cells were cultured in RPMI 1640 media (Invitrogen, Cat no. 61870044) containing 10% fetal bovine serum and 50 units/mL penicillin/streptomycin in a humidified incubator (5%) at 37°C, and cultures were tested for Mycoplasma periodically.

Cellular internalization in L3.6pl cells was evaluated by Confocal Laser Microscopy (CLM; Leica Microscope SP8®, Germany). $6x10^4$ cells were seeded in an 8-well chamber slide plate and growth O/N at 37ºC. Fluorescent-labelled TopFluor®-SM SNs and ANK-SNs (0.2 mg/mL) were added and let interact for 2 hours. Treatment was then removed, cells were fixed with 4% PFA (15 min) and cell nuclei were stained with Hoechst 33342 (ThermoFisher, USA).

Cell viability assays were conducted in L3.pl6 cells seeded at a density of 25,000 cell/well into a clear-bottomed and black walls P96-multiwell plate and incubated for 24 hours at 37ºC. To determine the toxicity of SNs and ANK-SNs, each was tested in separate experiments. Both were applied in increasing order of concentrations and incubated for 4 and 24 hours. Cell viability was determined using 1:10 dilution AlamarBlue™ assay. Fluorescence was read using a Victor Nivo™ multimode plate reader at 530 nm excitation and emission of 590 nm. Data were normalized to negative control 100% viability and reagent itself used as fluorescence background.

Establishment of CAF cell lines

Primary cultures of CAFs were obtained from PDAC surgical samples as described in *Yasuda et al*[23]. Briefly, tumor pieces were put in culture in IMDM medium (Lonza) plus 10% FBS, and CAFs obtained by outgrowth. CAFs were characterized for expression of the fibroblast-activation protein (FAP) marker by flow cytometry.

CAFs at 3rd-4th culture passage were stably transfected to express the human Telomerase Reverse Transcriptase gene (huTERT) by lentiviral infection using huTERT Cell Immortalization KIT (ALSTEM), according to manufacturer's instructions. 72h after infection, puromycin (SIGMA) selection applied at 1.5μg/mL final concentration. Puromycin resistant colonies were checked for hTERT expression by Real Time-qPCR. CAF cell lines were periodically tested for Mycoplasma contamination using the MycoBlue Mycoplasma Detector kit (D101, Vazyme).

CAF stimulation

CAFs were seeded at $3x10^4$ cells/well in IMDM 10% FBS in flat-bottom 96-well-plates and starved overnight without serum. The next day, medium was replaced with IMDM 2% FBS alone or with 20 ng/mL each recombinant human IL-1α plus IL-1β (R&D System). In the inhibition

experiments, ANK (Kineret, Amgen Europe), ANK-SNs and empty SNs were added at the indicated concentrations. After 4h incubation, medium was replaced with IMDM 2% FBS for 72h. Cell viability was tested as described below, and reported in Supplementary figure S1A. TSLP, IL-6 and IL-8 secretion in CAF supernatants was measured by ELISA (TSLP, R&D System; IL-6 and IL-8, Mabtech).

Th17 differentiation

Peripheral blood mononuclear cells (PBMCs) were obtained by Ficoll-hypaque gradient stratification from healthy donor buffy coats. Naïve $CD4^+$ T cells were magnetically isolated from PBMCs after two rounds of Naïve $CD4^+$ T cell Isolation Kit (Miltenyi Biotec), and plated at $1x10^6$ cells/well in 48 well-plates containing X-VIVO 20 in the presence of anti-CD2, anti-CD3 and anti-CD28 coated beads (Miltenyi Biotec). The following cytokines were added: IL-1β (10 ng/mL) (PeproTech or R&D System), IL-6 (20 ng/mL) (PeproTech), TGF-β (1 ng/mL) (PeproTech) and IL-23 (50 ng/mL) (PeproTech or R&D System). Th0 cells were obtained by stimulation of purified naïve $CD4^+$ T cells with the antibody-coated beads in the absence of the polarizing cytokines. In inhibition experiments, ANK, and ANK-SNs and empty SNs of the 4 formulations, were added at the different concentrations indicated. After 5 days, cells were collected and washed extensively, and their viability was determined by trypan blue exclusion and flow cytometry. $CD4^+$ T cells ($1x10^6$/mL) were restimulated for 24h with anti-CD2, anti-CD3 and anti-CD28 coated beads (one bead per cell). Cell viability was tested as described below and reported in Supp. Info **figure S4B-D**. Secretion of IL-17 and IFN-γ in culture supernatants was measured by ELISA (Mabtech).

Cell viability test

CAFs were stimulated with proinflammatory cytokines, and Th17 cells were differentiated both in the absence and in the presence of inhibitory stimuli, as described above. At the end of stimulation, CAFs were washed with PBS and 100 µl of IMDM 10% FBS culture medium was replaced, Th17 were collected and cultured in 100 µl X-VIVO 20. Cell viability was evaluated by addition of 20 µl/well of CellTiter 96 Aqueous One Solution Cell Proliferation Assay (PROMEGA) for 4 h. The absorbance was recorded at 490 nm and 650 nm to subtract background. Viability of Th17 cells was also tested by flow cytometry by staining with Live/Dead Aqua (Invitrogen).

Confocal microscopy

For CAF experiments, 1 x 10^5 cells/well were plated on glass coverslip previously treated with Poly-L-lysine solution 0,01% (Sigma) and starved overnight. The next day, CAFs were stimulated with IL-1α plus IL-1β (20 ng/mL/each) and treated with ± ANK or ANK-SNs-Top Fluor or Empty-SNs-Top Fluor for 4h, fixed with PFA 4% in PBS for 10 min at room temperature (RT) and washed with PBS. CAFs treated with SNs were permeabilized with 0,1% saponin in dH_2O for 15 min. The coverslips were then blocked overnight at 4°C with PBS 2% BSA. Successively, a first incubation with anti-IL-1R1 primary antibody (Invitrogen) for 1h at RT and a secondary incubation with Alexa Fluor 546 (Invitrogen) for 2h at RT were applied. Hoechst 33342 (Thermo Scientific) was added to mark the nuclei and the coverslips mounted in glycerol. Cells were imaged with Olympus FV3000 confocal laser scanning microscope.

For Th17 cell experiments, $CD4^+$ naïve T cells were magnetically isolated from PBMCs and plated at 1x10^6 cells/well on glass coverslip previously treated with Poly-L-lysine solution 0,01% (Sigma) and stimulated with IL-1β (10 ng/mL), IL-6 (20 ng/mL), TGF-β (1 ng/mL) and IL-23 (50 ng/mL) in presence of anti-CD2, anti-CD3 and anti-CD28 coated beads ± ANK-SNs-Top Fluor or Empty-SNs-Top Fluor for 5 days. Th17 cells were then harvested, fixed with PFA 4% in PBS for 10 min at RT, washed with PBS and blocked overnight at 4°C with PBS 2% BSA. Successively, a first incubation with anti-IL-1R1 primary antibody (Invitrogen) for 1h at RT and a secondary incubation with Alexa Fluor 546 (Invitrogen) for 2h at RT were applied. Hoechst 33342 (Thermo Scientific) is added to mark the nuclei and the coverslips are mounted in glycerol. Cells are imaged with Olympus FV3000 confocal laser scanning microscope.

For IL-1R quantification, area coverage for IL-1R1 on cellular surface was quantified using ImageJ Software. Z-plans were initially acquired and successively stacked obtaining a single image that was converted to 8-bit. After the threshold has been applied, the area of the image covered by the fluorochrome linked to IL-1RI was measured (Supp. Info **figure S5).** *In vitro* experiments performed in CAFs and Th17 cells were conducted in collaboration with the group of Dr. Maria Pia Protti "Tumor Immunology Unit" located in the Istituto di Ricovero e Cura a Carattere Scientifico (IRCCS) San Raffaele Scientific Institute, Milan, Italy.

Statistics

Differences between groups were statistically determined using two-tailed unpaired or paired Student *t*-test. The percentage of inhibition was calculated by considering the 100% expression the values of the positive controls in the case of ANK, and the empty-SNs in the case of ANK, SNs. All statistical analysis were performed using GraphPad Prism (Version 9.0 software) (GraphPadSoftware, San Diego, CA, USA). A p value < 0.05 was considered to be significant.

RESULTS AND DISCUSSION

Protein-based therapeutics are highly successful and have unprecedented potential in clinic accounting for more than 100 approved pharmaceutics by the EMA and the FDA to treat a wide variety of human conditions including cancer, autoimmunity/inflammation, exposure to infectious agents, and genetic disorders [24–27]. However, they suffer from enzymatic degradation, short half-life and low bioavailability which limits their translation from the bench to the market [28]. To overcome such issues, their delivery can be improved by combining therapeutic proteins with nanotechnology. In this regard, lipidic and polymeric nanocarriers have been described in the literature for this purpose [29,30]. In this work, the use of lipidic nanosystems enables covalent binding of the protein to the modified, hydrophobic carbon chains disposed onto the surface. This approach would not only enhance the incorporation of ANK to the nanosystem but also its interaction with the cytokines and other molecules released by TME components.

Development and characterization of ANK-SNs

In this work, blank-SNs were prepared by adapting the ethanol injection method for the single-step preparation and straightforward formation of nanosystems [22,31–34]. Followed by the dropwise addition of the recombinant protein ANK solution as represented in **figure 1A**. ANK was isolated from its pharmaceutical form Kineret® in order to incorporated it to the blank-SNs by using a desalting column and it was place in the suitable PBS buffer for its bioconjugation (**Fig. 1B**). Thus, to display ANK onto the surface of SNs, our strategy was to chemically conjugate it to a PEGylated stearic carbon chain containing a chemically active functional group to perform a covalent reaction

(DSPE-PEG(2k)-X; X = -NHS, -DBCO, -Maleimide) [35–37]. So far, PEGylated lipids have been extensively used to link biomolecules (such as proteins, peptides, and antibodies) to the nanostructures' surfaces. Moreover, PEG presents some features in drug delivery such as prolonged blood circulation times and reduced possible interactions with blood components (opsonization), giving 'stealth' properties to nanosystems [28,38,39]. Another strategy to incorporate ANK to blank-SNs was by adding a cationic lipid DOTAP. ANK (pI 5.46) presents a negative charge at physiological pH (7.4) used to synthesized ANK-SNs. Based on these assumptions, ANK will interact with the cationic lipid thanks to electrostatic interactions between charges. Nanosystems were physicochemical characterized in terms of size and surface charge by DLS and LDA (**Supp. Information Figures S1 and Tables S1-2**). As we will further explain, ANK-SNs composed by Vit E, SM, DSPE-PEG(2k)-NHS and ANK gave better results in TME cell cultures. From this point, characterization of ANK-SNs containing DSPE-PEG(2k)-X (X = -DBCO, -Maleimide) and DOTAP will be explained in "supporting information" data.

A

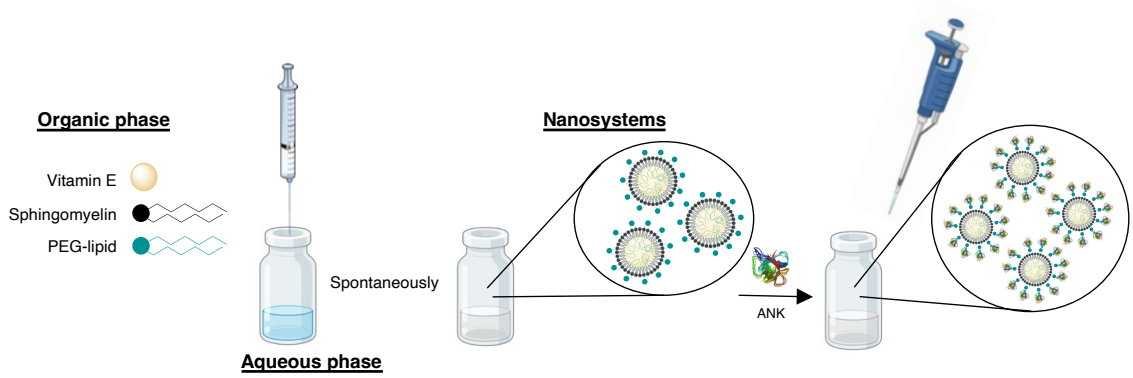

B

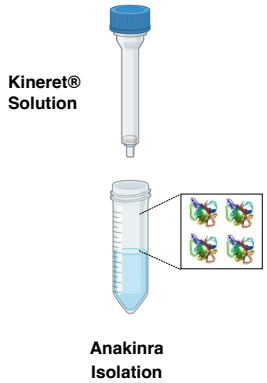

Figure 1. (A) Schematic representation of the single-step SNs nanosystems preparation by ethanol injection method. Followed by the dropwise addition of ANK solution in PBS at physiological pH. **(B)** Anakinra isolation from its pharmaceutical form (Kineret®) by using desalting columns.

Thus, blank-SNs and ANK-SNs presented a small particle size, a monodisperse population, and a negative zeta potential (**Table 1**). It must be noted that particles of this size (<200 nm) are more likely to accumulate in tumors thanks to the enhanced permeation retention (EPR) effect [40] (**Fig. 2A**). Furthermore, nanosystems with negative charged surface can reduce undesirable clearance by RES, improve blood compatibility, making delivery more efficiently to tumor sites [41]. It also makes it more biocompatible in comparison to positively charged nanosystems which interacts with cells structures by electrostatic interactions [41,42]. Likewise, its simple and safe composition based on GRAS (Generally Recognized as Safe by the United States FDA) materials (Vitamin E) and cell components (SM) makes it perfect candidates for the intended application and, its one-step formulation makes it more favorable from a pharmaceutical point of view. ANK-SNs was purified to remove ANK excess using spin filters as previously reported in the *chapter II*. Then, ANK incorporated to SNs was quantified by the microBCA method based on the Bradford's assay. It was calculated a 75% of ANK linked to SNs (**Table 1**).

Table 1. Physicochemical Characterization of blank-SNs and ANK-SNs measured by DLS and LDA. Percentage of ANK associated to SNs quantified by microBCA assay (Results are expressed as Mean ± SD, n = 5).

Formulation	Size (nm)	PdI	ZP (mV)	% ANK
Blank-SNs	60 ± 3	<0.2	- 21 ± 4	-
ANK-SNs	136 ± 2	0.2	- 23 ± 1	75 ± 2

To further characterize the physicochemical properties of blank-SNs and ANK-SNs (containing DSPE-PEG(2k)-NHS), other methods were used. As illustrated in **figure 2B** as complementary methods to DLS, nanosystems were characterized by NTA. Compared to blank-SNs, ANK-SNs presented a higher mean particle size as well as span value due to the incorporation of the protein

and the interaction of the nanoparticles with the buffer saline as shown in NTA data (**Table 2**). NTA analysis is based on the combination of a laser light scattering microscopy with a charge-coupled device camera that identifies and individual tracks nanoparticles moving under Brownian motion, calculating particle size and concentration [43,44]. D-values D10, D50, and D90, are representative of the particle diameter at 10, 50 and 90% cumulative distribution (**Table 2**). These findings correlate with DLS data.

Table 2. Physicochemical properties of blank-SNs and ANK-SNs determined by NTA. Mean particle size (diameter), D-values (D10, D50, D90), calculated SPAN value and sample concentration in particles per millilitre (particle/mL) (mean ± SD, n= 5).

Formulation	Mean size (nm)	D10	D50	D90	Span	Concentration (particles/mL)
Blank-SNs	87 ± 2	49 ± 5	85 ± 1	129 ± 3	0.7	5.4×10^{11}
ANK-SNs	133 ± 6	96 ± 2	132 ± 2	178 ± 3	0.9	6.2×10^{11}

MALDI-Tof spectrometry was also performed to evaluate an increase in ANK mass due to the covalent bond to DSPE-PEG(2k)-NHS (stimated ~2.8 kDa; **Fig. S2**). We observed an increment in mass of native form of ANK (17.3 kDa) compared to the ~20 kDa calculated for ANK linked to the nanosystems (**Fig. 2C**). Other nanosystems components such as VitE and SM are not detected by this technique as they are not coupled to the protein. Field Emission Scanning Electron Microscopy (FESEM) was used to check the particle distribution and spatial disposition. As shown in **figure 2D**, representative images were acquired clearly indicating the characteristic morphology and spherical shape of the SNs reported by our group [22]. The spherical distribution did not seem to be affected by the incorporation of ANK protein pointing out the good stability of the nanosystems. In the case of ANK-SNs, we observed a slightly increment in the particle size, also reported by DLS and NTA data.

As confirmed and verified by DLS, NTA, MALDI-Tof and FESEM analysis, ANK protein was successfully and efficiently incorporated in SNs surface. As expected, ANK association led to an increment in size of about 60-65 nm was observed. This extensive characterization of blank-SNs

and ANK-SNs is of extreme importance to understand subsequent interaction in both *in vitro* and *in vivo* scenarios.

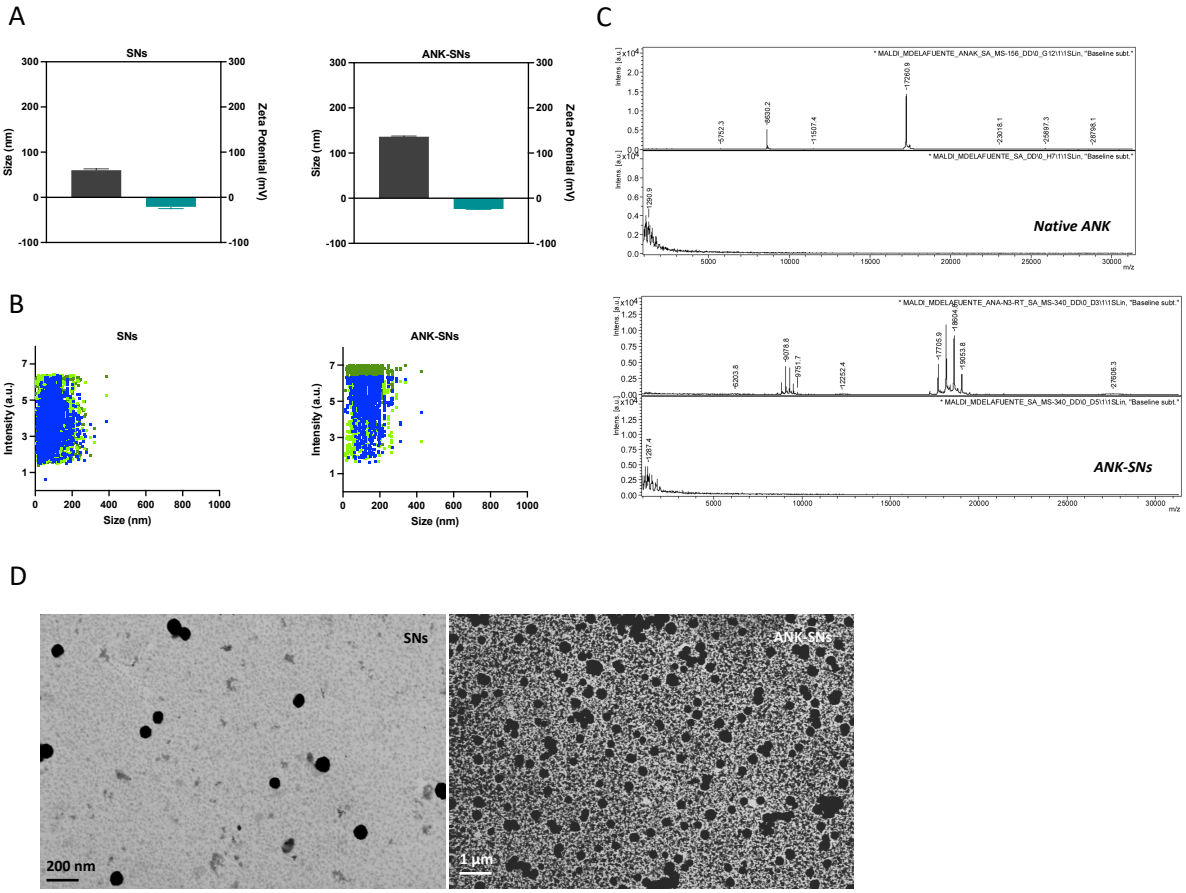

Figure 2. Physicochemical characterization of SNs vs. ANK-SNs nanosystems by several analytical techniques. (A) Size (nm) and surface charge (mV) of blank-SNs and ANK-SNs. Data are expressed as mean ± SD, at least n=5. **(B)** Complementary physicochemical characterization by Nanoparticle Tracking Analysis (NTA) of blank-SNs and ANK-SNs (n ± 5). **(C)** MALDI-Tof analysis of native ANK enzyme (calculated exact mass 17.260 kDa) and ANK-SNs (Calculated mean mass ~20 kDa). **(D)** Representative FESEM images of SNs (left) and ANK-SNs (right). SNs scale bar: 200 nm. ANK-SNs scale bar: 1µm.

ANK-SNs stability over time and in biorelevant media

To evidence the fate of nanosystems upon administration, monitoring the stability over time and at storage conditions in biological relevant media is essential. Colloidal stability under storage conditions was assessed for blank-SNs and ANK-SNs by DLS showing that both were stable for at least 1 month (**Fig. 3A**). Other ANK-SNs prototypes stability was studied for also 1 month (**Fig. S3**).

To determine the feasibility of these formulations for their testing *in vitro*, stability of blank-SNs and ANK-SNs were incubated in cell culture media (DMEM and RPMI supplement with 10% FBS) at 37 ºC and their particle size was monitored for 48 hours (**Fig. 3B-C**). Nanosystems remain stable in cell culture media containing serum proteins (FBS). This can be explained due to the adsorption of the serum proteins to the nanosystems surface due to charges balance. Also, ANK-SNs seemed to be stabilized thanks to the electrostatic interactions between ANK enzyme and serum proteins. Thereby, formulations maintained their colloidal properties, so, we proceeded with their internalization and cytotoxic evaluation *in vitro*.

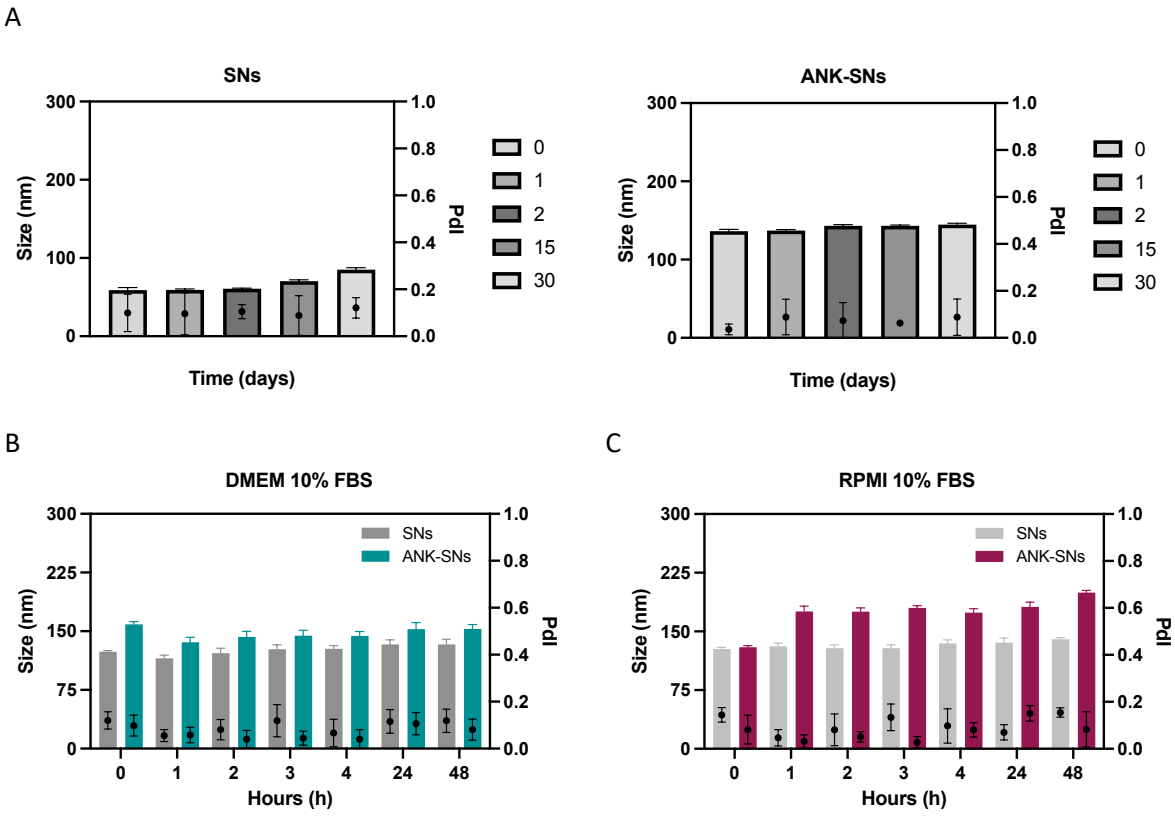

Figure 3. (A) Size (nm) and polydispersity index (PdI) measurements of blank-SNs and ANK-SNs, stability tested up to 30 days at storage conditions (4ºC). Stability of SNs and ANK-SNs upon incubation up to 48h in **(B)** DMEM and **(C)** RPMI, supplemented with 10% FBS at 37 ºC and under orbital stirring (300 r.p.m.).

In vitro evaluation of the nanosystems in metastatic PDAC cell line

As a first proof-of-concept that our developed nanosystems were able to efficiently interact with cancer cells, a highly metastatic PDAC cell line, L3.6pl was used for these experiments. Aside from internalization, we also assessed the cytotoxic profile of blank-SNs and ANK-SNs to establish a range of working dose and to avoid undesired side effects. This estimation is useful for subsequent experiments with the cells that compose the TME which is the aim of this study.

Internalization studies were conducted in L3.6pl cell line and evaluated by confocal microscopy. Fluorescent-labelled TopFluor®-SM was added to the lipid composition and nanosystems were prepared as previously described. As displayed in **figure 4A**, we detected high fluorescent signals at the two different time points tested, 2 and 4 hours. It was also noted that internalization was slightly more efficient in ANK-SNs compared to blank-SNs, probably related to the interaction of the enzyme with the components in cell membranes. All in all, both nanosystems resulted in a great uptake activity.

Regarding cell viability assays, cells were treated for 4 and 24 hours at increasing concentrations of total lipid composition of nanosystems (0.1 mg/mL to 10 mg/mL corresponding to 2.2 μg/mL to 220 μg/mL of ANK). Cytotoxicity was revealed by adding a 1:10 dilution of Alamar Blue™ fluorescent assay to each condition. **Figure 4B** shows that at lower concentrations nanosystems did not show toxicity. However, at higher concentrations a decreased in viability close to 50% is seen at 4-hour treatment in case of blank-SNs and at 24-hour testing, IC50 is reached for blank-SNs and ANK-SNs. On the other hand, we can confirm dose-dependent cytotoxicity. We have also observed that the incorporation of the enzyme in ANK-SNs led to increased % of viability in the two times evaluated. This may be due to the surface disposition of the ANK in SNs and its interaction with cells.

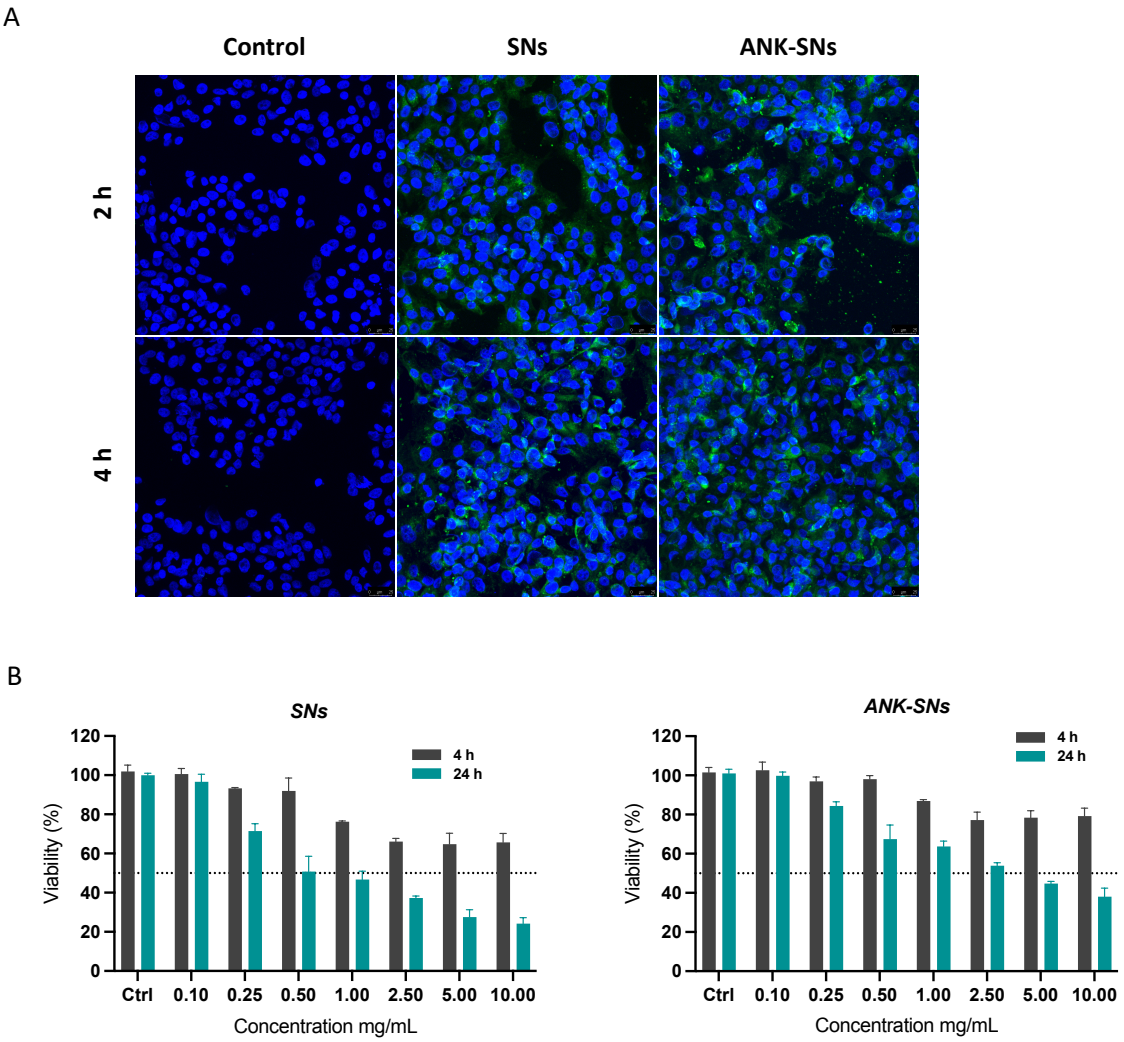

Figure 4. (A) Representative confocal microscopy images after 2- and 4-hours treatment incubation in metastatic PDAC cell line 'L3.6pl'. Fluorescent labelled TopFluor®-SNs and TopFluor®-ANK-SNs in green. Cell nuclei stained with Hoechst 33342 in blue. **(B)** Cell viability determined by Alamar Blue™ assay after treatment with SNs and ANK-SNs (0.1 mg/mL to 10 mg/mL) for 4- and 24- hours. Data are expressed as mean ± SD, (n > 3).

Cytokine release from IL-1-activated CAFs is inhibited by ANK-SNs

Several cytokines with tumor-promoting functions secreted by CAFs depend on the IL-1-IL-1R signaling. We previously set an *in vitro* system in which CAFs obtained by primary PDAC surgical samples were activated *in vitro* with recombinant IL-1α and IL-1β (or IL-1 containing supernatants from PDAC microenvironment cultures), and TSLP release was measured as a readout for Th2 cell differentiation [9–11]. We reported that addition of ANK in culture inhibited TSLP secretion, and thus, TSLP-dependent Th2 cell differentiation [9]. To test the function of ANK-SNs in the same system we performed *in vitro* experiments following the scheme reported in **figure 5A**. CAFs were stimulated with IL-1α and IL-1β in the absence and in the presence of ANK as free drug or ANK-SNs or empty-SNs (i.e., to evaluate the basal level of cytokine modulation by the SNs alone), after 2 days the supernatant was collected and TSLP, IL-6 and IL-8 release measured by ELISA. A dose-response curve was first performed to identify the optimal ANK concentrations (**Fig. 5B**). Based on the results we decided to use 5 μg/mL (i.e., the lower concentration to obtain the maximum inhibitory effect) and 0.1 μg/mL (i.e., concentration without inhibitory effects). We then tested the 4 formulations that use different ANK linking strategies, to detect the best performing one/s using the two selected concentrations (**Fig. 5C**). We found that formulation VitE/SM/NHS gave the best performance, and it was chosen for the following experiments (**Fig. 5C, right panel**). TSLP secretion was highly inhibited (70-80%) at concentration of 5 μg/mL ANK both used as free drug and linked to SNs (70-90%), whereas empty-SNs did not greatly influence TSLP secretion (**Fig. 5D**). Similar results were obtained when measuring the release of IL-6 (**Fig. 5E**) and IL-8 (**Fig. 5F**).

Collectively, ANK-SNs exert anti-tumor activity by interfering with the secretion of TSLP (i.e., Th2 cell differentiation), IL-6 and IL-8, thus dampening their tumor-promoting functions.

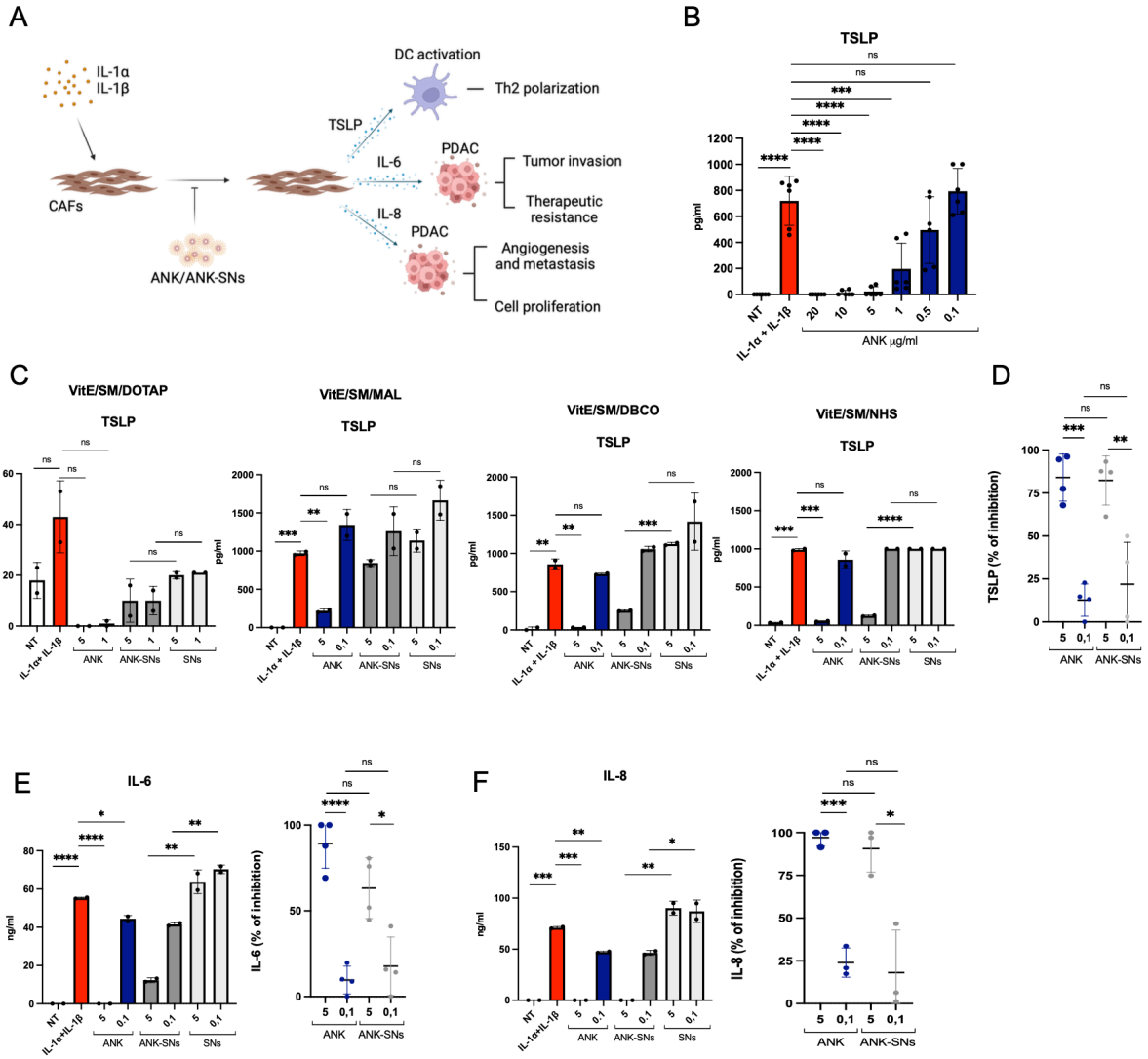

Figure 5. TSLP, IL-6 and IL-8 secretion by IL-1-treated CAFs is similarly downmodulated by targeting the IL-1-IL-1R pathway by both free ANK and ANK-SNs. (A) Experimental model. Tumor-derived IL-1 activates CAFs to secrete the tumor-promoting cytokines TSLP, IL-6 and IL-8, as indicated. CAFs were activated *in vitro* with IL-1α+IL-1β in the absence or in the presence of ANK or ANK-SNs or empty-SNs, and cytokine release measured after culture (see *Materials and Methods* for details). **(B)** Dose-response curve to detect the best concentrations of ANK to inhibit TSLP secretion by CAFs. NT=not treated, IL-1α+IL-1β were used as positive control for TSLP secretion.

ANK was added at the indicated concentrations. **(C)** The indicated 4 formulations of ANK-SNs were tested for their capacity to downmodulate TSLP secretion by IL-1 activated CAFs. NT = not treated. IL-1α+IL-1β were used as positive control. ANK concentrations 5 and 0.5 μg/mL were chosen based on the titration curve reported in B. Empty SNs (SNs) were used to calculate the basal level of cytokine secretion in the presence of the SNs. Based on these results the following experiments were performed using the VitE/SM/NHS formulation. **(D)** Percentage inhibition of cumulative experiments (n=4) calculated as described in *Materials and Methods*. **(E)** Left, representative example of IL-6 secretion. Right, % of inhibition of cumulative experiments (n=4) calculated as described in *Materials and Methods*. **(F)** Left, representative example of IL-8 secretion. Right, % of inhibition of cumulative experiments (n=4) calculated as described in *Materials and Methods*. Significance was calculated by Student's t-test and values were considered significantly different for *p<0.05, **p<0.01, **p<0.001.

ANK-SNs are superior to free ANK in dampening IL-17 secretion by *in vitro* differentiated Th17 cells

Due to the role of IL-1 in differentiation of Th17 cells [14,15,45,46], we then evaluate the effect of ANK-SNs added in culture during *in vitro* Th17 differentiation from naïve $CD4^+$ T cells. The experimental scheme is depicted in **figure 6A**. Naïve $CD4^+$ T cells were activated with antibody-coated beads in the presence of polarizing cytokines, and in the absence or the presence of ANK, used as free drug or linked to SNs. We first detected the best concentration of ANK, used as positive control, to inhibit IL-17 secretion by Th17 cells. Based on the titration curve, we decided to use 10 and 0.5 μg/mL (**Fig. 6B**). The 4 ANK-SNs formulations were then tested using as read out IL-17 secretion and, similarly to the results obtained with CAFs, formulation VitE/SM/NHS gave the best performance (**Fig. 6C**). At difference with what we observed in the CAF experiments, however, the presence of empty-SNs either did not impact on or lead to increase of IL-17 secretion (examples are reported in **Fig. 6C**, *right*; **Fig. 6D** l*eft* and *middle*), so that the final activity of ANK-SNs is the result of inhibitory but possibly also stimulatory effects (**Fig. 6D**, right). Importantly, ANK-SNs, at both 10 and 0,5 μg/mL, induced a significantly higher inhibition of IL-17 secretion compared with free ANK, demonstrating a superior activity of ANK-SNs than the free drug (**Fig. 6D**, right). As Th17 cells, in addition to IL-17, may secrete IFNγ, we measured this cytokine in the same experiments. As shown in **figure 6E**, both ANK and ANK-SNs inhibited IFNγ secretion, although when considering the highest drug concentrations inhibition of IFNγ secretion was much lower than IL-17. Due to the different behavior of the linked and free drug on IL-17 secretion,

collectively ANK-SNs exerted their modulatory effects principally by reducing the availability of pro-tumor IL-17.

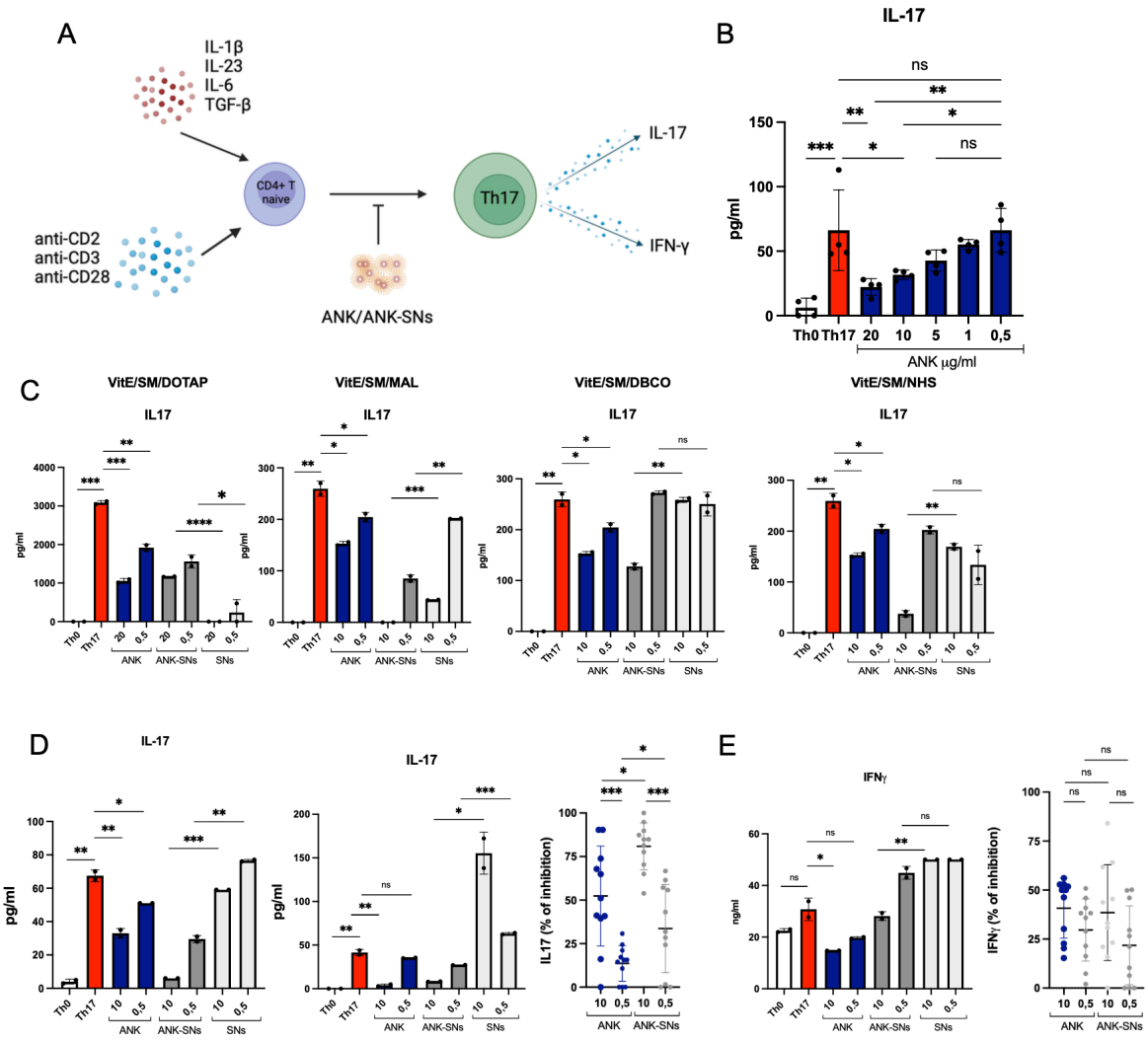

Figure 6. ANK-SNs are superior to free ANK in downmodulation of IL-17 secretion by *in vitro* differentiated Th17 cells. **(A)** Experimental model. Naïve CD4+ T cells were stimulated with anti-CD2, anti-CD3 and anti-CD28-coated beads, in the presence or in the absence of the polarizing cytokines IL-1β, IL-23, IL-6 and TGF-β. At day 5 of culture, cells were collected, restimulated with the antibody-coated beads and IL-17 and IFN-γ secretion was measured by ELISA. **(B)** Dose-response curve to detect the best concentrations of ANK to inhibit IL-17 secretion by Th17 cells. Th0= naïve CD4+ T cells activated with the antibody-coated beads in the absence of polarizing cytokines. Th17= CD4+ T cells differentiated as described above, and in the *Materials and Methods*. ANK was added at the indicated

concentrations. **(C)** The indicated 4 formulations of ANK-SNs were tested for their capacity to downmodulate IL-17 secretion by *in vitro* Th17 differentiated CD4+ T cells. Th0 cells were used as negative control. ANK, ANK-SNs and Empty SNs were added at the indicated concentrations, based on titration curves shown in B. Based on these results the following experiments were performed using the VitE/SM/NHS formulation. **(D)** Left and middle, representative experiments of IL-17 secretion with irrelevant or stimulatory activity of empty SNs. Right, % of inhibition of cumulative experiments (n=11) calculated as described in *Materials and Methods*. **(E)** Left, representative experiment of IFN-γ secretion. Right, % of inhibition of cumulative experiments (n=11) calculated as described in *Materials and Methods*. Significance was calculated by Student's t-test and values were considered significantly different for *$p<0.05$, **$p<0.01$, **$p<0.001$.

CONCLUSIONS

IL1 present a direct and indirect role in tumor-promoting inflammation in PDAC by promoting the secretion of several tumor-promoting cytokines by CAFs and Th17 differentiated cells. In this context, IL-1R antagonist, anakinra (ANK) has been previously described as an effective anti-tumor agent. In this study, our developed sphingomyelin nanosystems loaded with anakinra (ANK-SNs) have demonstrated to exert immunomodulatory effects in PDAC upon *in vitro* testing of TME cells. Thus, ANK-SNs inhibited the secretion of TSLP (i.e., Th2 cell differentiation), IL-6 and IL-8 by CAFs, diminishing their tumor-promoting functions. Regarding Th17 differentiated cells, ANK-SNs also highly inhibited IL-17 secretion significantly superior to the free form of ANK.

Our aim, in further research, is to translate the *in vitro* data to the appropriate *in vivo* models to test the feasibility of ANK-SNs.

SUPPORTING INFORMATION

MATERIALS AND METHODS

Azide-modified anakinra (N3-ANK) preparation and characterization

Protein ANK (0.058 μmol) was modified with Azido-dPEG®$_8$-NHS linker (1.16 μmol) (Sigma, Darmstadt, Germany) in phosphate buffer saline (PBS; 10mM). Reaction was performed at RT for 6 hours and storage at 4ºC. Linker excess was removed by using spin filters (Amicon® Ultra Centrifugal Filters, 10k, 0.5mL, Merck).

N3-ANK modification was characterized by HPLC-MS (TimsTof Pro, Bruker; coupled to the ELUTE UHPLC) by dissolving 5 pmol of sample in ultrapure water. Analysis method used was positive ESI ionization, acquisition range 500-3000 m/z, chromatographic separation with column C4, mobile phases employed were A: Water/formic acid 0.1%, B: acetonitrile/formic acid 0.1%; and chromatographic separation time 15 minutes. MALDI Tof analysis was carried out in Ultraflex III TOF/TOF (Bruker), analysis method chosen was MALDI linear mode ionization using a SA matrix (Sinapinic Acid).

RESULTS

In order to perform SPAAC 'click' chemistry reaction to SNs containing DSPE-PEG(2k)-DBCO, ANK must be modified with a linker to incorporate to its structure the highly reactive group azide (-N_3). For that, we have made to react the lysines (amino acids) that have a terminal amine group (-NH_2) to the -NHS ester present in the linker.

As explained in the 'main', a set of ANK-SNs formulations were prepared using different lipid composition and chemical strategies to further test them in TME cells to observe which formulation offered a better performance. However, due to its physicochemical properties (particle size) and lower ANK association, nanosystems composed by VitE/SM/TFP were discarded (**Tables S1-2**). The rest of nanosystems were tested in TME PDAC cells such as CAFs and TILs.

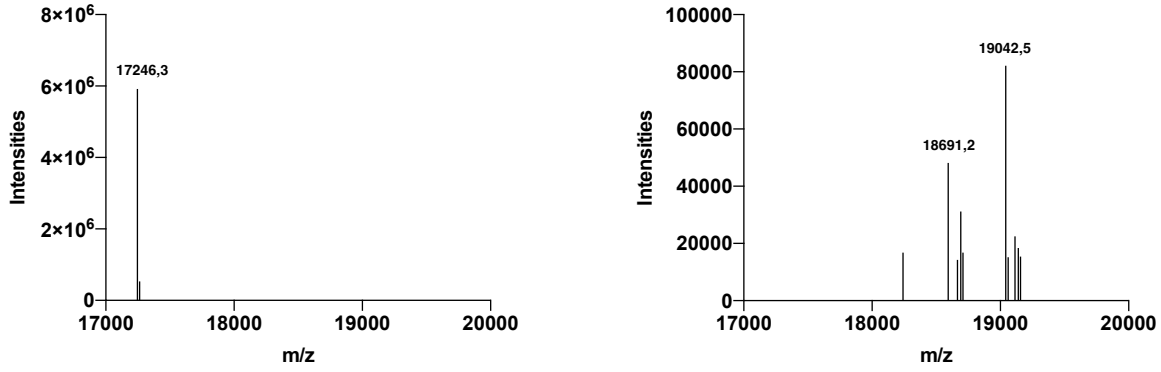

Figure S1. Characterization of Azide-modified anakinra (N3-ANK) with Azido-dPEG®8-NHS by HPLC-MS spectrometry. Left panel: native ANK enzyme; Right panel: N3-ANK modified enzyme.

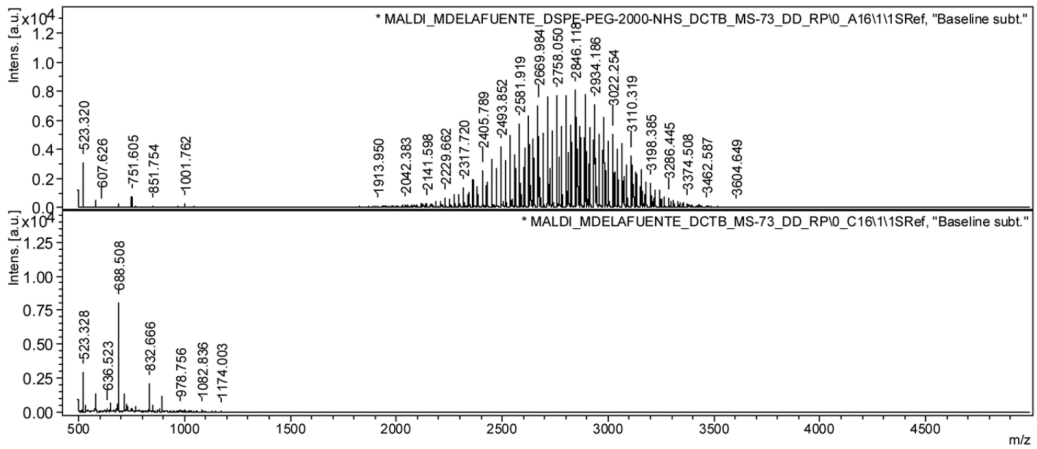

MALDI-TOF: DSPE-PEG(2000)-NHS

Figure S2. MALDI-Tof analysis of DSPE-PEG(2k)-NHS to calculate its mass(2.8 kDa) corresponding to the one given by the manufacturer.

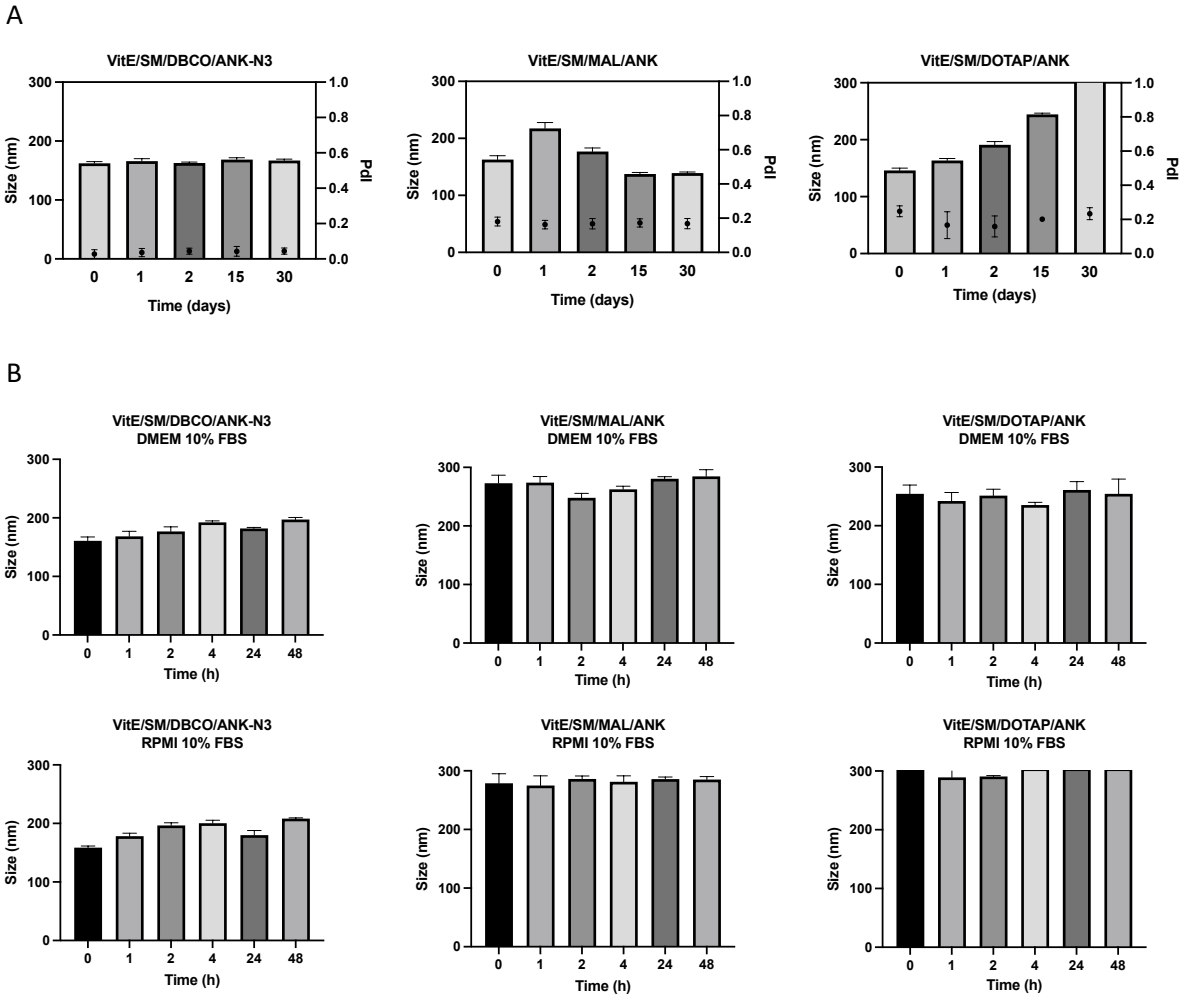

Figure S3. **(A)** Stability over time under at 4 ºC storage conditions of ANK-SNs (different lipid compositions as indicated in the graphs) measured by DLS . **(B)** Stability of ANK-SNs upon incubation in biorelevant media, namely, DMEM (upper panel) and RPMI (lower panel) supplemented with 10% FBS at 37 ºC and under orbital stirring (300 r.p.m.).

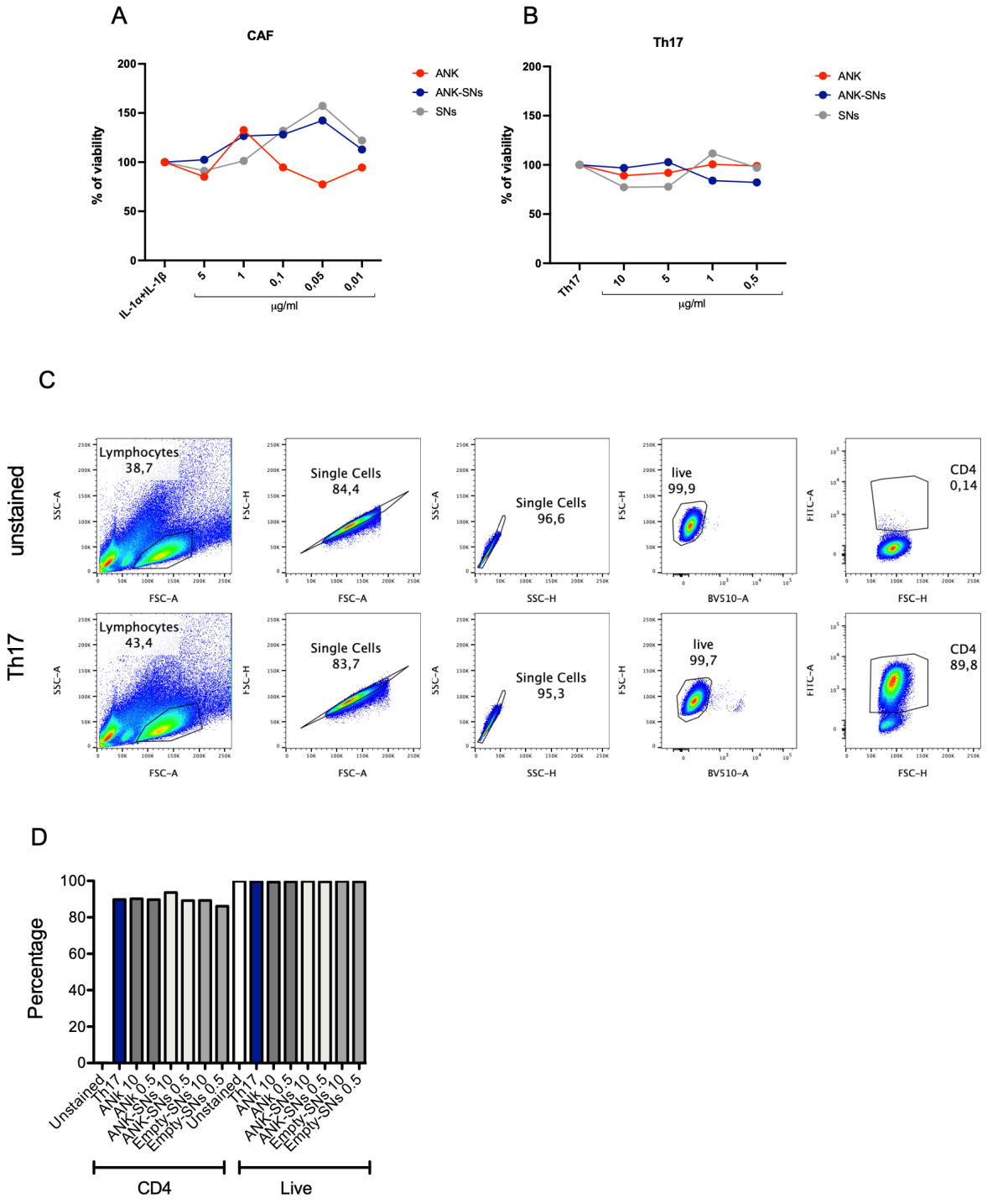

Figure S4. Inhibitory stimuli do not impact on cell viability. **(A)** Percentage cell viability detected by colorimetric assay of CAFs in the presence of the pro-inflammatory cytokines (IL-1α plus IL-1β) alone, or in the presence of ANK, ANK-SNs and empty SNs. **(B)** Percentage cell viability detected by colorimetric assay of Th17 cells differentiated, as described in the Materials and Methods, in the absence or in the presence of ANK, ANK-SNs and empty SNs. **(C)** Percentage live cells detected by flow cytometry of Th17 cells either untreated or treated with ANK or ANK-SNs. Representative plots of unstained and stained Th17 cells. **(D)** Percentage of CD4+ T and live cells in the different experimental conditions.

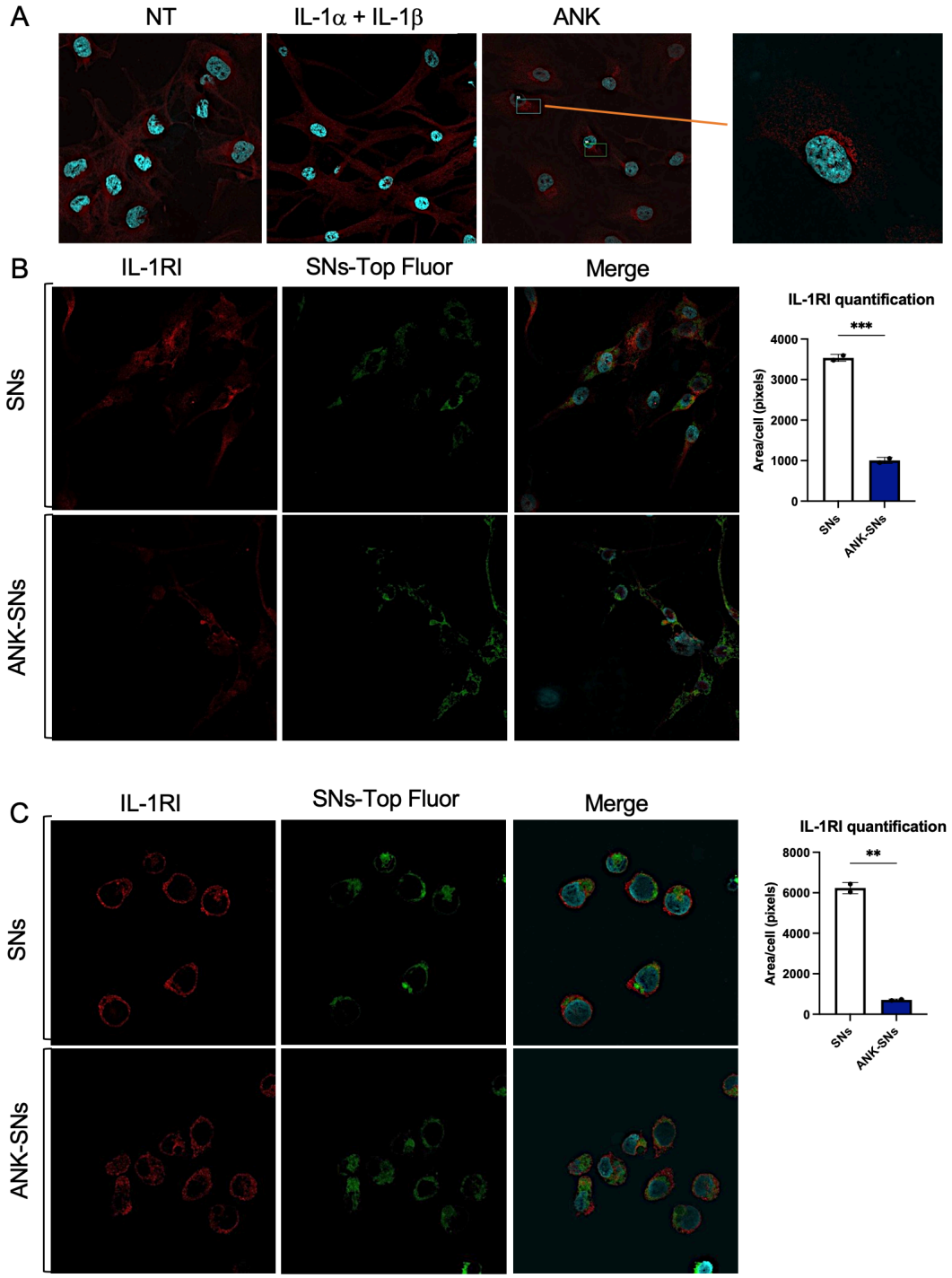

Figure S5. (A) Confocal laser scanning images of CAFs either untreated (NT) (left), or treated with IL-1α and IL-1β (middle), or treated with ANK (right). The IL-1R (red) distribution/internalization is shown. Cell nuclei are counterstained with Hoechst (blue). Confocal microscopy images of IL-1RI (red) present on cell surface of CAFs **(B)** and Th17 **(C)** after the treatment with ANK-SNs (Top Fluor, green, lower panels) compared to empty SNs (upper panels). Cell nuclei are counterstained with Hoechst (blue). Right, histograms represent the quantification of the area covered by IL-1RI analyzed by the ImageJ software. Significance was calculated by Student's t-test and values were considered significantly different for **p<0.01, and **p<0.001.

Table S1. Physicochemical Characterization of blank-SNs (composed by VitE/SM/PEG-lipid-X) measured by DLS and LDA (Results are expressed as Mean ± SD, n = 5). Abbreviations: nm: nanometer, PdI: polydispersity index, ZP: zeta potential in millivolts (mV).

Formulation	Size (nm)	PdI	ZP (mV)
VitE/SM/DBCO	55 ± 1	<0.2	-26 ± 1
VitE/SM/Maleimide	61 ± 2	<0.2	-28 ± 1
VitE/SM/NHS	60 ± 3	0.2	-21 ± 4
VitE/SM/TFP	71 ± 1	0.2	-30 ± 3
VitE/SM/DOTAP	56 ± 6	0.2	27 ± 6

Table S2. Physicochemical Characterization of ANK-SNs measured by DLS and LDA. Percentage of ANK associated to SNs quantified by microBCA assay. (Results are expressed as Mean ± SD, n = 5). Abbreviations: nm: nanometer, PdI: polydispersity index, ZP: zeta potential in millivolts (mV).

Formulation	Size (nm)	PdI	ZP (mV)	% ANK
VitE/SM/DBCO/ANK	162 ± 2	<0.1	-28 ± 1	92 ± 2
VitE/SM/Maleimide/ANK	163 ± 7	0.2	-22 ± 1	72 ± 1
VitE/SM/NHS/ANK	136 ± 2	0.2	-23 ± 1	75 ± 2
VitE/SM/TFP/ANK	215 ± 6	0.2	-33 ± 1	52 ± 3
VitE/SM/DOTAP/ANK	166 ± 11	0.2	22 ± 2	-

REFERENCES

1. Hidalgo, M. Pancreatic Cancer. *New England Journal of Medicine* **362**, 1605–1617 (2010).

2. Rahib, L. *et al.* Projecting cancer incidence and deaths to 2030: The unexpected burden of thyroid, liver, and pancreas cancers in the united states. *Cancer Research* vol. 74 2913–2921 Preprint at https://doi.org/10.1158/0008-5472.CAN-14-0155 (2014).

3. Leinwand, J. & Miller, G. Regulation and modulation of antitumor immunity in pancreatic cancer. *Nature Immunology* vol. 21 1152–1159 Preprint at https://doi.org/10.1038/s41590-020-0761-y (2020).

4. Garlanda, C. & Mantovani, A. Interleukin-1 in tumor progression, therapy, and prevention. *Cancer Cell* **39**, 1023–1027 (2021).

5. Dosch, A. R., Singh, S., Nagathihalli, N. S., Datta, J. & Merchant, N. B. Interleukin-1 signaling in solid organ malignancies. *Biochimica et Biophysica Acta - Reviews on Cancer* vol. 1877 Preprint at https://doi.org/10.1016/j.bbcan.2021.188670 (2022).

6. Gukovsky, I., Li, N., Todoric, J., Gukovskaya, A. & Karin, M. Inflammation, autophagy, and obesity: Common features in the pathogenesis of pancreatitis and pancreatic cancer. *Gastroenterology* **144**, (2013).

7. Hausmann, S., Kong, B., Michalski, C., Erkan, M. & Friess, H. The Role of Inflammation in Pancreatic Cancer. in *Inflammation and Cancer. Advances in Experimental Medicine and Biology* vol. 816 129–151 (2014).

8. Wörmann, S. M., Diakopoulos, K. N., Lesina, M. & Algül, H. The immune network in pancreatic cancer development and progression. *Oncogene* vol. 33 2956–2967 Preprint at https://doi.org/10.1038/onc.2013.257 (2014).

9. De Monte, L. *et al.* Intratumor T helper type 2 cell infiltrate correlates with cancer-associated fibroblast thymic stromal lymphopoietin production and reduced survival in pancreatic cancer. *Journal of Experimental Medicine* **208**, 469–478 (2011).

10. De Monte, L. *et al.* Basophil recruitment into tumor-draining lymph nodes correlates with Th2 inflammation and reduced survival in pancreatic cancer patients. *Cancer Res* **76**, 1792–1803 (2016).

11. Brunetto, E. *et al.* The IL-1/IL-1 receptor axis and tumor cell released inflammasome adaptor ASC are key regulators of TSLP secretion by cancer associated fibroblasts in pancreatic cancer. *J Immunother Cancer* **7**, (2019).

12. Lang, C., Wang, J. & Chen, L. CD25-expressing Th17 cells mediate CD8+ T cell suppression in CTLA-4 dependent mechanisms in pancreatic ductal adenocarcinoma. *Exp Cell Res* **360**, 384–389 (2017).

13. Chellappa, S. *et al.* Regulatory T cells that co-express RORγt and FOXP3 are pro-inflammatory and immunosuppressive and expand in human pancreatic cancer. *Oncoimmunology* **5**, (2016).

14. Barilla, R. M. *et al.* Specialized dendritic cells induce tumor-promoting IL-10 + IL-17 + FoxP3 neg regulatory CD4 + T cells in pancreatic carcinoma. *Nat Commun* **10**, (2019).

15. He, S. *et al.* Distribution and clinical significance of Th17 cells in the tumor microenvironment and peripheral blood of pancreatic cancer patients. *Int J Mol Sci* **12**, 7424–7437 (2011).

16. McAllister, F. *et al.* Oncogenic kras activates a hematopoietic-to-epithelial IL-17 signaling axis in preinvasive pancreatic neoplasia. *Cancer Cell* **25**, 621–637 (2014).

17. Zhuang, Z. *et al.* IL1 receptor antagonist inhibits pancreatic cancer growth by abrogating NF-κB activation. *Clinical Cancer Research* **22**, 1432–1444 (2016).

18. Dosch, A. R. *et al.* Targeting tumor-stromal IL6/STAT3 signaling through IL1 receptor inhibition in pancreatic cancer. *Mol Cancer Ther* **20**, 2280–2290 (2021).

19. Takahashi, R. *et al.* Interleukin-1β-induced pancreatitis promotes pancreatic ductal adenocarcinoma via B lymphocyte-mediated immune suppression. *Gut* **70**, 330–341 (2021).

20. Mucciolo, G. *et al.* IL17A critically shapes the transcriptional program of fibroblasts in pancreatic cancer and switches on their protumorigenic functions. *Proceedings of the National Academy of Sciences* **118**, (2021).

21. Carlos Becerra, Andrew Scott Paulson, Keith M Cavaness & Scott A. Celinski. Gemcitabine, nab-paclitaxel, cisplatin, and anakinra (AGAP) treatment in patients with localized pancreatic ductal adenocarcinoma (PDAC). *Journal of Clinical Oncology* **36**, (2018).

22. Bouzo, B. L., Calvelo, M., Martín-Pastor, M., García-Fandiño, R. & De La Fuente, M. *In Vitro*- In Silico Modeling Approach to Rationally Designed Simple and Versatile Drug Delivery Systems. *Journal of Physical Chemistry B* **124**, 5788–5800 (2020).

23. Yasuda, T. *et al.* Protocol to establish cancer-associated fibroblasts from surgically resected tissues and generate senescent fibroblasts. *STAR Protoc* **2**, (2021).

24. Keservani, R. K., Sharma, A. K. & Jarouliya, U. U. *Correspondencia Correspondence Protein and Peptide in Drug Targeting and its Therapeutic Approach*. *Ars Pharm* vol. 56 (2015).

25. Sauna, Z. E. *et al.* Recent advances in (therapeutic protein) drug development. *F1000Research* vol. 6 Preprint at https://doi.org/10.12688/f1000research.9970.1 (2017).

26. Dimitrov, D. S. Therapeutic proteins. *Methods in Molecular Biology* **899**, 1–26 (2012).

27. Golan, D., Beca, Q. & Leader, B. Protein therapeutics: a summary and pharmacological classification. *Nat Rev Drug Discov* **7**, 21–39 (2008).

28. Viegas, C., Seck, F. & Fonte, P. An insight on lipid nanoparticles for therapeutic proteins delivery. *Journal of Drug Delivery Science and Technology* vol. 77 Preprint at https://doi.org/10.1016/j.jddst.2022.103839 (2022).

29. Dilliard, S. A. & Siegwart, D. J. Passive, active and endogenous organ-targeted lipid and polymer nanoparticles for delivery of genetic drugs. *Nature Reviews Materials* vol. 8 282–300 Preprint at https://doi.org/10.1038/s41578-022-00529-7 (2023).

30. Sivadasan, D., Sultan, M. H., Madkhali, O., Almoshari, Y. & Thangavel, N. Polymeric lipid hybrid nanoparticles (Plns) as emerging drug delivery platform—a comprehensive review of their properties, preparation methods, and therapeutic applications. *Pharmaceutics* vol. 13 Preprint at https://doi.org/10.3390/pharmaceutics13081291 (2021).

31. Nagachinta, S. *et al.* Radiolabelling of lipid-based nanocarriers with fluorine-18 for *in vivo* tracking by PET. *Colloids Surf B Biointerfaces* **188**, (2020).

32. Nagachinta, S., Bouzo, B. L., Vazquez-Rios, A. J., Lopez, R. & de la Fuente, M. Sphingomyelin-based nanosystems (SNs) for the development of anticancer miRNA therapeutics. *Pharmaceutics* **12**, (2020).

33. Bouzo, B. L. *et al.* Sphingomyelin nanosystems loaded with uroguanylin and etoposide for treating metastatic colorectal cancer. *Sci Rep* **11**, (2021).

34. Díez-Villares, S. *et al.* Quantitative PET tracking of intra-articularly administered 89Zr-peptide-decorated nanoemulsions. *Journal of Controlled Release* **356**, 702–713 (2023).

35. Wang, L., Jiang, R., Wang, L., Liu, Y. & Sun, X. L. Preparation of chain-end clickable recombinant protein and its bio-orthogonal modification. *Bioorg Chem* **65**, 159–166 (2016).

36. Yoon, H. Y., Lee, D., Lim, D. K., Koo, H. & Kim, K. Copper-Free Click Chemistry: Applications in Drug Delivery, Cell Tracking, and Tissue Engineering. *Advanced Materials* vol. 34 Preprint at https://doi.org/10.1002/adma.202107192 (2022).

37. Menon, I., Zaroudi, M., Zhang, Y., Aisenbrey, E. & Hui, L. Fabrication of active targeting lipid nanoparticles: Challenges and perspectives. *Mater Today Adv* **16**, (2022).

38. Suk, J. S., Xu, Q., Kim, N., Hanes, J. & Ensign, L. M. PEGylation as a strategy for improving nanoparticle-based drug and gene delivery. *Advanced Drug Delivery Reviews* vol. 99 28–51 Preprint at https://doi.org/10.1016/j.addr.2015.09.012 (2016).

39. Milton Harris, J. & Chess, R. B. Effect of pegylation on pharmaceuticals. *Nature Reviews Drug Discovery* vol. 2 214–221 Preprint at https://doi.org/10.1038/nrd1033 (2003).

40. Fang, J., Nakamura, H. & Maeda, H. The EPR effect: Unique features of tumor blood vessels for drug delivery, factors involved, and limitations and augmentation of the effect. *Advanced Drug Delivery Reviews* vol. 63 136–151 Preprint at https://doi.org/10.1016/j.addr.2010.04.009 (2011).

41. Duan, X. & Li, Y. Physicochemical characteristics of nanoparticles affect circulation, biodistribution, cellular internalization, and trafficking. *Small* vol. 9 1521–1532 Preprint at https://doi.org/10.1002/smll.201201390 (2013).

42. Cheng, Q. *et al.* Selective organ targeting (SORT) nanoparticles for tissue-specific mRNA delivery and CRISPR–Cas gene editing. *Nat Nanotechnol* **15**, 313–320 (2020).

43. Filipe, V., Hawe, A. & Jiskoot, W. Critical evaluation of nanoparticle tracking analysis (NTA) by NanoSight for the measurement of nanoparticles and protein aggregates. *Pharm Res* **27**, 796–810 (2010).

44. Kim, A., Ng, W. B., Bernt, W. & Cho, N. J. Validation of Size Estimation of Nanoparticle Tracking Analysis on Polydisperse Macromolecule Assembly. *Sci Rep* **9**, (2019).

45. Chung, Y. *et al.* Critical Regulation of Early Th17 Cell Differentiation by Interleukin-1 Signaling. *Immunity* **30**, 576–587 (2009).

46. Sha, Y. & Markovic-Plese, S. Activated IL-1RI signaling pathway induces th17 cell differentiation via interferon regulatory factor 4 signaling in patients with relapsing-remitting multiple sclerosis. *Front Immunol* **7**, (2016).

Chapter V

Sphingomyelin Nanoparticles (SNPs) for the efficient intracellular delivery of CRISPR/Cas9 genome editing systems

MARCELINA ABAL SANISIDRO

Sphingomyelin Nanoparticles (SNPs) for the efficient intracellular delivery of CRISPR/Cas9 genome editing systems

ABSTRACT

CRISPR/Cas9 has emerged as a potent tool for the efficient genome editing for several applications such as disease modelling, cell therapy, diagnosis and treatment of many diseases including cancer and rare genetic metabolic diseases among others. However, its application is hampered by poor stability, pharmacokinetic profile, and limited trespassing of biological barriers of CRISPR payloads. Viral vectors have been exploited for the efficient delivery of CRISPR components. Nevertheless, they present associated high immunogenicity and toxicity, hindering clinical translation. Thus, new delivery methods based on the use of nanotechnology have come up. In this study, we have developed Sphingomyelin nanoparticles (SNPs) for the efficient delivery of CRISPR/Cas9. We have performed a proof-of-concept of the gene editing by disrupting PLK1 gene in HEK293T and A549 cancer cell line. Finally, we have translated our developed nanoplatform for the delivery of CRISPR systems to *ex vivo* cultures of human samples for the treatment of rare genetic metabolic diseases.

Overall discussion

OVERALL DISCUSSION

Proteins are the most dynamic and diverse biological macromolecules in the body. Their roles comprise biochemical catalysis, forming receptors and channels in the membranes, provide structural support and transport molecules, among others [1]. It is estimated that there are more than 40,000 proteins in our bodies, which may contain mutations and/or abnormalities. These features make a great opportunity to harness proteins as therapeutics to alleviate many diseases [2–5]. To this date, more than 130 protein therapeutics have been approved by the US Food and Drug Administration (FDA) and many more are currently in clinical trials and under development for a variety of diseases[2,4,6,7] (**Figure 1**).

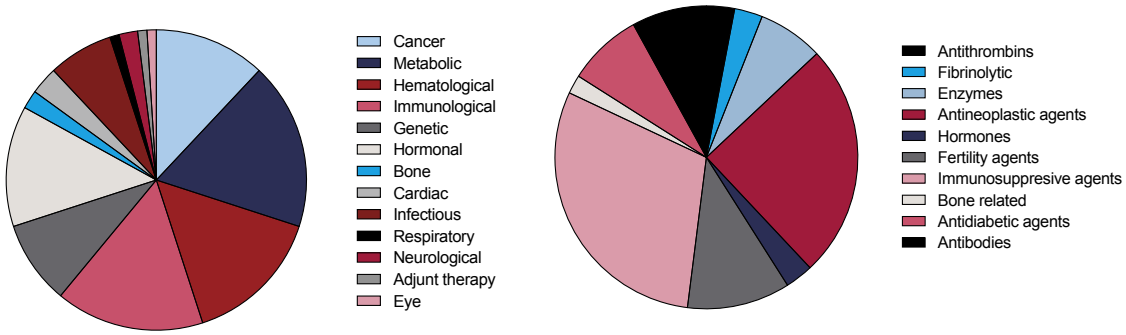

Figure 1. A schematic representation of the distribution of therapeutic proteins based on disease, and pharmacological class [6].

In addition, protein therapeutics offer several advantages compared to small drugs. There are multiple specific and complex functions that cannot be mimicked by small chemical compounds. Due to their specificity, proteins have less potential to interfere with biological processes and cause side effects, as well as they are less prone to trigger immunogenic responses [7]. Protein therapeutics

seem to be adequate for their use in protein replacement therapies when a gene is deleted or mutated as an alternative to recent developed and approved gene therapies that are not still available for many disorders [8]. However, protein therapeutics based on the administration of naked recombinant proteins or antibodies present some drawbacks [3,9]. For instance, glycosylation patterns must be well preserved to not alter protein activity, half-life, and immunogenicity in the body. This also is translated to antibodies, whose application can be limited due to the immune response generated, being necessary the replacement of antigen-binding specificity with human Ig sequences that confer stability and biological activity [10,11]. Furthermore, proteins solubility, stability and bioavailability, hinder the successful protein therapies use. Such challenges may be alleviated by the combination of the protein therapeutics and nanotechnology, which has emerged as a promising tool in medicine for the development of innovative therapeutics among other applications. Many nanomedicines have been approved in the last decades and many more are being developed [12]. Notably, lipid-based nanoparticles, polymeric nanoparticles, and inorganic nanomaterials, present several advantages as drug carriers. Importantly, the success of nanoparticle formulations of small drugs such as Doxil®, DaunoXome® and Abraxane®, has paved the way for the use of nanotechnology for protein delivery. Thus, in the context of protein therapeutics, nanoparticles can protect proteins from degradation or unfolding, increase the half-life and circulation times, control release and dose at specific sites, and target intracellular and extracellular compartments [13,14]. Nevertheless, nanoparticles tend to form aggregates once in blood circulation which can trigger opsonization and fast clearance reducing their effectiveness [15]. Therefore, for protein delivery, tailoring nanoparticles to increase blood circulation while maintaining protein function is the goal. Controlling surface materials that offer stealth properties, nanoparticles' size and charge is very important. Smaller nanoparticles (< 200 nm) are known to escape phagocytosis and tend to circulate longer compared to larger nanoparticles that are more easily cleared by the liver, spleen, and lungs. Also, a neutral charge is desired to avoid nonspecific internalization and to not activate plasma complement proteins [15,16]. It should be remarked that leaky vasculature and angiogenesis in inflammatory tissues in several diseases including cancer, atherosclerosis, and neurodegenerative diseases, improve access to nanoparticles that can extravasate from the blood circulation to local sites and accumulate. This mechanism is called the enhanced permeability and retention (EPR) effect, and it allows passive targeting and selective accumulation of nanoparticles in these lesions[17] (**Figure 2**). Nonetheless, vessel heterogeneity, low blood supply, and blood flow distribution limit the penetration of nanoparticles via EPR effect alone. Retention of nanoparticles can be enhanced by attaching targeting ligands such as antibodies, peptides, or small drugs onto the surface

increasing accumulation at specific sites (active targeting). Tailoring the coating materials and targeting ligands play a key role for a satisfactory endocytosis of nanoparticles [18]. Consequently, nanoparticles must perform endosomal escape to release active protein cargoes. In this sense, nanoparticles could be designed as stimuli-responsive materials under specific cellular conditions. For instance, pH or light can activate cargo release of proteins. Several studies have been published in this field based on stimuli-responsive polymeric nanoparticles, lipid-based nanoparticles, and inorganic materials [19,20]. Other important issue is the administration route. Protein therapeutics are often administered intravenously (i.v.), intramuscularly (i.m.) or subcutaneously (s.c.). Although, non-invasive routes, mucosal (oral, nasal, pulmonary) and transdermal are painless and simpler. However, these administration routes still result unpredictable/low bioavailability for protein delivery. In addition, the extreme conditions in the gastrointestinal tract, poor penetration of the proteins across mucosal or skin barriers, and/or variable inhalation efficiency limit protein therapies [13,14,21]. Nanotechnology arises as a potent and novel platform for protein delivery nanocarriers to address these non-traditional administration routes.

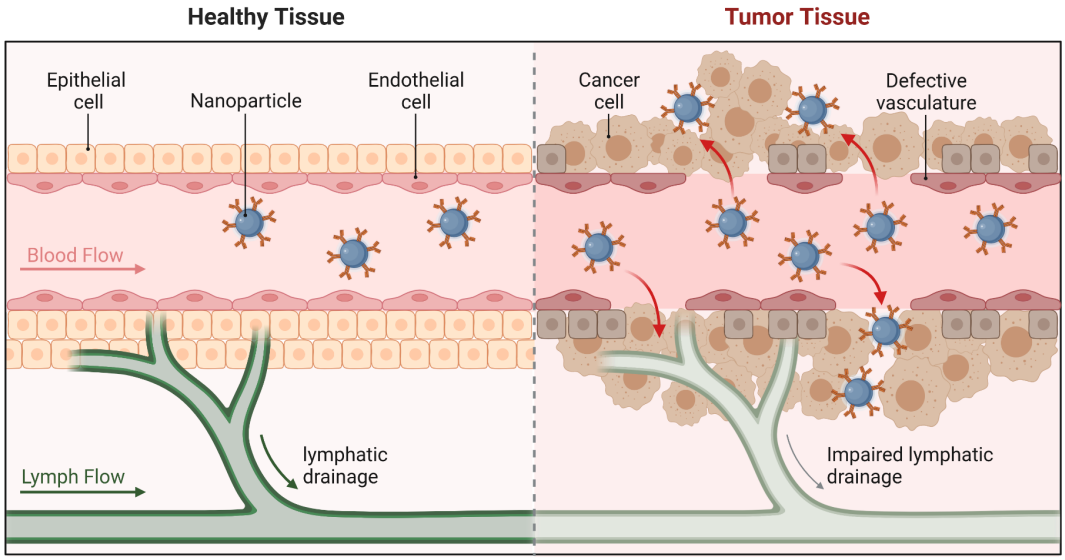

Figure 2. An illustration representing the Enhanced Permeability and Retention (EPR) effect in damaged tumor vasculature and leaky drainage in comparison to healthy tissue. (*Reprinted from "Passive Targeting of Nanoparticles to Cancer Cells.", by BioRender.com (2023), with permission*).

Alongside this thesis work, we have developed a set of different nanoparticles for the efficient delivery of protein therapeutics for their application in multiple diseases including cancer and rare diseases. We first explored the association of a bioluminescent enzyme (RLuc8) to metallic quantum dots to have an application in pancreatic cancer by triggering a photodynamic therapy (PDT) treatment. Due to the toxicity that the heavy metals of the quantum dots' core might cause, we translated this PDT application to more biocompatible nanosystems. Subsequently, we developed lipid-based nanosystems tailoring the lipid and surface composition to associate RLuc8. These lipid-based nanosystems were inspired by the patented nanosystems by our group developed by *Bouzo et al.,*[22], composed by a Vitamin E oil core and stabilized by the lipid surfactant sphingomyelin. These formulations present numerous advantages such as optimal colloidal stability in relevant biological media and storage conditions, and a reproducible and cost-effective preparation methodology using a single-step methodology. Notably, sphingomyelin nanoemulsions (SNs) have been decorated with a set of anticancer agents, varying from small molecules to nucleic acids, and imaging agents to test their *in vivo* fate [23–26]. On view of the promising results with SNs and RLuc8 for PDT, the same strategy was pursued to associate different types of proteins, providing examples with enzymes, fluorescent proteins and immunogenic proteins, and adding alternative chemical strategies for efficient association. A second example of a biomedical application for pancreatic cancer was explored with the immunostimulatory protein Anakinra. *[Confidential section]*

Therefore, this thesis provides the following general achievements, i) a bioluminescent enzyme (RLuc8) can be chemically bonded to metallic quantum dots or to specific tailored SNs in combination with a photosensitive drug (e.g., verteporfin, rose bengal) to perform an effective PDT treatment in pancreatic cancer; ii) SNs can be chemically tailored to have different reactive groups displayed onto their surface to performed a range of chemical strategies to associate proteins independently of their MW and pI, showing the versatility of the developed nanosystems for their use in protein delivery for multiple biomedical applications; iii) SNs can efficiently associate the therapeutic enzyme "anakinra" to modulate the tumor microenvironment (TME) in pancreatic cancer by inhibiting cytokine release from IL-1 in cancer-associated fibroblasts (CAFs) and Th17 differentiated cells; iv) *[Confidential section]*. Keeping this in mind, the following paragraphs are intended to provide a more in-depth discussion to give an overview of the future perspectives of SNs for efficient protein delivery and development of innovative therapeutics.

Nanosystems can be decorated with a bioluminescent enzyme to trigger PDT.

Traditional PDT is based on the administration of a photosensitizer in the impaired tissue followed by the illumination (excitation) of the photosensitive drug at the appropriate wavelength by an external laser [27–29]. This treatment has achieved important results in lesions in the skin, eyes, or small and external breast tumors as examples. However, laser light does not penetrate deep tissues resulting non-beneficial for internal organs. For this reason, there are reported in literature preclinical studies of the association of a bioluminescent enzyme (luciferase) to quantum dots to, in combination with a photosensitizer, trigger a PDT treatment in the very deep tissue as the light is produced by the enzyme not being necessary external light application [30]. We first explored the association of RLuc8 bioluminescent enzyme to QDots 705 and in combination with the photosensitizer verteporfin induced apoptosis and subsequently cell death in pancreatic cancer cells. Overall, we obtained satisfactory results *in vitro* and *in vivo*. Assays to evaluate the production of ROS, apoptosis and viability were successfully performed *in vitro*. Subsequently, pancreatic orthotopic tumors were implanted in male NOD/SCID mice. Although we observed a strong tendency in the reduction of cell proliferation in the treatment group, it was not significantly reduced. However, TUNEL assays showed an increased levels of apoptosis in the treated samples. This led us to suggest that probably and increased dose of RLuc8-QDots 705 nanoconjugates would be beneficial for PDT treatment *in vivo*. Nevertheless, it was necessary to tightly adjust the dose due to the intrinsic toxicity of QDots' heavy metals core. Although we achieved a higher dose with respect to the one reported in the literature using QDots, it should be noted that the outcome of QDots results may be involved by several parameters that affect their cytotoxic effect such as mean diameter, surface properties, metallic core and, of course, exposure time.

To develop an optimized formulation, following a more biocompatible approach, and therefore safer-by-design, we decided to explore SNs for their application in bioluminescent PDT. SNs composed by Vitamin E and SM were previously developed by our group and proved their potential for drug delivery and gene therapy applications [22–24,31]. In this thesis, the lipid composition and ratio were optimized to chemically bond the RLuc8. Thus, we added a DSPE-PEG(2k)-DBCO lipid and modified the RLuc8 with an azide linker (N3-) to perform SPAAC "click" chemistry reaction (SI-NS) [32,33]. Also, the photosensitizer *Rose Bengal* was added to the oil core and encapsulated into the resulting nanosystem (SI-RB-NS). We obtained a very robust and stable "self-illuminating" nanosystem (SI-NS), in-depth characterized by multiple analytical techniques. PDT treatment efficacy was evaluated in a variety of pancreatic established cancer cells and PDX primary

cultures giving excellent results. After PDT treatment with SI-RB-NS, it was observed a strong drop in the viability, an increased in the levels of ROS and the production of the apoptosis in different assays. SI-RB-NS achieved great results compared to the previous attempts of applying RLuc8 linked to rose Bengal for an effective PDT [34]. Regarding *in vivo* experiments with SI-RB-NS, mice were orthotopically implanted in the pancreas with Panc185 cells. Two mice of the therapy group suffered from a marked tumor reduction compared to untreated group. In addition, H&E staining and quantification experiments showed that the totality of the tissue was healthy pancreas. But this tendency was not observed in all the mice treated, letting the possibility to increase dose or the number substrate injections since mice did not present any sign of toxicity. Even so, it must be remarked that the biocompatible lipid-based SI-RB-NS outperformed SI-NCs (RLuc8-QDots 705) for the PDT in pancreatic tumors (**Figure 3**).

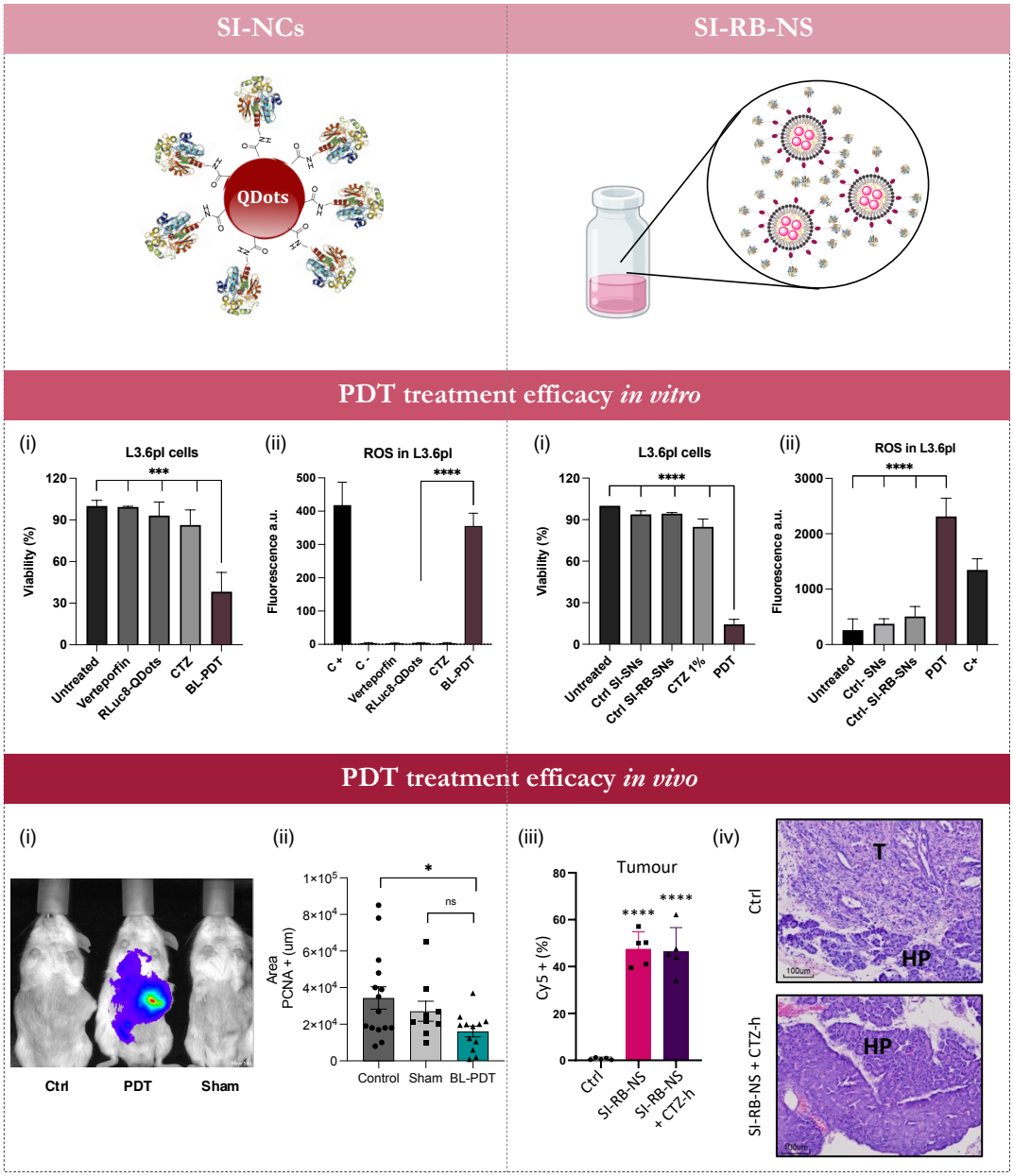

Figure 3. Comparison of the PDT treatment performance by SI-NCs (RLuc8-QDots 705) and SI-NS (Lipid-based nanosystems). On the top there is a schematic illustration of both nanosystems. In the middle (left) there are represented the (i) viability achieved after PDT treatment with the combination of QDots and the photosensitizer verteporfin and (ii) ROS formation. On the right, there are represented the same assays performed after the PDT treatment with SI-RB-NS in L3.6pl cancer cell line. On the bottom (left) it is evaluated the efficacy *in vivo* of SI-NCs. (i) By IVIS, it is observed how SI-NCs reached the tumor in the pancreas of mice. (ii)Proliferating Cell Nuclear Antigen (PCNA) Assay showed a tendency in the reduction of cell proliferation in the therapy group. Bottom (right) *in vivo* data obtained with SI-RB-NS. (iii) Cy5-labelled SI-RB-NS successfully reached the tumor and accumulate. (iv) It is observed

in H&E staining in two of the mice treated healthy tissue compared to untreated mice; T: Tumor; HP: Healthy Pancreas. Differences mean n.s. for not significant, * ($p < 0.05$), ** ($p < 0.005$), *** ($p < 0.0005$) and **** ($p < 0.0001$).

In this regard, inorganic nanoparticles offer clinically unique diagnostic and therapeutic opportunities. For instance, AuNP are a promising tool for detection and imaging purposes and can be easily modified to contain targeting ligands [35]. Another example are quantum dots, used in this work and further studied for preclinical *in vivo* imaging, although they have been limited to preclinical studies because of their doubtable biocompatibility and metallic core toxicity [36–38]. Despite inorganic nanoparticles' unique properties to respond to external stimuli and being applied therapeutically, they have not been yet approved for any drug delivery application [35]. In this sense, organic nanoparticles seem to be most attractive in terms of clinical translation as they provide the advantages of biocompatibility and ease of encapsulation [39,40]. Since the approval of Doxil® in 1995 a liposome-encapsulated doxorubicin for its application in cancer, nanoparticles' research has remarkably increased. The development nanotheranostics is a current trend as therapeutic and diagnostic agents are simultaneously encapsulated in a single nanoparticle. Furthermore, organic nanoparticles are internalized via endocytosis, so mechanism underlying and to promote endosomal escape must be taken into consideration when designing the nanoparticles such as lipid components or surface stimuli responsive decoration. *In vivo* fate of the nanoparticles is also a major issue. For instance, nanoparticles without surface-modification often tend to accumulate in the liver and spleen, followed by rapid clearance, regardless of their physicochemical properties. The incorporation of polyethylene glycol (PEG) is often used as a "stealth" polymer to reduce clearance[15,41]. In our SI-NS the incorporation of DSPE-PEG(2k)-DBCO enabled us to incorporate the RLuc8 enzyme but also, conferred stability and avoided fast clearance to effectively reach pancreatic tumor *in vivo*. All in all, advantages and limitations must be considered while designing therapeutic nanocarriers, including particle morphology, composition, encapsulation of multiple agents, and promote strategies for enhanced endosomal escape.

SNs can be chemically tailored to be a nanoplatform for the efficiently intracellular delivery of proteins.

Protein therapeutics have evolved as key factors for the treatment of many diseases due to their endogenous biological nature and high level of specificity. However, the administration of naked

proteins is hampered by various obstacles such as short half-life circulation and degradation by proteases resulting in poor bioavailability. Thereby, frequent administrations are needed leading to undesired side effects and immune responses [3,42]. As we explained throughout this thesis work, nanotechnology as carriers or delivery systems are presented to be ideal for protein therapeutics. Drug delivery systems (DDS) as before described can be advantageous in order to improve protein therapies by enhancing protein solubility; controlled and sustained release instead of burst release, avoiding side-effects; improving biodistribution, thus bioavailability; and targeting specific tissues. The optimal nanocarriers or DDS for protein delivery should decrease the rate of drug clearance, meaning that low doses are needed. Also, proteins must be incorporated to DDS in a way that does not affect their conformation and bioactivity. In addition, DDS formulated with biocompatible and biodegradable materials would provide advantageous properties to avoid and minimize adverse toxic or immune responses in patients [13,14,43]. Several types of carriers have been reported in literature for protein delivery mainly based on microparticles and nanoparticles. Microparticles are particles between 1 and 1000 μm and have been studied since the seventies. There is some approved microparticles drug delivery formulations as the case of PROSTAP® 3 DCS a leuprorelin acetate, a synthetic nonapeptide analogue of naturally occurring gonadotrophin releasing hormone (GnRH) for the treatment of prostate cancer and some cases of breast cancer and endometriosis. However, microparticles present some drawbacks regarding their formulation as protein therapeutics. Microparticle DDS are formulated with a wide variety of formulations methods and materials depending on the characteristics of the protein to deliver, having to design a specific microparticle depending on the cargo, limiting clinical translation. Also, the size of microparticles is a major issue that contributes to the efficacy of the formulation. There exists a concern about opsonization that microparticles will encounter once in circulation [44,45]. In this regard, nanoparticles being much smaller, seem to be a better carrier for proteins. There have been reported numerous studies of nanoparticles for protein delivery using different types such as lipid-based and polymeric nanoparticles, among others. Liposomes first described in the sixties, were the first ones adapted for protein delivery. For instance, liposomes delivery of protein therapeutics was attempted as vaccine candidate against genital Chlamydia infection [44,46] and insulin-containing multivesicular liposomes (MVLs), with the addition of novel chitosan and Carbopol coating (CS/P-MVLs) as sustained release protein delivery systems via the nasal and ocular routes to treat diabetes [44,46]. However, problems related to the varied liposomes compositions depending on the properties such as structure, surface charge and solubility of the protein of interest limit their translation. Furthermore, liposomes are often formulated using complex techniques hindering scale-up

procedures. Another limitation might be due to the size of liposomes that can vary between 100-500 nm but also reach the micrometer range, resulting in the possibility of triggering opsonization effect by the macrophages or other components of the immune system [46–48]. The trend is to develop nano-scale carriers. As an example, BMP-2 containing bovine serum albumin (BSA) nanoparticles (NPs) with a polyethyleneimine (PEI) coating was synthesized to stimulate bone growth at implantation sites in bone healing showing promising results [44,49]. Nevertheless, they were encountered some drawbacks in terms of translation, related to PEI toxicity that reduced the BMP-2 bioactivity. Researchers should consider using safer and natural materials to avoid negative interactions and side effects. In addition, simpler methodologies, and less complex chemicals in order to form nanoparticles are necessary for GMP and scale-up processes. Despite, the good results that many nanocarriers for protein delivery have accomplished, there is still a lack of good systems available for current clinical therapies [46,47].

In this context, the aim of this thesis was to develop a simply nanoplatform delivery for a wide variety of proteins without compromising their bioactivity, which is still an important need in medicine. Thus, the development of a unique nanoparticle that fulfills the translational requirements of containing non-immunogenic biocompatible and biodegradable materials, simple methodology of preparation, versatile application in a wide range of proteins and preservation of proteins conformation and activity was our next aim in this thesis. With this in mind, and all the previous research in the development of nanoparticles for the delivery of proteins in the previous chapters, we have developed a nanoplatform for the delivery of a wide range of proteins comprising a broad range of MW and pI. Based on the SNs, we introduce PEGylated lipids modified with active chemical groups to carry covalently link proteins to SNs. Charged lipids were also studied to explore the association by electrostatic interactions. The aim of Chapter III was to validate if a simply and reproducible lipid-based nanosystem (SNs) could act as an effective carrier for proteins, and to prove versatility to adapt SNs to different requirements and biomedical applications. In **figure 4**, they are represented the proteins that were used for these studies.

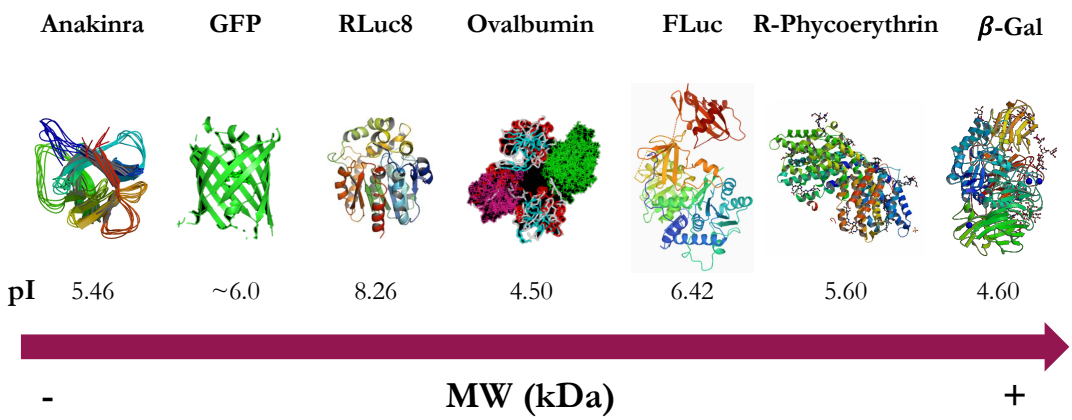

Figure 4. Representation of the model proteins used in this thesis for the development of our versatile nanoplatform for their delivery. Proteins are disposed in from smallest to largest in terms of molecular size. pI was calculated using the specific sequence of each protein used in this thesis by pI calculator software (https://web.expasy.org/compute_pi/).

Among of chemical strategies evaluated, SPAAC "click" chemistry gave the best performance with all proteins. Thus, nanosystems containing DBCO group resulted in a very robust and versatile nanosystem (**Table 1**). In addition, DBCO nanosystems were very stable through time at storage conditions without compromising proteins activities, being functional for a year as bioluminescence of RLuc8-SNs(DBCO) nanosystem exhibits in **figure 5a**. Furthermore, it was also the best nanosystem in terms of cellular internalization compared to the other SNs prototypes (Maleimide, NHS, TFP and DOTAP) represented for GFP-SNs(DBCO) and PE-SNs(DBCO) using GFP (**Fig. 5b**) and PE (**Fig. 5c**) as model proteins.

Table 1. Physicochemical Characterization of P-SNs(DBCO) measured by DLS and LDA. Percentage of proteins linked to SNs quantified by microBCA assay (Results are expressed as Mean ± SD, n = 5). Abbreviations: nm: nanometer, PdI: polydispersity index, ZP: zeta potential in millivolts (mV), P-SNs(DBCO): Protein loaded- Sphingomyelin DBCO-nanosystems .

Formulation	Size (nm)	PdI	ZP (mV)	% Association
ANK-SNs(DBCO)	166 ± 4	<0.1	- 20 ± 1	92 ± 3
GFP-SNs(DBCO)	177 ± 5	<0.1	- 29 ± 3	91 ± 3
RLuc8-SNs(DBCO)	165 ± 4	<0.1	- 26 ± 1	95 ± 3
OVA-SNs(DBCO)	85 ± 2	<0.1	- 24 ± 1	92 ± 2
FLuc-SNs(DBCO)	158 ± 5	<0.1	- 28 ± 2	94 ± 3
PE-SNs(DBCO)	162 ± 7	<0.1	- 27 ± 3	-
B-GAL-SNs(DBCO)	166 ± 3	<0.1	- 30 ± 3	-

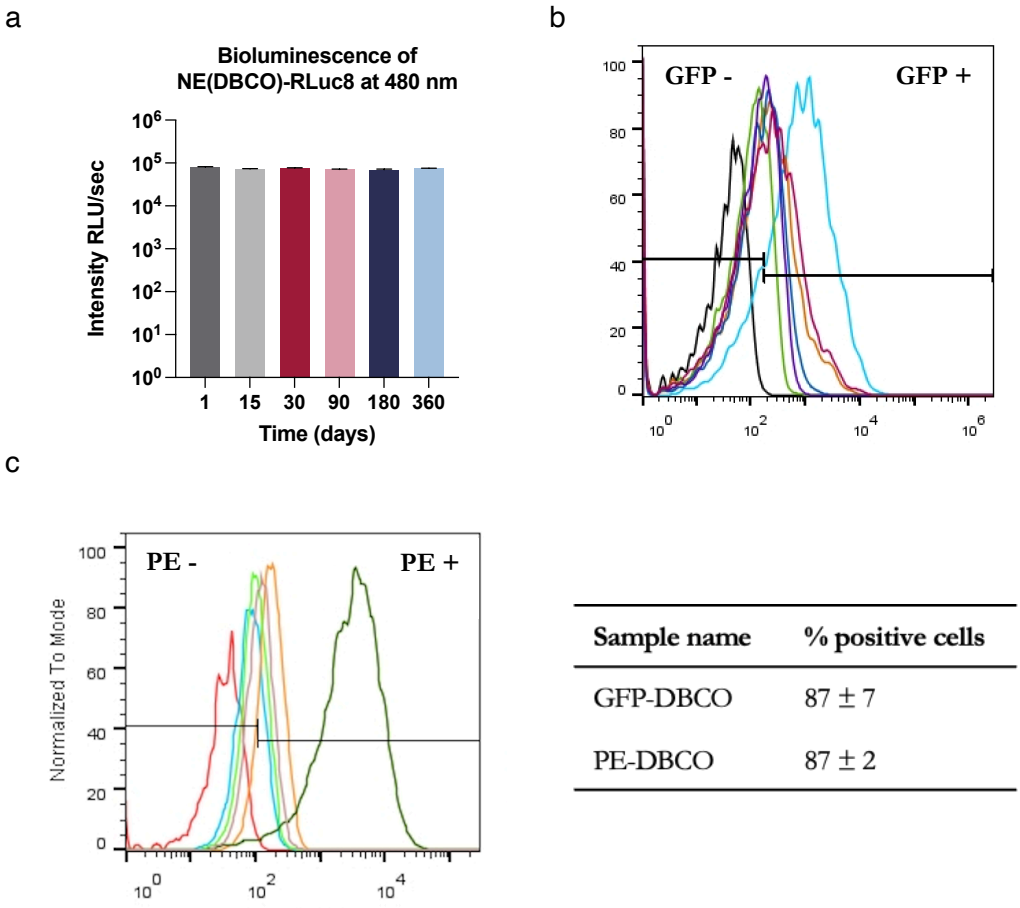

Sample name	% positive cells
GFP-DBCO	87 ± 7
PE-DBCO	87 ± 2

Figure 5. (a) Evaluation of RLuc8-SNs(DBCO) bioluminescent activity for a year under storage conditions (4ºC). Bioluminescence was measured at 480 nm (RLuc8 emission wavelength) upon CTZ activation (40µM). **(b)** GFP-SNs(DBCO) (light blue line) and **(c)** PE-SNs(DBCO) (dark green line) were selected to evaluate internalization in L3.6pl cell line after 2h incubation in comparison to other SNs prototypes (Maleimide, NHS, TFP and DOTAP). (n>3; data expressed as mean ± SD).

Notably, our developed nanoplatform might be applicable for either extracellular or intracellular targets. Although proteins are displayed onto the surface of the nanosystems, covalently linking and nanosystems composition offer protection and increase circulation. Thus, this protein-decorated surface let the oil core of the nanosystems free to be loaded with other molecules such as drugs (Chapter II) or nucleic acids (Chapter V). In addition, we have proved the successful interaction with toll-like receptor IL-1R that have a key role in inflammatory responses by delivering its antagonist anakinra molecule (Chapter IV). Regarding intracellular targets, we have

intracellularly delivery several reporter proteins such as GFP and R-phycoerythrin. But the most remarkable was the efficacious delivery of β-galactosidase enzyme due to its high MW (~465 kDa) and maintaining its four structural domains and activity (**Figure 6**).

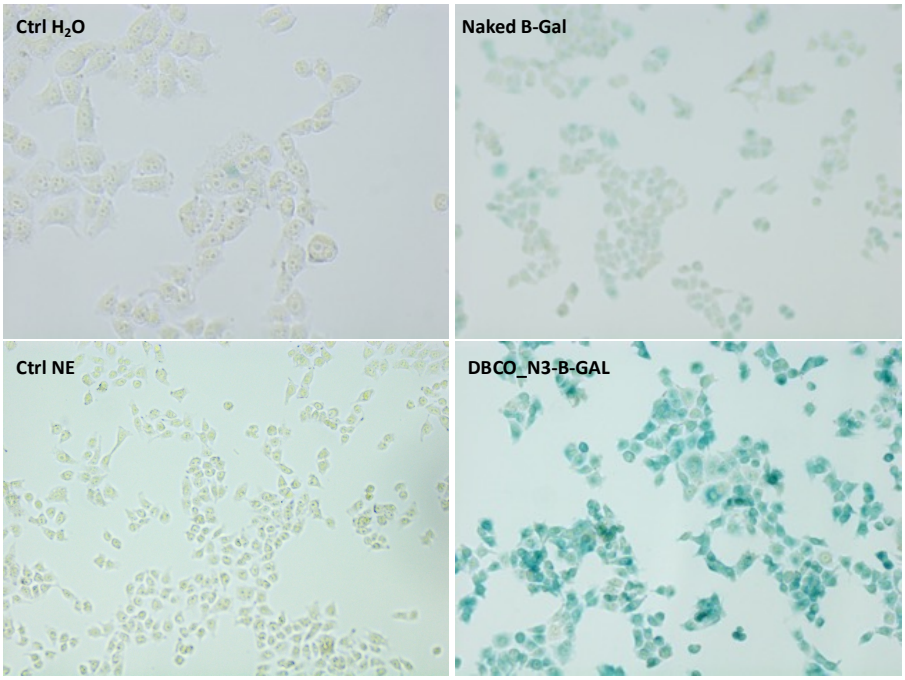

Figure 6. X-GAL assay to evaluate the internalization B-GAL-SNs(DBCO) and the maintenance of B-GAL bioactivity after effective intracellular delivery in cells (intracellular target). As negative controls for the detection of B-GAL, we have added (i) H2O; (ii) naked enzyme B-GAL (does not trespass cell membranes); (iii) SNs without B-GAL. B-GAL-SNs formulations were added in non-supplemented cell culture RMPI medium (Dose corresponding to 2μg of B-Gal in all conditions; incubation time 2h; expression of B-Gal was performed by X-Gal staining at 12h post incubation).

In the context of reaching extracellular targets, in chapter IV, we have developed a nanosystem for the efficiently delivery of the therapeutic enzyme 'Anakinra' for its application in pancreatic cancer. Anakinra is an IL-1R antagonist that have been studied in preclinical studies as an effective anti-tumor agent [50]. Thus, considering the key role of IL-1 in tumor-promoting inflammation in PDAC we aimed to prove that the delivery of ANK-SNs would enhance the outcome of TME modulation in the differentiation of pro-tumoral cells compared to free anakinra administration [51–54]. Based on the research performed in chapters II and III to associate proteins to SNs we prepared a set of ANK-SNs linked through different chemical strategies, namely SPAAC "click" chemistry

(DBCO), thiol-maleimide (MAL), NHS-active ester (NHS) reaction and via electrostatic interactions (DOTAP). These modified PEGylated stearic carbon chain with chemically active functional groups offer the advantage of associate biomolecules but also PEG present some features such as prolonged blood circulation times and reduced possible interactions with blood components (opsonisation). Overall, ANK-SNs prototypes presented small particle size (<200 nm) and a monodispersed population (PdI) as well as stability through time at storage conditions and in biorelevant medium. ANK-SNs prototypes, empty-SNs and free ANK drug were added to CAFs extracted from PDAC surgical samples previously stimulated with IL-1α and IL-1β. Subsequently, TSLP, IL-6 and IL-8 release was measured by ELISA. We found that formulation ANK-SNs(NHS) gave the best performance, and it was chosen for the following experiments (**Figure 7**). All in all, we concluded that ANK-SNs inhibited the cytokine release from IL-1 activated CAFs. In addition, ANK-SNs outperformed ANK free drug by restraining IL-17 secretion in differentiated Th17 cells. ANK-SNs succeeded in the role of immunomodulate the TME components (CAFs and TILs) to interfere with the secretion of pro-tumoral cytokines.

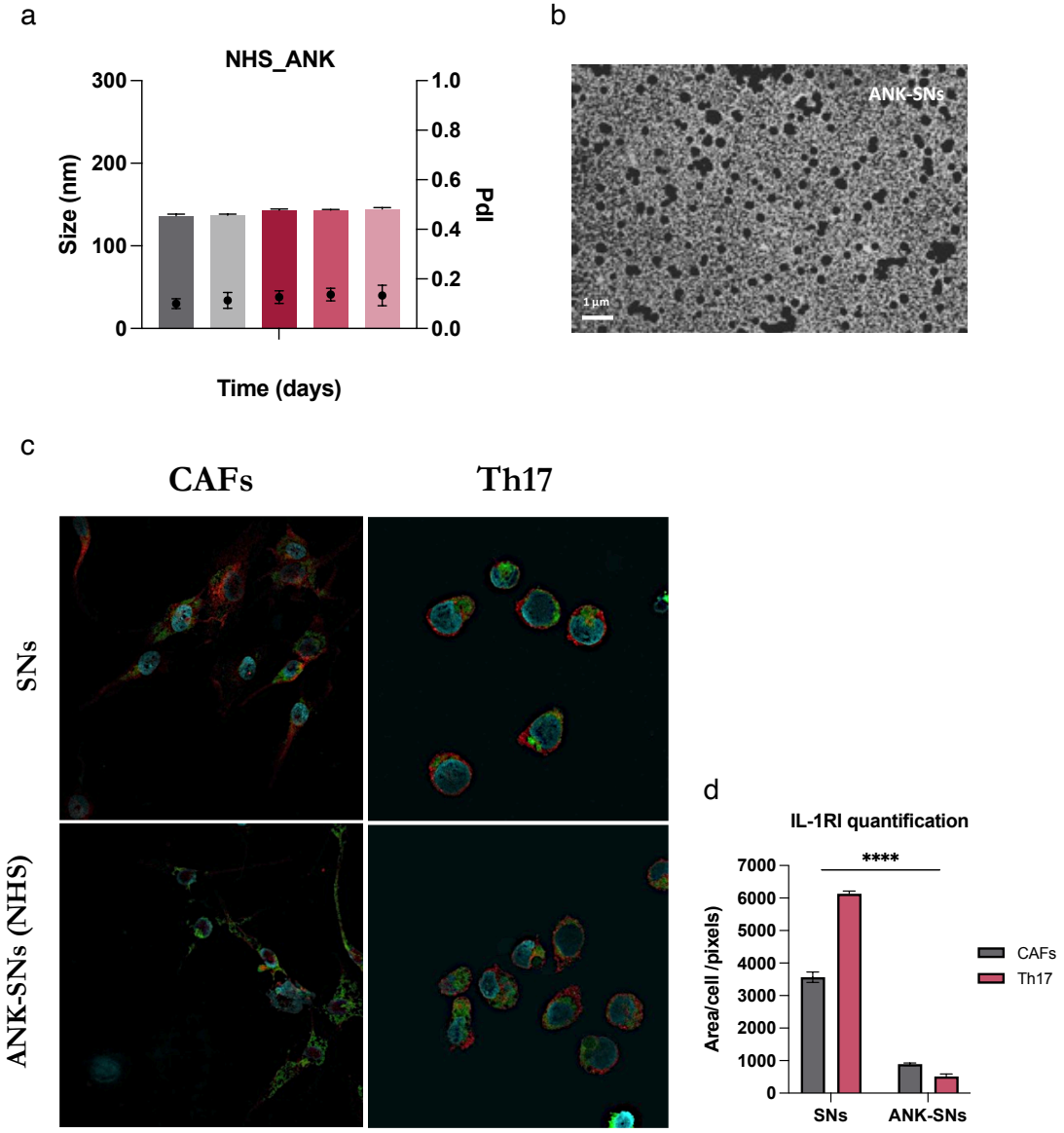

Figure 7. (a) Stability of ANK-SNs (NHS) measured over a month in terms of size and PdI at storage conditions (4ºC). **(b)** ANK-SNs spherical distribution morphology observed by Field Emission Scanning Electron Microscopy (FESEM). **(c)** Immunofluorescence to confirm ANK-SNs inhibit IL-1 cytokine release in CAFs and Th17 differentiated cells. Confocal Laser Microscopy (CLM) images to observe the reduction in IL-1R (red) when ANK-SNs were administered (in green labelled SNs and ANK-SNs). Nuclei were stained with Hoechst 33342. **(d)** Quantification of IL-1R inhibition caused by ANK-SNs in CAFs and Th17 cells.

[Confidential section]

In this thesis, we paved the way for the design and development of a lipid-based nanosystems for the versatile delivery of a broad set of proteins and its application in a vary type of biomedical applications and diseases. Thus, we have overcome challenges related to the safety and biocompatibility of the nanocarriers, protein loading and maintenance of the therapeutic effect, simply preparation methodologies, biodegradability of components and cost of production. However, the next aim will be to further investigate the *in vivo* fate of our developed nanosystems for protein delivery. First studies were carried out in chapter II, but more research must be done.

OVERVIEW AND FUTURE PERSPECTIVES

In general, in this thesis, we have settled the understanding for the bioconjugation of proteins to nanoparticles through a varied of chemical strategies for their application in multiple diseases and biomedical areas. Remarkedly, we have demonstrated the efficacy of two different "self-illuminating" nanosystems for their use in PDT in pancreatic cancer either *in vitro* or *in vivo*. As well as the tropism of "self-illuminating" SNs for tumors when intraperitoneal administered, letting the door open for other applications in cancer. In addition, the versatility of SNs allowed us to co-encapsulate drugs (photosensitizer), and *[Confidential section]* alongside the surface decoration to proteins. SNs could be precisely tailored for the incorporation of a broad spectrum of proteins resulting in a promising nanoplatform for extracellular and intracellular protein delivery. Of course, further studies regarding the *in vivo* fate, such as toxicological studies, capacity to trigger immune responses, and elucidating the pharmacokinetic profile of protein-SNs are aimed to be performed.

The great plasticity that SNs present is a clear advantage. In this regard, imaging agents can be loaded to SNs to further study their biodistribution, accumulation and clearance from the body. The ability to quantify these parameters in preclinical models would provide valuable information for future translation of protein nanomedicines. All in all, the latest advances and emergence of clinically approved nanomedicines and the improvements in protein delivery, we figure up that the drawbacks will be soon addressed to bring into the clinic safer and more effective nanomedicines for protein delivery for a great deal of diseases.

REFERENCES

1. Rukhlenko, O., Kholodenko, B. N. & Kolch, W. Systems biology approaches to macromolecules: the role of dynamic protein assemblies in information processing. *Current Opinion in Structural Biology* vol. 67 61–68 Preprint at https://doi.org/10.1016/j.sbi.2020.09.007 (2021).

2. Golan, D., Beca, Q. & Leader, B. Protein therapeutics: a summary and pharmacological classification. *Nat Rev Drug Discov* **7**, 21–39 (2008).

3. Dimitrov, D. S. Therapeutic proteins. *Methods in Molecular Biology* **899**, 1–26 (2012).

4. Sauna, Z. E. *et al.* Recent advances in (therapeutic protein) drug development. *F1000Research* vol. 6 Preprint at https://doi.org/10.12688/f1000research.9970.1 (2017).

5. Grandori, R. Protein structure and dynamics in the era of integrative structural biology. *Frontiers in Biophysics* **1**, (2023).

6. Usmani, S. S. *et al.* THPdb: Database of FDA-approved peptide and protein therapeutics. *PLoS One* **12**, (2017).

7. Ebrahimi, S. B. & Samanta, D. Engineering protein-based therapeutics through structural and chemical design. *Nature Communications* vol. 14 Preprint at https://doi.org/10.1038/s41467-023-38039-x (2023).

8. Sharma, A. R. *et al.* Next generation delivery system for proteins and genes of therapeutic purpose: Why and how? *BioMed Research International* vol. 2014 Preprint at https://doi.org/10.1155/2014/327950 (2014).

9. Pisal, D. S., Kosloski, M. P. & Balu-Iyer, S. V. Delivery of therapeutic proteins. *Journal of Pharmaceutical Sciences* vol. 99 2557–2575 Preprint at https://doi.org/10.1002/jps.22054 (2010).

10. Boune, S., Hu, P., Epstein, A. L. & Khawli, L. A. Principles of N-linked glycosylation variations of igg-based therapeutics: Pharmacokinetic and functional considerations. *Antibodies* vol. 9 1–20 Preprint at https://doi.org/10.3390/antib9020022 (2020).

11. Wolf, B. *et al.* Therapeutic antibody glycosylation impacts antigen recognition and immunogenicity. *Immunology* **166**, 380–407 (2022).

12. Kaltbeitzel, J. & Wich, P. R. Protein-based Nanoparticles: From Drug Delivery to Imaging, Nanocatalysis and Protein Therapy. *Angewandte Chemie International Edition* (2023) doi:10.1002/anie.202216097.

13. Yu, M., Wu, J., Shi, J. & Farokhzad, O. C. Nanotechnology for protein delivery: Overview and perspectives. *Journal of Controlled Release* **240**, 24–37 (2016).

14. Viegas, C., Seck, F. & Fonte, P. An insight on lipid nanoparticles for therapeutic proteins delivery. *Journal of Drug Delivery Science and Technology* vol. 77 Preprint at https://doi.org/10.1016/j.jddst.2022.103839 (2022).

15. Suk, J. S., Xu, Q., Kim, N., Hanes, J. & Ensign, L. M. PEGylation as a strategy for improving nanoparticle-based drug and gene delivery. *Advanced Drug Delivery Reviews* vol. 99 28–51 Preprint at https://doi.org/10.1016/j.addr.2015.09.012 (2016).

16. Nikitin, M. P. *et al.* Enhancement of the blood-circulation time and performance of nanomedicines via the forced clearance of erythrocytes. *Nat Biomed Eng* **4**, 717–731 (2020).

17. Fang, J., Nakamura, H. & Maeda, H. The EPR effect: Unique features of tumor blood vessels for drug delivery, factors involved, and limitations and augmentation of the effect. *Advanced Drug Delivery Reviews* vol. 63 136–151 Preprint at https://doi.org/10.1016/j.addr.2010.04.009 (2011).

18. Menon, I., Zaroudi, M., Zhang, Y., Aisenbrey, E. & Hui, L. Fabrication of active targeting lipid nanoparticles: Challenges and perspectives. *Mater Today Adv* **16**, (2022).

19. Lu, Y., Sun, W. & Gu, Z. Stimuli-responsive nanomaterials for therapeutic protein delivery. *Journal of Controlled Release* vol. 194 1–19 Preprint at https://doi.org/10.1016/j.jconrel.2014.08.015 (2014).

20. Mura, S., Nicolas, J. & Couvreur, P. Stimuli-responsive nanocarriers for drug delivery. *Nature Materials* vol. 12 991–1003 Preprint at https://doi.org/10.1038/nmat3776 (2013).

21. Bajracharya, R., Song, J. G., Back, S. Y. & Han, H. K. Recent Advancements in Non-Invasive Formulations for Protein Drug Delivery. *Computational and Structural Biotechnology Journal* vol. 17 1290–1308 Preprint at https://doi.org/10.1016/j.csbj.2019.09.004 (2019).

22. Bouzo, B. L., Calvelo, M., Martín-Pastor, M., García-Fandiño, R. & De La Fuente, M. *In Vitro*- In Silico Modeling Approach to Rationally Designed Simple and Versatile Drug Delivery Systems. *Journal of Physical Chemistry B* **124**, 5788–5800 (2020).

23. Nagachinta, S., Bouzo, B. L., Vazquez-Rios, A. J., Lopez, R. & de la Fuente, M. Sphingomyelin-based nanosystems (SNs) for the development of anticancer miRNA therapeutics. *Pharmaceutics* **12**, (2020).

24. Bouzo, B. L. *et al.* Sphingomyelin nanosystems loaded with uroguanylin and etoposide for treating metastatic colorectal cancer. *Sci Rep* **11**, (2021).

25. Díez-Villares, S. *et al.* Quantitative PET tracking of intra-articularly administered 89Zr-peptide-decorated nanoemulsions. *Journal of Controlled Release* **356**, 702–713 (2023).

26. Nagachinta, S. *et al.* Radiolabelling of lipid-based nanocarriers with fluorine-18 for *in vivo* tracking by PET. *Colloids Surf B Biointerfaces* **188**, (2020).

27. Abrahamse, H. & Hamblin, M. R. New photossensitizersfot photodynamic therapy. *Biochemical Journal* **473**, 347–364 (2017).

28. Correia, J. H., Rodrigues, J. A., Pimenta, S., Dong, T. & Yang, Z. Photodynamic therapy review: Principles, photosensitizers, applications, and future directions. *Pharmaceutics* **13**, (2021).

29. Dos Santos, A. F., De Almeida, D. R. Q., Terra, L. F., Baptista, M. S. & Labriola, L. Photodynamic therapy in cancer treatment - an update review. *J Cancer Metastasis Treat* **2019**, (2019).

30. So, M. K., Loening, A. M., Gambhir, S. S. & Rao, J. Creating self-illuminating quantum dot conjugates. *Nat Protoc* **1**, 1160–1164 (2006).

31. Bidan, N. *et al.* Before *in vivo* studies: screening of sphingomyelin nanosystems using a relevant 3D multicellular pancreatic tumor spheroid model. *Int J Pharm* **617**, (2022).

32. Wang, L., Jiang, R., Wang, L., Liu, Y. & Sun, X. L. Preparation of chain-end clickable recombinant protein and its bio-orthogonal modification. *Bioorg Chem* **65**, 159–166 (2016).

33. Yoon, H. Y., Lee, D., Lim, D. K., Koo, H. & Kim, K. Copper-Free Click Chemistry: Applications in Drug Delivery, Cell Tracking, and Tissue Engineering. *Advanced Materials* vol. 34 Preprint at https://doi.org/10.1002/adma.202107192 (2022).

34. Kim, S. *et al.* Luciferase-Rose Bengal conjugates for singlet oxygen generation by bioluminescence resonance energy transfer. *Chemical Communications* **53**, 4569–4572 (2017).

35. Anselmo, A. C. & Mitragotri, S. A Review of Clinical Translation of Inorganic Nanoparticles. *AAPS Journal* **17**, 1041–1054 (2015).

36. Segets, D. Analysis of particle size distributions of quantum dots: From theory to application. *KONA Powder and Particle Journal* **2016**, 48–62 (2016).

37. Oh, E. *et al.* Meta-analysis of cellular toxicity for cadmium-containing quantum dots. *Nat Nanotechnol* **11**, 479–486 (2016).

38. Ramachandran, S., Sathishkumar, M., Kothurkar, N. K. & Senthilkumar, R. Synthesis and characterization of graphene quantum dots/cobalt ferrite nanocomposite. *IOP Conf Ser Mater Sci Eng* **310**, (2018).

39. Sindhwani, S. & Chan, W. C. W. Nanotechnology for modern medicine: next step towards clinical translation. *Journal of Internal Medicine* vol. 290 486–498 Preprint at https://doi.org/10.1111/joim.13254 (2021).

40. Mitragotri, S. & Stayton, P. Organic nanoparticles for drug delivery and imaging. *MRS Bull* **39**, 219–223 (2014).

41. Veronese, F. M. & Mero, A. *The Impact of PEGylation on Biological Therapies. Biodrugs* vol. 22 (2008).

42. Berdan, V. Y., Klauser, P. C. & Wang, L. Covalent peptides and proteins for therapeutics. *Bioorg Med Chem* **29**, (2021).

43. Yau, A., Lee, J. & Chen, Y. pharmaceutics Nanomaterials for Protein Delivery in Anticancer Applications. (2021) doi:10.3390/pharmaceutics.

44. Tan, M. L., Choong, P. F. M. & Dass, C. R. Recent developments in liposomes, microparticles and nanoparticles for protein and peptide drug delivery. *Peptides* vol. 31 184–193 Preprint at https://doi.org/10.1016/j.peptides.2009.10.002 (2010).

45. Lengyel, M., Kállai-Szabó, N., Antal, V., Laki, A. J. & Antal, I. Microparticles, microspheres, and microcapsules for advanced drug delivery. *Scientia Pharmaceutica* vol. 87 Preprint at https://doi.org/10.3390/scipharm87030020 (2019).

46. Liu, P., Chen, G. & Zhang, J. A Review of Liposomes as a Drug Delivery System: Current Status of Approved Products, Regulatory Environments, and Future Perspectives. *Molecules* vol. 27 Preprint at https://doi.org/10.3390/molecules27041372 (2022).

47. Nsairat, H. *et al.* Liposomes: structure, composition, types, and clinical applications. *Heliyon* vol. 8 Preprint at https://doi.org/10.1016/j.heliyon.2022.e09394 (2022).

48. Tenchov, R., Bird, R., Curtze, A. E. & Zhou, Q. Lipid Nanoparticles from Liposomes to mRNA Vaccine Delivery, a Landscape of Research Diversity and Advancement. *ACS Nano* vol. 15 16982–17015 Preprint at https://doi.org/10.1021/acsnano.1c04996 (2021).

49. Zhang, S., Kucharski, C., Doschak, M. R., Sebald, W. & Uludağ, H. Polyethylenimine-PEG coated albumin nanoparticles for BMP-2 delivery. *Biomaterials* **31**, 952–963 (2010).

50. Carlos Becerra, Andrew Scott Paulson, Keith M Cavaness & Scott A. Celinski. Gemcitabine, nab-paclitaxel, cisplatin, and anakinra (AGAP) treatment in patients with localized pancreatic ductal adenocarcinoma (PDAC). *Journal of Clinical Oncology* **36**, (2018).

51. Sha, Y. & Markovic-Plese, S. Activated IL-1RI signaling pathway induces th17 cell differentiation via interferon regulatory factor 4 signaling in patients with relapsing-remitting multiple sclerosis. *Front Immunol* **7**, (2016).

52. Brunetto, E. *et al.* The IL-1/IL-1 receptor axis and tumor cell released inflammasome adaptor ASC are key regulators of TSLP secretion by cancer associated fibroblasts in pancreatic cancer. *J Immunother Cancer* **7**, (2019).

53. McAllister, F. *et al.* Oncogenic kras activates a hematopoietic-to-epithelial IL-17 signaling axis in preinvasive pancreatic neoplasia. *Cancer Cell* **25**, 621–637 (2014).

54. Barilla, R. M. *et al.* Specialized dendritic cells induce tumor-promoting IL-10 + IL-17 + FoxP3 neg regulatory CD4 + T cells in pancreatic carcinoma. *Nat Commun* **10**, (2019).

Conclusions

CONCLUSIONS

The scope of this thesis was to develop innovative protein therapeutics by implementing bioconjugation strategies enabling the efficient association of functional proteins with biocompatible nanosystems. Additionally, the thesis aimed to provide evidence of the therapeutic potential of the resulting formulations, utilizing *in vitro* and *in vivo* models for pancreatic cancer, as well as organoids for neurological disorders.

The experimental data obtained from this study led us to withdraw the following conclusions:

1. Self-illuminated nanosystems were successfully developed by specific bioconjugation of the enzyme RLuc8 to QDots 705 (SI-NCs) and SNs (SI-NS).

2. BioLight-PDT was successfully accomplished with SI-NCs *in vitro* in pancreatic cancer cell lines and PDX cultures, revealing the potential of this treatment without an external light source. *In vivo* experiments in two pancreatic tumor orthotopic models proved the real prospective of the developed nanoplatform.

3. A second type of self-illuminating nanosystems was successfully developed upon efficient bioconjugation of RLuc8 to a more biocompatible nanostructure, SNs. It has been proved the potential of this versatile and biodegradable SI-NS for *in vitro* and *in vivo* cell tracking, imaging, and BioLight-PDT treatment, making room for new therapeutic approaches.

4. SNs have the capacity to associate a versatile set of proteins and enzymes independently of their MW and net charge at physiological pH (pI), opening new venues for the development

of advanced protein therapeutics (P-SNs). It has been proved that proteins can be efficiently associated in their active form, by carefully selecting the most appropriate bioconjugation strategy.

5. The robustness facilitated by the copper-free SPAAC 'click' chemistry union for the development of SI-NS should be emphasized. This was thoroughly confirmed through an extensive physicochemical characterization employing various analytical methods, including NMR, MALDI-Toff, HPLC-MS, STEM, NTA, among others.

6. P-SNs showed high efficacy trespassing cellular membranes at short times and in different cell lines. In addition, they did not present toxic effects in comparison with commercial delivery reagents.

7. P-SNs can also be developed for an efficient extracellular target delivery. Indeed, Anakinra-loaded SNs (ANK-SNs) inhibited cytokine release from IL-1 in cells from the tumor microenvironment, cancer associated fibroblasts (CAFs) and Th17 differentiated cells obtaining superior results to free ANK administration.

[Confidential section]

Abbreviations

ABBREVIATIONS

%EE	Percentage of encapsulation efficiency
306-O12B	tetrakis(2-(octyldisulfaneyl)ethyl) 3,3',3'',3'''-(((methylazanediyl)bis(propane-3,1-diyl))bis(azanetriyl))tetrapropionate
^{13}C-NMR	Carbon-13 nuclear magnetic resonance
^{1}H-NMR	Proton nuclear magnetic resonance
$^{1}O_2$	Singlet oxygen
β-Gal	βeta-Galactosidase
µg	Microgram
µL	Microliter
µM	Micromolar
µm	Micrometer
AAVs	Adeno-associated viruses
ACN	Acetonitrile
ALC-0315	Decanoic acid, 2-hexyl-, 1,1'-[[(4-hydroxybutyl)imino]di-6,1-hexanediyl] ester
ANK	Anakinra
ANK-SNs	Sphingomyelin nanosystems bearing anakinra
API	Active pharmaceutical ingredient
ATCC	American Type Culture Collection

ATP	Adenosine triphosphate
Azido-dPEG®$_8$-NHS	2,5-Dioxo-1-pyrrolidinyl 3-[(23-azido-3,6,9,12,15,18,21-heptaoxatricos-1-yl)oxy]propanoate
BL-PDT	Bio-Light Photodynamic Therapy
BRET	Bioluminescence resonance energy transfer
BSA	Bovine serum albumin
C11 TopFluor® SM	N-[11-(dipyrromethene boron difluoride)undecanoyl]-D-erythro-sphingosylphosphorylcholine
C12-200	1,1'-[[2-[4-[2-[[2-[bis(2-hydroxydodecyl)amino]ethyl](2-hydroxydodecyl)amino]ethyl]-1-piperazinyl]ethyl]imino]bis-2-dodecanol
C16 Cy5 SM	N-palmitoyl sphingomyelin-N-(Cyanine 5)
CAFs	Cancer associated fibroblasts
Cas9	CRISPR associated protein 9
CD	Circular dichroism
Chl	Cholesterol; (3β)-cholest-5-en-3-ol
CLM	Confocal Laser Microscopy
cm^2	Square centimeter
CO_2	Carbon dioxide
COVID-19	Coronavirus disease
CRISPR	Clustered Regularly Interspaced Short Palindromic Repeats
CTZ	Coelenterazine-*h*
DAPI	4',6-diamidino-2-phenylindole
DBCO	dibenzocyclooctyne
DDS	Drug delivery systems

D-Lin-MC3-DMA (MC3)	(6Z,9Z,28Z,31Z)-heptatriacont-6,9,28,31-tetraene-19-yl 4-(dimethylamino)butanoate
DLS	Dynamic light scattering
DMEM	Dulbecco's modified Eagle's culture medium
DMG-PEG2000	1,2-Dimyristoyl-rac-glycero-3-methoxypolyethylene glycol-2000
DMSO	Dimethyl sulfoxide
DMSO-d_6	Deuterated dimethyl sulfoxide
DNA	Deoxyribonucleic acid
DOPC	1,2-dioleoyl-sn-glycero-3-phosphocholine
DOPE	1,2-dioleoyl-sn-glycero-3-phosphoethanolamine
DOTAP (18:1 TAP)	1,2-dioleoyl-3-trimethylammonium-propane (methyl sulfate salt)
DPBS	Dulbecco's Phosphate Buffered Saline
DPPG	1,2-Dipalmitoyl-sn-glycero-3-phosphoglycerol
DSB	Double-strand breakage
DSPC	1,2-distearoyl-sn-glycero-3-phosphocholine
DSPE-PEG(2k)-COOH	1,2-distearoyl-sn-glycero-3-phosphoethanolamine-N-[carboxy(polyethylene glycol)-2000] (sodium salt)
DSPE-PEG(2k)-DBCO	1,2-distearoyl-sn-glycero-3-phosphoethanolamine-N-[dibenzocyclooctyl(polyethylene glycol)-2000] (ammonium salt)
DSPE-PEG(2k)-Maleimide	1,2-distearoyl-sn-glycero-3-phosphoethanolamine-N-[maleimide(polyethylene glycol)-2000] (ammonium salt)
DSPE-PEG(2k)-NHS	1,2-distearoyl-sn-glycero-3-phosphoethanolamine-N-[carboxy(polyethylene glycol)-2000, NHS ester] (sodium salt)
EDC	1-Ethyl-3-(3-dimethylaminopropyl) carbodiimide
EDTA	Ethylenediaminetetraacetic acid
ELISA	Enzyme-linked immunosorbent assay

EMA	European Medicines Agency
EPR	Enhanced permeability and retention effect
ERT	Enzyme Replacement Therapy
ESI-MS	Electrospray ionization mass spectrometry
EtOH	Ethanol
Ex/Em	Excitation/Emission wavelength
FACS	Fluorescence-activated cell sorting
FAP	Fibroblast-activation protein
FBS	Fetal bovine serum
FDA	Food and Drug Administration
FESEM	Field emission scanning electron microscopy
FLuc	Firefly luciferase
GFP	Green fluorescence protein
GMP	Good Manufacturing Practices
GPCRs	G-protein coupled receptors
GRAS	Generally recognized as safe
H	Hypotheses
h	Hour
H_2DCFDA	2',7'-dichlorodihydrofluorescein diacetate
HEPES	4-(2-hydroxyethyl)-1-piperazineethanesulfonic acid
hiPSCs	Human-induced pluripotent stem cells
HOCl	Hypochlorous acid
HPLC	High performance liquid chromatography

HPLC-MS	High performance liquid chromatography coupled with mass spectrometry
HR	Homologous recombination
HSPCs	Hematopoietic Stem and Progenitor Cells
huTERT	Human Telomerase Reverse Transcriptase gene
IC50	Half maximal inhibitory concentration
iEDDA	Inverse-electron-demand Diels–Alder
IF	Immunofluorescence assay
IgE	Immunoglobulin E
IHC	Immunohistochemical analysis
IL-1	Interleukin-1 (cytokine)
IL-1R1	Interleukin 1 receptor, type I
i.m.	Intramuscularly
IMDM	Iscove's Modified Dulbecco's Medium
InLENS	Immersion-lens
i.p.	Intraperitoneal injection
IPA	2-propanol or isopropanol
IR	Infrared
i.v.	Intravenous injection
IVIS	*In vivo* imaging system
J	Joule
kDa	Kilodaltons
Kg	Kilogram
LDA	Laser Doppler anemometry

LNPs	Lipid nanoparticles
LSDs	Lysosomal storage diseases
M	Molar
mAb	Monoclonal antibody
MAL	Maleimide
MALDI-Tof	Matrix-Assisted Laser Desorption/Ionization - Time-Of-Flight
MenSCs	Menstrual Mesenchymal Stem Cells
MES	2-(N-morpholino)ethanesulfonic acid
MET	Mesenchymal-epithelial transition
mg	Milligram
min	Minute
mL	Millilitre
mM	Millimolar
mPEG-DSPE(2k)	1,2-Distearoyl-sn-Glycero-3-Phosphoethanolamine
mRNA	Messenger RNA
MTT	3-(4,5-dimethylthiazol-2-yl)-2,5-diphenyltetrazolium bromide
mV	Millivolt
MW	Molecular weight
NaCl	Sodium chloride
NF-κB	Nuclear factor kappa B
NIR	Near infrared
NKs	Natural killer cells (type of lymphocytes)
nm	Nanometer

NMR	Nuclear magnetic resonance
NPs	Nanoparticles
NS	Empty DBCO-nanosystems
NTA	Nanoparticle tracking analysis
NTA buffer	N', N-bis-(carboxymethyl)-L-lysine
O	Objectives
O_2	Molecular Oxygen
O/N	Overnight
OVA	Ovalbumin
PBS	Phosphate buffered saline
PCNA	Proliferating cell nuclear antigen
PDAC	Pancreatic ductal adenocarcinoma
PdI	Polydispersity index
PDT	Photodynamic therapy
PDX	Patient derived xenograft
PEG	Polyethylene glycol
PFA	Paraformaldehyde
pH	Potential of hydrogen
pI	Isoelectric point
PI	Propidium iodide
PLA-PEG	Poly(lactic acid)/poly(ethylene glycol)
PLGA	Poly(lactic-co-glycolic acid)
pmol	Picomole

P-NEs	Protein nanoemulsions
PS	Photosensitizer
PTT	Photothermal Therapy
QDots 705	Quantum dots 705
qPCR	Quantitative real-time polymerase chain reaction
RB	Rose bengal
RB-NS	Rose Bengal DBCO-nanosystems
rcf	Relative centrifugal forces
RLuc8	*Renilla reniformis* luciferase mutant
RLuc8-QDots 705 SI-NCs	*Renilla* luciferase – quantum dots 705 nanosystem self-illuminating Nanoconjugates
RNA	Ribonucleic acid
RNP	Ribonucleoprotein
ROS	Reactive oxygen species
R-PE	R-Phycoerythrin
RPMI	Roswell Park Memorial Institute
RT	Room temperature
s	Second
SARS-CoV- 2	Severe acute respiratory syndrome coronavirus 2
s.c.	Subcutaneously
SD	Standard deviation
SDS-PAGE	Sodium dodecyl sulfate polyacrylamide gel electrophoresis
sgRNA	Single guide Ribonucleic acid
SI-NS	"Self-illuminating" nanosystem

SI-RB-NS	Self-illuminating- Rose Bengal-nanosystems
siRNA	Small interfering Ribonucleic acid
SNPs	Sphingomyelin nanoparticles
SM	Sphingomyelin
SM-102	Octanoic acid, 8-[(2-hydroxyethyl)[6-oxo-6-(undecyloxy)hexyl]amino]-, 1-octylnonyl ester
SNs	Sphingomyelin nanoemulsions
SNs-B-GAL	Sphingomyelin nanoemulsions bearing β-galactosidase
SNs-FLuc	Sphingomyelin nanoemulsions bearing firefly luciferase
SNs-GFP	Sphingomyelin nanoemulsions bearing green fluorescence protein
SNs-OVA	Sphingomyelin nanoemulsions bearing ovalbumin
SNs-PE	Sphingomyelin nanoemulsions bearing R-phycoerythrin
NEs_RLuc8	Sphingomyelin nanoemulsions bearing *renilla* luciferase
SOPC	1-stearoyl-2-oleoyl-sn-glycero-3-phosphocholine
SPAAC	Strain-promoted azide-alkyne cycloaddition
STEM	Scanning transmission electron microscopy
t	Time
TAE buffer	Tris-acetate-EDTA (Ethylenediaminetetraacetic acid)
t-BHP	tert-butyl hydroperoxide
Tcells	T lymphocytes
TCO	Trans–cyclooctene
TEM	Transmission electron microscopy
TES	N-[Tris(hydroxymethyl)-methyl]-2-aminoethanesulfonic acid
TFA	Trifluoroacetic acid

TGF-β	Transforming growth factor-beta
TIC	Total ion count
TME	Tumor microenvironment
TSLP	Thymic Stromal Lymphopoietin
TUNEL	Terminal deoxynucleotidyl transferase (TdT) dUTP Nick-End Labeling
Tz	Tetrazine
UHPLC	Ultra-High-Performance Liquid Chromatography
UPLC	Ultra Performance Liquid Chromatography
UV	Ultraviolet
Vit E	Vitamin E
WHO	World Health Organization
X-GAL	5-bromo-4-chloro-3-indolyl-β-d-galactopyranoside
ZP	Zeta Potential

Agradecimientos

AGRADECIMIENTOS

Finalmente ha llegado este momento, quien me iba a decir que después de haber escrito una tesis, estas líneas iban a ser las más difíciles. Los que me conocen, saben que no soy una persona de muchas palabras y menos cuando se trata de abrirme y expresar sentimientos. Tantas son las personas que me he cruzado en esta etapa y tantas a las que realmente agradecer su apoyo y/o ayuda que unas palabras en estos agradecimientos no son suficientes. Pero allá vamos…

En primer lugar, me gustaría agradecer a mi directora de tesis María de la Fuente, y a mi tutor Rafael López por haberme acogido en el grupo y permitirme desarrollar esta tesis. María, a ti especialmente por tu confianza desde el primer momento siendo tan solo una alumna de máster, donde mis ideas y opiniones siempre fueron valoradas y tenidas en cuenta. Gracias también por tu implicación en nuestra formación llevándonos y animándonos a presentar nuestros resultados en tantos congresos.

Durante esta tesis, he tenido la suerte de colaborar con personas increíbles y visitar algunos de sus laboratorios donde siempre me han acogido con los brazos abiertos.

A Miguel González Blanco, en cuyo laboratorio empecé mi trabajo de máster. Gracias por el acogimiento, por tu apoyo, por tu disponibilidad siempre, incluso cuando ya estaba en la tesis, y tenía alguna duda sobre proteínas o necesitaba ir a purificar más proteína a tu lab. A los del lab de "DNA Repair and Genome Integrity", Javi, Tomás, Diana, Vanessa y Eva. Pero en especial a Raquel, por siempre estar con una sonrisa y tan happy contagiando buen rollo.

A los de Madrid. En primer lugar, agradecer a Bruno Sainz por recibirme con los brazos abiertos, siempre dispuesto a todo lo que te proponíamos con nuestras nanopartículas, por la motivación y las ideas, ha sido un verdadero placer colaborar con vosotros y trabajar en vuestro laboratorio. A JC, Sandra, Sonia y Diego. Pero en especial a Lala y Adri muchas gracias por vuestra ayuda, por vuestra playlist en el lab amenizando experimentos y porque con colaboradores así es un gusto trabajar.

To Annarita Miccio, thank you a lot for welcoming me to your group. Thank you for your support, for your encouraging ideas, and for the love for science. To my Parisian mates. Mathieu, Pierre, Giulia, Steicy, Mégane, Simone, Letizia, Tristan, Priyanka, Federico, Ilaria and Annalisa thanks a lot for your warm welcome and making me feel as one of the group. But especially to Anne and Maria for being the nicest lab mates in Paris, always smiling and willing to help. Merci beaucoup!!

A mis parisinas favoritas, Lidia y Rita, encontraros en esta maravillosa ciudad ha sido una suerte y un regalo. Gracias por los paseos, por las charlas, por las birras (vermús en mi caso) en el río, por descubrirme vuestro París, como lo echaré de menos.

Mil gracias a mi grupo de nano, del que me llevo a tantas personas en mi corazón. Abi, Sandra D, Saínza, María C, Raneem, Miguel, Aurora, Álex, Inés, Jen, Laura R, Soraya, Nere, Emma, Irene, Juliane, Gabriela, Laura C, Javi y Sheila. Sandra Alijas, gracias por haberle enseñado tanto de células a esta química que no sabía hacer absolutamente nada en ellas y por mantener el laboratorio. A Rebeca, porque a pesar de que coincidimos pocos meses, siempre me has tratado con mucho cariño y que me lo sigues trasmitiendo cada vez que nos encontramos. A Laura T, gracias por tu apoyo, por escucharme, por desahogarnos la una con la otra, por estar ahí cuando se me venía el laboratorio encima, por los viajes a los congresos juntas que se convirtieron en grandes aventuras. Estoy segura de que conseguirás todo lo que te propongas porque no tienes miedo a nada y siempre vas a por todas. A Sofi, por ser tan buena y generosa, por saber escuchar, por tu apoyo, por tu ayuda, por tus palabras bonitas, por lo que he aprendido contigo, por el cariño que desprendes, aquí me tienes siempre. A mi gran descubrimiento Bárbara, en tan poquito tiempo te convertiste en imprescindible en el lab. Gracias por todo lo que he aprendido contigo y de ti, eres una persona increíble y como científica igual. Eres rigurosa, persistente, inteligente, te adaptas al entorno… y como persona ya ni te cuento, me llevo una amiga para siempre. Gracias por aguantarme, por desahogarnos la una con la otra con audios de mil horas, por entendernos tan bien desde el minuto uno, por apoyarnos en las decisiones y estar ahí, ya sea en Santiago, Madrid o donde nos toque estar. Pero especialmente a Cris y Olaia, sin vosotras esta etapa no sería la misma. La verdad es que aquí no voy a escribir nada que no sepáis ya. Cris, por lo que he aprendido de ti, por las charlas, los cafés en el Mario, por los buenos momentos, por estar siempre, por tu apoyo constante, porque sin tu apoyo me habría costado seguir muchas veces, por tantas razones y tantos momentos... Olaia, porque sin ti esta tesis no sería la que es. Gracias por tu apoyo, por tu ayuda, por estar siempre que necesitaba resolver cualquier duda, por tu sabiduría, por tu infinita confianza, por tus palabras

bonitas y de ánimo, por tus ideas, por las reuniones a primera hora de la mañana donde acabábamos hablando de todo un poco, por los cafés en el Mario, por un larguísimo etcétera que ya sabes. ¡¡¡Infinitas gracias a las dos!!!

Me gustaría agradecer al laboratorio de nanomedicina del CiMUS, pero en especial a Iago, Catarina y Ana López a los que tanto he dado la turra para ir a usar el luminómetro día sí y día también. También agradecer al resto de personas del IDIS y técnicos de la USC que me han ayudado de una manera u otra durante esta época.

Á miña Sariña, la mejor compañera y amiga que el máster me ha podido dar. Qué bonito verte lograr lo que te propones, llegarás muy lejos.

A mis niñas del Son da Pacah, Laura (Agu), Berta (Tolis), Antía (Roomie), Noemi (mi Paquita) y Lucía (mi Luchi). Gracias porque este viaje empezó con vosotras hace mucho. Gracias por las horas y horas de risas, birras, a veces estudio, dramas, los Albariños, medievales, etc. Agu, por dejar de combinar esa sudadera con tu camiseta de Bob Marley por mí (jajaja), por las risas interminables, tus lavadoras constantes y las resacas en clase. Tolis, por ser la más cuqui del mundo, por tener un burro, tus tortillas y comida en general y ser la mejor madrina de graduación. Antía, mi roomie, por tantas anécdotas y momentos que aquí no puedo mencionar, por tus charlas de tableros, cañas infinitas y mil cosas más. Noe y Lu, porque las mejores noches de Santiago tienen vuestro nombre, y los días también. Noe, mi teniente alcaldesa favorita, porque sigas perdiéndote en la zona vieja después de tantos años y cayéndote en cada esquina, por dejarte liar por esta loca, por "Carballiño way", porque sigas poniéndole purpurina y lentejuelas a la vida (y a los tenis) tqm. Luchi, madre mía cuantas cosas podría poner aquí, jugar al precio justo, ir de paseo a zara, al súper o al tiger, los 150 cafés o cañas al día, las pelis románticas, los vídeos de Ylenia o los Simpson... Por estar siempre y para siempre, donde sea Santiago, Varsovia, Gdansk … hasta Padrón (jajaja) te quiero infinito princesa. Os quiero mucho chicas, cada quedada con vosotras me da años de vida.

Gracias a mis amigas de Cambados, porque sois casa y familia. Ra, Pau, Lau (Almudenita), Nadi, Kelly, Ana, Merry y Ali. Por apoyarme en esta etapa, aunque sigáis sin entender que investigo JAJAJAJA. Por seguir creciendo juntas y celebrando los éxitos de cada una como si fuesen propios. Por los veranos juntas de playa, sol y cañas. Pero, sobre todo, por seguir juntas desde enanas a pesar de la distancia.

Por último y más importante, a mi familia, porque me lo habéis dado todo. Sin vuestro apoyo esta tesis no existiría. A mis padres, las mayores GRACIAS porque sin vosotros no habría podido

llegar hasta aquí, sois los mejores. Mamá, porque ver el orgullo en tus ojos merece la pena haber pasado por esta tesis que a veces se me ha hecho más que cuesta arriba. Aunque cada vez que te pregunte qué hago (por mucho que te lo explique) dices una cosa distinta. Papá, porque para ti tus hijas son las mejores siempre y no es discutible. Nana, mi primera mejor amiga, la mejor hermana mayor que existe, por entendernos solo con mirarnos, por apoyarme siempre y animarme a hacer lo que quería en cada momento, por seguir desbloqueando logros juntas, te quiero infinito. Luli, mi niñita, verte crecer es uno de los mejores regalos que me ha dado esta vida. Mi lapita, seguiremos descubriendo el mundo juntas, y siempre te llevaré conmigo a donde haga falta. Por tu amor infinito y ojalá verme con los ojos con los que tú me miras. A mis peluditos Coco y Kenzo porque sois anti-estrés naturales. Pero especialmente a mi princesa Kira, porque eras el ser más perfecto. Porque un abrazo tuyo era lo más sanador que tenía, al estar contigo se me pasaban todos los males. Porque cuando estoy escribiendo esto, ya hace 3 meses que te fuiste, pero solo puedo darte las gracias por los 12 años y medio que me regalaste de puro amor y felicidad.

Finalmente, David porque esta tesis es casi tanto tuya como mía. Porque sin tu apoyo diario, y ayuda constante, no podría estar escribiendo estas líneas. Por escucharme hablar de nanos y experimentos TODOS los días a TODAS horas, se podría hacer esto o aquello o tengo una idea y podría hacer esto, aunque no entendieses de que te estaba hablando. Por aguantarme ni cuando yo misma lo hacía. Por seguirme allá donde vaya cambiando de ciudad cada poco. Por millones de cosas más. Pero lo más importante, por quererme como lo haces de la forma más sana, desinteresada y bonita. To the moon and back.

Gracias a todas y cada una de las personas que menciono, y también a todas las que seguro me he olvidado de nombrar. Pero no puedo terminar sin mencionar a todas las mujeres que me han inspirado y me inspiran día a día y que gracias a su constancia y lucha yo puedo estar firmando esta tesis. Por las que fueron silenciadas por la historia y las que jamás se rindieron, no por ellas sino por las que vendríamos detrás.

"Que nada nos defina. Que nada nos sujete. Que sea la libertad nuestra propia sustancia".
SIMONE DE BEAUVOIR

Ethical issues and annexes

ETHICAL ISSUES

1. ANIMAL STUDIES

All animal procedures were conducted in accordance with the institutional and national guidelines for the animal care and welfare, the ARRIVE guidelines. Procedures were approved by the internal ethical research and welfare committee (IIB, UAM), and by the Local Authorities (Comunidad de Madrid, PROEX 294/19), according to the Spanish Government rules (Real Decreto RD53/2013) and European Union legislation (86/609/CEE, 2003/65/CE and 2010/63/EU). Experimental procedures were executed in the animal facilities of "Alberto Sols" Biomedical Research Institute (IIB).

2. HUMAN CELL CULTURE

All established cell lines (derived from healthy and cancer tissues) used in this work were acquired from commercially available resources (American Tissue Culture Collection, ATCC) and cultured in the conditions recommended by the manufacturers and only used for the research purposes specifically described in the present thesis.

3. PATIENT'S SAMPLES

The establishment of the CAF cell lines in the "Chapter IV" was included in the study (PDACTREAT) that has been approved by the Institutional Ethics Committee (Comitato Etico Fondazione Centro San Raffaele, Istituto Scientifico Ospedale San Raffaele, Milan, Italy) under IRB number 57/INT/2014.

Human pancreatic tumor-derived xenografts to establish PDAC-PDX cancer cell lines PancA6L, Panc185 and Panc354 used in this thesis were obtained from Dr. Manuel Hidalgo under a Material Transfer Agreement with the Spanish National Cancer Centre (CNIO), Madrid, Spain (Reference no. I409181220BSMH).

Blood samples were collected in accordance with the guidelines and protocols approved by the Institutional Ethical Committees, Galician Clinical Research Ethics Committee, SERGAS: code approval: 2017/538. All individuals signed informed consent forms and could withdraw their consent at any time. The study was performed in accordance with the Declaration of Helsinki.

4. BIOLOGICAL SAMPLES

Plasmid pBAD-RLuc8 to obtain the protein RLuc8 was transferred to our laboratory from Dr. Sanjiv Sam Gambhir, director of the Molecular Imaging Program at Stanford (MIPS), School of Medicine under a Material Transfer Agreement with the Stanford University, Palo Alto (CA), USA.

5. IMAGES USE

Unless clarified, I have produced all the images presented in this thesis. In the case of images reused or adapted from other manuscripts, permission has been asked to the publishers, and the mode of legal use has been clarified at the bottom of the corresponding figures. In addition, the paid subscription software 'Biorender.com' (License 71C183AB) and the free resource Flaticon.com was used for the figure's preparation.

ANNEXES

LIST OF ANNEXES

ANNEX I……..298

Ethical approvals for animal experimentation

ANNEX II…….303

Ethical approval and Material Transfer Agreement for patient's samples

ANNEX III…….314

Ethical approval and Material Transfer Agreement for biological samples

ANNEX IV…….315

Licenses and certificates to perform the preclinical experimental work

ANNEX I. Ethical approvals for animal experimentation.

Comunidad de Madrid

Dirección General de Agricultura,
Ganadería y Alimentación
CONSEJERÍA DE MEDIO AMBIENTE, ORDENACIÓN DEL
TERRITORIO Y SOSTENIBILIDAD

Vista la solicitud presentada por BRUNO SAINZ ANDING, para la autorización del proyecto de memoria técnica titulada UNA ESTRATEGIA MULTIFACTORIAL PARA ENTENDER Y TRATAR EL CÁNCER DE PÁNCREAS Y COLON, a desarrollar en el centro usuario GABINETE VATERINARIO UAM con código de registro ES28079000097 y en el INSTITUTO DE INVESTIGACIONES BIOMEDICAS ALBERTO SOLS con código de registro ES280790000188 y siendo el responsable del proyecto BRUNO SAINZ ANDING:

Visto el informe del Área de Protección Animal.

Considerando que el citado proyecto se ajusta a lo establecido en el Real Decreto 53/2013 de 1 de febrero por el que se establecen las normas básicas aplicables para la protección de los animales utilizados en experimentación y otros fines científicos, incluyendo la docencia.

Esta Dirección General ha resuelto: autorizar la realización del proyecto referenciado siempre que se mantengan las condiciones que dieron lugar a la autorización y que el personal que intervenga tenga la preparación y formación adecuada que se especifica en el citado Real Decreto.

Tal y como se indica en el informe de evaluación del proyecto presentado, éste debe ser sometido a una evaluación retrospectiva en el momento que indica dicho informe.

Contra esta Resolución, que no agota la vía administrativa, cabe interponer recurso de alzada en el plazo de un mes, contado desde el día siguiente a la recepción de esta notificación, ante el Viceconsejero de Medio Ambiente, Ordenación del Territorio y Sostenibilidad, conforme a lo establecido en el artículo 121 y siguientes de la Ley 39/2015, de 1 de octubre, del Procedimiento Administrativo Común de las Administraciones Públicas

Si a lo largo del plazo de ejecución del proyecto apareciera un método alternativo, esta resolución quedaría sin efecto.

Madrid, a fecha de la firma

EL DIRECTOR GENERAL DE AGRICULTURA, GANADERIA Y ALIMENTACION
(P.D.F. Resolución de 15 de junio de 2018)
Subdirector General de Producción Agroalimentaria

Ref PROEX 294/19

La autenticidad de este documento se puede comprobar en www.madrid.org/cove
mediante el siguiente código seguro de verificacin: 09087344395945405302 13

MINISTERIO
DE CIENCIA, INNOVACIÓN
Y UNIVERSIDADES

CSIC

INSTITUTO DE INVESTIGACIONES
BIOMÉDICAS "ALBERTO SOLS", IIBM

El Comité de Ética en Experimentación Humana y Animal (CEEHA) Órgano encargado del Bienestar animal (OEBA) del Servicio de Medicina Comparativa del Instituto de Investigaciones Biomédicas "Alberto Sols" CSIC. UAM

I N F O R M A

Que ha revisado desde el punto de vista técnico el Proyecto de Investigación titulado **"Una estrategia multifactorial para entender y tratar el cáncer de páncreas y colon".** Remitido por el **Dr. Bruno Sainz Anding**, en el que se utilizarán como modelos experimentales Ratones.

Que ha aprobado la estabulación de los animales y la realización de los procedimientos, que vienen definidos en el Proyecto, en las instalaciones del Servicio de Medicina Comparativa del Instituto de Investigaciones Biomédicas "Alberto Sols" CSIC con Nº de Registro. ES 280790000188.

Asimismo, el investigador principal del proyecto, **Dr. Bruno Sainz Anding** informa que el responsable de diseñar y supervisar los procedimientos realizados con animales, está acreditado con categoría C (funciones c y d – RD53/2013-Orden ECC/566/2015), y que no existen técnicas alternativas que suplan el uso de estos animales, si bien las técnicas utilizadas permiten reducir el número de animales a utilizar y cumplen con los requisitos de refinamiento establecidos en la legislación.

Este informe favorable se ha realizado en cumplimiento de los artículos 33.1 y 38.1 del Real Decreto 53/2013 de 1 de Febrero (BOE 8 de Febrero) sobre la protección de los animales utilizados en experimentación y otros fines científicos incluyendo la docencia.

Madrid, 4 de noviembre de 2019

Guillermo De Cárcer Díez
Presidente CEEHA

Marta Miró Murillo
Secretario CEEHA
Responsable en Bienestar
Animal del I.I.B.m (CSIC)

C.E. INVESTIGACIONES BIOMÉDICA "ALBERTO SOLS" INSTITUTO CSIC UAM

Gabinete Veterinario

El Órgano encargado del Bienestar animal (OEBA) del Gabinete Veterinario de la Universidad Autónoma de Madrid

I N F O R M A

Que ha revisado desde el punto de vista técnico el Proyecto de Investigación **"Una estrategia multifactorial para entender y tratar el cáncer de páncreas y colon"** remitido por el investigador **Dr. Bruno Sainz Anding**, en el que se utilizará como modelo experimental, en este centro usuario, **el ratón (*Mus musculus)***

Que ha aprobado la estabulación de los animales y la realización de los procedimientos que vienen definidos en el Proyecto en las instalaciones del Gabinete Veterinario de la UAM con número de registro ES-28079-0000097.

Asimismo, el investigador principal del proyecto informa que el responsable de diseñar y supervisar los procedimientos realizados con animales es **él mismo**, acreditado para la **función d** (diseño experimental, según RD 53/2013), y que no existen técnicas alternativas que suplan el uso de estos animales, si bien las técnicas utilizadas permiten reducir el número de animales a utilizar y cumplen con los requisitos de refinamiento establecidos en la legislación.

Este informe favorable se ha realizado en cumplimiento de los artículos 33.1 y 38.1 del Real Decreto 53/2013 de 1 de febrero (BOE 8 de febrero) sobre la protección de los animales utilizados en experimentación y otros fines científicos incluyendo la docencia.

Madrid, 08 de noviembre de 2019

David Muñoz Valverde
Responsable de bienestar animal
Gabinete Veterinario de la UAM

GABINETE VETERINARIO/ UNIVERSIDAD AUTÓNOMA DE MADRID
C/ Arzobispo Morcillo,4 28029 MADRID
Tel: 91 497 3830 Fax: 91 497 5353 e-mail: gabinete.veterinario@uam.es

UNIVERSIDAD AUTÓNOMA DE MADRID

CEI 103 – 1958 -A337

El Comité de Ética/Subcomité de Experimentación Animal de la Universidad Autónoma de Madrid, como Órgano Habilitado por la Comunidad de Madrid(Resolución de 24 de septiembre de 2013) para evaluación de proyectos en base a lo señalado en el RD 53/2013 de 1 de febrero, por el que se establecen las normas básicas aplicables para la protección de los animales utilizados en experimentación y otros fines científicos, incluyendo la docencia, ha evaluado la propuesta de Proyecto que a continuación se relaciona, presentada por **D. Bruno Sainz Anding,** con **DNI 50336136S**

Conforme a lo establecido en el artículo 33 del RD 53/2013, para la evaluación se ha requerido cumplimentar el formulario oficial aprobado por este Órgano Habilitado, que recoge toda la información incluida en el Anexo X, la evaluación se ha realizado sin existir conflicto de intereses (Art. 43.b del RD 53/2013) y con un nivel de detalle apropiado al tipo de proyecto (Art. 34, del RD 53/2013)

En base a las respuestas obtenidas se ha llegado a las siguientes conclusiones

Título del proyecto:

Una estrategia multifactorial para entender y tratar el cáncer de páncreas y colon

Investigador Principal, responsable del diseño y de los procedimientos: Bruno Sainz Anding, capacitado para la Función d), diseño de proyectos y procedimientos

Centro donde se realizan los procedimientos: Animalario del Gabinete veterinario UAM con Número de Registro ES 28079000097 y Animalario del IIB Alberto Sols con número de Registro ES-28079-0000188

EVALUACIÓN

1. Evaluada la finalidad y beneficios científicos ó docentes justifica el uso de animales **(Art. 34, 2a) FAVORABLE**

2. Evaluada la conformidad con los requisitos de reemplazo, reducción y refinamiento **(Art. 34 2b) FAVORABLE**

3. Evaluación y clasificación de los procedimientos **(Art. 34, 2c)**
   a) **Severidad del proyecto:** ***SEVERO***
   b) **Clasificación final del proyecto:** ***Proyecto Tipo III***

4. Evaluado el análisis de los daños y beneficios, para determinar si los daños, el sufrimiento, el dolor y la angustia que se les puedan causar a los animales están justificados por los resultados esperados, teniendo en cuenta consideraciones éticas y los beneficios que, en definitiva, pueda suponer el proyecto para los seres humanos, los animales o el medio ambiente **(Art. 34, 2d) FAVORABLE**

UNIVERSIDAD AUTONOMA DE MADRID

CEI 103 – 1958 A 337

5. Examen de la/s situaciones y excepciones previstas en los artículos 6, 7, 9.1, 19, 20, 21, 22, 23, 25.3 y 5, 26 y 29 del RD 53/2013, de 1 de febrero **(Art. 34, 2e)**
   Art. 6, Condiciones generales de alojamiento y cuidado de los animales ***Favorable***
   Art. 7, Métodos de eutanasia ***Favorable***
   Art.9.1, transporte de animales conforme a normativa vigente ***Favorable.***
   Art. 19 Animales criados para ser utilizados en los procedimientos ***Favorable.***
   Art. 20 Animales de especies amenazadas ***No aplica.***
   Art. 21 Primates ***No aplica.***
   Art. 22 Animales capturados en la naturaleza ***No aplica.***
   Art. 23 Animales asilvestrados y animales vagabundos de especien domésticas ***No aplica.***
   Art. 25.3 Los procedimientos se realizan evitando cualquier dolor sufrimiento, angustia o daño duradero innecesario. ***Favorable***
   Art. 25.5 Condiciones generales de los procedimientos para que puedan ser realizados por personas capacitadas o autorizadas de forma temporal en las condiciones fijadas en el art.15.3 ***No aplica***
   Art. 26 Anestesia y analgesia durante el procedimiento ***Favorable***

Examinadas las excepciones previstas en el artículo 34.2, e) ***no se ha encontrado ninguna*** *situación que requiera autorización expresa por parte de la Autoridad competente*

6. **Determinación de la necesidad de evaluar el Proyecto de forma retrospectiva** y en su caso cuando debería hacerse. **(Art. 34.2f): SÍ requiere evaluación retrospectiva** que deberá presentarse a la finalización del periodo de autorización del proyecto.

Por lo expuesto este Órgano Habilitado emite una **EVALUACIÓN FAVORABLE**

Este informe solo tiene validez para el proyecto o procedimiento propuesto y en las condiciones en ellos descritas. Cualquier cambio que afecte a las implicaciones bioéticas y/o de bioseguridad del mismo, invalida este informe y deberá ser puesto en conocimiento de este Órgano Habilitado para su valoración.

Fecha
25 de noviembre de 2019

La Secretaria del CEI-UAM

Isabel Martínez Cabañas

UNIVERSIDAD AUTÓNOMA DE MADRID – COMITÉ DE ÉTICA DE LA INVESTIGACIÓN –

El Presidente del CEI-UAM

José Manuel González Sancho

ANNEX II. Ethical approval and Material Transfer Agreement for patient's samples.

October 9, 2014

MATERIAL TRANSFER AGREEMENT
Non-commercial Research Use Only

REQUESTED MATERIAL:
Several human pancreatic tumor-derived xenografts and cell lines have been requested by the recipient

MATERIAL TO BE SENT (the "Material"):
The following human pancreatic tumor-derived xenografts will be distributed:
Model code:
PancA6L
Panc185
Panc215
Panc253
Panc247
Panc354
Panc265
Panc286

RECIPIENT INSTITUTION:
Universidad Autónoma de Madrid

RECIPIENT SCIENTIST(PRINCIPAL INVESTIGATOR):
Bruno Sainz Anding

DESCRIPTION OF RESEARCH PURPOSE:
Departamento de Medicina Preventiva y Salud Pública y Microbiología

PROVIDER INSTITUTION: **FUNDACIÓN CENTRO NACIONAL DE INVESTIGACIONES ONCOLÓGICAS CARLOS III (CNIO)**

PROVIDER SCIENTIST (HEAD OF GROUP/UNIT/SECTION):
Manuel Hidalgo Medina (Head of GI CRUnit)

In response to the request by the RECIPIENT SCIENTIST for the MATERIAL, the PROVIDER INSTITUTION asks that the RECIPIENT INSTITUTION and the RECIPIENT SCIENTIST (from now on collectively referred to as the "RECIPIENT") agree to the following before the RECIPIENT receives the MATERIAL:

1. The above MATERIAL is the property of the PROVIDER INSTITUTION and is made available as a service to the research community. The RECIPIENT shall acknowledge PROVIDER as the source of the MATERIAL in any publication involving the use of the MATERIAL. Should this obligation be neglected in a given publication, the PROVIDER reserves the right to request the RECIPIENT to have such publication rectified as soon as practicable after the PROVIDER's request.
2. The PROVIDER INSTITUTION retains ownership of the original MATERIAL and unmodified derivatives and will be free, in its sole discretion, to distribute the MATERIAL to others and to use it for ists own purposes.
3. The PROVIDER INSTITUTION will be co-owner of any modified derivatives as well as any other substances or organisms that could not have been created or derived but for the use of the MATERIAL ("Newly Developed Material"). The parties agree to negotiate suitable agreements in good faith which shall provide for the further development of this joint ownership. In any case each co-owner shall have the right to use and exploit by itself the Newly Developed Material, but licenses to third parties shall be granted jointly by both co-owners.

4. The RECIPIENT agrees to notify the PROVIDER of any filed patent application or other type of Intellectual Property Right ("IPR") claiming inventions or new developments made through the use of the MATERIAL provided by the PROVIDER

   INSTITUTION or through the use of any Modified or Unmodified Derivatives thereof (an "INVENTION").
   RECIPIENT agrees that in the event RECIPIENT makes any INVENTION whether patentable or not, RECIPIENT shall promptly bring the INVENTION and any patent application filed thereon to the attention of the PROVIDER. In case of joint INVENTIONS, PROVIDER and RECIPIENT shall conclude in good faith a separate agreement concerning the use, patenting and commercialization of those joint INVENTIONS, subject to the regime established in clause 3. In case of other INVENTIONS, RECIPIENT shall grant to the PROVIDER and its affiliated institutes an irrevocable non-exclusive royalty free license to practice the INVENTION for scientific research purposes; and RECIPIENT shall grant to the licensees of the PROVIDER an irrevocable non-exclusive royalty-bearing license to practise the INVENTION for commercial purposes if such license is necessary for the licensees of the PROVIDER to exercise their rights granted by the PROVIDER. For the purpose of this paragraph, any reference to patents or patent applications shall be deemed indistinctly referred to other IPR.

5. The MATERIAL and any Unmodified Derivatives thereof:

   - shall not be used for any commercial purpose or in any research that is subject to consulting, licensing, or other commercial obligations to a third party;
   - will only be used for non-profit pre-clinical research or teaching purposes and solely in connection with the RESEARCH PURPOSE;
   - will not be used in humans;
   - will not be further distributed to others without the PROVIDER INSTITUTION's written consent; the RECIPIENT shall refer any request for the MATERIAL by a third party to the PROVIDER INSTITUTION.
   - will not be used by the RECIPIENT INSTITUTION in any laboratories other than the RECIPIENT SCIENTIST's laboratory, and the RECIPIENT shall ensure that no one will be allowed to take or send the MATERIAL and any Unmodified Derivatives thereof to any other location than mentioned above.

6. Except as provided in this Agreement, no express or implied licenses or other rights are provided to the RECIPIENT.

7. The MATERIAL provided hereunder is understood to be experimental in nature and may have hazardous properties. The MATERIAL is provided without warranty of merchantability or fitness for a particular purpose or any other warranty express or implied, or that the use of the MATERIAL will not infringe any patent, copyright, trademark, or other proprietary rights.

8. Unless prohibited by law, the RECIPIENT assumes all liability for claims for damages against it by third parties which may arise from the use, storage or disposal of the MATERIAL except that, to the extent permitted by law, the PROVIDER INSTITUTION shall be liable to the RECIPIENT when the damage is caused by the gross negligence or willful misconduct of the PROVIDER INSTITUTION.

9. The RECIPIENT agrees to use the MATERIAL in compliance with all applicable statutes and regulations.

10. PROVIDER INSTITUTION personnel will have reasonable access to consult informally with the RECIPIENT SCIENTIST regarding the Research carried out using the MATERIAL. Upon request, the RECIPIENT will give the PROVIDER or its personnel information on the execution of the RESEARCH PURPOSE.

11. This Agreement may not be assigned or otherwise transferred by the RECIPIENT without the prior written consent of the PROVIDER.

12. The RECIPIENT shall be responsible for the fulfillment of the obligations established in the present Agreement by the researchers or personnel working with the RECIPIENT SCIENTIST in the execution of the RESEARCH PURPOSE.

13. The PROVIDER reserves the right to request the immediate return or destruction of the MATERIAL in case the RECIPIENT does not comply with its obligations under this Agreement or in any other case provided that a term of notice of two months is taken into account.

14. This Agreement shall be governed by Spanish law. The Parties expressly agree to submit all conflicts resulting from the execution or interpretation of this Agreement to the courts and tribunals of the city of Madrid, with express waiver of their own forum.

15. Should any provision or portion of this Agreement be found to be illegal, invalid or unenforceable, the remaining provisions shall remain in full force and effect.

IN WITNESS WHEREOF, the Parties execute this Agreement in two original counterparts but to one sole effect at the place and date indicated at the top of this document.

SIGNATURES BEGIN ON THE FOLLOWING PAGE

For and on behalf of the PROVIDER:

Name of the Institution (printed): **FUNDACIÓN CENTRO NACIONAL DE INVESTIGACIONES ONCOLÓGICAS CARLOS III**	Address (printed): **C/ Melchor Fernández Almagro, 3** **28029 Madrid, Spain**
Name of Legal Representative (printed): **Juan Arroyo**	Name of Scientist (printed): **Manuel Hidalgo Medina (Head of GI CRUnit)**
Title (printed): **Managing Director**	Title (printed): **Head of the GI Clinical Research Unit**
13 oct 14. Date and signature of Legal Representative	13.10.14 Date and signature of Scientist

For and on behalf of the RECIPIENT:

Name of the Institution (printed): **Universidad Autónoma de Madrid**	Address (printed): **Universidad Autónoma de Madrid** **Carretera Colmenar Viejo** **Km. 15 Cantoblanco** **28049 Madrid, España**
Name of Legal Representative (printed): **Nuria Fernández Monsalve**	Name of Scientist (printed): **Bruno Sainz Anding**
Title (printed): **Vicedirectora de Investigación**	Title (printed): **Investigador Ramón y Cajal**
9.10.14 Date and signature of Legal Representative	9.10.14 Date and signature of Scientist

UNIVERSIDAD AUTÓNOMA DE MADRID · VICERRECTORADO DE INVESTIGACIÓN ·

ANY NOTICE PURSUANT TO THIS AGREEMENT SHALL BE MADE TO:

If to the PROVIDER INSTITUTION:
Technology Transfer (technologytransfer@cnio.es)
Centro Nacional de Investigaciones Oncológicas
C/ Melchor Fernández Almagro, 3, 28029 Madrid, Spain.

If to the RECIPIENT INSTITUTION:
Name of contact person
Dr. Bruno Sainz Anding

Title
Investigador Ramón y Cajal

Name of Recipient Institution
Universidad Autónoma de Madrid
Facultad de Medicina, Departamento de Medicina Preventiva y Salud Pública y Microbiología

Address Recipient Institution
Calle del Arzobispo Morcillo 4
28049 Madrid, España

e-mail contact person
bruno.sainz@uam.es

30 OSR

IL COMITATO ETICO
dell'Ospedale San Raffaele - Milano
Istituto di Ricovero e Cura a Carattere Scientifico
Istituito ai sensi del D.M. 08.02.2013

riunito in data 17/07/2014

costituito da:

ANZANI ALFREDO	Clinico, Ospedale San Raffaele, **Presidente Comitato Etico OSR**	Presente
POZZA GUIDO	Clinico, Ospedale San Raffaele, **Vice-Presidente Comitato Etico OSR**	Presente
ARRIGONI CRISTINA	Rappresentante Area Professioni Sanitarie, Univ. Studi di Pavia	Assente
BASILE GIUSEPPE ******	Medico Legale, IRCCS Ist. Ortopedico Galeazzi	Assente
CABITZA PAOLO	Esperto Dispositivi Medici, IRCCS Policlinico San Donato	Presente
CALORI GILIOLA	Biostatistico, Ospedale San Raffaele	Presente
CARRETTA ILARIA	Esperto in Psicologia, San Raffaele	Presente
CHIODI MAURIZIO	Esperto Teologia Morale, Facoltà Teologica di Milano	Presente
CHIUMELLO GIUSEPPE	Pediatra, Ospedale San Raffaele – Univ. Vita Salute San Raffaele	Presente
CLEMENTI FRANCESCO	Farmacologo, Prof. Emerito di Farmacologia, Università di Milano	Presente
COLLOCA STEFANO	Esperto in Bioetica, Università degli Studi di Pavia	Presente
FERRARI MAURIZIO	Esperto in Genetica, Ospedale San Raffaele – Univ. Vita Salute S.Raffaele	Presente
MARTINELLI VITTORIO	Clinico, Ospedale San Raffaele	Presente
MEOLA GIOVANNI	Clinico, IRCCS Policlinico San Donato – Univ. di Milano	Presente
MICIELI GIUSEPPE	Clinico, Istituto Neurologico Mondino	Assente
ORLANDO M. ELISABETTA	Rappr. Volontariato/Associaz.	Assente
PROCOPIO GIUSEPPE	Clinico, Ist. Nazionale Tumori di Milano	Presente
REICHLIN MASSIMO	Esperto in Bioetica, Università Vita-Salute San Raffaele	Presente
RICHELMI PLINIO	Farmacologo, Università degli Studi di Pavia	Assente
SORGHI MASSIMO	Medico Medicina Generale, ASL Milano 2	Assente
TADINI PATRIZIA *	Farmacista SSR, Ospedale San Raffaele	Assente
ZOPPEI GIANNA	Esperto Umanizzazione Cure, Ospedale San Raffaele	Presente

Componenti in relazione alla qualifica

LUCIANI DIEGO	Ingegnere Clinico, Ospedale San Raffaele	Presente
PONTIROLI ANTONIO	Esperto in Diabetologia e Nutrizione, Univ. Studi di Milano	Presente
TRIBERTI CESARE	Esperto in Diritto Sanitario, Libero Professionista	Presente

Componenti IRCCS Ospedale San Raffaele

MAZZUCONI ROBERTS	Direttore Sanitario, Ospedale San Raffaele	Assente
MANDELLI PAOLO	Sostituto DS, Ospedale San Raffaele	Presente
TADINI PATRIZIA *	Farmacista SSR, Ospedale San Raffaele	Assente
FRANZIN MICHELA ****	Sostituto Farmacista, Ospedale San Raffaele	Presente
MONTORSI FRANCESCO	Direttore Scientifico, Ospedale San Raffaele	Presente
GUIDOTTI LUCA	Sostituto DSC, Ospedale San Raffaele	Assente

Componenti IRCCS Policlinico San Donato

CUPPONE M. TERESA	Direttore Sanitario, IRCCS Policlinico San Donato	Presente
CARPINELLI LUCA	Sostituto DS, IRCCS Policlinico San Donato	Assente
CAVALLAZZI MARIO **	Farmacista, IRCCS Policlinico San Donato	Assente
FELISATTI MONICA ***	Sostituto Farmacista, IRCCS Policlinico San Donato	Presente
TETTAMANTI GUIDO	Direttore Scientifico, IRCCS Policlinico San Donato	Presente
MENICANTI LORENZO	Sostituto DSC, IRCCS Policlinico San Donato	Assente

Componenti IRCCS Istituto Ortopedico Galeazzi

PREGLIASCO FABRIZIO	Direttore Sanitario, IRCCS Ist. Ortopedico Galeazzi	Assente
VINCI ANNA	Sostituto DS, IRCCS Ist. Ortopedico Galeazzi	Presente
CAVALLAZZI MARIO **	Farmacista, IRCCS Ist. Ortopedico Galeazzi	Assente
FELISATTI MONICA ***	Sostituto Farmacista, IRCCS Ist. Ortopedico Galeazzi	Presente
BANFI GIUSEPPE	Direttore Scientifico, IRCCS Ist. Ortopedico Galeazzi	Assente
CITTERA ELENA	Sostituto DSC, IRCCS Ist. Ortopedico Galeazzi	Presente

Componenti IRCCS Istituto Mondino

MONETA ANGELA	Direttore Sanitario, IRCCS Ist. Mondino di Pavia	Presente
	Sostituto DS, IRCCS Ist. Mondino di Pavia	
GERVASIO LUISA	Farmacista, IRCCS Ist. Mondino di Pavia	Presente
	Sostituto Farmacista, IRCCS Ist. Mondino di Pavia	
NAPPI GIUSEPPE	Direttore Scientifico, IRCCS Ist. Mondino di Pavia	Assente
BLANDINI FABIO	Sostituto DSC, IRCCS Ist. Mondino di Pavia	Presente

Componenti San Raffaele Turro

MAZZITELLI SALVATORE	Direttore Sanitario, San Raffaele Turro	Assente
BENEDETTI FRANCESCO	Sostituto DS, San Raffaele Turro	Assente
TADINI PATRIZIA *	Farmacista, San Raffaele Turro	Assente
FRANZIN MICHELA ****	Sostituto Farmacista, San Raffaele Turro	Presente

Componenti Istituti Clinici Sant'Ambrogio e San Siro

BISSOLATI MORENA	Direttore Sanitario, Istituti Clinici Sant'Ambrogio e San Siro	Assente
CIRRI SILVIA	Sostituto DS, Istituti Clinici Sant'Ambrogio e San Siro	Presente
FELISATTI MONICA ***	Farmacista, Istituti Clinici Sant'Ambrogio e San Siro	Presente
CAVALLAZZI MARIO **	Sostituto Farmacista, Istituti Clinici Sant'Ambrogio e San Siro	Assente

* TADINI PATRIZIA : farmacista SSR e farmacista OSR
** CAVALLAZZI MARIO : farmacista Policlinico S. Donato e farmacista Ist. Ortopedico Galeazzi, sostituto farmacista Istituti Clinici Sant'Ambrogio e San Siro
*** FELISATTI MONICA : farmacista Istituti Clinici Sant'Ambrogio e San Siro, sostituto farmacista Policlinico S. Donato e sostituto farmacista Ist. Ortopedico Galeazzi
**** FRANZIN MICHELA : sostituto farmacista Ospedale San Raffaele e sostituto farmacista San Raffaele Turro
***** BASILE GIUSEPPE : ha valutato la documentazione per la parte di competenza in sede di pre-istruttoria

per esaminare

il protocollo N° PDACTREAT, versione 1 del 10/06/2014, avente per titolo:

Studio del ruolo del microambiente tumorale nel carcinoma del pancreas e sviluppo preclinico di strategie terapeutiche atte a interferire con meccanismi di immunosoppressione

v i s t i

- la scheda informativa redatta dal Primario Dott. Gianpaolo Balzano;
- il protocollo sopra indicato;
- la lettera di trasmissione del 10/06/2014;

- il foglio informativo e la dichiarazione di consenso per un paziente adulto capace di dare personalmente il consenso, versione 1 del 09/06/2014;
- il foglio informativo e la dichiarazione di consenso per il volontario sano, versione 1 del 09/06/2014;
- la copia del Grant AIRC (anno 2011);
- il form costi del 10/06/2014;
- il CV ed il Modello di Dichiarazione pubblica sul conflitto di interessi del PI e Co-Inv;

s e n t i t a

l'illustrazione del protocollo fatta dal relatore, prof. F. Clementi, di cui si riporta il testo:
".....E' uno studio spontaneo che coinvolge sperimentatori e clinici e che vuole studiare l'aspetto immunologico correlato con lo sviluppo del tumore pancreatico per meglio identificare in modelle preclinici possibili terapie efficaci.
In breve lo studio si propone di studiare il ruolo dell'ipossia e morte cellulare nel rilascio di citochine da parte di cellule tumorali; localizzare ex vivo zone ipossiche di tumore pancreatico che esprimano citochine; studiare in animali immunodeficienti strategie per contrastare il rilascio di citochine; studiare in modelli murini di tumore pancreatico possibili strategie terapeutiche a base immunologica. E' uno studio di tipo sperimentale che utilizza parte di tessuti umani, in particolare frammenti di tumore pancreatico, linfonodi e sangue da pazienti e sangue da donatori sani. Per questo motivo è richiesto il parere del C.E. Mi sembra che non ci siano problemi etici riguardanti i pazienti, che mettono a disposizione parti di reperti chirurgici che andrebbero distrutti, e nemmeno per i donatori sani che si limitano a donare una modesta quantità di sangue....."

Relativamente al modulo di consenso informato si raccomanda di:
Modello A
- Punto 2.2: spiegare con termini semplici "modelli preclinici", come nel capoverso successivo
- Punto 3: con collaboratori si intendono solo medici o anche infermieri?
- Punto 7: sostituire "in questo caso" con in ogni caso

Modello C
- Punto 2.2: spiegare con termini semplici "modelli preclinici", come nel capoverso successivo
- Punto 3: con collaboratori si intendono solo medici o anche infermieri?
- Verificare la sequenza numerica

Nell'informativa al trattamento dei dati eliminare nel testo "l'Ente/Associazione/Istituto...."

v e r i f i c a t o c h e

detto protocollo sarà condotto in conformità ai principi etici che traggono la loro origine dalla Dichiarazione di Helsinki, nel rispetto della Good Clinical Practice e delle disposizioni normative applicabili

esprime parere favorevole
e resta in attesa del modulo di consenso informato modificato

Nota generale: Si raccomanda al proponente di aggiornare costantemente il Comitato Etico sull'andamento della ricerca, a cominciare dalla comunicazione del primo caso reclutato, della sua conclusione o eventuale interruzione, di fornire un rapporto annuale sullo stato avanzamento studio e di quanto altro richiesto dalle normative. In particolare il Comitato dovrà essere tempestivamente informato di eventuali gravi effetti collaterali riscontrati nel corso della sperimentazione e di eventuali modifiche che si intendessero apportare al protocollo.

Si ricorda che per indagini cliniche con dispositivi marcati CE, utilizzati secondo destinazione d'uso (Art. 14, comma 8 D.Lgs. 46/97 emendato dal D.Lgs 25/01/2010, n. 37), il promotore dovrà comunicare l'avvio dell'indagine clinica al Ministero della Salute, ivi comprese la data di conclusione o interruzione.

La versione modificata del testo di Consenso Informato, qualora il Comitato Etico lo richiedesse, dovrà essere sottoposta all'Ufficio di Presidenza del Comitato Etico per convalida.

IL PRESIDENTE
(Dott. Alfredo Anzani)

Milano, 17/07/2014
Numero del registro dei pareri del CE: 57/INT/2014
Copia conforme agli atti originali depositati presso la segreteria del Comitato Etico OSR.

XUNTA DE GALICIA
CONSELLERÍA DE SANIDADE
Secretaría Xeral Técnica

Secretaria Técnica
Comité Autonómico de Ética da Investigación de Galicia
Secretaria Xeral. Consellería de Sanidade
Edificio Administrativo San Lázaro
15703 SANTIAGO DE COMPOSTELA
Tel: 881546425. Correo-e: ceic@sergas.es

galicia

DICTAMEN DEL COMITÉ DE ÉTICA DE LA INVESTIGACIÓN DE SANTIAGO-LUGO

Guillermo José Prada Ramallal, Secretario del Comité de Ética de la Investigación de Santiago-Lugo,

CERTIFICA:

Que este Comité evaluó en su reunión del día 21 de diciembre de 2017 el estudio**:**

Título: Identificación de marcadores de diagnóstico, pronóstico y seguimiento mediante el análisis de Biopsia Líquida en pacientes con cáncer
Promotor*:* Rafael López López
Tipo de estudio: Outros
Versión: Versión 1 de 31 de Octubre de 2017
Código del Promotor:
Código de Registro: 2017/538

Y, tomando en consideración las siguientes cuestiones:

- La pertinencia del estudio, teniendo en cuenta el conocimiento disponible, así como los requisitos legales aplicables, y en particular la Ley 14/2007, de investigación biomédica, el Real Decreto 1716/2011, de 18 de noviembre, por el que se establecen los requisitos básicos de autorización y funcionamiento de los biobancos con fines de investigación biomédica y del tratamiento de las muestras biológicas de origen humana, y se regula el funcionamiento y organización del Registro Nacional de Biobancos para investigación biomédica, la ORDEN SAS/3470/2009, de 16 de diciembre, por la que se publican las Directrices sobre estudios Postautorización de Tipo Observacional para medicamentos de uso humano, y la Circular nº 07/2004, de investigaciones clínicas con productos sanitarios.
- La idoneidad del protocolo en relación con los objetivos del estudio, justificación de los riesgos y molestias previsibles para el sujeto, así como los beneficios esperados.
- Los principios éticos da Declaración de Helsinki vigente.
- Los Procedimientos Normalizados de Trabajo del Comité.

Emite un dictamen **FAVORABLE** para la realización del estudio **por el/la investigador/a del centro**:

Centros	**Investigadores Principales**
C.H. Universitario de Santiago	Rafael López López, Laura Muinelo Romay, Roberto Díaz Peña

En Santiago de Compostela, a 28 de diciembre 2017.

El Secretario del Comité Territorial de Ética de la Investigación de Santiago Lugo,

Guillermo José Prada Ramallal

XUNTA DE GALICIA
CONSELLERÍA DE SANIDADE
Secretaría Xeral Técnica

Secretaria Técnica
Comité Autonómico de Ética da Investigación de Galicia
Secretaria Xeral. Consellería de Sanidade
Edificio Administrativo San Lázaro
15703 SANTIAGO DE COMPOSTELA
Tel: 881546425. Correo-e: ceic@sergas.es

galicia

Guillermo José Prada Ramallal, Secretario del Comité de Ética de la Investigación de Santiago-Lugo,

HACE CONSTAR QUE:

1.- El Comité Territorial de Ética de la Investigación de Santiago-Lugo cumple tanto en su composición como en sus PNTs los requisitos legales vigentes (RD 1090/2015 de ensayos clínicos, y la Ley 14/2007 de Investigación Biomédica).

2.- La composición actual del Comité Territorial de Ética de la Investigación de Santiago-Lugo es:

- **Juan Manuel Vázquez Lago (Presidente).** Médico especialista en Medicina Preventiva y Salud Pública. Área de Gestión Integrada de Santiago**.**
- **Pilar Rodríguez Ledo (Vicepresidenta).** Médico especialista en Medicina Familiar y Comunitaria. Área de Gestión Integrada de Lugo.
- **Guillermo José Prada Ramallal (Secretario).** Médico especialista en Farmacología Clínica. Área de Gestión Integrada de Santiago. Fundación Ramón Domínguez.
- **Lorenzo Armenteros del Olmo (Vicesecretario).** Médico especialista en Medicina Familiar y Comunitaria. Área de Gestión Integrada de Lugo.
- **Francisco Campos Pérez.** Biólogo. Instituto de Investigación Sanitaria de Santiago de Compostela.
- **Rosana Castelo Domínguez.** Farmacéutica de Atención Primaria. Área de Gestión Integrada de Santiago.
- **Ricardo García Martínez.** Licenciado en Derecho. Área de Gestión Integrada de Lugo.
- **Jaime Gulín Dávila**. Farmacéutico especialista en Farmacia Hospitalaria. Área de Gestión Integrada de Lugo.
- **Victor Herrán Carreira.** Paciente. ADIL-Asociación de Diabéticos Lucense.
- **María Jesús Lamas Díaz.** Farmacéutica especialista en Farmacia Hospitalaria. Área de Gestión Integrada de Santiago.
- **Carlos Rodríguez Moreno.** Médico especialista en Farmacología Clínica. Área de Gestión Integrada de Santiago.
- **Rafael Carlos Vidal Pérez.** Médico especialista en Cardiología. Área de Gestión Integrada de Lugo.
- **María Jesús Wandosell Picatoste.** Enfermera. Área de Gestión Integrada de Santiago.

Para que conste donde proceda, y a petición del promotor/investigador, en Santiago de Compostela, a 28 de diciembre de 2017.

El Secretario del Comité Territorial de Ética de la Investigación de Santiago Lugo,

Guillermo José Prada Ramallal

ANNEX III. Ethical approval and Material Transfer Agreement for biological samples.

Dept. of Radiology and Bio-X program
E150, Clark Center, School of Medicine
Stanford University

Materials Transfer
(Non-Profit Recipients)

Investigator Name	Department	Date
Sanjiv Sam Gambhir (M.D., Ph.D)	Dept. of Radiology	08/29/2018
Recipient Investigator	**Recipient Institution**	**Date**
María de la Fuente Freire, PhD	Consorcio Centro de Investigación Biomédica en Red, M.P. (CIBER)	09/07/2018

The material described below is being provided to you by Sanjiv Sam Gambhir, Director, Molecular Imaging Program at Stanford (MIPS), Dept. of Radiology, School of Medicine at the Stanford University for research purposes in your laboratory only. The material is experimental in nature and must be used with prudence and appropriate caution, since not all of its characteristics are known. **The material is provided without warranty of merchantability or fitness for a particular purpose or any other warranty, express or implied. The material is provided without representation or warranty that the use of the material will not infringe any patent or other proprietary right.** It cannot be used for any commercial purpose or for work in human subjects, or diagnostic testing. Should the use of this material result in one or more scientific publication(s) you should acknowledge in the paper(s) that the material was given to you by the investigator mentioned above. The material must not be distributed to other laboratories without Investigator's prior consent.

Description of the material provided
pBAD-RLuc8

I have received the material listed above and agree to abide by the conditions under which it was provided to me.

Signed: (Recipient Investigator)	Date
	09/07/2018

Approved: Office of Technology Licensing, Stanford University
By: _____
Date: 9/17/18

BRIAN HUANG
INDUSTRIAL CONTRACTS OFFICER

Recipient Institution Approval:

Signed: Manuel Sánchez Delgado	Date
	09/07/2018

ANNEX IV. Licenses and certificates to perform the preclinical experimental work.

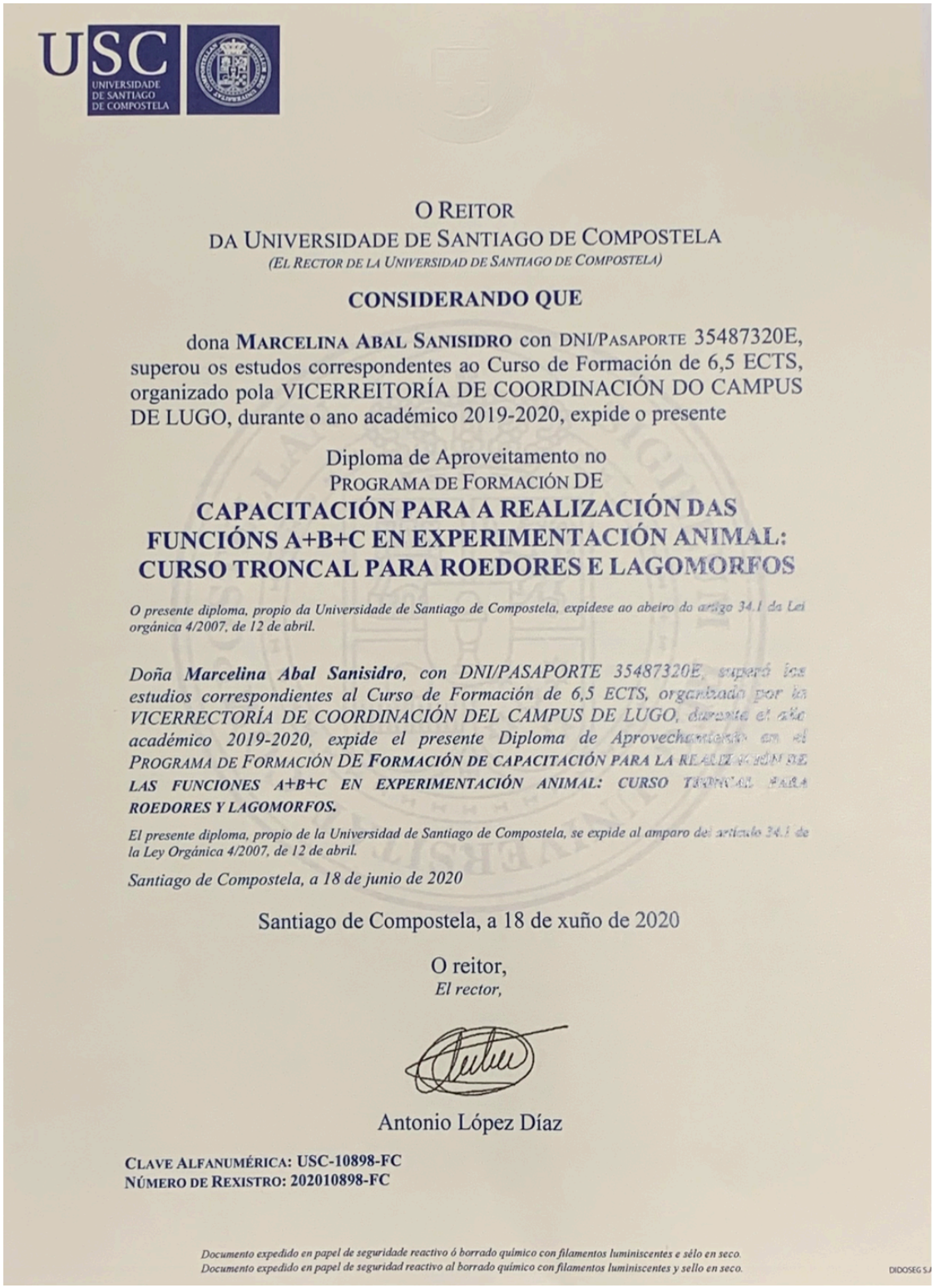

USC
UNIVERSIDADE DE SANTIAGO DE COMPOSTELA

O REITOR
DA UNIVERSIDADE DE SANTIAGO DE COMPOSTELA
(EL RECTOR DE LA UNIVERSIDAD DE SANTIAGO DE COMPOSTELA)

CONSIDERANDO QUE

dona **MARCELINA ABAL SANISIDRO** con DNI/PASAPORTE 35487320E, superou os estudos correspondentes ao Curso de Formación de 6,5 ECTS, organizado pola VICERREITORÍA DE COORDINACIÓN DO CAMPUS DE LUGO, durante o ano académico 2019-2020, expide o presente

Diploma de Aproveitamento no
PROGRAMA DE FORMACIÓN DE
CAPACITACIÓN PARA A REALIZACIÓN DAS FUNCIÓNS A+B+C EN EXPERIMENTACIÓN ANIMAL: CURSO TRONCAL PARA ROEDORES E LAGOMORFOS

O presente diploma, propio da Universidade de Santiago de Compostela, expídese ao abeiro do artigo 34.1 da Lei orgánica 4/2007, de 12 de abril.

*Doña **Marcelina Abal Sanisidro**, con DNI/PASAPORTE 35487320E, superó los estudios correspondientes al Curso de Formación de 6,5 ECTS, organizado por la VICERRECTORÍA DE COORDINACIÓN DEL CAMPUS DE LUGO, durante el año académico 2019-2020, expide el presente Diploma de Aprovechamiento en el PROGRAMA DE FORMACIÓN DE **FORMACIÓN DE CAPACITACIÓN PARA LA REALIZACIÓN DE LAS FUNCIONES A+B+C EN EXPERIMENTACIÓN ANIMAL: CURSO TRONCAL PARA ROEDORES Y LAGOMORFOS.***

El presente diploma, propio de la Universidad de Santiago de Compostela, se expide al amparo del artículo 34.1 de la Ley Orgánica 4/2007, de 12 de abril.

Santiago de Compostela, a 18 de junio de 2020

Santiago de Compostela, a 18 de xuño de 2020

O reitor,
El rector,

Antonio López Díaz

CLAVE ALFANUMÉRICA: USC-10898-FC
NÚMERO DE REXISTRO: 202010898-FC

Documento expedido en papel de seguridade reactivo ó borrado químico con filamentos luminiscentes e sélo en seco.
Documento expedido en papel de seguridad reactivo al borrado químico con filamentos luminiscentes y sello en seco.

DIDOSEG S.A

CLAVE ALFANUMÉRICA: USC-10898-FC **NÚMERO DE REXISTRO: 202010898-FC**

FORMACIÓN CONTINUA

Reverso do Diploma de Aproveitamento no PROGRAMA DE FORMACIÓN EN FORMACIÓN DE CAPACITACIÓN PARA A REALIZACIÓN DAS FUNCIÓNS A+B+C EN EXPERIMENTACIÓN ANIMAL: CURSO TRONCAL PARA ROEDORES E LAGOMORFOS, expedido a dona **MARCELINA ABAL SANISIDRO**, con DNI/PASAPORTE 35487320E, superado no ano académico 2019-2020.

*Reverso del Diploma de Aprovechamiento en el PROGRAMA DE FORMACIÓN EN FORMACIÓN DE CAPACITACIÓN PARA LA REALIZACIÓN DE LAS FUNCIONES A+B+C EN EXPERIMENTACIÓN ANIMAL: CURSO TRONCAL PARA ROEDORES Y LAGOMORFOS, expedido a doña **Marcelina Abal Sanisidro**, con DNI/PASAPORTE 35487320E, superado en el año académico 2019-2020.*

CONTIDOS DO CURSO	ECTS*	CONTENIDOS DEL CURSO
Lexislación nacional	0,1	Legislación nacional
Ética, benestar animal e as 3 Rs	0,2	Ética, bienestar animal y las Rs
Bioloxía básica nivel 1	0,4	Biología básica nivel 1
Coidado, saúde e manexo dos animais nivel 1	0,5	Cuidado, salud y manejo de los animales nivel 1
Recoñecemento da dor, sufrimento e angustia	0,3	Reconocimiento del dolor, sufrimiento y angustia
Métodos incruentos de sacrificio nivel 1	0,2	Métodos incruentos de sacrificio nivel 1
Bioloxía básica nivel 2	0,4	Biología básica nivel 2
Métodos incruentos de sacrificio nivel 2	0,4	Métodos incruentos de sacrificio nivel 2
Procedementos mínimamente invasivos sen anestesia nivel 1	0,6	Procedimientos mínimamente invasivos sin anestesia nivel 1
Procedementos mínimamente invasivos sen anestesia nivel 2	1	Procedimientos mínimamente invasivos sin anestesia nivel 2
Anestesia para procedementos menores	0,5	Anestesia para procedimientos menores
Anestesia avanzada para intervencións quirúrxicas ou procedementos prolongados	1,2	Anestesia avanzada para intervenciones quirúrgicas o procedimientos prolongados
Principios da cirurxía	0,7	Principios da cirugía

Este Diploma expídese unha vez verificado que a interesada reúne os requisitos para a súa obtención.
Este Diploma se expide una vez verificado que la interesada reúne los requisitos para su obtención.

A xefa da Sección de Títulos,
La jefa de la Sección de Títulos,

María Salomé García Rielo

Este diploma queda asentado co número USC-10898-FC do Libro de Rexistro Número 5 de Expedición e Entrega de Diplomas de Formación Continua co nº de expediente **202010898-FC**.

Este diploma queda asentado con el número USC-10898-FC del Libro de Registro Número 5 de Expedición y Entrega de Diplomas de Formación Continua con el nº de expediente **202010898-FC**

Santiago de Compostela, 25 de xuño de 2020

A xefa do Negociado de Títulos,
La jefa del Negociado de Títulos,

María das Mercedes Alonso Pequeño

(*) 1 ECTS (European Credit Transfer and Accumulation System) equivale a 25 horas de traballo total do alumno. No caso de realizar prácticas en empresas, cada 25 horas de presenza na entidade equivale a 1 ECTS.
1 ECTS (European Credit Transfer and Accumulation System) equivale a 25 horas de trabajo total del alumno. En el caso de realizar prácticas en empresas, cada 25 horas de presencia en la entidad equivale a 1 ECTS.

MARÍA DEL MAR YLLERA FERNÁNDEZ, con DNI 05897752T, Profesora Titular de Universidad y directora del "Programa Formativo en Experimentación Animal", en el que se integra el curso "Programa de Formación de capacitación para a realización das funcións a+b+c en experimentación animal: curso troncal para roedores e lagomorfos", realizado en Lugo desde el 6 de noviembre de 2019 al 12 de marzo del 2020, con un total de 65 horas de docencia teórico-práctica,

INFORMA

Que Doña MARCELINA ABAL SANISIDRO, con DNI 35487320E, ha asistido al mismo como alumna y superado los exámenes correspondientes a las funciones a, b y c.

Para que conste a los efectos oportunos

Lugo, 2 de noviembre de 2020

YLLERA FERNANDEZ MARIA DEL MAR - 05897752T

Firmado digitalmente por YLLERA FERNANDEZ MARIA DEL MAR - 05897752T
Nombre de reconocimiento (DN): c=ES, serialNumber=IDCES-05897752T, givenName=MARIA DEL MAR, sn=YLLERA FERNANDEZ, cn=YLLERA FERNANDEZ MARIA DEL MAR - 05897752T
Fecha: 2020.11.02 10:29:20 +01'00'

Fdo: María del Mar Yllera Fernández

MINISTERIO
DE CIENCIA
E INNOVACIÓN

CSIC

UAM
Universidad Autónoma
de Madrid

INSTITUTO DE INVESTIGACIONES BIOMÉDICAS "ALBERTO SOLS", IIBM

CERTIFICADO DEL CENTRO DE TRABAJO

Dña. **Marcelina Abal Sanisidro** ha realizado prácticas supervisadas en el Animalario del INSTITUTO DE INVESTIGACIONES BIOMÉDICAS ALBERTO SOLS (CSIC – UAM), registrado con el código REGA ES280790000188 realizando las funciones de CUIDADO DE LOS ANIMALES (a), EUTANASIA DE LOS ANIMALES (b) y REALIZACION DE PROCEDIMIENTOS (c) en el marco del proyecto autorizado con el número **PROEX 294/19** durante 160 horas.

- Función a: 25 horas
- Función b: 15 horas
- Función c: 120 horas

Las funciones las ha ejercido con **ROEDORES** de manera satisfactoria.

El periodo de prácticas que aquí se refleja no es parte de un curso y los animales empleados han sido los utilizados en el marco de trabajo habitual del centro, no destinados exclusivamente a formación, en aras del principio de Reducción.

Sus prácticas han sido supervisadas por **Laura Ruiz Cañas**, que cuenta con la competencia para las funciones supervisadas, y que ha velado para que en el desarrollo de las mismas los animales no sufran ningún daño adicional innecesario, en aras del principio de Refinamiento.

El interesado ha sido evaluado en las funciones que solicita, considerándose que está capacitado para realizarlas de forma autónoma y sin supervisión.

Madrid, 23 de febrero de 2023

INSTITUTO DE INVESTIGACIÓN BIOMÉDICAS "ALBERTO SOLS" CSIC UAM

Fdo.: Isabel Ocaña Fernández
Responsable Administrativo IIBM

Fdo.: Marta Miró Murillo
Responsable de Bienestar Animal
Veterinario (nºcol: 7837)

http://www.iib.uam.es

C/ Arturo Duperier, nº 4
28029 MADRID ESPAÑA
TEL.: 91 585 4400

Proteins are biomacromolecules that catalyze multiple biological processes, being promising therapeutic agents. However, issues such as enzymatic degradation, short half-life and low bioavailability make their use in the clinic inefficient. In this respect, nanotechnology arises as a potent tool to overcome these limitations, offering protection of cargo, increased bioavailability and reduced immunogenicity. Within this frame, the main aim of this thesis is the development of novel protein nanotherapeutics by exploring several bioconjugation strategies, providing evidence of their benefits in cancer therapy and gene editing. Altogether, this thesis sheds light on the potential of a versatile nanoplatform for protein delivery as translational medicines and open the door for further application in advanced therapies.